KU LEUVEN

Arenberg Doctoral School
Faculty of Science

A Comprehensive Study on PCCD-based Materials: Morphology, Crystallization and Physical Ageing

Mouna Hamid

Supervisor(s):
Prof. Bart Goderis
Prof. Peter Van Puyvelde

Dissertation presented in partial fulfillment of the requirements for the degree of Doctor of Science

November 2025

A Comprehensive Study of PCCD-based Materials: Morphology, Crystallization and Physical ageing

Mouna HAMID

Supervisor(s):
Prof. B. Goderis
Prof. P. Van Puyvelde

Members of the Examination Committee:
Prof. E. Debroye
Prof. W. Thielemans
Prof. S. Van Cleuvenbergen
Prof. R. Cardinaels
Prof. L. Pitet
L. Gardet

Dissertation presented in partial fulfilment of the requirements for the degree of Doctor of Science

November 2025

© 2025 KU Leuven – Faculty of Sciences
Uitgegeven in eigen beheer, Mouna Hamid, Leuven

Alle rechten voorbehouden. Niets uit deze uitgave mag worden vermenigvuldigd en/of openbaar gemaakt worden door middel van druk, fotokopie, microfilm, elektronisch of op welke andere wijze ook zonder voorafgaandelijke schriftelijke toestemming van de uitgever.

All rights reserved. No part of the publication may be reproduced in any form by print, photoprint, microfilm, electronic, or any other means, without written permission from the publisher.

Preface

Dearest Gentle Reader,

The time has finally arrived, my PhD journey has reached its end.
Before diving into this thesis, I want to take the time to show my gratitude to the people who contributed directly or indirectly to this work and to my PhD experience.

First of all, I want to express my deep appreciation to **Bart** Goderis, my promotor, and in the summer, my office mate. Bart, you are a great scientist and teacher. You know everything about X-rays and you can explain very complex concepts in such an easy way that the listener thinks they understand everything… but actually doesn't. Luckily, your patience and willingness to repeat things many (many) times means that I am now also completely absorbed (or scattered) by the X-ray world. You gave me the opportunity to go to the ESRF multiple times, and even though it is usually very hard work, I always enjoyed these trips a lot. I especially remember the first time I went where we talked the whole drive to Grenoble and back about science, family, interests, frustrations, ... Thank you for always giving me the space to express myself, for always making time to listen, for encouraging me and for being… a great human being.

I would also like to express my gratitude to Peter Van Puyvelde, my co-promotor, and the other members of my **examination committee**: Stijn Van Cleuvenbergen, Wim Thielemans, Ruth Cardinaels, Louis Pitet and Ludovic Gardet, for reading my thesis, showing interest in my work and giving constructive feedback. Thank you to Elke Debroye for chairing my defense.

This PhD manuscript is the result of my hard work and effort, yes. But it would have been so much harder (and so much less fun) without the people I have in my life. I want to take some time to thank them.

First of all, my colleagues: Bronwen, Alberto, Ilya and Hiromi. After a few years of being alone in the office, it was so nice to have it filled with your laughter and positive energy. I couldn't have wished for better colleagues to eat lunch with (Enjoy! Smakelijk! Bon appetit! Buon appetito! いただきます! Приятного!), to attend conferences with and to spend weekends together at the sea or in the Ardennes. **Bronwen**, it was maybe not the best idea to sit next to each other in the office (only one look to each other could result in hours of discussion or therapy sessions) but I wouldn't want it any other way. Even on the hard days you keep smiling, even when it's okay not to. You are a force of nature, never forget that.

The days where I was determined to have a productive day, I would come in early and find **Alberto**. We would work in silence for hours without disturbing each other (as it should!), but I knew that once I turned my chair to him and started talking, there would be no more work done. Sometimes, you can say you have to work, Alberto! But never change who you are, you have a pure heart.

Ilya, as your mentor for your master's thesis, I was impressed by your scientific mindset. As my colleague, you were the one I could turn to for new input or help to make sense of my data, or just someone to talk to. We have completely different interests and hobbies, yet we bonded anyway. I appreciate you a lot. And thank you for bringing Emy into our group!

Hiromi, you're the ambiance maker of the office. You arrived in our group like a bolt of lightning, full of energy. You immediately engaged with everyone and asked all sorts of questions. You love sharing things about Japanese culture, and after my trips to Japan, it brought us closer. Keep this light in you and continue spreading it. Don't let this PhD intimidate you, it's only temporarily.

Thank you, colleagues, for being genuinely kind and respectful people, always there for me. As the mom of the group, I want to say: I'm very proud of you.

I also want to thank the SMaRT people, especially **Andrea, Govind, Anja** and Carlo. Thank you for taking the time to talk and help me whenever I had questions. **Carlo**, You were always there when I had technical issues with my instruments and you always found a solution. These moments often turned into long conversations in the hallway, going from "thermocouples" to "Tomorrowland" to "thesis writing" to plain gossip. You could make me laugh even when I was in a bad mood. I truly want to thank you for everything. I hope we will still see each other in the future, Lab Dad.

Then there is my ex-SMaRT colleague, **Charlotte**. When I look back on our time together, I mainly think of Grenoble. During the night shifts where everything went wrong, we still found the energy to laugh until it hurt. Being around you felt natural and often very needed. Thank you for your kindness and your book recommendations!

Apart from my direct colleagues, other friends on campus shaped my PhD experience. **Aline**, we met during our studies and lived together, so our friendship started well before the PhD. You have a very logical mindset, you are hardworking and always ready to help. But once I really got to know you, I discovered another side: the loving, thoughtful and empathetic Aline. You made my PhD years so much nicer. Especially when I arrived in the morning and saw you at your desk, I knew I would get the classic 2pm "koffie?" Skype message where we would complain about thesis students and promotors. Thank you for that.

Lilly, Lilly, Lilly… Just thinking of you makes me smile. You are a special little creature living in your own little world — and I love you for it. We met almost by force (two people alone in an aula!) and it was love at first sight. We spent so much time in our private office during our master thesis and even when it became mine

during the PhD (oops, sorry Bart). You are a sparkle everyone needs in their life, and I'm so happy you're in mine. Love you to Australia and back.

Thanks to Lilly, I also met **Yen** and **Charlotte** (the one with the dog). I loved our craft nights, sleepovers, dance parties, food parties (all at Charlotte's place) and also our Paris and Morocco trips. These moments made me forget my Excel problems and paper stress. Thank you, girls!

What also helped me forget my worries was dancing, especially because I did it with **Charlotte** (the one I met in Indonesia). We saw each other once a week, only a few minutes to talk, but still enough to share all our life updates. We see each other less now, but I know you'll always be a constant in my life. You are a truly beautiful person, thank you for being there.

And now, the most difficult part. Not because I don't know what to write about these people, but because I don't know how to thank them for everything they've done for me.

Sara, you started as my thesis student and ended up as my sister. We bonded over science (and its struggles), got closer over our Moroccan roots, and connected deeply through our shared values and principles. You are one of the strongest women I know, hardworking with the biggest heart. When I think of someone who "made it", I think of you. When I think of someone who would sacrifice everything for her family, I think of you. You make me a better person — you're an inspiration. Stay as you are… maybe with just a little less chaos.

Ik zou ook graag mijn Vlaamse familie bedanken, en in het bijzonder mijn **oma**. Dank je, oma, dat je genoeg vertrouwen in mij had om mij de laatste paar jaren maar een paar opmerkingen te geven over het feit dat ik "altijd op vakantie ben en niet werk" of wanneer ik "nu eindelijk eens mijn studies ga afronden". Dus hierbij speciaal voor jou: ik ben eindelijk klaar voor het "échte leven"! Dank je om mij te blijven motiveren, oma, en voor de koffietjes bij Aperoni.

My Moroccan family (spread across different countries) has a special place in my heart. Même si on ne se voit que quelques fois par an, ils sont les sœurs et le frère que je n'ai jamais eus, et ma seconde maman et mon second papa: **Oumayma, Lina, Adam, Salima & Mehdi**. Loin des yeux, loin du cœur? Non, non: loin des yeux, encore plus proche du cœur. Merci pour votre soutien moral et pour tous les fous rires. Vous êtes ma safe space. Je vous aime énormément.

Rachida et Vincent, vous faites désormais partie de ma famille, tout comme vous m'avez accueillie dans la vôtre. Merci pour vos mots doux, votre soutien, pour toujours prendre de mes nouvelles, pour votre bienveillance et pour m'accepter comme l'une des vôtres.

My family also expanded in the most unexpected way, through a meeting four years ago. That meeting led to a (very) long-distance relationship of two years (something

I always said I would never do) and to a new adventure in Switzerland. **Nabil**, merci pour tout ce que tu as fait et fais encore pour moi. Tu as toujours été là, même à 10 000 km. Tu trouves toujours le moyen de me faire rire, même dans les moments les plus stressants, comme ces derniers mois. Tu as fait preuve d'une immense patience, tu m'as toujours motivée, tu as mis mes besoins en premier et je t'en serai toujours reconnaissante. Une partie de ce doctorat te revient. Excited to see what life will bring us! Je t'aime.

Mama, Papa, je ne sais même pas par où commencer. C'est grâce à vos sacrifices et à votre soutien que j'ai pu faire ce que je voulais faire et devenir la personne que je voulais être. Vous m'avez ouvert des portes qui étaient fermées pour vous. Vous m'avez encouragée à bien étudier, à être respectueuse et à devenir indépendante. Je n'ai jamais manqué de rien, surtout pas d'amour. Ce doctorat est le fruit de votre travail autant que du mien, et c'est pour cela qu'il vous appartient autant qu'à moi. Je vous aime.

And last but not least,

.

Yours Truly,

dr. Mouna Hamid

Abstract

Amphora™ SP1621 was recently introduced to the market by Eastman Chemical Company as a material for selective laser sintering (SLS). SLS, one of the most widely used additive manufacturing techniques, employs a high-power laser to sinter polymer powders in a layer-by-layer fashion, producing solid printed parts. The method is well known for its ability to fabricate components with complex geometries and favorable mechanical properties. Amphora SP1621 is marketed as recyclable and, being a thermoplastic elastomer, it offers elastomeric properties—an attractive feature in a market largely dominated by thermoplastic materials such as PA12 and PA11.

Amphora SP1621 is a semi-crystalline segmented copolyesterether consisting of crystallizable poly(1,4-cyclohexylidene cyclohexane-1,4-dicarboxylate) (PCCD) blocks and amorphous polytetrahydrofuran (PTHF) blocks. PCCD as a homopolymer is known as a crystallizable, tough, and rigid polyester. However, literature on PCCD-PTHF block copolymers is very limited, and almost no data are available on their semi-crystalline morphology or crystallization kinetics. This lack of information hinders the optimization of thermal processing protocols and complicates property assessments of Amphora SP1621. Furthermore, PCCD can also be obtained in its amorphous form. Amorphous polymers are notoriously difficult to print via SLS as this technique tends to induce physical ageing. In the context of SLS, two thermal phenomena are particularly critical for print quality: crystallization for crystallizable polymers and physical ageing for amorphous ones. Addressing these aspects provides the foundation for tuning sintering conditions, minimizing warpage, and improving recyclability.

To address these gaps, a full morphological and phase-behavior study of PCCD-PTHF was carried out using NMR, DSC, time-resolved SAXS/WAXS, FSC, POM, and AFM. At a cooling rate of 10 K/min, the copolymer was found to crystallize in a triclinic unit cell via a two-step mechanism: primary crystallization produced spherulites with amorphous pools between primary lamellar stacks, followed by secondary crystallization forming new stacks in these amorphous regions with lamellae of the same thickness.

To isolate the crystalline behavior of PCCD without the influence of amorphous PTHF, a PCCD homopolymer was synthesized. It also crystallized into spherulites from lamellae, but the extent of secondary crystallization was far less pronounced than in the copolymer.

Both PCCD and PCCD-PTHF were found to be thermally unstable under prolonged high-temperature annealing. The main mechanisms were identified as transesterification for PCCD-PTHF and a combination of condensation reactions and isomerization for PCCD, increasing the molar mass. Stabilization strategies were developed and successfully applied, which was crucial for enabling reliable crystallization kinetics studies requiring long heating times.

Crystallization kinetics were then investigated using FSC, POM, and SAXS/WAXS, with a focus on PCCD-PTHF. This material exhibited two distinct temperature regimes, where different nucleation pathways dominated depending on the crystallization temperature when crystallization occurred isothermally from the melt or during non-isothermal cooling at different rates. This bimodal behavior was absent in crystallizations from the glassy state and in PCCD homopolymer, which crystallized similarly regardless of whether it originated from the melt or glass. To complete the analysis, Amphora SP1621 powder was also studied; unlike PCCD-PTHF, it did not display strong rate dependence in the studied rate range, likely due to additives present in the commercial formulation.

Finally, a low-molecular-weight, fully amorphous PCCD was synthesized to study physical ageing via FSC. Ageing, defined as structural relaxation in the supercooled liquid state near and below the glass transition, leads to embrittlement of the material. While polystyrene has been extensively studied in this context, no data previously existed for PCCD-based materials. Therefore, PS samples of varying characteristics were included as references. Temperature-dependent relaxation behavior was mapped, revealing that, similar to PS, PCCD relaxes through more complex mechanisms far below T_g than can be explained by the standard α-relaxation alone.

Overall, this study provides the first comprehensive understanding of the crystallization, morphology, and ageing behavior of PCCD–PTHF systems and their relevance to SLS processing. These insights offer valuable guidelines for the design

and stabilization of next-generation copolyester-based SLS materials with improved printability and mechanical performance.

Beknopte samenvatting

Amphora™ SP1621 werd recentelijk door Eastman Chemical Company op de markt gebracht als materiaal voor Selective Laser Sintering (SLS). SLS, één van de meest gebruikte 3D-printingtechnieken, maakt gebruik van een krachtige laser om polymeerpoeders laag voor laag te sinteren tot vaste geprinte onderdelen. De methode staat bekend om haar vermogen om componenten met complexe geometrieën en gunstige mechanische eigenschappen te vervaardigen. Amphora SP1621 wordt gepresenteerd als recycleerbaar en biedt, als thermoplastisch elastomeer, elastomeerachtige eigenschappen, een aantrekkelijk kenmerk in een markt die grotendeels wordt gedomineerd door thermoplastische materialen zoals PA12 en PA11.

Amphora SP1621 is een semikristallijn gesegmenteerd copolyesterether, bestaande uit kristalliseerbare poly(1,4-cyclohexylideen cyclohexaan-1,4-dicarboxylaat) (PCCD)-blokken en amorfe polytetrahydrofuraan (PTHF)-blokken. PCCD als homopolymeer staat bekend als een kristalliseerbaar en rigide polyester. De literatuur over PCCD-PTHF-blokcopolymeren is echter zeer beperkt, en er bestaan zo goed als geen gegevens over hun semikristallijne morfologie of kristallisatiesnelheden. Dit gebrek aan informatie belemmert de optimalisatie van thermische verwerkingsprotocollen en maakt het lastig om materiaaleigenschappen correct te beoordelen. Bovendien kan PCCD ook in amorfe vorm worden verkregen. Amorf polymeer zijn moeilijk te printen via SLS, aangezien met deze techniek *physical ageing* van het polymer kan optreden. In de context van SLS zijn twee thermische verschijnselen cruciaal voor de printkwaliteit: kristallisatie bij kristalliseerbare polymer en *physical ageing* bij amorfe polymeren. Het onderzoeken van deze aspecten vormt de basis voor het optimaliseren van de sinteromstandigheden, het minimaliseren van vervorming en het verbeteren van de recycleerbaarheid.

Om deze kennislacunes te overbruggen, werd een uitgebreid morfologisch en fase-gedragsonderzoek uitgevoerd op PCCD-PTHF met behulp van NMR, DSC, FSC, POM, AFM and synchrotron SAXS/WAXS. Bij een koelsnelheid van 10 K/min bleek het copolymeer te kristalliseren in een trikliene eenheidscel via een tweestapsmechanisme: primaire kristallisatie leverde sferulieten met amorfe gebieden tussen de lamellaire stapels, gevolgd door secundaire kristallisatie waarbij nieuwe stapels ontstonden in deze amorfe zones.

Om het kristallisatiegedrag van PCCD zonder de invloed van amorfe PTHF te isoleren, werd een PCCD-homopolymeer gesynthetiseerd. Dit materiaal kristalliseerde eveneens in sferulieten vanuit lamellen, maar vertoonde veel minder uitgesproken secundaire kristallisatie dan het copolymeer.

Zowel PCCD als PCCD-PTHF bleken thermisch instabiel bij langdurige hoge-temperatuur-annealing. De belangrijkste degradatiemechanismen werden geïdentificeerd als transesterificatie voor PCCD-PTHF en condensatiereacties an isomerisatie voor PCCD. Stabilisatiestrategieën werden ontwikkeld en met succes toegepast, wat essentieel was om betrouwbare studies naar kristallisatiekinetiek, die langdurige verhitting vereisten, mogelijk te maken.

De kristallisatiekinetiek werd vervolgens onderzocht met FSC, POM en SAXS/WAXS, met een focus op PCCD-PTHF. Dit materiaal vertoonde twee verschillende temperatuurbereiken, waarbij verschillende nucleatiemechanismen domineerden afhankelijk bij isotherme kristallisatie vanuit de smelt of niet-isotherme kristallisatie bij verschillende koelsnelheden. Dit bimodale gedrag trad niet op bij kristallisatie vanuit de glasachtige toestand, noch bij PCCD-homopolymeer, dat op gelijkaardige wijze kristalliseerde ongeacht of het vanuit de smelt of glasfase vertrok. Ter afronding werd ook commercieel Amphora SP1621-poeder onderzocht; in tegenstelling tot PCCD-PTHF vertoonde dit materiaal geen sterke snelheidsafhankelijkheid in het onderzochte selheidsgebied, vermoedelijk door de aanwezigheid van additieven in de commerciële formulering.

Tot slot werd een laagmoleculair, volledig amorf PCCD gesynthetiseerd om *phsyical ageing* te bestuderen met behulp van FSC. *Phsyical ageing*, gedefinieerd als structurele relaxatie in de onderkoelde vloeistof nabij en onder de glasovergang, leidt tot brosheid van het polymeer. Hoewel polystyreen uitgebreid in dit kader is

onderzocht, waren er geen gegevens beschikbaar voor PCCD-gebaseerde materialen. Daarom werden PS materialen met verschillende eigenschappen gebruikt als referentie. De temperatuurafhankelijke relaxatie werd in kaart gebracht en toonde aan dat, net als PS, PCCD ontspant via meer complexe mechanismen ver onder T_g dan kan worden verklaard door enkel de klassieke α-relaxatie.

Deze studie biedt een eerste uitgebreid inzicht in het kristallisatie-, morfologie- en verouderingsgedrag van PCCD–PTHF-systemen en hun relevantie voor SLS-verwerking. Deze bevindingen leveren waardevolle richtlijnen op voor het ontwerp en de stabilisatie van nieuwe copolyester-gebaseerde SLS-materialen met verbeterde verwerkbaarheid en mechanische prestaties.

Abbreviations and Symbols

NMR	Proton Nuclear Magnetic Resonance
3D	three-dimensional
CC	Cold Crystallization
AFM	Atomic Force Microscopy
DCM	Dichloromethane
DSC	Differential Scanning Calorimetry
ESRF	European Synchrotron Radiation Facility
FSC	Fast-Scanning Calorimetry
HF	Heat Flow
SLS	Selective Laser Sintering
MRR	Melting-Recrystallization-Relting
MS	Microphase Separation
M_W	Molecular Weight
PA11	Polyamide-11
PA12	Polyamide-12
PBT	Poly(butylene)terephtalate
PC	Polycarbonate
PCCD	Poly(1,4-cyclohexylidene cyclohexane-1,4-dicarboxylate)
PCDM	Poly(1-4 cyclohexane dimethanol)
KWW	Kohlrausch-Williams-Watts
PET	Polyethylene Terephtalate
POM	Polarized Optical Microscopy
PP	Polypropylene
PS	Polystyrene
PTHF	Polytetrahydrofuran
RT	Room Temperature
SAXS	Small-Angle X-ray Scattering
SLS	Selective Laser Sintering
TGA	Thermographic Analysis

TPE	Thermoplastic Elastomer
TPU	Thermoplastic Polyurethane
TTS	Time-Temperature Superposition
USA	United-States of America
VFT	Vogel-Fulcher-Tammann
WAXS	Wide-Angle X-ray Scattering
WLF	Williams-Landel-Ferry

T	Temperature
T_m	Melting temperature
r_c	Critical radius
T_g	Glass transition temperature
$t_{1/2}$	Half-time temperature
T_a	Annealing temperature or ageing temperature
τ	Characteristic relaxation time
τ_{KWW}	KWW characteristic relaxation time
T_f	Fictive temperature
H_a	Ageing enthalpy
H_{eq}	Equilibrium enthalpy
T_{f0}	Reference fictive temperature
ϕ	Extent of ageing
y_0	Front factor
t	Time
β_{KWW}	KWW Expansion coefficient
τ_0	Front factor
T_0	Vogel Temperature
C_1	Material parameter
C_2	Material parameter
M_e	Entanglement molar mass
C_p	Heat capacity

C_{pl}	Liquid heat capacity
C_{pg}	Glassy heat capacity
M_n	Number molar mass
H_{eq}	Equilibrium enthalpy
δ	Departure from equilibrium
H_{up}	Enthalpy after up-jump experiment
H_{down}	Enthalpy after down-jump experiment
Đ	Polydispersity index
Å	Angström
l_c	Crystalline layer thickness
l_a	Amorphous layer thickness
L_p	Periodicity
N_2	Nitrogen gas
mL	Milliliter
mg	Milligram
min	Minutes
°C	Degrees Celsius
s	Seconds
T_c	Crystallization temperature
t_c	Crystallization time
$T_{c,max}$	Maximum crystallization temperature
mW	Milliwatt
T_m^0	Equilibrium melting point
µm	Micrometer
T_{gh}	Glass transition temperature upon heating
T_{gc}	Glass transition temperature upon cooling
J	Joule
g	Grams
a_T	Shift factor
β	Cooling rate
Pa	Pascal
q	Scattering vector

Contents

Preface ..... **III**
Abstract ..... **VII**
Beknopte samenvatting ..... **IX**
Abbreviations and Symbols ..... **XII**
1. Introduction and background **1**
1.1 PCCD-based materials 2
1.2 Selective Laser Sintering (SLS) as application for Amphora SP1621 4
1.3 Crystallization and physical ageing in polymers 6
1.4 Polymer crystallization 7
1.4.1 Concept 7
1.4.2 Factors influencing crystallization 11
1.5 Physical ageing in polymers 12
1.5.1 Concept 12
1.5.2 VFT/WLF: a model to describe physical ageing 14
1.5.3 Beyond the α-relaxation 16
1.6 Aims and outline 17
2. The Molecular Structure and Phase Behavior of a Segmented PCCD-PTHF Block Copolymer **19**
2.1 Introduction 21
2.2 Experimental section 23
2.2.1 Materials 23
2.2.2 Methods 23
2.3 Results and Discussion 27
2.3.1 Molecular structure of PCCD-PTHF 27
2.3.2 Block length distribution 29
2.3.3 Thermal behavior 34
2.3.4 Morphology through Polarized Optical Microscopy (POM) and Atomic Force Microscopy (AFM) 39
2.3.5 PCCD crystallography and crystallinity through WAXS 44
2.3.6 The semi-crystalline morphology by SAXS 51

2.4 Conclusions 66

3. Synthesis of PCCD and its Crystallization Behavior under Typical DSC Conditions 68

3.1 Introduction 69

3.2 Experimental section 71

3.2.1 Materials 71

3.2.2 Methods 72

3.3 Results and discussion 74

3.3.1 Synthesis 74

3.3.2 ^{1}H NMR Spectroscopy 76

3.3.3 Thermal behavior 78

3.3.4 POM 82

3.3.5 Time-resolved SAXS/WAXS 83

3.3.6 Instability of PCCD and end-capping 88

3.4 Conclusions 94

4. The Isothermal Crystallization of the Segmented PCCD-PTHF Block Copolymer and pure PCCD from the Glass Transition Temperature to the Melting Point 96

4.1. Introduction 97

4.2 Experimental section 100

4.2.1 Materials 100

4.2.2 Methods 100

4.3 Results and Discussion 106

4.3.1 Thermal stabilization or ageing of PCCD-PTHF 106

4.3.2 Overall isothermal crystallization behavior of PCCD-PTHF and PCCD 113

4.3.3 Morphology of PCCD-PTHF 122

4.4 Conclusions 128

5. Non-isothermal crystallization of PCCD-PTHF and Amphora SP1621 129

5.1 Introduction 130

5.2 Experimental section 132

5.2.1 Materials 132

5.2.2 Methods 132

5.3 Results and discussion 134

5.3.1 Cooling rate dependent crystallization in PCCD-PTHF and Amphora SP1621 134
5.3.2 FSC: extending the cooling rate range up to amorphization 143
5.4 Conclusions 145
6. Physical ageing of glassy amorphous PCCD and PS over a wide temperature range far below T_g 147
6.1 Introduction 148
6.2 Background 150
6.3 Experimental section 154
6.3.1 Materials 154
6.3.2 Methods 155
6.4 Results and Discussion 159
6.4.1 Isothermal ageing of amorphous PCCD and PS 159
6.4.2. Non-isothermal ageing of PCCD3 and PS 173
6.5 Conclusions 175
7. Conclusions and outlook 177
7.1 General conclusions 178
7.2 Outlook 181
Appendices 184
Appendix A to Chapter 2 184
Appendix B to chapter 3 189
Appendix C to Chapter 4 190
List of publications 194
Bibliography 195
Statement on the use of generative AI 209

Chapter 1

Introduction and background

This doctoral dissertation investigates the crystallization and glassy, physical ageing of poly(1,4-cyclohexylidene cyclohexane-1,4-dicarboxylate) (PCCD)-based materials, with a focus on their structure and solidification behavior. The motivation stems from the development of Amphora™ SP1621, a recyclable polymer powder designed for 3D printing and non-laser sintering applications. During the course of this work, Amphora SP1621 was identified as a PCCD-based copolymer, which highlighted the need for a deeper understanding of its morphology and thermal behavior in order to fully unlock its potential.

The overarching goal of this thesis is to establish a comprehensive understanding of PCCD and PCCD-based copolymers, while also contributing insights into experimental methods for characterizing crystallization and ageing phenomena. This introductory chapter presents the studied PCCD-based materials, outlines the basic concepts of crystallization and physical ageing, and defines the objectives addressed in the work. At the beginning of each subsequent chapter, a focused introduction and literature overview are provided to contextualize the experimental results.

1.1 PCCD-based materials

Eastman Chemical Company has recently introduced Amphora SP1621, a recyclable polyester-based sintering powder that combines high performance with thermoplastic elastomeric (TPE) behavior.[1,2] The term *recyclability* refers to the ability to reuse the unsintered portion of the powder in subsequent sintering processes without degrading the properties of the final product. Its unique property profile positions it alongside established flexible sintering materials such as thermoplastic polyurethanes (TPUs).[3] Amphora SP1621 is reported to be ideal for laser and non-laser powder-based sintering processes.[1]

Through the course of this work, Amphora SP1621 was found to be based on a semi-crystalline segmented block copolymer with poly(1,4-cyclohexylidene cyclohexane-1,4-dicarboxylate) (PCCD) (**Figure 1**) as the crystalline and polytetrahydrofuran (PTHF) as the amorphous block. To the best of our knowledge, the copolymer is only used for Amphora SP1621. The PCCD as a homopolymer is

more known and is mostly used in outdoor applications (e.g. automotive industry) thanks to its good weatherability as it does not absorb UV radiation. Photo-degradation is therefore limited compared to other polyesters such as poly(butylene)terephtalate (PBT).[4]

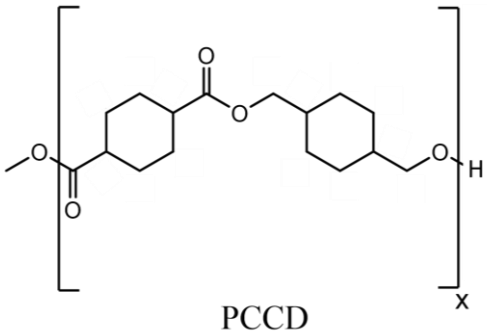


Figure 1. *Molecular structure of poly(1,4-cyclohexylidene cyclohexane-1,4-dicarboxylate) (PCCD).*

To gain a comprehensive understanding of the material's behavior, four PCCD-based systems were selected, each investigated for targeted aspects that together contribute to building the overall picture (**Figure 2**): i) the commercial powder Amphora SP1621, ii) the specific PCCD-PTHF block copolymer it is based upon, iii) a semi-crystalline PCCD and iv) a glassy, amorphous PCCD. These systems have been only sparsely studied in terms of structure–property relationships, which motivated their selection as the central focus of this thesis.

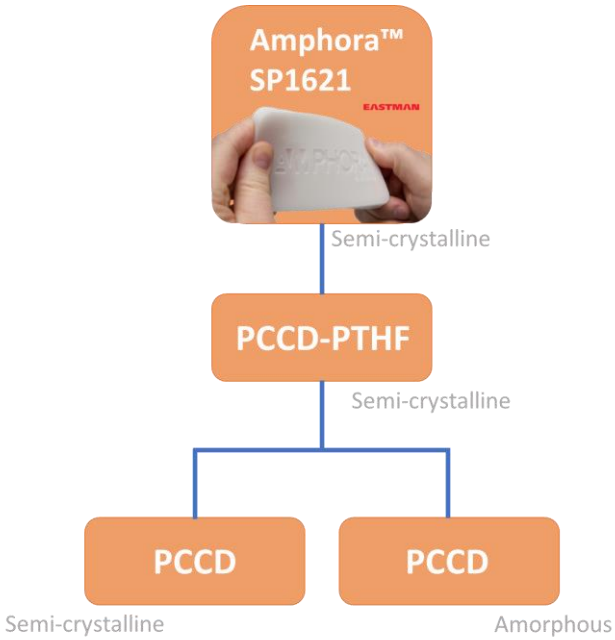


***Figure 2**. Overview of the PCCD-based materials used in the thesis. More details can be found in Chapters 2-6.*

1.2 Selective Laser Sintering (SLS) as application for Amphora SP1621

SLS is one of the most widely used Additive Manufacturing (AM) techniques, with polymer-powder SLS being particularly attractive due to its ability to produce parts with complex geometries and good mechanical performance.[5]

A typical SLS setup (**Figure 3**), consists of a powder bed (or "build bed"), feed supplies, a CO_2 laser, mirrors, a leveling roller, and pistons. In such a process, the powder bed and feed supplies are filled with the polymer material in the form of powder. Then, the powder bed is heated to a certain bed temperature (T_{bed}) and kept at that temperature during the whole sintering procedure. When this is done, the actual layer-by-layer sintering starts, which consists of three continuously repeating steps: 1) the pistons lower the build bed and push one of the power supplies up so that the levelling roller deposits a thin layer of powder in the build bed, 2) the freshly deposited powder is heated to T_{bed} and 3) the laser selectively melts the polymer particles in the

build that belong to the printed part.[6] These steps are repeated until the complete part is built, after which the powder bed is cooled to room temperature and the printed part is retrieved.

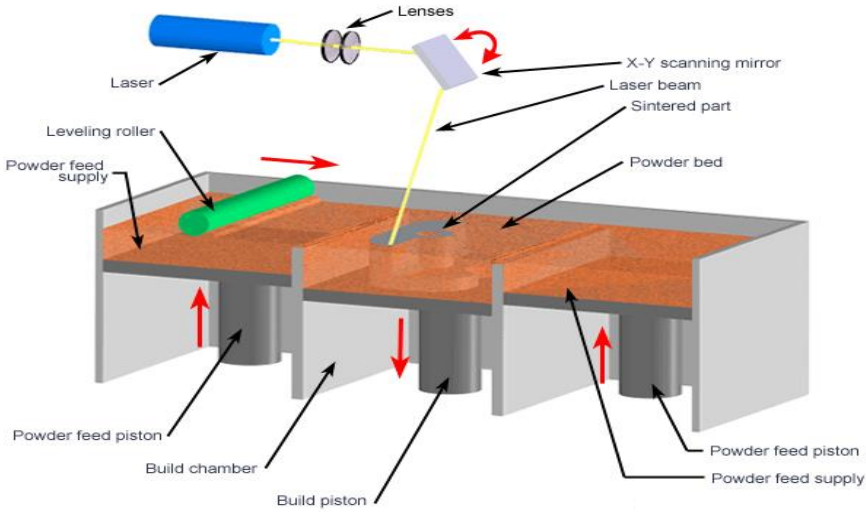


Figure 3. *Typical SLS setup with the most important parts indicated.*[7]

Polymeric materials must fulfil an extensive list of requirements to produce high-quality parts in a sustainable manner, including controlled particle size, good flowability, low zero-shear viscosity, strong particle coalescence, thermal stability, a broad processing window, and recyclability of unfused powder. To some extent, these properties can be enhanced via material modification. For instance, particle coalescence can be increased by increasing the polymer's dispersity, which also influences zero-shear viscosity.[8] However, despite these strategies, only a limited set of polymers can currently be processed successfully in selective laser sintering.

Amphora SP1621 is a promising candidate. It combines a broad processing window with recyclability of unfused powder, minimal post-processing requirements, and mechanical properties comparable to PA12, the benchmark SLS polymer.[1,9,10] Its thermoplastic elastomer (TPE) character further imparts toughness, flexibility, abrasion resistance, and fatigue resistance, positioning it as a potential alternative to thermoplastic polyurethanes (TPUs).

Semi-crystalline polymers are the most used polymers in SLS.[11] Their T_{bed} is typically set just above the melting temperature (T_m), where viscosity is sufficiently low to allow extensive particle coalescence, resulting in mechanically strong parts. By contrast, **amorphous** polymers require T_{bed} just below the glass transition temperature (T_g) to preserve powder integrity. Their high viscosity just below T_g limits particle coalescence, leading to incomplete consolidation, high porosity, and lower mechanical strength. While higher energy input can enhance consolidation, it often leads to over-sintering, warping, or even material degradation. [11]

1.3 Crystallization and physical ageing in polymers

Amphora SP1621 is a semi-crystalline polymer, and for such systems, crystallization is the key process that determines the final properties of printed parts. Controlling crystallization is therefore essential and occurs mostly at the end of the process when the powder bed is cooled down to room temperature (RT). Uniform crystallization across the printed part is crucial to ensure consistent crystal morphology, which in turn governs the mechanical performance.

In contrast, amorphous polymers do not crystallize. However, at temperatures just below T_g, physical ageing readily takes place, leading to embrittlement and a deterioration of mechanical quality.[12] Minimizing physical ageing is therefore essential for ensuring the reliability of amorphous polymer parts.

To better understand these differences between crystallizable and amorphous materials, it is useful to consider how polymers solidify upon cooling. Depending on their type (semi-crystalline vs amorphous), they undergo solidification either through crystallization and/or vitrification. **Crystallization** is the ordering of chain segments into regularly packed regions and **vitrification** is the transition from a rubbery to a glassy state where polymer chains lose their mobility. These processes are reversible upon heating. This distinction is clearly reflected in the evolution of the enthalpy of the system (the total heat content) during the heating (**Figure 4**). Semi-crystalline have

crystalline and amorphous regions, so go through devitrification around the glass transition temperature T_g and melting around the melting temperature (T_m). In contrast, **amorphous** polymers will only go through devitrification at T_g, reflecting the transition from a rigid, glassy state to a rubbery one, without any melting transition.[13]

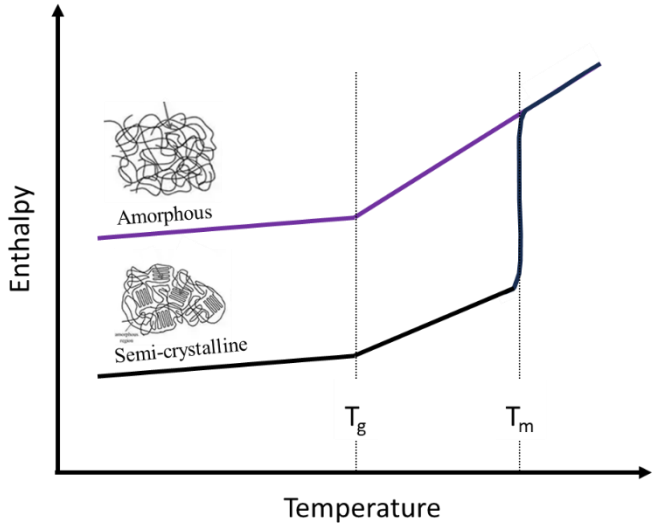


***Figure 4**. Evolution of enthalpy of amorphous and semi-crystalline materials upon heating after vitrification and crystallization, respectively, upon solidification.*

1.4 Polymer crystallization

1.4.1 Concept

Crystallization occurs when a polymer is cooled to temperatures below its T_m, where it transitions from a disordered melt to an ordered crystalline phase. This transition becomes thermodynamically favorable because the crystalline phase has a lower free energy than the amorphous melt.

Polymer crystallization typically proceeds through two main steps: nucleation and growth. During nucleation, small, ordered clusters of polymer chains form. These nuclei can form homogeneously, from the polymer itself, or heterogeneously, initiated at impurities or surfaces. Once a nucleus exceeds a critical

size, it becomes stable and begins to grow. In the growth phase, polymer chains are added to the existing nuclei, extending the crystalline regions.[14]

Semi-crystalline polymers usually crystallize into a typical two-phase system. The growth of the crystals consists of the folding of the randomly oriented chains into lamellae in an amorphous matrix, forming alternating crystalline and amorphous layers, that further grow into spherulites by growing radially from the nucleus (**Figure 5**).

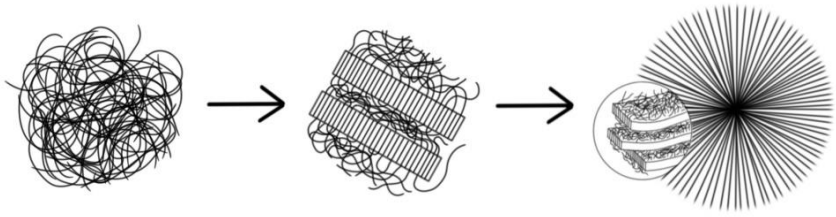


Figure 5*. Schematic illustration of the primary crystallization mechanism in a spherulite-forming polymer, showing the transition from the melt state to lamellar structures and ultimately to a spherulite. Adapted from* [14].

The formation and growing of spherulites is the *primary crystallization*. A following *secondary crystallization* can occur in many different forms depending on the polymer system involved. Examples of secondary crystallization are crystal perfectioning, lamellae thickening, formation of new lamellar stacks and insertion of lamellae in between existing lamellae.[15,16] Identifying the exact process of secondary crystallization can be intricate and not straight-forward.

Crystallization occurs below T_m, however, not spontaneously at all temperatures. For polymer chains to organize into ordered structures, they must possess sufficient segmental mobility, which decreases as temperature decreases. This kinetic limitation sets a lower bound near the T_g, below which molecular motion is too restricted for crystallization to proceed (**Figure 6**). At the same time, moving further below T_m increases the thermodynamic driving force for crystallization. As a result, crystallization is confined to a temperature window between T_g and T_m,

governed by the interplay between thermodynamic favorability and kinetic feasibility.[14,17]

According to the Hoffman–Lauritzen theory,[14] the overall crystallization rate of a polymer is governed by two key processes: primary nucleation and crystal growth. Primary nucleation refers to the initial formation of stable crystalline nuclei, while growth is mainly controlled by secondary nucleation and surface completion, where new crystalline layers are added to existing structures. A critical factor in crystallization is supercooling, the difference between the equilibrium melting temperature, T_m^0, and the actual crystallization temperature T_c. As supercooling increases, the thermodynamic driving force for crystallization becomes larger, which enhances both primary and secondary nucleation. However, polymer chain mobility—which reflects how easily chains can reorganize into ordered structures—decreases as the temperature approaches the glass transition temperature, T_g. At high temperatures close to T_m^0, mobility is high but the driving force is weak, leading to slow crystallization. At low temperatures near T_g, the driving force is strong but mobility becomes too limited for chains to rearrange effectively. As a result, the crystallization rate reaches a maximum at an intermediate temperature between T_g and T_m^0, where the balance between driving force and chain mobility is optimal. The peak of this curve marks the transition between a nucleation-controlled regime at higher temperatures (where the driving force is low) and a growth-controlled regime at lower temperatures (where molecular mobility is limited). As discussed throughout this thesis, deviations from this idealized curve can occur depending on the polymer system, molecular structure, and processing conditions.[14]

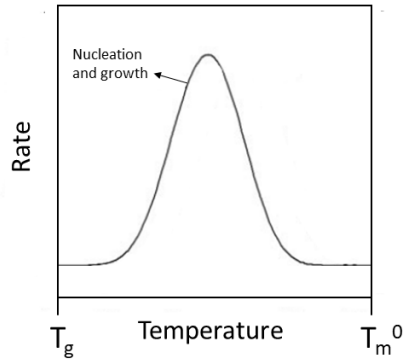


Figure 6. *Crystallization rate of polymers as a function of temperature showing a bell-shaped dependence between T_g and T_m^0 due to a competition between segmental flexibility and thermodynamic driving force. Illustration adapted from* [18].

Generally, the high thermodynamic driving force and low mobility at low temperatures result in the formation of many small primary nuclei and as a result smaller spherulites. At higher temperatures the thermodynamic driving force is weak but the molecular mobility is high leading to fewer primary nuclei and larger spherulites.[14,15]

Besides the spherulite size, also the lamellar thickness is affected by the supercooling at which they are generated. Following the Hoffman–Lauritzen theory,[14] the initial lamellar thickness observed at T_c is given by $\frac{2\sigma_e}{\Delta G_f} + \delta l$. σ_e is the fold surface crystal/melt interfacial energy, ΔG_f is the bulk free energy of melting at T_c and δl is the thickness increment above the minimum lamellar thickness for secondary nucleation, to ensure stability at T_c. ΔG_f can be approximated by $\Delta H_f \left(\frac{T_m^0 - T_c}{T_m^0}\right)$, with ΔH_f the bulk enthalpy of fusion. Combining these equations demonstrates that the lamellar thickness decreases with increasing ΔG_f, which increases with the supercooling $T_m^0 - T_c$.

The melting point of a lamellar crystal, T_m, depends on its thickness, l_c, according to the Gibbs-Thomson equation $T_m = T_m^0 \left(1 - \frac{2\sigma_e}{\Delta H_f l_c}\right)$. [19] T_m thus increases with increasing l_c. Note that if the thickness of the secondary nucleus, $\frac{2\sigma_e}{\Delta G_f}$, is inserted as value for l_c and with $\Delta G_f = \Delta H_f \left(\frac{T_m^0 - T_c}{T_m^0}\right)$, one obtains $T_m = T_c$. The latter implies

that lamellae with a thickness $\frac{2\sigma_e}{\Delta G_f}$ would melt at the temperature they crystallized. Hence the need for δl to ensure thermodynamic stability.

1.4.2 Factors influencing crystallization

Several factors influence polymer crystallization behavior, including the chemical structure of the polymer. The molecular architecture, such as chain flexibility, conformation, and stereochemistry, plays a central role in determining a polymer's ability to form ordered structures.

For instance, rigid chains containing cyclic units, such as in PCCD, tend to crystallize more readily than flexible, linear chains like PTHF, due to their restricted conformational freedom.[20] Isomerism can also significantly affect crystallization behavior. In the case of 1,4-substituted cyclohexanes, the *trans* configuration promotes more extended and linear chain conformations, facilitating close packing and efficient crystallization. In contrast, the *cis* configuration introduces kinks into the backbone, hindering regular packing and thus reducing crystallinity.[21]

In block copolymers, crystallization is influenced by the presence of chemically distinct blocks that may also undergo microphase separation (MS), a self-assembly process where blocks organize into nanoscale domains.[22] MS can occur alongside or independently of crystallization, and the sequence in which they occur is crucial: if MS precedes crystallization, it can direct or restrict how crystals develop within the nanostructure, while if crystallization occurs first, it may dominate and suppress domain ordering.

Together, these factors influence key morphological features, including spherulite size, lamellar thickness, crystal orientation and degree of crystallinity. In some polymers, crystallization can also result in polymorphism, where multiple crystalline forms may develop depending on processing conditions or thermal history.

1.5 Physical ageing in polymers

1.5.1 Concept

Physical ageing is generally defined as the relaxation of a material on a segmental scale, during which the system slowly approaches thermodynamic equilibrium. When a polymer is quenched to temperatures under T_g it reaches its so-called *super liquid state* or the "frozen" state where mobility is assumed to have ceased (**Figure 7**). However, segmental motions in the form of vibration are still possible. When the individual segments vibrate, they can unlock a motion on larger scale so that the whole chains start to rearrange into a denser conformation (= *α-relaxation*). This reduces the unoccupied space within the polymer matrix (= *free volume*)[23] (based on the well-known *Free Volume* Theory) and creates then local densities through the whole material, which causes the increase in brittleness.[12,24] Depending on the polymer system and ageing temperature, the exact nature of the motions can differ. As the material relaxes toward a more thermodynamically stable conformation, its enthalpy decreases, reflecting its approach to equilibrium. Consequently, both the specific volume and the enthalpy of the system decrease simultaneously during ageing. They exhibit the same temperature dependence because their respective derivatives with temperature, the heat capacity and the thermal expansion coefficient, are both governed by the same underlying structural relaxation processes and therefore vary with temperature in a similar way.[25]

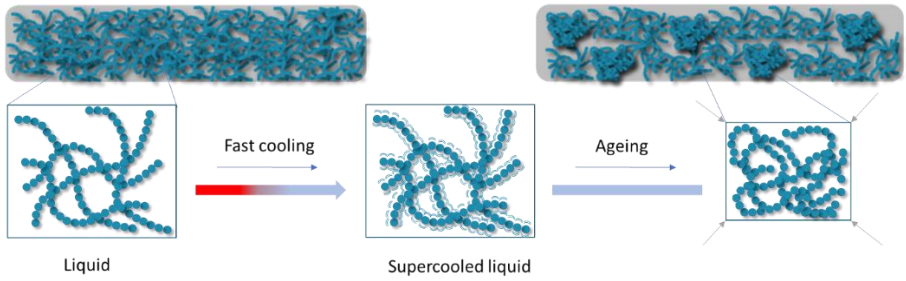


Figure 7. *Illustration of the process of physical ageing in glassy, amorphous polymers where the material is fast cooled to form a supercooled liquid and then allowed to age at low temperature, resulting in a decreased volume and local densities in the material*

(increased brittleness). The color gradient in the arrow represents de cooling from high (red) to low (light blue) temperatures. The light blue rectangle represents an isothermal period at a temperature near or below T_g.

In earlier studies, dilatometry was employed to monitor the volume changes as an indicator of the extent of physical ageing.[26–28] However, these experiments are limited and complex. Fortunately, the volume and enthalpy of the system exhibit the same temperature dependence, allowing the extent of ageing to be measured through more accessible calorimetry experiments. **Figure 8** illustrates this for an isothermal ageing experiment. The evolution of enthalpy of the system can be described by three consecutive events: 1) vitrification, 2) ageing and 3) devitrification.

1) Vitrification

The material is quenched to the desired ageing temperature T_a. Upon quenching, the material follows the liquid-like, equilibrium line (black line) until a certain point where the chain mobility is so low that it cannot follow the cooling anymore and "freezes". This occurs at the T_g and creates the deviation of the enthalpy curve from the liquid line (= vitrification) into a plateau (purple curve). The plateau is positioned above the extrapolated melt line (dashed curve), which means that the material is not in its equilibrium state. The T_g is usually determined from the intersection of the extrapolation of the liquid and the glass line.

2) Physical ageing

The sample is held at T_a and allowed to relax. This decreases the volume and enthalpy of the system (green arrow). It will try to reach the equilibrium, which is the enthalpy value at T_a on the equilibrium line. **Figure 8** illustrates an example where the ageing is stopped before equilibrium is reached (red plateau).

3) Devitrification

Finally, the material is heated up where it follows the enthalpy plateau, devitrifies (red curve), and reaches the liquid state. If ageing has taken place, the devitrification is accompanied by an endothermic *enthalpy recovery* peak or overshoot, representing

the amount of heat needed to disrupt the structural arrangements made during ageing. The (partially) relaxed material is characterized by the **fictive temperature T_f**, which is the intersection between the equilibrium and the glass line.

In general, increased physical ageing results in lower enthalpy and reduced T_f values. Calorimetric experiments allow this process to be quantified, either through changes in enthalpy or T_f.

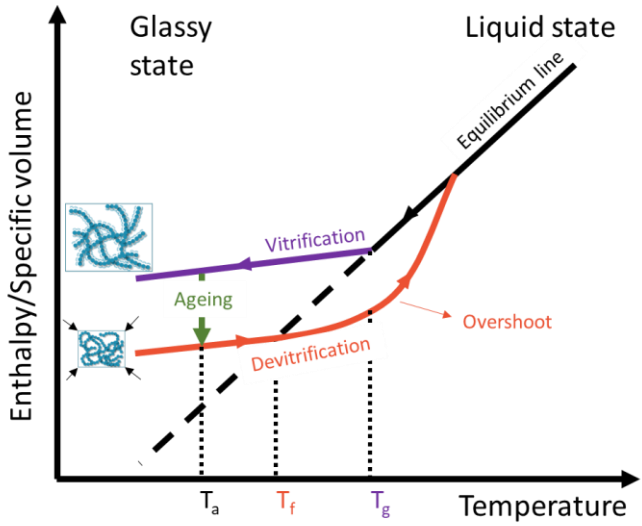


Figure 8. *Illustration of an example of vitrification, physical ageing and devitrification in an enthalpy/specific volume vs temperature graph. In this example, the material undergoes vitrification upon cooling (purple) where it transitions from the liquid to the glassy state at T_g. Then, the material is aged (green) where it is kept at T_a below T_g and the enthalpy and volume decreases. Lastly, the material is devitrified (red) upon heating and shows an overshoot, which is used to quantify physical ageing.*

1.5.2 VFT/WLF: a model to describe physical ageing

The progression of relaxation toward equilibrium is usually monitored through the system's recovery upon heating after a period of physical ageing. By plotting the changes in enthalpy recovery or devitrification, one obtains so-called **intrinsic isotherms**, which represent the equilibrium baseline approached during ageing. In 1854, Kolrausch [29] first introduced the idea that these intrinsic isotherms can be described as stretched exponential curves, leading eventually to the well-known Kohlrausch-Williams-Watts (KWW) equation:

$$\phi(t) = y_0 exp\left[-\left(\frac{t}{\tau_{KWW}}\right)^{\beta_{KWW}}\right] \quad (1)$$

with ϕ(t) the extent of ageing, y_0 a front factor, t the time, τ_{KWW} is the characteristic KWW relaxation time and β_{KWW} the KWW stretching factor.

The Vogel-Fulcher-Tammann (VFT),[30–32] or the Williams-Landel-Ferry (WLF) model for polymeric materials,[33] is the most known model to describe the temperature-dependency of τ. The equation is the following:

$$\tau = \tau_0 exp\left[\frac{B}{T_a - T_0}\right] \quad (2)$$

with τ_0 a front factor, T_0 a material parameter and sometimes defined as T_g, and T_0 the Vogel temperature, a hypothetical temperature at which the material is an immobile glass, and the relaxation is infinitely long. B is a shape parameter describing the temperature dependency. The VFT is used fit to the τ-T curve by using the fitting parameters τ_0, T_{eq} and B. The related WLF equation is

$$\log\left(\frac{\tau}{\tau_{ref}}\right) = \frac{-C_1(T_a - T_f)}{[C_2 + (T_a - T_f)]} \quad (3)$$

with τ_{ref} the τ for a chosen reference temperature and C_1 and C_2 as material parameters. Equations 2 and 3 are interchangeable.

The VFT/WLF model assumes **super-Arrhenius** kinetics of relaxation at all ageing temperatures and is based on the Free Volume Theory (where α-relaxation is the only relaxation mechanism occurring). The relaxation times at low temperatures increase more rapidly in a super-Arrhenius manner than predicted by the Arrhenius behavior (**Figure 9**). This difference arises from the denominator in the expressions for both models: the VFT-type equation (Equation 2) and the Arrhenius equation for relaxation times $\tau = \tau_0 exp\left[\frac{E_a}{RT_a}\right]$, where E_a is the activation energy and R the gas constant. When both functions are plotted as $\ln(\tau)$ versus $1/T_a$, the Arrhenius behavior appears as a straight line, while the super-Arrhenius behavior exhibits a non-linear (upward-curving) dependence.

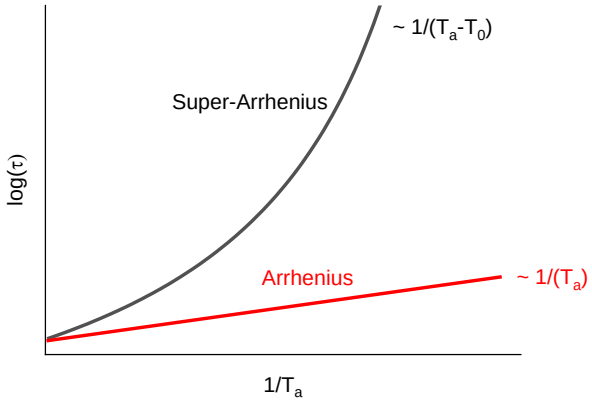


***Figure 9**. Illustration of the logarithmic evolution of the relaxation time as a function of the inverse of the ageing temperature for super-Arrhenius (black) and Arrhenius (red) behavior.*

1.5.3 Beyond the α-relaxation

This model, however, has been challenged by the upcoming of new techniques and technological advances, reaching longer ageing times and a broader range of ageing temperatures. As the temperature approaches and drops below the nominal T_g, experimental evidence strongly suggests that the equilibrium dynamic response does not continue along the super-Arrhenius trend, but instead shifts toward

a weaker temperature dependence, potentially even approaching Arrhenius-like behavior. A extensive review on the matter is given by McKenna and Simon (2017).[34]

α-relaxation, the only relaxation mechanism accounted for by VFT, involves large-scale, cooperative movements of the polymer chains. It is argued that a second, faster relaxation mechanism can occur that involves more localized, small-scale molecular motions, referred to as the β-relaxation.[35] At low temperatures, the cooperative movements of the α-relaxation would require too much thermal energy so that the β-relaxation becomes more dominant as they require movements of smaller segments of the polymer chain. Others explain the complexity by a change in activation energy with temperature.[36] Microstructural variations, physical constraints like entanglements, molecular interactions and impurities could hinder or facilitate ageing by increasing or decreasing the activation energy, respectively.

1.6 Aims and outline

The general aim of this doctoral dissertation is to investigate the structure-property relationship of PCCD-based materials in terms morphology, crystallization and physical ageing in the glassy state under various thermal conditions, with a focus on gaining more insights in the behavior of Amphora SP1621. To achieve this, a combination of experimental methods, including thermal and structural characterization techniques, is employed. Each chapter of this thesis focuses on specific objectives and methods that contribute to the overall goal.

Chapter 1 provides a general introduction on the PCCD-based materials used in this work along with an informative background on crystallization and the physical ageing of polymeric glasses to help the reader understand the results discussed in the next chapters. At the start of every chapter, a more specific, relevant introduction is given, as well as a literature review on the topic.

Chapter 2 delivers an extensive and in-depth study on semi-crystalline PCCD-PTHF to gain a fundamental understanding of its morphology, crystallization mechanism and phase behavior under typical DSC conditions. This initial study was essential to establish a clear picture of the material and to form the basis for the subsequent work.

Chapter 3 discusses the synthesis and characterization of the homopolymer PCCD, as well as its morphology and crystallization behavior, which are examined in comparison to PCCD-PTHF under the same DSC conditions. In addition, the non-isothermal crystallization at DSC rates is discussed and an end-capping method was proposed to thermally stabilize the material.

Chapter 4 presents an isothermal crystallization study on thermally stabilized PCCD-PTHF and PCCD, building on the insights gained in Chapter 2 and 3. The results were used to describe the crystallization process and kinetics in a broad temperature range. It also provided a thermal stabilization method of PCCD-PTHF.

In **Chapter 5,** the crystallization study on PCCD-PTHF was extended to non-isothermal crystallization. The non-treated PCCD-PTHF was compared to the commercial material Amphora SP1621. Moreover, the results were put into the context of laser sintering.

Chapter 6 provides an extensive study on the physical ageing of amorphous, glassy PCCD and different polystyrene grades. The emphasize is placed onto mapping of the kinetics and investigating the influence of different material-related parameters on the ageing behavior.

Finally, **Chapter 7** synthesizes the conclusions of Chapters 2-6 and explores the potential avenues for further research based on the findings presented in this thesis.

Chapter 2

The Molecular Structure and Phase Behavior of a Segmented PCCD-PTHF Block Copolymer

This chapter is based on following publication:
Hamid, M., Mongilyov, I., Ianiro, A., Van Puyvelde, P. & Goderis, B. The Molecular Structure and Phase Behavior of a Segmented PCCD-PTHF Block Copolymer. Polymer. 334, (2025)

Author contributions

Mouna Hamid: Conceptualization, Investigation, Methodology, Formal analysis, Writing – original draft. **Ilya Mongilyov**: Methodology, Formal analysis. **Alessandro Ianiro**: Methodology, Formal Analysis, Writing – review and editing. **Peter Van Puyvelde**: Supervision, Writing – review and editing. **Bart Goderis**: Supervision, Conceptualization, Methodology, Formal analysis, Writing – review and editing.

Abstract

This study investigates the molecular structure, crystallization behavior, melting characteristics, and morphology of a segmented block copolymer made from crystallizable poly(1,4-cyclohexylidene cyclohexane-1,4-dicarboxylate) (PCCD) and soft polytetrahydrofuran (PTHF-1000) blocks. The polymer is the main component of the commercially available Amphora SP1621 powder, designed for additive manufacturing via laser sintering. Block length distributions were computed through simulations, incorporating NMR data for the monomeric content and Gel Permeation Chromatography for the molecular weight distribution. Fast Scanning Chip calorimetry confirmed the melt miscibility of the PCCD and PTHF blocks. Differential Scanning Calorimetry (DSC), coupled with optical and atomic force microscopy, as well as time-resolved synchrotron small-angle (SAXS) and wide-angle X-ray diffraction (WAXS), revealed that the material crystallizes as spherulites when cooled at 10 K/min. Primary PCCD crystallization creates intraspherulitic amorphous regions, which later undergo secondary crystallization, forming randomly oriented semi-crystalline stacks. A new SAXS data interpretation method was introduced to quantify the fractions of the different stack types, aligning the overall SAXS crystallinity with the WAXS and DSC results. The thickness of the crystalline

PCCD lamellae correlated with the most probable PCCD block length. By combining DSC data with the WAXS-derived crystallinity, an equation for the transition enthalpy of fully crystalline PCCD was derived. Crystallographic analysis of an oriented, injection-molded sample showed that the PCCD segments align perpendicularly to the lamellar surface and pack at a crystalline density of 1.40 g/cm³.

2.1 Introduction

Polymeric Additive Manufacturing (AM) or 3D printing has become essential in today's world. It is widely used in automotive, aerospace, manufacturing and robotic industries for rapid prototyping as well as end-user applications. One of the most used AM techniques is Selective Laser Sintering (SLS), which makes use of a high-power laser to sinter polymer powder in a layer-by-layer manner, creating solid printed parts. This technique is well-known for its ability to print parts with complex geometrical designs and favorable mechanical properties. Polyamide 12 (PA12) and polyamide 11 (PA11), both rigid thermoplastics, are currently most often used.[37] However, there is a global need for new sintering materials with properties that cannot be covered by PA11 or PA12, such as e.g. elasticity. Moreover, sustainability on the material and process level has become a significant focus nowadays. Typically, the printer powder bed contains large amounts of non-sintered powder, which in the case of polyamides can only be recycled to a limited extent in a next printing run due to degrading post-condensation reactions at the powder bed's high temperatures.[38]

Against this background, Eastman Chemical Company recently introduced Amphora SP1621, a new recyclable, high performance polyester-based sintering powder with thermoplastic elastomeric (TPE) properties.[1] This makes it a great candidate to join the family of tough and flexible sintering materials alongside other TPEs, such as thermoplastic polyurethanes (TPUs).[3]

Vande Ryse et al. (2022) studied the influence of selected processing parameters on the mechanical properties of printed Amphora SP1621 parts.[9] However, this work remained somewhat empirical since information on the polymer microstructure and mesoscopic semi-crystalline morphology was not reported.

Eastman Chemical Company confirmed that Amphora SP1621 essentially is a semi-crystalline segmented copolyesterether block copolymer, consisting of poly(1,4-cyclohexylidene cyclohexane-1,4-dicarboxylate) (PCCD) and polytetrahydrofuran (PTHF) blocks.[39] PCCD, when used as a homopolymer, is well-documented as a crystallizable, tough, and rigid polyester, first introduced in the 1950s.[21,40,41] PTHF, on the other hand, is a widely recognized amorphous soft macrodiol commonly found in block copolymers like TPUs. Besides the recent study by Vande Ryse et al. (2022) on commercial Amphora SP1621,[9] there is limited literature on PCCD-PTHF block copolymers.[20] To our knowledge, no data exist on the segmental melt miscibility or semi-crystalline morphology of this material. Additionally, while Differential Scanning Calorimetry (DSC) is frequently used to assess thermal transitions and crystallinity for process optimization, no reference enthalpy is available for PCCD to correlate experimental transition enthalpies with crystallinity values. Consequently, the lack of detailed information on this material limits the optimization of thermal processing protocols and hinders accurate property assessments.

This paper presents the first comprehensive study of the crystallization, melting behavior, and morphology of PCCD-PTHF. The material's molecular structure was analyzed in detail using NMR spectroscopy, and block length distributions were calculated through a simulation incorporating the monomeric composition and the polymer's molecular weight distribution. Segment melt miscibility was investigated thermally using Fast Scanning Chip Calorimetry (FSC). Differential Scanning Calorimetry (DSC), coupled with optical and atomic force microscopy, as well as time-resolved synchrotron small-angle (SAXS) and wide-angle X-ray scattering (WAXS) was used to assess the material’s thermal behavior and semi-crystalline morphology over a wide range of length scales during cooling and heating at 10 K/min. By combining DSC data with the WAXS-derived crystallinity, an equation for the transition enthalpy of fully crystalline PCCD was derived. A crystal unit cell for PCCD was proposed based on X-ray diffraction of an oriented injection-molded PCCD-PTHF sample.

2.2 Experimental section

2.2.1 Materials

The PCCD-PTHF block copolymer studied in this manuscript was provided by Eastman Chemical Technology BV (Ghent, Belgium) under the form of extruded pellets.[39] In contrast to commercial Amphora SP1621 sintering powder, the polymer pellets are free from powder flow agents. According to Gel Permeation Chromatography (GPC) by the supplier, the M_n, M_w and M_z values are 12.7, 75.3 and 399.1 kg/mol respectively. The dispersity, M_w/M_n, is 5.95. The high dispersity aids the proper sintering of the powder (Chapter 1).

2.2.2 Methods

Nuclear Magnetic Resonance (NMR) Spectroscopy

^{1}H NMR, Correlated Spectroscopy (COSY), Nuclear Overhauser Enhancement Spectroscopy (NOESY) and Heteronuclear Multiple Bond Correlation (HMBC) experiments were performed with a Bruker Avance III HD 400 MHz Spectrometer. Samples of approximately 5 mg were dissolved in deuterated (99.9 %) chloroform and complemented with 0.1 (v/v)% tetramethylsilane (TMS) as reference. The data were analyzed using the Topsin 4.0 software.

Thermogravimetric Analysis (TGA)

A TGA heating experiment using a Q500 instrument (TA instruments, New Castle, USA) at 10 K/min from room temperature to 500 °C was performed on 6 mg PCCD-PTHF in an aluminum pan. Heating occurred under a constant nitrogen flow of 50 mL/min. The temperatures at which 1% and 5% mass were lost, were 367.6 and 392.6 °C. The full degradation profile can be found in Appendix A, **Figure A.1**.

Differential Scanning Calorimetry (DSC)

DSC experiments were performed with a Q2000 heat-flux DSC (TA instruments, New Castle, USA), calibrated for the temperature, heat flow and heat capacity with indium and sapphire standards. Approximately 8 mg PCCD-PTHF was heated from room temperature to 250 °C at 10 K/min followed by a cooling to -50 °C and a second heating to 250 °C at 10 K/min. Every heating and cooling step was followed by a 10 min isothermal step. Only the cooling and second heating runs are discussed in this manuscript. The sample was measured in an open Tzero aluminum pan without lid under a constant nitrogen flow of 50 mL/min. The heat flow data were converted into specific heat capacity $c_p(T)$ ($Jg^{-1}K^{-1}$) values by subtracting an empty pan measurement and subsequent normalization to the scanning rate and sample mass.

Fast-Scanning Chip Calorimetry (FSC)

FSC experiments were performed under a constant nitrogen flow with a Flash DSC 1 (Mettler Toledo, Colombus, USA) in conjunction with a Huber TC100 intracooler (Huber, Offenburg, Germany). Sub µg pieces were cut from a PCCD-PTHF pellet under a microscope and transferred onto the chips. Prior to sample deposition, the Multistar UFS1 chips were conditioned and temperature-corrected.[42] **Figure 10** outlines the thermal protocols carried out to study a) ageing at temperatures (T*) below the glass transition temperature and b) the polymer segment miscibility in the melt at temperatures (T_a) above the crystallization onset when cooled at 10 K/min. Panel a) also contains the reference protocol used to confirm the sample's stability.

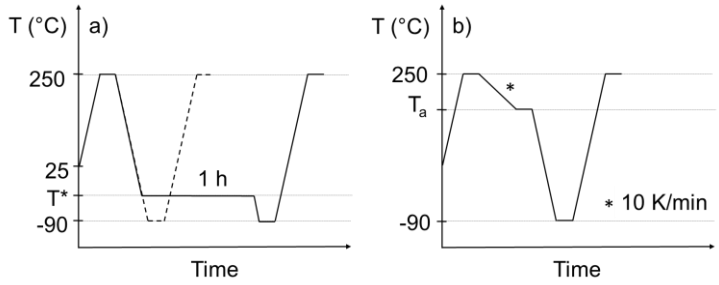


Figure 10. *Thermal protocols used for the FSC experiments. a) the protocol to study ageing at temperatures T* (solid lines) and a reference protocol (dashed lines). b) the protocol used to study the polymer melt miscibility at high temperatures, T_a. All scanning rates were 1000 K/s and the isothermal times were 1 s, except for the 1 h*

*stay in the protocol under a) and the * labelled ramp under b), which was conducted at 10 K/min.*

Polarized Optical Microscopy (POM).

POM experiments were performed using a BHS microscope (Olympus, Tokyo, Japan), coupled to a TK-C1381 color camera (JVC, Kanagawa, Japan) and operated by Leica Qwin software (Solms, Germany). A small piece of PCCD-PTHF was placed in a 2x2 mm aluminum foil frame (11 μm thickness) and melt pressed between two thin cover glasses. The sample was cooled after 10 min at 240 °C to 0 °C at 10 K/min in a TMS 600 hot stage (Linkam Scientific Instruments, Surrey, UK), held at 0 °C for 10 min and then heated again to 240 °C at the same rate. The hot stage was flushed with nitrogen gas and a liquid nitrogen pump was used for cooling. Images of the sample between crossed polarizers were taken every degree Celsius and the intensities were integrated using a script in V++ (Digital Optics Limited, Auckland, New Zealand).

Atomic Force Microscopy (AFM)

A room temperature AFM experiment was performed on a POM sample cooled at 10 K/min using a PicoLE 5100 (Agilent Technologies, California, USA) in tapping mode. The sample was prepared by removing the top cover glass and aluminum foil under liquid nitrogen to prevent deformation.

Static X-ray diffraction on an oriented injection molded sample

An oriented material was prepared via injection molding using a DSM Xplore micro-injection molding machine. PCCD-PTHF pellets were molten at 230 °C for 5 min and injected in the tensile specimen mold at room temperature to form specimens of about 6 cm long and 1.5 mm thick. Quick solidification during quenching fixed the injection-induced molecular and crystallographic orientation. The central shaft of the tensile bar was subjected to an X-ray diffraction experiment using an XeuSS X-ray camera (Xenocs, Sassenage, France) with a GeniX 3D Molybdenum ultralow divergence X-ray beam source (wavelength: $\lambda = 0.71$ Å, power: 50 kV, 1 mA) and a Mar345 image plate detector (MARresearch, Norder-stedt, Germany) following a He flushed flight tube. The pattern was corrected for the dark image and

empty sample holder scattering, taking into account the sample and holder transmission. Scattering angles, 2θ, were calibrated with silver behenate and α-alumina standards. The two dimensional scattering pattern was analyzed as a function of 2θ and the azimuthal angle φ using ConeX software.[43] Intensities were collected over the range $0.17° \leq 2\theta \leq 15°$, corresponding to a scattering vector range of $0.03 \leq q \leq 2.3$ Å^{-1}, with $q = (4\pi sin\theta)/\lambda$.

Time-resolved synchrotron Small-Angle and Wide-Angle X-rays Scattering (SAXS/WAXS)

Time-resolved synchrotron SAXS/WAXS experiments were performed at BM26, the Belgian beam line at the European Synchrotron Radiation Facility (ESRF) in Grenoble, France, using an X-ray wavelength λ of 1.03 Å. The SAXS and WAXS intensities were collected simultaneously with, respectively, a Pilatus 1M detector at 1.20 m from the sample after an evacuated tube and a Pilatus 300k detector close to the sample. Structural information was retrieved over the ranges $0.02 \leq q \leq 0.80$ Å^{-1} for SAXS and $0.60 \leq q \leq 3.60$ Å^{-1} for WAXS.

The PCCD-PTHF samples with a thickness of about 1 mm were wrapped in one-layered aluminum foil and placed in a TMS 600 hotstage (Linkam Scientific Instruments, Surrey, UK). Liquid nitrogen was used for cooling. The exposure time was 4 s and one image per degree Celsius was taken during cooling and subsequent heating at 10 K/min between 230 and 22 °C.

The scattering angles were calibrated against α-alumina and silver behenate standards and the isotropic powder patterns were azimuthally averaged using ConeX software.[43] The one-dimensional data were corrected for the scattering of an empty sample holder, taking the sample transmission into account as derived from the transmitted primary beam intensity measured by a photodiode downstream from the sample. Intensities were normalized to the intensity of the incoming beam, measured by an ionization chamber upstream from the sample.

2.3 Results and Discussion

2.3.1 Molecular structure of PCCD-PTHF

Figure 11 shows the molecular structure of the segmented PCCD-PTHF block copolymer in (a) and the ^{1}H NMR spectrum with identification of the main peaks in (b). PCCD is a polyester, which can be synthesized via condensation reactions between 1,4-cyclohexanedimethanol (CHDM) and either 1,4-cyclohexanedicarboxylic acid (CHDA) (releasing water) or dimethyl 1,4-cyclohexanedicarboxylate (DMCD) (releasing methanol).[40,41,44] The signal at 3.67 ppm due to methoxy protons, reveals that DMCD was used in the synthesis. In what follows, the CHDM residues within the polymer chain will be referred to as C and the DMCD residues as D for brevity.

The cyclohexane moieties can have a *cis* (c) or *trans* (t) configuration. The corresponding proton signals are labeled H_{1c} and H_{1t} for D, and H_{3c} and H_{3t} for C. The D and C *trans* contents are 95% and 70% respectively. D is linked either to C in the PCCD block or to the PTHF macrodiol (abbreviated as 'P' in **Figure 11a**) via an ester bond. The ester bond to the C residues is identified through the H_3 peaks at around 4 ppm, whereas the ester bond to the PTHF macrodiol is revealed through the H_{6*} signal. H_{6*} experiences a higher chemical shift compared to H_6 due to the deshielding effect by the strong electronegative ester group. H_{6*} and H_{7*} as well as H_6 and H_7 were found to be coupled based on 2D COSY and NOESY NMR experiments. H_{6*} appeared to be coupled to the neighboring ester carbon according to the HMBC experiment. It also showed no coupling between H_6 and C_3. The 2D COSY, NOESY and HMBC NMR spectra can be found in the **Figures A.2** to **A.4** of Appendix A.

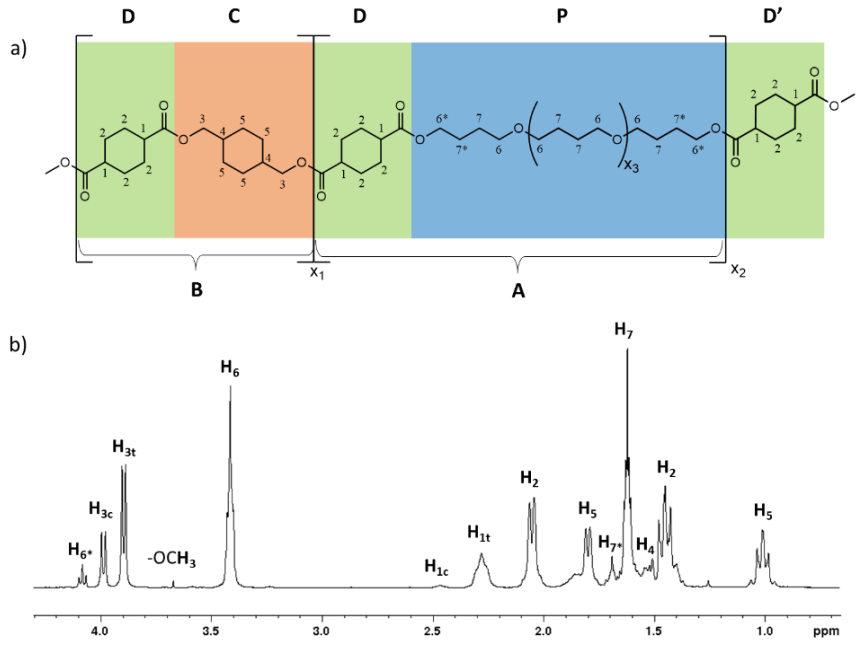


Figure 11. *a) Molecular structure of PCCD-PTHF and b) the corresponding ^{1}H NMR spectrum of PCCD-PTHF with the identified peaks (chemical shift, relative peak area) corresponding to H_{6*} (4.08 ppm, 0.83), H_{3c} (3.99 ppm, 2.48), H_{3t} (3.90 ppm, 5.55), -OCH_3 (3.67 ppm, 0.08), H_6 (3.41 ppm, 10.0), H_{1c} (2.47 ppm, 0.21), H_{1t} (2.28 ppm, 4.37) H_2 (2.05 ppm, 8.59), H_5 (1.80 ppm, 5.57), H_{7*} (1.69 ppm, 1.64), H_7 (1.62 ppm, 13.1), H_4 (1.52 ppm, 2.86), H_2 (1.45 ppm, 11.2) and H_5 (1.01 ppm, 5.71).*

The average number of THF units per P unit is 13 and was calculated from the ratio of the summed H_{6*} and H_6 intensities over the area of the H_{6*} peak. The corresponding PTHF number average molecular weight M_n equals 936 g/mol. This M_n corresponds to PTHF 1000, an often used macrodiol for the soft segments also in other thermoplastic elastomers like TPUs and PBT-PTHF.[45,46]

The molar and mass ratios of D, C and P were calculated by using the H_{1c} and H_{1t} peaks for D, H_{3c} and H_{3t} for C and H_{6*} for P. This resulted in mole fractions φ for D ($\varphi_D = 0.508$), C ($\varphi_C = 0.446$) and P ($\varphi_P = 0.046$). The PTHF (P) mass percentage is 25 %. There is a molar D excess compared to the molar sum of P and C, implying that chains are terminated by D units, which are termed D' units (**Figure 11a**). The D' mole fraction is given by $\varphi_{D'} = \varphi_D - \varphi_C - \varphi_P = 0.017$, with φ_D the mole fraction of D species within A or B units and at the end of the chains. A and B units

are defined as coupled D-C and D-P units respectively (**Figure 11a**). Therefore, the average number of coupled A and B units $\bar{x}$ can be calculated from the ratio of the total number of A and B units over the number of chain ends:

$$\bar{x} = \frac{\varphi_C + \varphi_P}{\varphi_{D\prime}} = 29.5 \quad (4)$$

The probability that an A or B unit is added along the chain is given by respectively P_A and P_B and can be calculated from:

$$P_A = \frac{\varphi_P}{\varphi_P + \varphi_C} \cong 0.1 \quad (5)$$

$$P_B = \frac{\varphi_C}{\varphi_P + \varphi_C} \cong 0.9 \quad (6)$$

An average chain contains $\bar{x}P_A = 2.95$ A-units, $\bar{x}P_B = 26.55$ B units, a D' unit and two terminal methoxy groups, leading to $M_n \cong 11\ kg/mol$, which is close to M_n given by the supplier.

2.3.2 Block length distribution

For infinitely long chains, the Flory equation[47] can be used to compute the normalized weight distribution, $W_A(n)$ or $W_B(n)$, of A or B type blocks of length n:

$$W_A(n) = n{P_B}^2{P_A}^{n-1} \quad (7)$$

$$W_B(n) = n{P_A}^2{P_B}^{n-1} \quad (8)$$

n is an integer corresponding to the number of A or B units in the block. However, polymers with infinite molar masses are unrealistic and the block lengths of finite chains will be shorter, limiting crystallizability and potentially the size of morphological features. To model more realistic block length distributions, we used stochastic simulations, assuming a random coupling of the A and B units and a molecular weight distribution based on the molecular weight averages from the supplier (section 1.2.1).

Several options were tried, among which the Flory-Schultz distribution, but ultimately only a lognormal distribution, $f(x)$, for the total number of units (A and B) per chain, x, was able to cover the supplier's molecular weight averages:

$$f(x) = \frac{1}{x\sigma\sqrt{2\pi}} exp\left(-\frac{(lnx-\mu)^2}{2\sigma^2}\right) \quad (9)$$

with

$$\mu = ln\left(\frac{\bar{x}^2}{\sqrt{\bar{x}^2+{\sigma_x}^2}}\right) \quad (10)$$

in which $\bar{x}$ is the average number of units per chain and ${\sigma_x}^2$ is the distribution variance. The parameter σ relates to $\bar{x}$ and ${\sigma_x}^2$ via:

$$\sigma = \sqrt{ln\left(1+\frac{{\sigma_x}^2}{\bar{x}^2}\right)} \quad (11)$$

Neglecting (at this stage) the presence of A and B type units, the molar mass, M_x, of chains with x units can be calculated with $\overline{M_m}$, the average molar mass (g/mol) of a unit:

$$M_x = x\overline{M_m} + M_{end} = x(P_A M_A + P_B M_B) + M_{end} \quad (12)$$

M_A and M_B are the molar masses of the A and B units and M_{end} is the total molar mass ($200\ g/mol$) of the terminal D' unit and two methoxy end groups (**Figure 11a**). The molecular weight averages are calculated from:

$$M_n = \frac{\sum_x f(x)M_x}{\sum_x f(x)} \quad M_w = \frac{\sum_x f(x){M_x}^2}{\sum_x f(x)M_x} \quad M_z = \frac{\sum_x f(x){M_x}^3}{\sum_x f(x){M_x}^2} \quad (13)$$

To approach the supplier input, $\bar{x}$ was set to $(12{,}654 - M_{end})/\overline{M_m}$ and ${\sigma_x}^2$ was varied up to a best match with the supplier's M_w/M_n was reached (${\sigma_x}^2 = 6{,}362.7$). $12{,}654\ g/mol$ is the supplier's M_n. The result is collected in **Table 1** and agrees very well with the supplier input. The upper x value in the calculations was arbitrarily set at 13,180.

***Table 1**. Comparison of molecular weight parameters from the supplier (section 2.2.1)[a]; by assuming a lognormal $f(x)$ distribution and average molar masses of the units[b]; and from the simulation in which A and B type units are implemented[c].*

	M_n	M_w	M_z	M_w/M_n

	(g/mol)	(g/mol)	(g/mol)	
Supplier input[a]	12,654	75,304	399,111	5.95
$f(x)$ with averaged monomers[b]	12,715	75,668	406,126	5.95
Simulation[c]	12,734	76,722	451,659	6.03

In a next step, the molar mass distribution was refined by introducing A and B units in the chains according to the probabilities, P_A and P_B. The probability, $f(x,k)$, of finding a chain with x units of which there are k of the A-type is:

$$f(x,k) = f(x) \cdot {P_B}^{x-k} {P_A}^{k} \cdot \frac{x!}{k!(x-k)!} \tag{14}$$

$f(x)$ represents the probability for a chain with x units. The product of the second and third factor is the probability to have k A-type units in the chain. The third (binomial) factor describes the number of equivalent cases in which the k A-units occupy different places in the chain. k can take values in the range $0 \leq k \leq x$.

For a chain with x units and k A-type units the molar mass, $M_{x,k}$, is:

$$M_{x,k} = kM_A + (x-k)M_B + M_{end} \tag{15}$$

The replacement of units with average molar mass by statistically relevant amounts of A and B units leaves M_n unaffected because the total mass and number of chains is preserved. This also implies that

$$f(x) \cdot M_x = \sum_{k=0}^{x} f(x,k)\, M_{x,k} \tag{16}$$

M_w and M_z are expected to increase but only moderately as stochastic simulations will show.

In total 10 million chains were generated with a length distribution given by $f(x)$ with the earlier defined $\bar{x}$ and ${\sigma_x}^2$ values. Next, A and B units were assigned in accordance with P_A and P_B and molar masses were computed using equation 15. **Figure 12a**

displays the outcome by means of black open symbols. The $M_{x,k}$ counts were normalized to 10 million, generating an $f(x,k)$ probability that closely aligns with the theoretical $f(x,k)$, calculated with equation 14 over the range $0 \leq M_{x,k} \leq 30{,}000$ (blue squares). Clearly, the simulation missed the $M_{x,k}$ with very low probability as theoretical (blue) data are present below the lowest simulated ones. The lowest simulated $f(x,k)$ values (besides the zero values) correspond to molecules that were counted only once, i.e. with a probability of 1 over 10 million or 10^{-7}. Many of these specific molecules are in fact overrepresented in the distribution, as they may not reappear if an additional 10 million chains were generated. This explains why the simulated $f(x,k)$ values at the highest $M_{x,k}$ exceed the theoretical $f(x)$ values (red data in **Figure 12a**). However, errors at these very low probabilities cannot affect the molecular weight averages heavily.

The product $f(x,k)M_{x,k}$ is proportional to the mass fraction of chains with mass $M_{x,k}$. These fractions were accumulated from low to high $M_{x,k}$ and the maximum value was rescaled to 100%. This mass accumulation is plotted as function of the logarithm of the molar mass ($logM$) in **Figure 12b** (open symbols) and resembles a cumulative Gaussian distribution (the red curve). The corresponding Gaussian is shown using a green curve and represents the lognormal mass distribution that e.g. GPC may deliver. The molar mass averages of the simulated chains were computed using equation 13 in which $f(x)$ and M_x were replaced by $f(x,k)$ and $M_{x,k}$. The result is displayed in **Figure 12b** and added to **Table 1**. As anticipated, M_n corresponds rather well to the value based on $f(x)$ whereas M_w and predominantly M_z are slightly higher.

The simulation of 10 million polymer chains did not target a description of the molar mass distribution as this can be done analytically (cfr. supra). It is more challenging to derive equations that deliver the block length distributions. Having confirmed that the simulated chains match the expected molar mass distribution, they can be used to derive realistic A and B block length distributions. The number ($N_A(n)$ and $N_B(n)$) and weight ($W_A(n)$ and $W_B(n)$) block length (n) distributions for the A and B blocks from the simulated chains are plotted in **Figure 12c** and **Figure 12d**, respectively. Clearly, most of the soft A blocks are isolated PTHF macrodiols (the most probable n value equals 1), sandwiched between B blocks (PCCD) of various

lengths. Note how $f(x,k)$ in **Figure 12a** reveals the presence of chains without A units (the molar masses covered with a green curve), with 1 A-unit per chain (magenta curve), 2 A-units (yellow curve), etc. Most of the PCCD mass in the system belongs to blocks with 7 PCCD monomers, as $W_B(n)$ peaks at $n = 7$. This value is lower than the value predicted by the Flory equation (equation 7), which suggests $n = 10$. In general, the simulation shows a higher proportion of shorter B blocks compared to the Flory prediction. For the very short A block, the simulation aligns perfectly with the Flory equation.

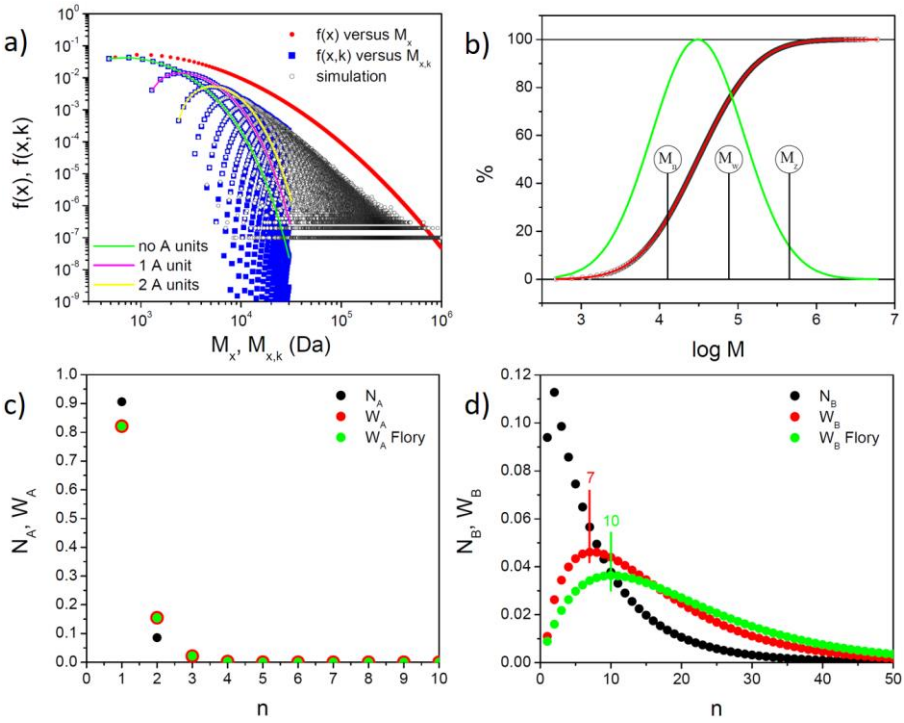


Figure 12. *a) $f(x)$ based on equation 9 as a function of M_x from equation 12 (red) and $f(x,k)$ based on equation 13 as a function of $M_{x,k}$ from equation 15 (blue) compared with $f(x,k)$ from a stochastic simulation (black). The green, magenta and yellow curves highlight the molar masses of chains without (green), 1 (magenta) or 2 A units in the chain. b) Cumulative polymer mass % as function of the logarithm of the molar mass of the simulated polymer chains (black), its cumulative Gaussian approximation (red) and the corresponding GPC-like lognormal mass distribution (green). c) Number (N_A, N_B, black) and weight (W_A, W_B, red and green) block length distributions of A units from the simulated chains (black and red) and based on the Flory equation (green). d) Number (black) and weight (red and green) block length distributions of B units from the simulated chains (black and red) and based on the*

Flory equation (green). The vertical lines in d) are the most probable block lengths from the simulation (red) and the Flory equation (green). Figure 12a is repeated in Appendix A (Figure A.5) using linear coordinate axes to highlight the skewed nature of the distribution functions.

2.3.3 Thermal behavior

The DSC specific heat capacity, $c_p(T)$, curves of PCCD-PTHF during cooling and subsequent heating at 10 K/min are shown in **Figure 13**, along with the PCCD crystallization, T_c, and melting, T_m, peak temperatures. T_m (207.2 °C) is a bit higher and T_c (118.2 °C) considerably lower than reported by Matsumoto *et al.* (T_m = 198.2 °C, T_c = 139.6 °C).[20] They observed a decrease of T_m from 5 to 25 wt% PTHF and a decrease of T_c up to 20 wt% PTHF.[20] Unexpectedly, T_c increased at 25 wt% PTHF, suggesting enhanced nucleation, possibly due to contamination. Our results indicate a continued downward trend.

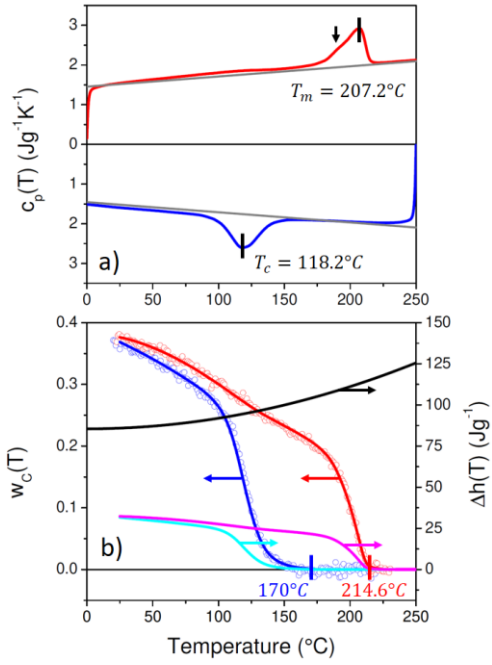


Figure 13. *a) DSC $c_p(T)$ curves of PCCD-PTHF during cooling (blue, downward) and subsequent heating (red) at 10 K/min, with the linear baselines (grey) for integration. T_c and T_m are marked with vertical lines, b) $\Delta h(T)$ (J/g) during cooling*

(cyan) and heating (magenta) along with $\Delta h_{ref}(T)_{PCCD}$ (black); DSC based $w_C(T)$ for cooling (blue) and heating (red) alongside the WAXS-based crystallinity (open circles in corresponding colors). Crystallization onset (170 °C, blue) and melting endset (214.6 °C, red) are defined where $\Delta h(T)$ equals 0.3 Jg^{-1}.

The melting peak shows a small low temperature shoulder (arrow in **Figure 13a**), attributed to a Melting-Recrystallization-Remelting (MRR) effect. In this process, crystals formed during cooling melt, recrystallize and melt again. Recrystallization can be suppressed by increasing the heating rate, with only the original low-temperature melting remaining at high rates. **Figure 14** shows the sample heated at 5, 10, and 50 K/min after cooling at 10 K/min. The melting peak temperature shifts to lower values and the low temperature shoulder vanishes upon increasing the heating rate, which can be considered as evidence for suppressed melting-recrystallization-remelting (MRR) effects.

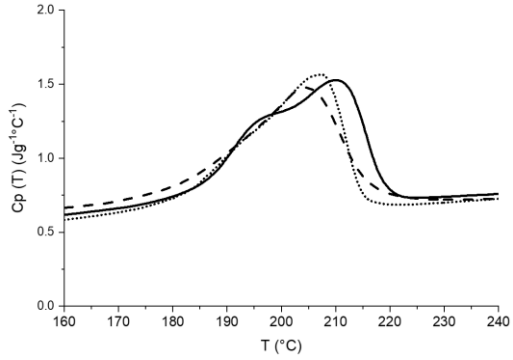


***Figure 14**. DSC heating curves of the PCCD-PTHF segmented block copolymer after cooling at 10 K/min from 230 °C down to room temperature and heating at 5 (solid line), 10 (dotted line), and 50 K/min (dashed line).*

In the case of pure PCCD, integrating the area between $c_p(T)$ and the extrapolated melt $c_p(T)$, would yield the transition enthalpy as function of the temperature, $\Delta h(T)_{PCCD}$.[13] Dividing $\Delta h(T)_{PCCD}$ by the (temperature dependent) reference transition enthalpy of fully crystalline PCCD, $\Delta h_{ref}(T)_{PCCD}$, would give the PCCD mass fraction crystallinity, $w_C(T)_{PCCD}$, according to

$$w_C(T)_{PCCD} = \frac{\Delta h(T)_{PCCD}}{\Delta h_{ref}(T)_{PCCD}} \quad (17)$$

In the present case, PCCD only represents 75 wt% of the material, implying that one needs to divide the overall block copolymer crystallinity $w_C(T)$ and overall transition enthalpy, $\Delta h(T)$, by this factor to obtain the PCCD crystallinity, $w_C(T)_{PCCD}$:

$$w_C(T)_{PCCD} = \frac{w_C(T)}{0.75} = \frac{\Delta h(T)}{0.75 \cdot \Delta h_{ref}(T)_{PCCD}} \quad (18)$$

The two right side parts of equation 18, permit stating that $w_C(T)$ can be obtained from

$$w_C(T) = \frac{\Delta h(T)}{\Delta h_{ref}(T)_{PCCD}} \quad (19)$$

To compute the PCCD crystallinity from the DSC based $\Delta h(T)$, one needs to know $\Delta h_{ref}(T)_{PCCD}$. To our knowledge, no values for $\Delta h_{ref}(T)_{PCCD}$ have been reported in the literature. As the mass fraction crystallinity is available from WAXS (discussed in section 2.3.5 and represented by the open symbols in **Figure 13b**), $\Delta h_{ref}(T)_{PCCD}$ can be obtained. Overlapping DSC and WAXS crystallinities are obtained when $\Delta h_{ref}(T)_{PCCD}$, which can be found in **Figure 13b** (black line), follows a quadratic equation:

$$\Delta h_{ref}(T)_{PCCD} = 85.5 + 0.00051 \cdot T + 0.00064 \cdot T^2 \ \ (Jg^{-1}) \quad (20)$$

This equation, with T in °C, was obtained using a least squares fitting procedure in which the integration baselines (depicted in grey in **Figure 13a**) and $\Delta h_{ref}(T)_{PCCD}$ were constraint to respectively depend linearly and quadratic on the temperature. These conditions impose that the heat capacities of crystalline and amorphous matter vary linearly with the temperature, as is often the case.[48] Equation 20 can be used to obtain the crystallinity in PCCD homopolymer or copolymers thereof from DSC data. In terms of magnitude and temperature dependence, $\Delta h_{ref}(T)_{PCCD}$ closely resembles that of poly(ethylene terephthalate) (PET).[49] The WAXS and DSC crystallinity in **Figure 13b** show a strong increase from ~ 160 to ~ 110 °C upon cooling, followed by

a weak but steady increase. This evolution is reversed upon heating with some hysteresis.

No clear glass transition temperature, T_g, was detected with DSC, even if cooled down to far below room temperature, likely because vitrification is spread over a large temperature range as a result of a PTHF enrichment in the remaining amorphous micro domains during crystallization (shifting the T_g locally down) and connectivity with crystallites (shifting the T_g locally up). To avoid issues related to crystallization and phase separation, FSC was used to determine the T_g of completely amorphous PCCD-PTHF (see **Figure 15**). A cooling/heating experiment was conducted at 1000 K/s, following the reference protocol shown in **Figure 10a**. The typical T_g step in the heat flow curves was visible during both cooling and heating with inflection points at respectively 0 °C (T_g^c) and 6 °C (T_g^h).

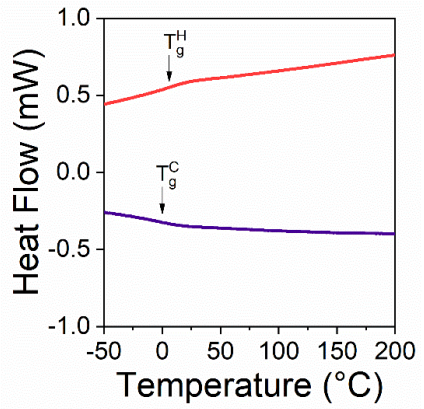


Figure 15. *FSC heat flow data of PCCD-PTHF upon cooling (purple) and heating (red) at 1000 K/s with the corresponding inflection point based T_g positions (T_g^c and T_g^h).*

The single T_g suggests that the melt was homogeneously mixed at the temperature from which the sample was quench cooled (250 °C) and that this mixed state was preserved during cooling to the glassy state. In that case, the copolymer glass transition temperature $T_{g,copol}$ should fall between the ones of pure PTHF ($T_{g,PTHF} = -84.2\ °C$ [50]) and pure PCCD ($T_{g,PCCD}$). Based on the Fox equation,[51] which makes use of the temperature in K, $T_{g,PCCD}$ can be calculated via:

$$\frac{1}{T_{g,copol}} = \frac{0.75}{T_{g,PCCD}} + \frac{0.25}{T_{g,PTHF}} \quad (21)$$

0.75 and 0.25 are the PCCD and PTHF mass fractions. Using T_g^h (6 °C) of PCCD-PTHF for $T_{g,copol}$ leads to a $T_{g,PCCD}$ of 58.8 °C.

In **Figure 16a**, experiments are included in which the sample is quenched and annealed at several temperatures (T^*) below $T_{g,copol}$, i.e. the thermal protocol shown in **Figure 10a.** Annealing may reveal the presence of closely overlapping glass transitions through separate endothermic enthalpy recovery peaks and reveal the partial separation of phases that are almost identical in composition. As single recovery peaks were observed for all annealing temperatures, it is safe to state that the glassy sample was homogeneously mixed. For all T^* a single recovery peak appears that grows and shifts to higher temperatures with increasing T^*. Remarkably, the low T^* recovery peaks occur below the inflection point $T_{g,copol}$ at 6 °C. More commonly, recovery peaks link up at the high temperature side of the glass transition, thereby adding an overshoot to the T_g step, similarly to the -30 °C curve. This more common behavior is due a so-called α-relaxation with super-Arrhenius characteristics.[52] However, for some glassy homopolymers such as poly(1-4 cyclohexane di-methanol)[53] and polystyrene[54] unusual low temperature relaxation peaks have been reported when aged at temperatures way below T_g. This was explained by the possible occurrence of secondary relaxation mechanisms that are faster than the α-relaxation and show an Arrhenius behavior.

Although the copolymer segments homogeneously mix at 250 °C, this is not necessarily so at lower temperatures. It is relevant to determine whether the melt remains homogeneous down to reaching the crystallization onset temperature as this would imply that any segment separation is induced by crystallization rather than by liquid-liquid demixing. Using the FSC protocol as depicted in **Figure 10b**, which is inspired by the work of Balko et al. (2017) on the melt miscibility of a TPU [55], the material was cooled at 10 K/min to the crystallization onset temperature (170°C), kept there for 1 s and quench cooled at 1000 K/s to -90°C. The ensuing heating run at 1000 K/s, depicted in **Figure 16b** (green), shows the same single T_g step as after quench

cooling from 250 °C without any endothermic trace of melting. It therefore seems that 1 s was insufficient to induce traceable crystallization, and that the liquid remained homogeneously mixed while being cooled down at 10 K/min to 170 °C. Crystallization thus starts from a homogeneous melt phase. This will be confirmed in section 3.6 where the synchrotron SAXS data are discussed. **Figure 16b** furthermore demonstrates that crystallization is permitted to a certain extent if cooled down to below 170 °C at 10 K/min. Indeed, the heating runs clearly display PCCD melting endotherms that grow with lower T_a values. In addition, the T_g step progressively broadens and shifts to lower temperatures due to the associated PTHF enrichment in the amorphous phase.

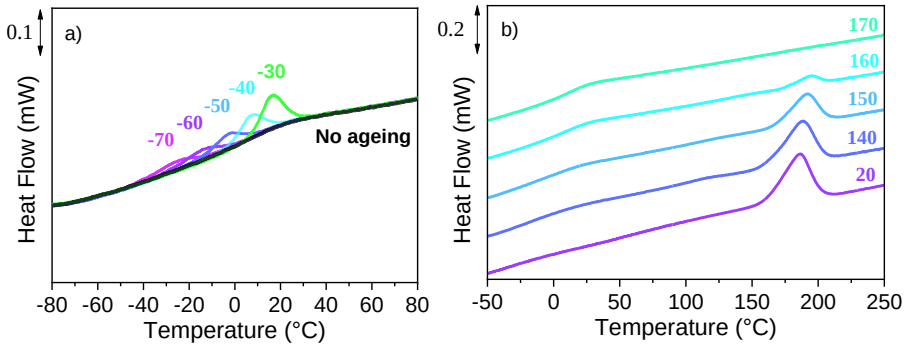


***Figure 16**. FSC Heat Flow (mW) heating curves at 1000 K/s following the thermal protocol as depicted in a) **Figure 10**a where T^* was varied between -30 and -70 °C and b) **Figure 1b** where T_a was varied between 20 and 170 °C as indicated next to the graphs.*

2.3.4 Morphology through Polarized Optical Microscopy (POM) and Atomic Force Microscopy (AFM)

POM experiments were performed during cooling and heating at 10 K/min. The micrographs recorded during cooling in **Figure 17(a-e)** reveal no structures in the

melt at 204 °C, followed by the formation and growth of birefringent spherulites with the typical Maltese cross at 135 °C (b) and 123 °C (c). Full impingement is reached at about 102 °C (d) after which little changes occur upon further cooling to 0 °C (e). PCCD-PTHF thus crystallizes into space filling spherulites of which the earliest formed, largest ones reach a diameter of approximately 100 µm.

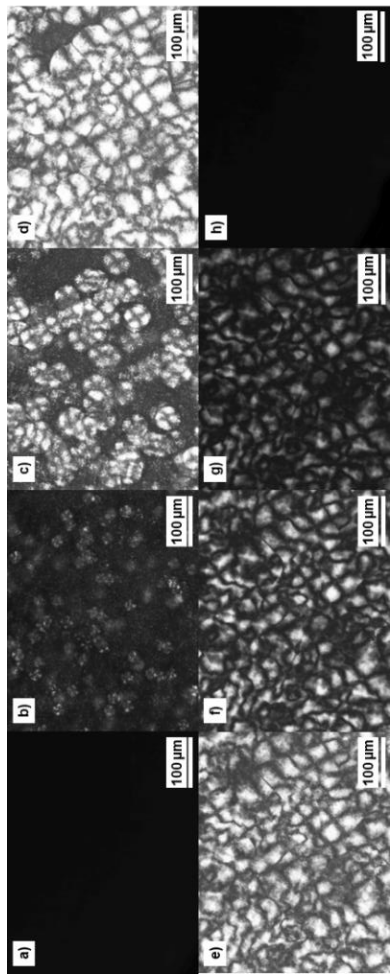

a)
b)
c)
d)
e)
f)
g)
h)
100 µm
i)
Normalized intensity
Temperature (°C)
0.0
0.2
0.4
0.6
0.8
1.0
0
50
100
150
200
250

Figure 17. *POM micrographs of PCCD-PTHF during cooling at 10 K/min at a) 204 °C, b) 135 °C, c) 123 °C, d) 102 °C and e) 0 °C and during subsequent heating from 0 °C at 10 K/min, at f) 201 °C, g) 207 °C and h) 239 °C. The error on the temperature is ±1 °C. i) shows the normalized, integrated POM image intensity as a function of temperature during cooling (purple) and subsequent heating (red).*

Upon heating, the spherulite intensity remains rather constant but homogeneously fades once 180 °C has been surpassed as illustrated for 201 °C (f) and 207 °C (g). Above 218 °C, featureless dark images are left as in (h) at 239 °C. **Figure 17i** shows the evolution of the normalized total image intensity, I_{POM}, which is proportional to the spherulite volume fraction, ϕ_s, the crystallinity inside the spherulites, $\phi_{cr,s}$, the orientation of the crystallites in the spherulites, P_2, and the intrinsic anisotropy of a pure crystal, δ_{cr}^0, according to [56]:

$$I_{POM} \sim \phi_s \left(\phi_{cr,s} \delta_{cr}^0 P_2\right)^2 \tag{22}$$

P_2 is a Hermans-type orientation function describing the orientation of the crystals (or more precisely, that of the crystal optical axis) with respect to the radius of the spherulite. It equals 1 for a perfect alignment and zero for a completely random orientation. The sigmoidal increase during cooling reflects the spherulite nucleation and growth through the increase of ϕ_s and follows the increase in the WAXS and DSC crystallinity from 0 to approximately 25 % (**Figure 13**). Upon further cooling, I_{POM} slightly decreases while the crystallinity continues to increase to 37 %. This increase in $\phi_{cr,s}$ with a factor of 1.5 needs to be compensated by an at least as large decrease in the product $\delta_{cr}^0 P_2$ to compensate for that. This might be accomplished by a rather random orientation of the secondary crystals growing in the amorphous pockets of the space filling spherulites. These secondary crystals reversibly melt upon heating as I_{POM} increases again. Only at the highest temperatures, I_{POM} collapses when the primary, spherulite-forming crystallites melt. The spherulites melt homogeneously, implying that ϕ_s essentially remains 1 up to the end of melting and that the collapse of I_{POM} results from a decrease of $\phi_{cr,s}$.

Classically, polymeric spherulites are composed of alternating crystalline and amorphous layers or lamellae. This two-phase morphology was probed by AFM at room temperature after cooling the sample at 10 K/min. The result is shown in **Figure 18**.

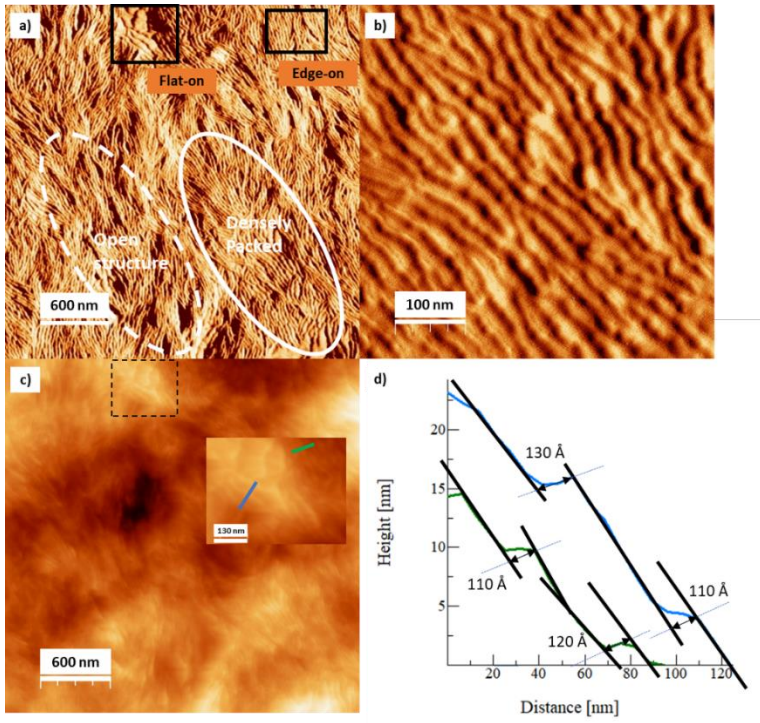


Figure 18. *a) 3 x 3 µm AFM phase image of a crystallized PCCD-PTHF sample at room temperature after cooling at 10 °C/min, with the black rectangles indicating stacks of flat-on and edge-on lamellae and the white ovals indicating open and densely packed structures, b) a 0.5 x 0.5 µm phase image of the same sample in a densely packed region c) height image of a) with a zoom in on the flat-on lamellae and with a green and a blue line indicating the height profiles analyzed in d). In d) two height profiles (blue and green) analyzed in terms of step heights with indicated sizes at the double headed arrows. Note the difference in scale of the height and (lateral) distance axes.*

The phase image in **Figure 18a** reveals lamellae in rather densely or openly packed stacks. A densely packed region is magnified in **Figure 18b** and uncovers frequent lamellar branching, likely due to impurity accumulation at the growth front and non-crystallographic growth tip splitting.[57] Impurities might be chain fragments rich in

PTHF, which cannot readily take part in the crystallization. Such branching occurs at rather small angles, producing densely packed lamellar stacks while leaving amorphous pockets in between the primary stacks as the spherulite grows. These pockets might be filled in with crystallites at a later stage by an independent nucleation step and with an orientation lacking correlation with the lamellae in the primary stacks, as suggested earlier. The more erratic crystallization in these secondary pockets might lead to the observed more openly stacked areas, which also leaves more options for the insertion of secondary lamellae in between earlier formed ones. As the orientation of these secondary lamellae has little to no relation with the spherulite radius, the spherulite birefringence might decline toward lower temperatures as is observed in **Figure 17i**. The insertion of secondary lamellae in between existing ones may be postponed to lower temperatures and stretched over a rather wide temperature range as the increased PTHF presence in the segregated interlamellar regions leads to a reduced supercooling for crystallization,[57] which can only be overcome by further cooling. As mentioned earlier, this insertion process is inverted upon heating and will be discussed and quantified in section 2.3.6.

The height image corresponding to **Figure 18a** and examples of height profiles are given in **Figure 18c,d**. From these profiles, the stack periodicity, say the long period L_P could be estimated as 118 Å, which agrees well with the SAXS based L_P value (see section 2.3.6).

2.3.5 PCCD crystallography and crystallinity through WAXS

To our knowledge, no report exists on the PCCD crystal structure. Therefore, an attempt was made to disclose the dimensions of the PCCD unit cell and the Miller indices of the reflections from an X-ray diffraction (XRD) pattern at room temperature of an oriented piece of PCCD-PTHF, produced via injection molding as explained in section 2.2.2.

The piece was presented to the X-ray beam with the machine direction (MD) and hence the molecules orientated vertically. At this direction, the azimuthal angle, φ, in the 2D XRD pattern was set to zero as illustrated in **Figure 19a**. **Figure 19b** magnifies

the SAXS part and reveals lobes at $\varphi = 0°$ and $\varphi = 180°$ due to the periodicity of the lamellar stacks, containing lamellae that are oriented perpendicular to the machine direction. As the PCCD molecules are aligned in the MD, they are aligned parallel to the lamellar normal.

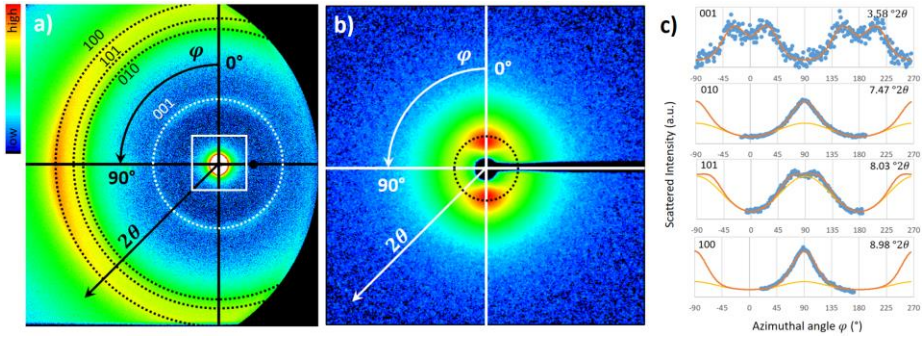


***Figure 19**. a) 2D scattering pattern of injection-molded PCCD-PTHF, with azimuthal (φ) and scattering angles (2θ) indicated. The machine direction is vertical, defining $\varphi = 0°$ at the meridian. Important reflections are marked with dotted rings and Miller indices. The white square encloses the SAXS region shown in b). Intensities are on a logarithmic color scale, with values below a threshold in black and above a maximum in white. The color scale in a) and b) corresponds to different absolute values. Panel c) shows azimuthal readings (blue markers) through the reflections in a), with Miller indices in the top left and 2θ angles in the top right. Angles are for Mo radiation ($\lambda = 0.709$ Å). Orange curves are fitted Gaussians, overlaid on a yellow background from the amorphous halo, showing maxima at $\varphi = 90°$ and $= -90°$ due to molecular orientation along the MD. The fitted curves are extrapolated outside the experimental φ windows.*

Strong reflections are highlighted with dotted rings at their 2θ values and labelled with Miller indices in **Figure 19a**. The intensities along these rings (**Figure 19c**) show a splitting of 27.2° on each side of the meridian for the 001 reflection and the equator for the 101 reflection. The 010 and 100 reflections are not split and occur at the equator. The splitting of the 001 reflection is explained in **Figure 20** where chains are drawn vertically along the MD but staggered to form plains, separated by $d_{001} = 11.8$ Å, with a normal tilted 27.2° from the meridian. The distance between the chains in the plane defines d_{100} with the unit cell a-axis connecting neighboring inter-chain lattice points. The β angle between the c and a axes is 62.8°, calculated as $90° - 27.2°$. The unit cell b-axis runs outside the plane, and its orientation determines whether the unit cell is monoclinic (perpendicular) or triclinic (non-perpendicular). In

the former case, lattice planes as in **Figure 20**, can be imagined at distances b above the sketch. In the triclinic case, the higher planes are shifted in position and the angles α and γ differ from 90°. Irrespective of the triclinic or monoclinic case, the 001 and 010 planes are aligned according to the MD and their random orientation around the MD produces reflections on the equator. The 101 planes (of which mirrored equivalents are shown in the top and bottom images of **Figure 20**) produce reflections at 27.2° on both sides of the equator as seen in **Figure 19c**. It will be shown in the next paragraph that α and γ deviate slightly from 90°. So, the d_{hkl} indications in **Figure 20** are in fact projections. The shown numerical values, however, correspond to the real inter planar distances and not to their projections on the ac plane.

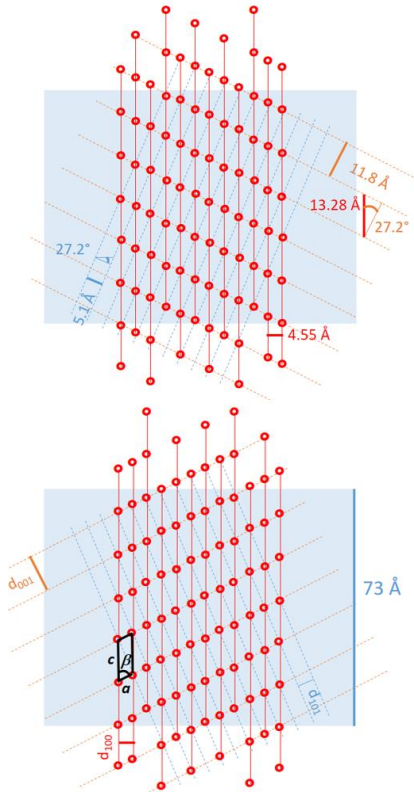


Figure 20. Sketches of the PCCD chain packing together with selected reflecting planes (bottom, d_{hkl}) and their associated Bragg spacings (top). The chain axes run parallel to the machine direction and defines the direction of the unit cell c-axis with a molecular repeat of 13.28 Å as indicated by the dot-like lattice points. The

horizontal blue shaded areas symbolize the lamellar thickness extracted from the integral breadth of the 001 *reflection.*

The blue curve in **Figure 21** shows the azimuthally averaged intensity of the 2D pattern in **Figure 19a**. To freeze in crystallographic orientation, the injection molding occurred at a high cooling rate. As high cooling rates are not conducive to well-developed crystals, the averaged pattern reveals a rather large amorphous halo centered at $q \sim 1.3$ Å^{-1} with broad and weak crystalline reflections on top. It was therefore decided to refine the unit cell based on the synchrotron SAXS and WAXS patterns collected at 20 °C after cooling at 10 K/min (the black curve in **Figure 21**). Based on the peak assignments made in the oriented pattern and a fitting procedure in which the unit cell parameters were varied up to a close match between the experimental and observed q_{hkl} values, the following triclinic unit cell parameters were obtained: a = 5.13 Å, b = 5.50 Å, c = 13.28 Å, α = 87.6 °, β = 62.8 ° and γ = 86.6 °. The labelled reflections in **Figure 21** were used in the refinement, and in **Table A-6** in Appendix A, the experimental and predicted q_{hkl} values are compared. The dots in **Figure 21** correspond to the positions of other predicted reflections. The crystalline share in this pattern closely resembles that of PCCD homopolymers published earlier.[21] The unit cell volume is 333 Å³, which with one PCCD monomeric unit leads to a density of 1.40 g/cm³. This value approaches the crystalline density of PET (1.50 g/cm³). [58]

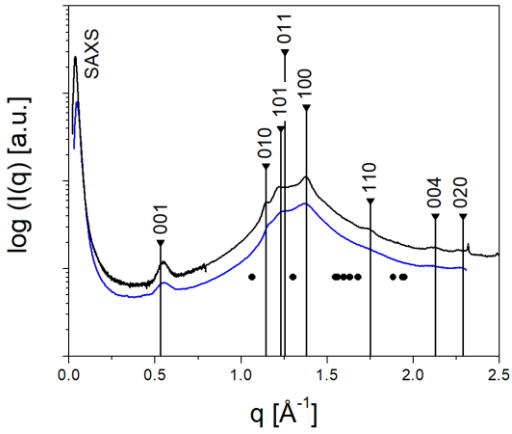


Figure 21. *Room temperature azimuthally averaged powder patterns of PCCD-PTHF cooled at 10 K/min (black) and of the 2D (oriented) scattering pattern of an injection molded sample (blue). The black pattern is a merged synchrotron SAXS and WAXS pattern. Strong reflections are labeled with the Miller indices of a triclinic lattice. The black dots are other predicted (weak) reflections.*

Figure 22 illustrates the synchrotron SAXS and WAXS patterns recorded during a) cooling and b) heating at 10 K/min between 230 and 22 °C. The melt patterns between 220 and 230 °C are not shown. The blue patterns collected at the DSC based crystallization onset (170 °C), are featureless in SAXS and testify the presence of amorphous matter in WAXS. The patterns in cyan were collected at 140 °C, which is where the DSC crystallinity has increased to 2 %. Here both the SAXS and WAXS patterns display first signs of structure formation, confirming that the (micro)phase separation (SAXS) concurs with crystallization (WAXS). The SAXS signal and the WAXS crystalline reflections fully disappeared upon heating where the DSC melting endset occurs (red patterns at 215 °C).

To determine the WAXS based mass fraction crystallinity, the crystalline and amorphous contributions needed to be separated. This was straightforward in the temperature range between 177 °C and 215 °C, where the material is semi-crystalline during heating but amorphous during cooling. The amorphous patterns of the cooling runs were scaled at corresponding temperatures during heating to match the semi-crystalline patterns where no Bragg reflections occurred.

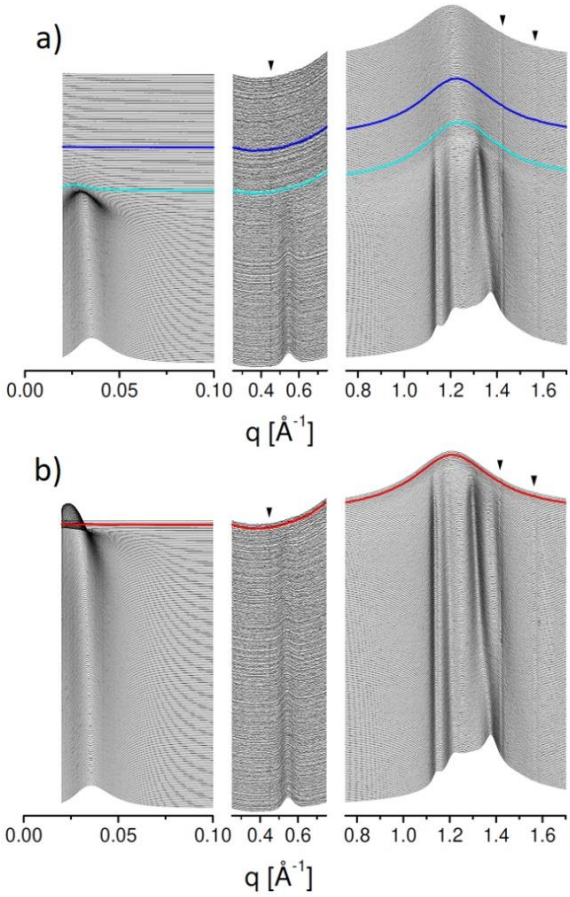


Figure 22. The time resolved synchrotron SAXS (left), 001 reflection (middle) and WAXS (right) q- ranges during cooling (a) and heating (b) at 10 K/min. From the top to the bottom, patterns are depicted from 220 °C to 22 °C. In panel a), the dark blue and cyan curves highlight patterns at 170 and 140 °C, respectively. In panel b), the red curve highlights the pattern at 215 °C. All patterns contain small background reflections at fixed q-values, marked with small triangles. The 001 reflection was recorded on the SAXS detector but was isolated for better visualization. The intensities are on a linear scale but magnified to different extends in the different q-ranges.

Next, a constant background was subtracted at the level of the scaled amorphous pattern at $q = 2.2\,\text{Å}^{-1}$ and the crystallinity was calculated from the ratio of the crystalline area to the full area of the semi-crystalline patterns. This procedure is illustrated for selected temperatures in **Figure 23**. The crystallinities in this

temperature range are rather small and therefore the shape of the amorphous halo is not strongly affected by the crystallization-induced PCCD extraction from it.

As representative amorphous halos are not available at lower temperatures and as only the 001 reflection (**Figure 22**, middle panels) can relatively easily be separated from the amorphous contribution, it was decided to isolate this reflection by approaching the amorphous halo underneath by a Lorentzian and the peak itself by a Gaussian. The Gaussian peak area was scaled to the absolute crystallinity determined at high temperatures during heating, assuming that this single peak area is proportional to the crystallinity. The resulting temperature dependent WAXS crystallinity can be found in **Figure 13b**.

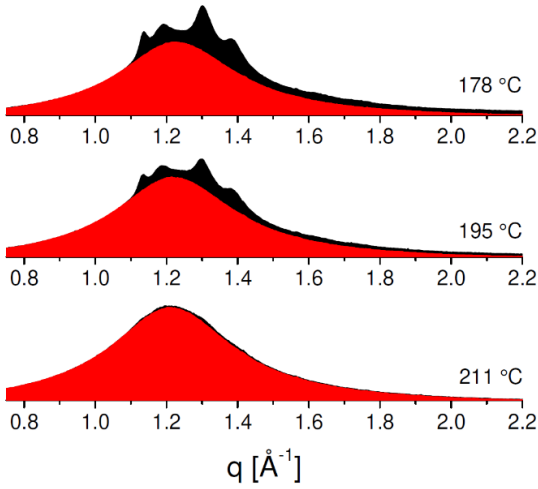


Figure 23. *Selected WAXS patterns at 178 °C, 195 °C and 211 °C during heating at 10 K/min, decomposed into amorphous (red) and crystalline (black) shares. The amorphous halos are scaled WAXS patterns, collected during cooling at the same temperatures. The crystalline shares amount to 25.4, 16.7 and 2.8 % for 178 °C, 195 °C and 211 °C respectively.*

The positions of the 001, 010, 101 and 011 reflections are rather temperature independent. Only the 100 reflection displays a strong shift to lower q-values with temperature, suggesting that the unit cell a dimension is most susceptible to thermal expansion. In **Figure A.7** of Appendix A, potential tracks of the earlier identified reflections are drawn over the WAXS heating patterns. No further analysis was,

however, conducted on the temperature dependence of the crystal unit cell as this – together with a full crystallographic assessment - is preferably made on a pure and highly crystalline PCCD sample with control over the *trans* content of the building blocks.

Finally, the integral breadth of the 001 Gaussian, L_{001}, was translated into a crystal size, D_{001}, measured parallel to the direction of d_{001} (see Figure 20), using the **Scherrer** equation:

$$D_{001} = \frac{K\lambda}{Lcos\theta} \tag{23}$$

with K being a constant equal to 0.9, λ the x-ray wavelength and θ half the scattering angle in radians. At room temperature, D_{001} measures 82 Å. As the normal to the 001 planes is inclined 27.2° with respect to the lamellar normal, the lamellar thickness, l_c, can be computed from the projection of D_{001} on the lamellar normal, i.e. $l_c = D_{001}\cos(27.2°)$. This leads to 73 Å for l_c. With the unit cell c dimension (13.28 Å), this leads to $73/13.28$ or ~ 6 PCCD units across the lamellar thickness. Blocks of 6 units are almost equally probably as blocks with 7 to 10 units (**Figure 12d**), implying that the crystal thickness is governed by the shortest of the most probable PCCD block lengths. Blocks shorter than 6 units likely are excluded from the crystals. The temperature dependence of l_c, along with other lamellar stack parameters derived from SAXS, will be discussed in the next section.

2.3.6 The semi-crystalline morphology by SAXS

Section 2.3.4 showed that the polymer crystallizes into semi-crystalline lamellar stacks. This forms the basis for the time-resolved synchrotron SAXS data treatment, which included direct fitting procedures and the use of linear correlation and interface distribution functions. The SAXS analysis of crystalline-amorphous two-phase systems provides size parameters and phase fractions but cannot distinguish which phase is crystalline. Based on **Figure 13b**, the crystalline phase is expected to be the minority at all temperatures. However, while microphase separation is driven by crystallization (**Figure 22**), PCCD separation may extend beyond its crystalline share.

The PCCD lamellae (**Figure 18**) could include internal stacking errors, such as *cis* moieties, which may not contribute to the WAXS-based crystallinity but could be part of the denser PCCD lamellae. These could be considered "crystalline" or dense by SAXS. Given that PCCD makes up 75 wt% of the polymer, the dense PCCD-rich phase may be the majority. Thus, independent size parameters can help guide the SAXS phase assignment, in addition to phase fractions, which might not be adequate.

Figure 24a displays the evolution of the WAXS based crystal thickness, l_c, obtained from the Scherrer analysis of the 001 reflection and a correction for the tilt of the 001 planes relative to the lamellar normal (see section 3.5). This tilt was assumed to be temperature independent. From the crystallization onset to about 125 °C, the l_c values are unstable due to the low intensity of the 001 reflection (**Figure 22**). Below 125 °C, l_c stabilizes to an average value of 73 Å. During heating, this value is maintained up to approximately 180 °C, after which an increase is observed, likely due to melting and recrystallization into thicker lamellae (see section 3.3). During cooling, the crystallinity more than triples from 125 °C to room temperature (**Figure 13b**). The constant l_c suggests that many new lamellae of identical thickness are formed. If thinner crystals had formed at lower temperatures, the 001 reflection would have broadened, but this was not observed. The constancy of l_c can be explained by a progressive PTHF enrichment of the amorphous phase as PCCD is extracted from the melt by crystallization. During crystallization at a given temperature, T_1, the increasing PCCD dilution lowers the PCCD equilibrium melting point and reduces the supercooling at T_1, which ultimately stops the crystallization process. Crystallization resumes only upon further cooling, leading to crystallites of similar thickness because of occurring at a regained comparable supercooling. This process is inverted upon heating until the mentioned recrystallization process leads to thicker crystallites. Recrystallization occurs at a reduced supercooling, aided by nucleation from oriented PCCD chain fragments left after primary melting. Notably, the increase in l_c is step-like with an increment corresponding to one molecular repeat (13.28 Å).

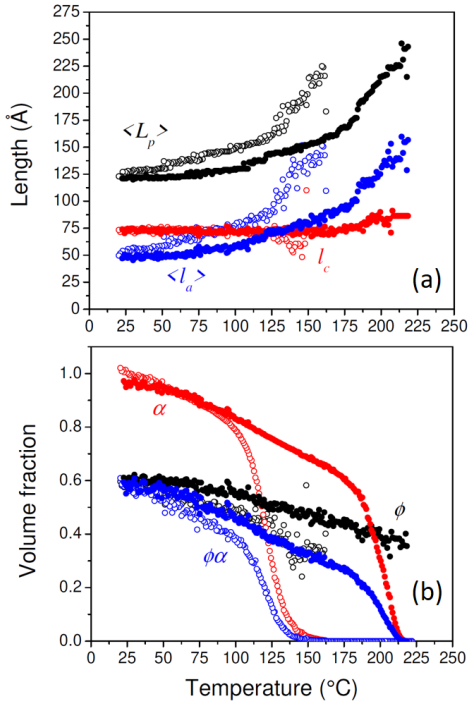


Figure 24. *The lamellar stack parameters during cooling (open symbols) and heating (closed symbols) at 10 K/min. In (a) the crystalline lamellar thickness, l_c, the long period, $\langle L_p \rangle$, and the average amorphous layer thickness, $\langle l_a \rangle$. In (b): the average local crystallinity within the semi-crystalline layers stacks, ϕ (black), the volume fraction of semi-crystalline stacks, α (red), and the overall SAXS based crystallinity, $\alpha\phi$ (blue).*

In an initial attempt to interpret the SAXS patterns, the data were fitted using a two-phase model, assuming paracrystalline stacks of alternating A and B layers with Gaussian thickness distributions centered around averages d_A and d_B and with standard deviations σ_A and σ_B.[59] **Figure 25** provides all results for d_A (green lines), d_B (blue lines), σ_A and σ_B during cooling (light colors) and heating (dark colors) compared to the crystallite thickness obtained via the WAXS 001 reflection, the Scherrer equation and a tilt correction (red symbols, open symbols for cooling and closed symbols for heating at 10 K/min). The full equation of the model patterns and details on the fitting procedure are given in the the section of the Appendix A.8. While

the model accounted for the possibility of smooth transition zones between the layers, the fitting revealed that the boundaries are sharp.

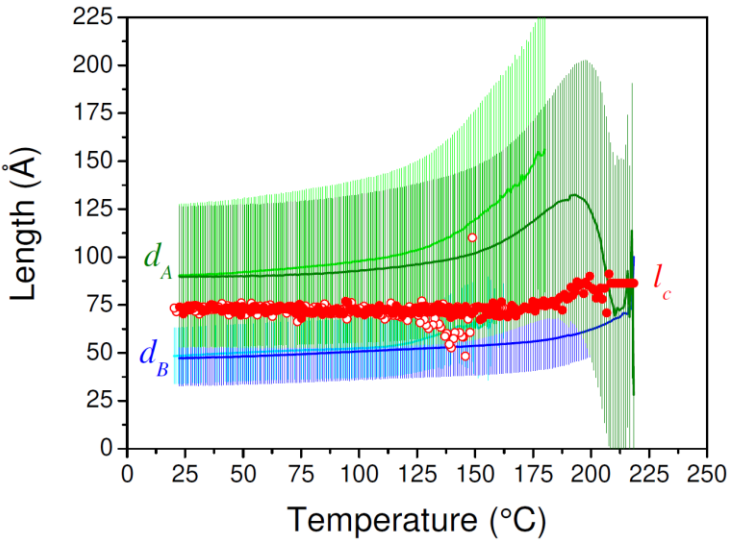


Figure 25. *Comparison between the crystallite thickness obtained via the WAXS* 001 *reflection, the Scherrer equation and a tilt correction (red symbols, open symbols for cooling and closed symbols for heating at 10 K/min) and the long (d_A, green lines) and short (d_B, blue lines) layer thicknesses obtained via a direct fitting of the SAXS patterns. Light blue and light green are data for the cooling runs, whereas the dark green and dark blue data are for the heating runs. The vertical bars over the data from the direct fitting represent the Gaussian spreads (plus and minus the standard deviation) around the average layer thicknesses d_A and d_B. The equation used to fit the SAXS data to a lamellar model of alternating A and B layers*

Figure 26 displays the fitting result for 4 selected temperatures during the heating run. The data are represented as $I_1(q)$, the Lorentz corrected version of $I(q)$ with $I_1(q) = 4\pi q^2 I(q)$.[60] $I(q)$ is the SAXS pattern with the background, defined during fitting, subtracted (see Appendix A.8). The agreement between the fits (cyan curves) and the data (open black symbols) at 22 °C and 122 °C is poor. Although the agreement improves at 182 °C and 202 °C, the resulting parameters (shown in the graphs) are unrealistic. The ratios $g_A = \sigma_A/d_A$ and $g_B = \sigma_B/d_B$ should remain below 0.4 to avoid large negative parts in the layer distributions, which is not the case for the B-type layers, particularly at 202 °C, even though the fit appears reasonable. Additionally, the fitting does not yield d_A or d_B values close to l_C. These issues suggests that the assumptions about the layer stacking in the model are not suitable to

the system. In what follows, we will argue that the amorphous layer thickness distribution is in fact bimodal.

The interpretation of linear correlation functions, $CF(x)$, and interface distribution functions, $IDF(x)$, is less dependent on assumption about the layer stacking. $CF(x)$ was calculated by a cos Fourier transformation:

$$CF(x) = \frac{\int_0^\infty I_1(q)\cos(qx)dq}{\int_0^\infty I_1(q)dq} \tag{24}$$

Integrations were performed up to $q = 0.8$ Å^{-1} after extrapolating the experimental data with the Porod behavior (i.e. $I(q) \sim K/q^4$ with K, the Porod constant) of the fits at high q-values. This integration limit is sufficiently high to avoid truncation errors.[60] Experimental data were replaced and extrapolated for $q \geq 0.15$ Å^{-1} or from slightly lower q-values when the patterns weakened at high temperatures. Extrapolation to low q-values was also done with the fitting result although the patterns at the lowest q-values, unlike the Porod behavior, depend on the stacking model. However, these low q data have minimal impact on the critical parts in $CF(x)$. The parts of the fits used in the extrapolations are highlighted in red in the top panels of **Figure 26**. $IDF(x)$ was calculated as the second derivative of $CF(x)$, i.e. $d^2[CF(x)]/dx^2$.[61] Examples of $CF(x)$ and $IDF(x)$ are shown in the bottom panels of **Figure 26**.

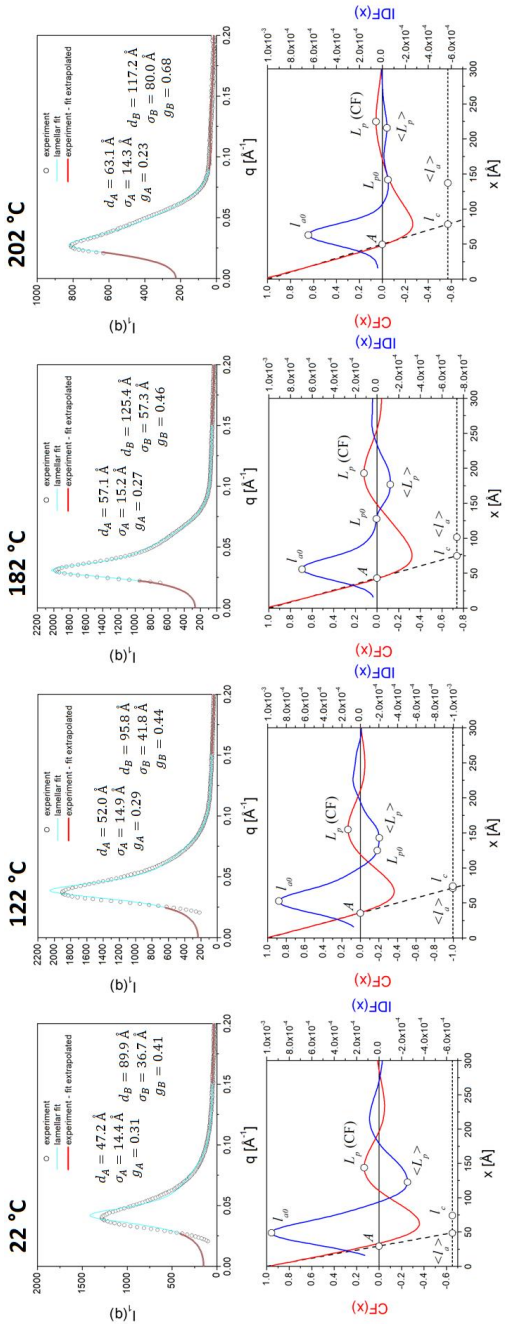


Figure 26. Lorentz and background corrected SAXS patterns, $I_1(q)$ (open circles), at selected temperatures during heating in the top panels and corresponding correlation, $CF(x)$ (red), and interface distribution functions, $IDF(x)$ (blue), in the bottom panels. The blue and red curves in the top panels are fits to a model of alternating A and B

layers, with the red parts being the shares that replaced and extrapolated $I_1(q)$ in the calculation of $CF(x)$. Reported parameters are the average layer thicknesses, d_A and d_B, their standard deviations σ_A and σ_B and the ratios $g_A = \sigma_A/d_A$ and $g_B = \sigma_B/d_B$. The dotted horizontal lines in the bottom panels are base lines at $-\phi_{min}/(1-\phi_{min})$ and the dashed lines through point A are linear approximations to the autocorrelation triangle. Other labelled points are explained in the text.

The stack periodicity, L_p, can be determined from the first side maximum in $CF(x)$, denoted as $L_p(CF)$, or from the first minimum in $IDF(x)$, denoted as $\langle L_p \rangle$ (**Figure 26**). Crist showed that these methods are not equivalent and that the most reliable measure of the average stack periodicity is the position of the minimum in $IDF(x)$.[62] The $\langle L_p \rangle$ values over the entire cooling and heating cycle are shown in **Figure 24a**. The average amorphous layer thickness, $\langle l_a \rangle$, follows from $\langle l_a \rangle = \langle L_p \rangle - l_c$ and the average local crystallinity within the semi-crystalline stacks, ϕ, is given by $\phi = l_c/\langle L_p \rangle$. The results for $\langle l_a \rangle$ and ϕ are presented in the **Figure 24a** and **Figure 24b**, respectively.

The layer thickness of the minority fraction can also be estimated from the intersection of the $CF(x)$ autocorrelation triangle with a baseline drawn at $-\phi_{min}/(1-\phi_{min})$ where ϕ_{min} is the minority fraction.[60] At high temperatures this corresponds to the crystalline fraction, ϕ, and at low temperatures, the amorphous fraction, $(1-\phi)$. The baselines, calculated from ϕ, are shown in the bottom panels of **Figure 26** with dotted lines and do not coincide with the minimum of $CF(x)$, indicating overlap between the amorphous and crystalline layer thickness distributions.[60] The values of l_c and $\langle l_a \rangle$ are marked on these baselines and coincide with the linear regression to the autocorrelation triangle (LRAT) for the minority phase layer thickness. In this case, the LRAT (represented by dashed lines in **Figure 26**) is not calculated through actual regression but by connecting its expected intersection with the base line $-\phi_{min}/(1-\phi_{min})$ with the abscissa at point A, with $A = \phi(1-\phi)\langle L_p \rangle$.[60] The resulting LRAT matches the $CF(x)$ autocorrelation triangle, demonstrating consistency.

Remarkably, the average local crystallinity ϕ (**Figure 24b**) does not match the overall crystallinity shown in **Figure 13b**. Initially, this difference was interpreted as a result of random melting of crystallites within the semi-crystalline stacks. It was

assumed that after a certain number of juxtaposed crystallite melting events, large amorphous pools would form, no longer contributing to the SAXS patterns or the local stack crystallinity, ϕ. However, this model could not be reconciled with the experimental $\langle L_p \rangle$. **Figure 27a** represents a series of lamellar stacks in which - from the bottom to the top - crystalline lamellae (represented by the black vertical bars and a density arbitrarily set to 1) disappear randomly by melting. The molten lamellae join the amorphous phase (with a density set to 0), represented in white. The number next to the left of each sketch, represents the fraction of crystalline lamellae not removed by melting, β. The original periodicity prior to melting is denoted as L_{p0} (some examples are indicated in red in panel a) and is the only periodicity occurring in the stack at 0% melting. Once melting starts, the removal of one crystalline lamella leads to a new separation distance, labelled L_{p1} (examples are indicated in green in panel a). At higher melting percentages, the random removal of lamellae may also lead to two lamellar removals next to each other, leading to L_{p2} (examples are indicated in blue in panel a) or even more juxtaposed removals, L_{p3}, L_{p4} etc… With β, one can define the number fraction, f_N, of periodicities L_{pN} due to N juxtaposed melting events as:

$$f_N = (1-\beta)^N \beta \tag{25}$$

With $\sum_{N=0}^{\infty} f_N = 1$. The number average periodicity when taking all periods into account, $\langle L_p \rangle_\infty$, follows from:

$$\langle L_p \rangle_\infty = \sum_{N=0}^{\infty} f_N L_{pN} \tag{26}$$

However, above a certain N value the periodicity will be so large that it escapes the SAXS observation. This can be taken into account by limiting the averaging to a certain finite N value, N_{fin}, according to:

$$\langle L_p \rangle_{N_{fin}} = \frac{\Sigma_{N=0}^{N_{fin}} f_N L_{pN}}{\Sigma_{N=0}^{N_{fin}} f_N} \tag{27}$$

This random melting model can be validated by comparing $\langle L_p \rangle_{N_{fin}}$ with the experimentally obtained $\langle L_p \rangle$ from IDF(x). For β the normalized WAXS crystallinity was used during heating at 10 K/min and L_{p0} was defined as $L_{p0} = l_c + l_{a0}$ with l_c being the crystal thickness obtained from the Scherrer analysis of the 001 reflection and a correction for the tilt of the 001 planes (see section 1.3.5) and l_{a0} being the amorphous layer thickness in the original stacks, read from the position of the first maximum in $IDF(x)$. Both l_c and l_{a0} are temperature dependent, hence so is L_{p0}. The melting of a lamella is assumed to add a value of L_{p0} to the amorphous layer thickness. In general, one can write for L_{pN} :

$$L_{pN} = L_{p0} + NL_{p0} \tag{28}$$

The L_{p0} increment upon melting likely is an underestimation because one expects a volume expansion when crystalline PCCD converts into amorphous matter.

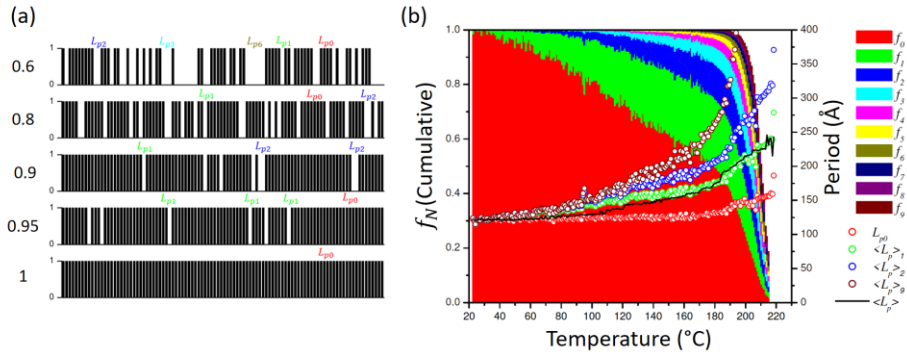


Figure 27. *a) represents a series of lamellar stacks upon heating (bottom to top) where the number next to the left of each sketch, represents the fraction of crystalline lamellae not removed by melting. The molten lamellae join the amorphous phase (with a density set to 0), represented in white. The newly formed periodicities are labelled* L_{p1}, L_{p2}, L_{p3} *etc.*.

In **Figure 27b**, the colored areas represent f_N as function of the temperature up to $N = 9$. The fractions are stacked in this representation and the sum reaches a value of

1 up to approximately 200 °C. Above 200 °C periods of $N > 9$ should be added to include all options and reach a sum of 1. Note that f_0 equals β. Using equation 27, values for L_{P0} (bright red open symbols), $\langle L_p \rangle_1$ (green open symbols), $\langle L_p \rangle_2$ (blue open symbols) and $\langle L_p \rangle_9$ (dark red open symbols) were computed and compared to $\langle L_p \rangle$ represented by a back full line. Clearly, $\langle L_p \rangle_1$ approaches $\langle L_p \rangle$ best. All other $\langle L_p \rangle_N$ are too large, implying that periods larger than L_{p1} do not contribute to the experimental SAXS $\langle L_p \rangle$. This observation indicates that lamellar melting is not a random process. It can produce L_{P1} periodicities through the local melting of a single lamella within a stack but once melting gets more vigorous, stacks are completely disappearing. Melting should thus also be considered on a stack level, as is done in the manuscript. Note that $\langle L_p \rangle_1$ in fact also exceeds $\langle L_p \rangle$, in particular at the lowest temperatures. This indicates that already at a very early stage, melting involves the removal of complete stacks. In the random melting model and the calculation of $\langle L_p \rangle_1$, stack melting (which is part of the experimental β) is fully allocated to an unrealistically large L_{P1} share, by which $\langle L_p \rangle_1$ is inflated compared to $\langle L_p \rangle$.

So, this analysis revealed that even early in the melting process, full stack melting should be considered. It also suggested that the observed $\langle L_p \rangle$ likely represents an average periodicity combining lamellae that remain packed at the original periodicity L_{p0}, and lamellae separated by a doubled periodicity, $L_{p1} = 2L_{p0}$, due to the melting of one lamella between the remaining ones. The SAXS data interpretation along these lines is explained in the next paragraphs.

Figure 28a illustrates the assumed melting process during heating. It shows a series of lamellar stacks where, from bottom to top, crystalline lamellae (represented by black vertical bars with a density set to 1) melt and merge into the amorphous phase (density set to 0). The number on the left of each sketch indicates the fraction of crystalline lamellae remaining after partial melting, β. Before melting, the original periodicity is L_{p0}, which is the only periodicity present when $\beta = 1$. As melting occurs, β decreases, resulting in either full stack melting or random melting of isolated lamellae, causing a locally doubled periodicity, L_{p1}. The volumes of intact stacks are shown in red, those with doubled periodicity in green, and fully melted stacks in blue.

The volume fractions for the different β values in **Figure 28a** are derived from the SAXS and WAXS melting data. **Figure 28c** shows the evolution of β during heating with a black line, along with the volume fractions of intact stacks (Z), stack fragments with doubled periodicity (Y) and of fully amorphous regions (X).

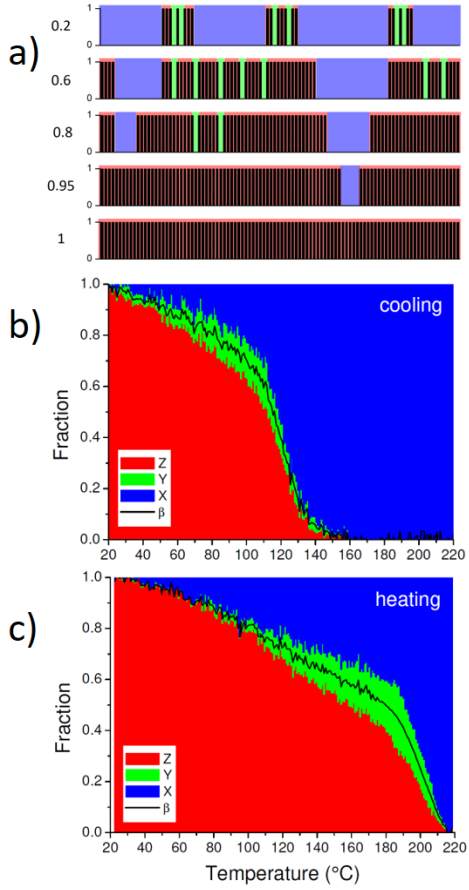


Figure 28. a) Schematic of lamellar stacks where crystalline lamellae (black bars, density = 1) melt and join the amorphous phase (density = 0, white). The number next to each sketch represents the fraction of crystalline lamellae remaining, β. Red-shaded regions (Z) retain the packing from $\beta = 0$, blue regions (X) represent fully melted stacks, and green regions (Y) correspond to stacks with one lamella out of two removed. The β values and fractions correspond to temperatures during heating: $\beta = 1$ (22 °C), $\beta = 0.95$ (50 °C), $\beta = 0.8$ (99 °C), $\beta = 0.6$ (153 °C), $\beta = 0.2$ (203 °C). In b) and c), the cumulative fractions of Z (red), Y (green), and X (blue) during cooling and heating are shown, with the β evolution indicated by the black line.

To obtain these values we start from the idea that the number of lamellar crystallites at any time, $\#_{cryst}$, is given by:

$$\#_{cryst} = Z \cdot \#_{max} + 0.5 \cdot Y \cdot \#_{max} \tag{29}$$

where $\#_{max}$ is the maximum number of crystallites before melting (as shown at the bottom in **Figure 27a**). The factor 0.5 accounts for having removed one crystal out of two in the Y volumes. Dividing both sides by $\#_{max}$ and with $\#_{cryst}/\#_{max} = \beta$ gives:

$$\beta = Z + 0.5 \cdot Y \tag{30}$$

Additionally, the three volume fractions satisfy:

$$Z + Y + X = 1 \tag{31}$$

And the average periodicity in the stacks, $\langle L_p \rangle$ can be computed from:

$$\langle L_p \rangle = \frac{ZL_{p0} + Y2L_{p0}}{Z+Y} \tag{32}$$

The factor 2 in the numerator assumes that melting one lamella between existing ones results in a double periodicity. This may be an underestimate, as volume expansion likely occurs when crystalline PCCD transitions to amorphous matter. Ignoring this, the equations 30, 31 and 32 can be solved to derive values for the volume fractions X, Y and Z, provided β, $\langle L_p \rangle$ and L_{p0} are known.

$\langle L_p \rangle$ is obtained from $IDF(x)$ (**Figure 26**). To determine β, we normalized the WAXS crystallinity (**Figure 13**) to its room temperature value, assuming space-filling stacks (i.e. $Z = 1$) at that temperature. Since all crystalline lamellae have equal thickness (**Figure 24a**), β should match the normalized WAXS crystallinity. For this WAXS estimate to apply in the SAXS context, we also assume that all crystalline lamellae contain an equal number of defects. These defects may not contribute to the WAXS crystallinity but are still part of the crystalline lamellae observed in SAXS.

L_{p0} is the sum of l_c and an amorphous layer thickness, l_{a0}, characteristic of intact stacks. As such stacks remain dominantly present from high to low β values (see **Figure 27a**), one can expect a positive maximum in $IDF(x)$ due to these amorphous layers as well as to the crystalline lamellae with a thickness l_c. At room temperature – when all stacks are intact - l_{a0} should be equal to $\langle l_a \rangle$. **Figure 26** at 22 °C demonstrates that the first maximum in $IDF(x)$ coincides with $\langle l_a \rangle$ while l_c falls within the peak, but not at the position of the maximum. This indicates an overlap of amorphous and crystalline layer thickness distributions (as indicated earlier), with the peak mainly dominated by the narrower amorphous layer distribution at that temperature. As many of these stacks remain at higher temperatures, the associated amorphous layers continue to contribute to the associated $IDF(x)$ peak. Thus l_{a0} can be read from the position of the first maximum in $IDF(x)$, as indicated in the bottom panels of **Figure 26**. Notably, l_{a0} at low temperatures is 48 Å, close to the length of a stretched PTHF macrodiol (936 g/mol), suggesting that it governs the limiting l_{a0}, though it does not imply that the amorphous layers are solely populated by these macrodiols. Isolated short PCCD segments and long PCCD segments connecting different crystalline lamellae are also expected to be present.

As β, $\langle L_p \rangle$ and L_{p0}, are available, values for X, Y and Z can be computed. Solving the equations 30, 31 and 32 to these volume fractions yields:

$$Z = \beta \left[\frac{4L_{p0} - 2\langle L_p \rangle}{3L_{p0} - \langle L_p \rangle} \right] \tag{33}$$

$$Y = \beta \left[\frac{2(\langle L_p \rangle - L_{p0})}{3L_{p0} - \langle L_p \rangle} \right] \tag{34}$$

$$X = 1 - \beta \left[\frac{2L_{p0}}{3L_{p0} - \langle L_p \rangle} \right] \tag{35}$$

The results for the cooling and heating runs are shown in the **Figures 13b** and **13c**, along with the WAXS based β values.

The volume fraction of the amorphous pools, X, equals $(1 - \alpha)$, where α is the volume fraction of semi-crystalline stacks. This parameter contributes to the total SAXS scattering power or invariant, Q_{ID}.[60]

$$Q_{ID} = \int_0^\infty I_1(q)dq = C\alpha\phi(1-\phi)(\rho_c - \rho_a)^2 \tag{36}$$

Q_{ID} is identical to the denominator of equation 24 and 'ID' denotes ideal two-phase systems with sharp boundaries between the crystalline and amorphous phases (layers) with electron densities ρ_C and ρ_a. C is a constant due to the experiments not being on an absolute scale. As densities often decrease linearly with temperature, the difference $(\rho_c - \rho_a)$ is also expected to evolve linearly. Using

$$\sqrt{\frac{Q_{ID}}{\alpha\phi(1-\phi)}} = \sqrt{C}(\rho_c - \rho_a) \tag{37}$$

with ϕ from **Figure 24b** and α from $(1 - X)$, the evolution of this density contrast is estimated. **Figure 29** shows that the data evolve linearly, demonstrating that $(1 - X)$ is a realistic measure for α, and that the methodology to obtain X is meaningful. The increase is due to the higher thermal expansion of the less dense amorphous phase compared to the crystalline phase. A deviation from linearity occurs at high temperatures, likely due to lower WAXS intensities and therefore a limited accuracy. Recall that X is based on β from WAXS. To avoid these problems, α shown in **Figure 24b**, was calculated differently from:

$$\alpha = \frac{Q_{id}}{\phi(1-\phi)\left(\sqrt{C}(\rho_c - \rho_a)\right)^2} \tag{38}$$

using the extrapolated linear regression from **Figure 29** for $\sqrt{C}(\rho_c - \rho_a)$. The overall SAXS crystallinity in **Figure 24b** is calculated from $\alpha\phi$. The evolution of $\alpha\phi$ closely follows the WAXS crystallinity from **Figure 13**, demonstrating consistency. The fact that $\alpha\phi$ exceeds the WAXS crystallinity, likely reflects non-crystalline defects within the crystalline lamellae that are part of the dense PCCD lamellae seen by SAXS but that do not contribute to the WAXS crystallinity.

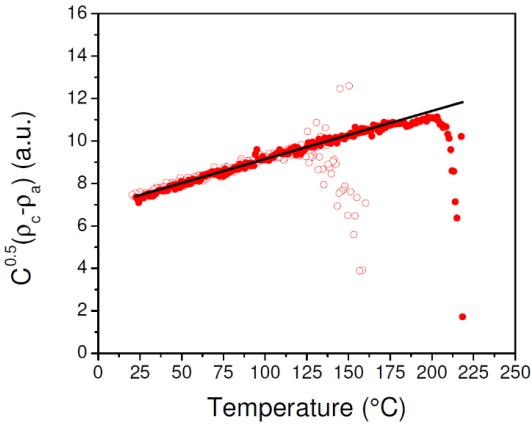


Figure 29. *Contrast function calculated from equation 37 during cooling (open symbols) and heating (closed symbols). The black curve represents a linear regression through the data, excluding the deviating points at the highest temperatures during cooling and heating.*

The bottom panels in **Figure 26** also show markers for L_{p0}, calculated from $l_{a0} + l_c$, on $IDF(x)$. At 122 and 182 °C, only minor traces of L_{p0} are visible. However, at 202 °C the clear minimum at L_{p0}, reveals a regained strong presence of closely packed stacks. These are likely due to new stacks from the recrystallization process (see section 3.3). These stacks were not considered in the analysis, which used the minimum in $IDF(x)$ at $\langle L_p \rangle$ throughout. As a result, the reported $\langle l_p \rangle$, $\langle l_a \rangle$, ϕ and α values in **Figure 24** above ~ 190 °C, are likely not representative for the entire system. The evolution of l_c is fine as it relies on the WAXS 001 reflection.

The main features of the crystallization and melting process are surely captured in **Figure 25**, showing good agreement with the WAXS crystallinity evolution. Secondly, the underlying model (**Figure 28**) in which intraspherulitic secondary crystallization (and its inverse during heating) is predominantly governed by the formation of new semi-crystalline layer stacks, aligns with the POM intensity stagnation in **Figure 17** and the idea that the orientation of these news stacks is not correlated with the direction of the radial spherulite growth. Therefore, the stacks replacing the (blue) amorphous volumes at higher β values in **Figure 28** should in fact not extend the already existing stacks. The difference in stack directionality was omitted in **Figure 28** for simplicity.

2.4 Conclusions

This study investigated a segmented co-polyesterether block copolymer with crystallizable poly(1,4-cyclohexylidene cyclohexane-1,4-dicarboxylate) (PCCD) A-units (90 mol%) and amorphous polytetrahydrofurane (PTHF-1000) B-units (10 mol%), with a PTHF mass percentage of 25%. This polymer is the primary component of Amphora SP1621, a high-performance polyester-based powder for laser sintering introduced by Eastman Chemical Company, with thermoplastic elastomeric (TPE) properties.

The A and B block length distributions were estimated via stochastic simulations, using the experimental molecular weight distribution and assuming random coupling of the A and B units. Most of the soft A blocks are isolated PTHF macrodiols, sandwiched between hard B blocks of varying lengths. The B block length distribution shows a higher proportion of shorter blocks compared to the Flory prediction for infinite chains. The simulation predicts a most probable PCCD block length of 7, whereas the Flory equation predicts 10.

Segment melt miscibility was confirmed by FSC while thermal behavior during cooling and heating at 10 K/min was analyzed using standard DSC. The PCCD crystallinity was determined with time-resolved synchrotron WAXS and combination with DSC led to an equation for the transition enthalpy of 100% crystalline PCCD.

Temperature-resolved POM and room-temperature AFM revealed that the material crystallizes spherulitically through the formation of lamellar PCCD crystallites. Primary crystallization leaves large pools of amorphous matter between the primary semi-crystalline layer stacks. During secondary crystallization, these pools transform into secondary stacks, with crystallites no longer oriented along the spherulite radial axis. This process reverses upon heating.

A crystal unit cell for PCCD was proposed based on room-temperature X-ray diffraction on an oriented injection molded PCCD-PTHF sample. This analysis also revealed that the PCCD chains orient perpendicular to the lamellar surfaces, which permitted calculating the PCCD lamellar thickness from the 001 reflection in

synchrotron WAXS measurements during cooling and heating at 10 K/min. The lamellar crystallite thickness was found to be rather temperature independent and measured 73 Å, except at high temperatures during heating where melting followed by recrystallization lead to slightly thicker crystallites. This thickness approaches the most probable PCCD block length.

SAXS interface distribution functions permitted obtaining values for the average amorphous layer thickness. It was argued that this amorphous layer thickness resulted from the average of amorphous layers in closely packed lamellar stacks (in which the limiting amorphous layer equals the length of a stretched PTHF macrodiol) and amorphous layers that separate crystalline lamellae, lacking one crystalline lamella in between to reach close packing.

A new SAXS data interpretation scheme was introduced to quantitatively estimate the fraction of amorphous pools that convert into semi-crystalline stacks during secondary crystallization, thereby reconciling all above-mentioned observations. The evolution of the overall crystallinity from this SAXS model is in good agreement with the WAXS crystallinity evolution although the SAXS crystallinity is larger, likely as a result of non-crystalline defects within the PCCD lamell

Chapter 3

Synthesis of PCCD and its Crystallization Behavior under Typical DSC Conditions

Author contributions

Mouna Hamid: Conceptualization, Investigation, Methodology, Formal analysis, Writing – original draft. **Ilya Mongilyov**: Conceptualization, Investigation, Methodology, Formal analysis. **Bart Goderis**: Supervision, Conceptualization, Methodology, Formal analysis, Writing – review and editing.

3.1 Introduction

PCCD, or poly(1,4-cyclohexylidene cyclohexane-1,4-dicarboxylate), is the homopolymer of the hard, crystallizable blocks of PCCD-PTHF. As a homopolymer it is a tough and rigid polymer and was first introduced in the 1950s.[40,41] It has excellent weatherability properties including high resistance to humidity, heat and UV. Moreover, the rigidity of the structure contributes to its excellent thermomechanical properties.[63]

While PCCD has been studied to a greater extent than PCCD-PTHF, knowledge on structure-property relationships remains limited. In the early years, the primary focus was on improving the synthesis method. Only towards the end of the 20th century did researchers start to explore the influence of stereochemistry on polymer crystallization behavior to a limited extend.[4,21,64] The two 1,4-cyclohexane rings in PCCD likely adopt, as most six-membered aliphatic rings, the chair conformation. The substituents are positioned either equatorially (in the ring plane) or axially (perpendicular to the ring plane). Whether the ring adopts a *cis* or *trans* configuration depends on the relative positions of the substituents. As shown in **Figure 30** for dimethyl 1,4-cyclohexanedicarboxylate (DMCD) and 1,4-cyclohexanedimethanol (CHDM), the monomers of PCCD, the *trans* form occurs when both substituents on the 1,4-cyclohexane ring are equatorial, while the *cis* form occurs when one is axial and the other equatorial.

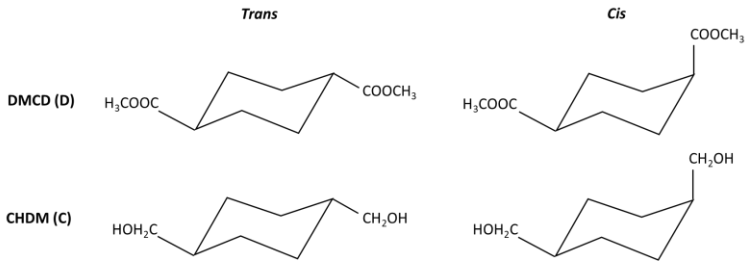


Figure 30. *Cis and trans conformations of DMCD and CHDM.*

In general, polymers with a high percentage of *trans* isomers form crystals with greater perfection, since chain packing is more efficient. By contrast, *cis* isomers introduce kinks into the chains, hindering packing and leading to a less ordered structure. This was also found in the case of PCCD, which was primarily investigated by Berti *et al*. (2008)[21] The *trans* content of the dicarboxylate (D) moiety was varied while maintaining the diol (C) moiety at a constant 66% *trans* content, which is reported to be the most thermodynamically stable composition.[65] DSC experiments showed that PCCD with a D *trans* content of ≤66% did not crystallize upon cooling at 20 K/min. In the range of 79–97%, crystallization was observed, with T_m, T_c and T_g all increasing as the D *trans* content rose, in agreement with previous studies.[44,66] By contrast, the influence of the C *trans* content has been little explored and remains not fully understood. This, however, is not the focus of this work.

The crystalline PCCD sample used here was synthesized with *trans* contents closely matching those of PCCD–PTHF described in Chapter 1, with values sufficiently high to promote a high degree of crystallinity. In addition, the PCCD homopolymer chains were longer than the average PCCD blocks in PCCD–PTHF, which, if of comparable length, would consist of fewer than 10 repeating units and therefore be considered oligomeric.

The homopolymer was expected to show similarities in crystallization behavior as PCCD-PTHF. Therefore, this study enabled confirmation of key aspects for PCCD-PTHF—such as the crystal unit cell and the influence of thermal expansion, while also assessing the validity of the determined reference enthalpy. PCCD was examined under identical experimental conditions. At the same time, it allowed an extensive characterization of the chosen synthetized PCCD. To date, only two studies

have reported morphological information on PCCD from WAXS measurements but the interpretation remained very qualitative.[21,67] For instance, Berti et al. (2008) performed WAXS on various PCCD samples, reporting diffraction peaks at positions identical to those of PCCD-PTHF, suggesting the same crystal unit cell.[21] They also carried out heating experiments on a high-*trans*-D PCCD sample, collecting WAXS patterns at 25, 90, and 160 °C, temperatures well below the melting point. Notably, the patterns at 90 and 160 °C showed subtle differences, consistent with the behavior of PCCD-PTHF. The authors attributed these changes qualitatively to differences in crystal perfection or possible unit cell modifications but provided no quantitative interpretation. The crystallization behavior of PCCD therefore remains only partially understood.

For these purposes, DSC measurements were performed at multiple scanning rates, POM was used to identify superstructures, and time-resolved SAXS/WAXS experiments were conducted to determine crystal thicknesses and track the evolution of crystallinity, following a similar methodology as applied to PCCD-PTHF.

This study addresses the gap, offering a detailed, quantitative assessment that clarifies its structure–property relationships. The results presented here also serve as the experimental foundation for the following chapter. Moreover, during this work PCCD was found to undergo chemical changes during prolonged annealing. To prevent this, a stabilization method based on end-capping was developed and shown to be effective.

3.2 Experimental section

3.2.1 Materials

The PCCD used in this study was synthesized at the Aachen–Maastricht Institute for Biobased Materials, located in Chemelot, the Netherlands. The synthesis procedure is described in detail in the *Results and Discussion* section. The resulting homopolymer exhibits a *trans* content of 98% of the carboxylic unit (D) and 70% of the diol unit (C). The number-average molar mass (M_n) was estimated to be 6,142 g/mol.

A polystyrene sample (M_n ~ 90,000 g/mol) from Agilent Technologies (Santa Clara, USA) was used for the calibration of the heat capacity values of PCCD.

3.2.2 Methods

^{1}H NMR Spectroscopy

The same apparatus, sample preparation procedures, and measurement conditions as described in Chapter 2 were employed. Four PCCD samples were examined: (i) as-synthesized, (ii) after 24 h of annealing in a closed system, (iii) after 24 h of annealing in an open system and (iv) end-capped PCCD.

Differential Scanning Calorimetry (DSC)

The same apparatus was used as described in Chapter 2. The thermal protocols used in this chapter are illustrated in **Figure 31-31.**

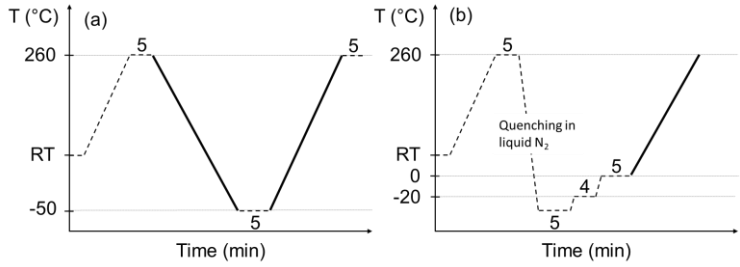


Figure 31. *Thermal protocols for PCCD, measured in hermetically closed pans. In protocol (a), the first cooling step was performed at rates between 2 and 50 K/min, followed by heating at 10 K/min. For the second heating, the rate was varied between 10 and 50 K/min, with both the cooling rate and the first heating rate fixed at 10 K/min. In protocol (b), the sample was first heated at 10 K/min, quenched in liquid nitrogen for 5 min, equilibrated at −20 °C, put in the DSC oven at 0 °C, and reheated at 10 K/min.*

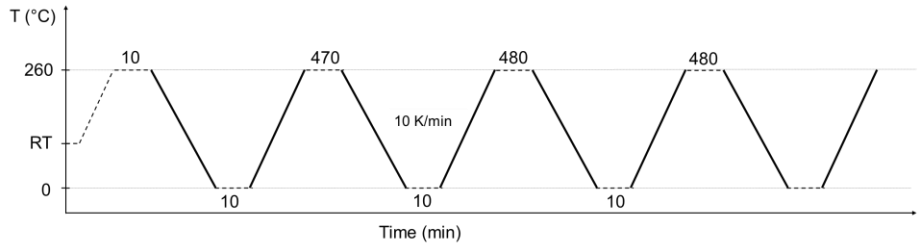


Figure 32. *Thermal protocol to investigate the stability of PCCD upon annealing at 260 °C. All the scanning rates were 10 K/min.*

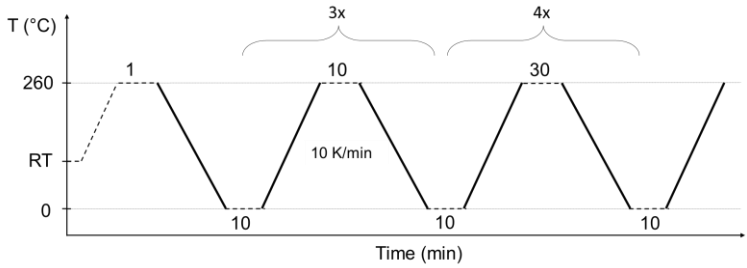


Figure 33. *Thermal protocol to investigate the influence of end-capping of PCCD upon repeated heating. All the scanning rates were 10 K/min.*

Polarized Optical Microscopy (POM)

The same apparatus and sample preparation was used as described in Chapter 2. The PCCD sample was heated to 260 °C, kept isothermally at 260 °C and cooled down at 10 K/min to RT. Images of the sample between crossed polarizers were taken every degree Celsius. The hot stage was flushed with nitrogen gas and a liquid nitrogen pump was used for cooling.

Time-resolved synchrotron Small-Angle and Wide-Angle X-ray Scattering (SAXS/WAXS)

X-ray scattering experiments were carried out at the ESRF (Grenoble, France) at BM26 and with the same setup described in Chapter 2, except that the SAXS detector was positioned approximately 4 m from the sample. The PCCD sample was tightly wrapped in Al foil, and the oven was not flushed with N_2. Heating followed the thermal protocol shown in **Figure 34**, while cooling and subsequent

heating were recorded in a time-resolved manner, with a frame captured at every degree.

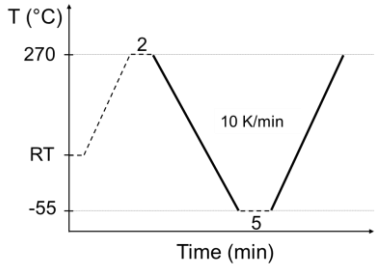


Figure 34. *Thermal profile used for the time-resolved SAXS/WAXS of the experiment. All the scanning rates are 10 K/min.*

A second measurement was performed in which PCCD was heated to 260 °C at 10 K/min and then immediately quenched in liquid nitrogen for 5 min, causing it to be fully amorphous in the glassy state. A frame was recorded after the sample had equilibrated to room temperature.

The scattering angles were calibrated against α-alumina and silver behenate standards and the isotropic powder patterns were azimuthally averaged using ConeX software.[43] The one-dimensional data were corrected for the scattering of an empty sample holder, taking the sample transmission into account as derived from the transmitted primary beam intensity measured by a photodiode downstream from the sample. Intensities were normalized to the intensity of the incoming beam, measured by an ionization chamber upstream from the sample.

3.3 Results and discussion

3.3.1 Synthesis

PCCD was synthesized via melt polycondensation under a nitrogen atmosphere (see **Figure 35**). The monomers were weighed with ±0.5 mg precision in a three-neck, tubular, round-bottom flask. A total of 7.00 g of 1,4-cyclohexanedimethanol (CHDM) and 9.77 g of dimethyl 1,4-

cyclohexanedicarboxylate (DMCD) were used, corresponding to a 0.5 mol% excess of DMCD (DMCD:CHDM molar ratio 1.3954:1). 7 mg of titanium(IV) butoxide was added as a catalyst. The reaction setup, inspired by Brunelle et al. (2006), [66] included a vertical distillation column, Liebig condenser, nitrogen inlet (2.5 ± 0.5 NL/min), and external temperature control via a thermocouple placed against the outer reactor wall. The entire system was mounted in a flask heater connected to a programmable temperature controller. To prevent monomer loss through splashing or premature evaporation, a distillation column was used as a physical barrier between the reactor and condenser. This design ensured that only methanol, the transesterification by-product, reached the condenser. A thermometer positioned at the condenser exit allowed for monitoring of the vapor temperature, and cold water was circulated through the condenser to facilitate efficient condensation (see blue arrows in **Figure 35**).

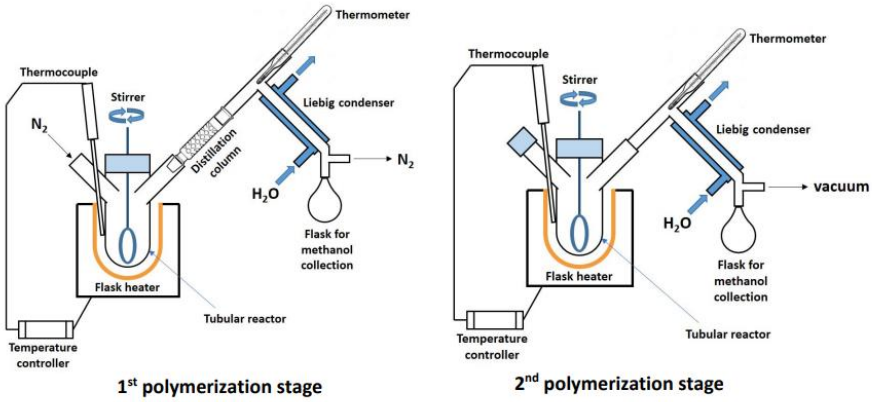


***Figure 35**. Experimental setups for the PCCD synthesis. Further details are provided in the text.*

The reaction began with solid, unmixed monomers. During the initial preparation phase, the temperature was gradually increased to 180 °C, allowing the monomers to melt (typically between 60–120 °C, depending on stereochemistry). Once fully molten, mechanical stirring was initiated and continued for 60 min to ensure homogeneity. In the first polymerization stage, the temperature was increased stepwise to 230 °C. As methanol evolution started, the temperature ramp was temporarily paused (~30–40 °C before target temperature) to prevent uncontrolled

boiling and to allow controlled distillation. Once methanol evolution slowed, the temperature was raised to the target 230 °C, and the system was held for approximately 50 min. At that point, the mixture was expected to consist of viscous, high-molecular-weight oligomers, with reduced splashing tendencies.

Following this, the distillation column was removed, and the reactor was directly connected to the condenser to improve methanol removal and reduce pressure drop. This change also improved system tightness in preparation for vacuum application, by minimizing glassware joints and potential leaks. The system was maintained at 230 °C for an additional 30 min, during which continued methanol condensation was observed.

In the second polymerization stage, the nitrogen inlet was hermetically sealed, and the outlet was connected to a vacuum pump (see **Figure 35**, right). The vacuum phase was conducted at 230 °C for 60 min, promoting further chain growth and reducing residual volatiles. During preliminary trials at 180 °C, 200 °C, and 230 °C, a second thermocouple was inserted directly into the melt to verify that the internal temperature corresponded to the reading from the external thermocouple—confirming accurate temperature control.

After the polymerization, the reactor content was cooled to room temperature, solidified in situ, and mechanically removed from the flask using a spatula. The polymerization reaction is illustrated in **Figure 36**.

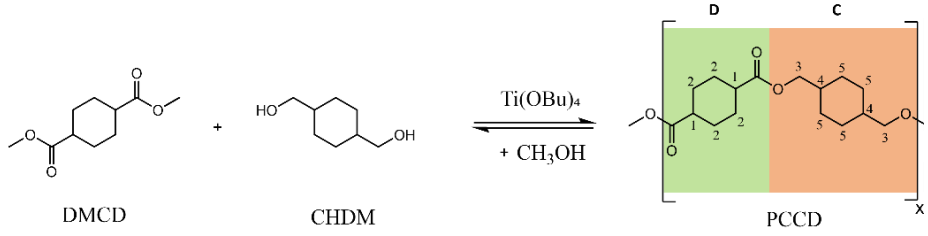


Figure 36. *Reaction of the synthesis of PCCD with dimethyl 1,4-cyclohexanedicarboxylate (DMCD) and 1,4-cyclohexanedimethanol (CHDM) in a nitrogen atmosphere.*

3.3.2 ^{1}H NMR Spectroscopy

After synthesis, a ^{1}H NMR spectrum was recorded at room temperature. The spectrum is shown in **Figure 37**, with signal assignments corresponding to the protons numbered in **Figure 36**. As expected, the spectrum closely resembles that of PCCD–PTHF, except for the absence of the PTHF signals. The cyclohexane moieties exhibit both *cis* (c) and *trans* (t) configurations. The corresponding proton signals are labeled H_{1c} and H_{1t} for the dicarboxylate (D) moiety, and H_{3c} and H_{3t} for the diol (C) moiety. The *trans* contents of **D** and **C** were determined to be **98%** and **70%**, respectively. These values were obtained using the same methodology previously applied for PCCD–PTHF, based on the relative integrals of the H_{1c}/H_{1t} (carboxylate) and H_{3c}/H_{3t} (diol) resonances. From these data, the fraction of fully *trans–trans* units was calculated to be (0.98 × 0.70) × 100% = 68.6%.

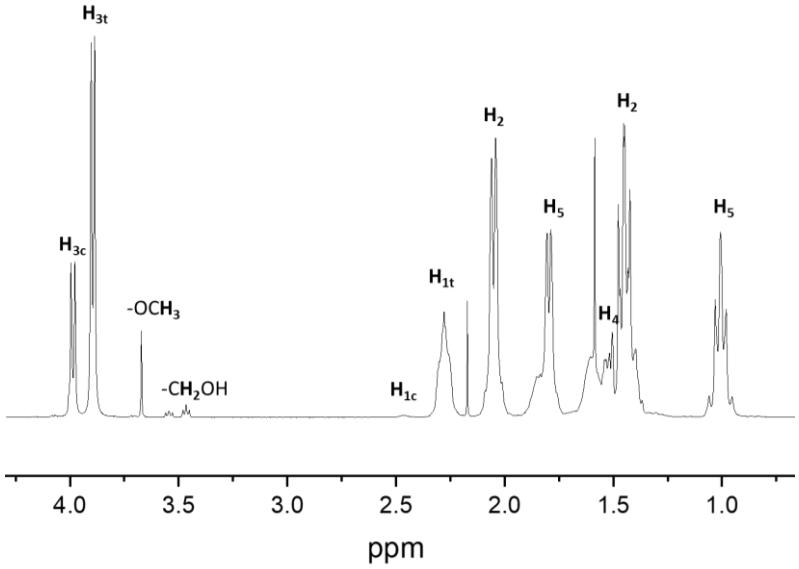


Figure 37. *The ^{1}H NMR spectrum of PCCD with the identified peaks (chemical shift, relative peak area) corresponding to H_{3c} (3.99 ppm, 0.56), H3t (3.90 ppm, 1.38), -OCH_3 (3.67 ppm, 0.09), -CH_2OH (3.50 ppm, 0.07), H_{1c} (2.47 ppm, 0.02), H_{1t} (2.28 ppm, 0.99) H_2 (2.05 ppm, 2.00), and H_5 (1.01 ppm, 1.44).*

The M_n was estimated to be 6,142 g/mol, corresponding to approximately three times the average block length of the PCCD segments in the PCCD–PTHF copolymer. This value was derived from the integration of the methyl ester end-group signal, using the equation: $M_n = M_{unit} * \frac{3}{2} * \frac{[H_{1c}]+[H_{1t}]}{[-OCH_3]} = 6{,}142\ g/mol$. Here, M_{unit}

denotes the molar mass of the repeating PCCD unit, and the factor 3/2 accounts for the two H_1 protons per repeat unit and three terminal protons of the -OCH_3 end group. This calculation assumes a stoichiometric end-group balance.

3.3.3 Thermal behavior

DSC measurements on PCCD were carried out in a hermetically closed pan following the thermal protocol shown in **Figure 31a** with all heating and cooling rates set to 10 K/min. The raw Heat Flow (HF) data obtained during cooling and subsequent heating were corrected for the empty pan, sample mass, and scanning rate to yield specific heat capacity values. No reference $c_p(T)$ data were available for PCCD, therefore, another method was used to retrieve the absolute $c_p(T)$ values. An extra DSC measurement was carried out on an amorphous polystyrene (PS) sample. After correcting the HF signals for the empty pan, heating rate, and sample mass, the $c_p(T)$ of the PS sample was fitted to its ATHAS data using a linear function, giving the calibration equation $-0.29 + 1.12 \cdot T$.[68] This calibration was then applied to the PCCD DSC $c_p(T)$ data to obtain the absolute $c_p(T)$ values for PCCD.

The $c_p(T)$ curves are presented in **Figure 38**, together with the melting temperature (T_m) and the crystallization temperature (T_c), determined as the peak temperatures. The T_m and T_c are both higher than in PCCD-PTHF. Also, the crystallization peak is narrower than for PCCD-PTHF, likely due to the absence of soft block segregation phenomena. The onset of crystallization upon cooling and the onset of melting upon heating are overlapping, categorizing PCCD as a fast-crystallizing polymer. In addition, the integration of the peaks resulted in $\Delta H_m = 45.2$ Jg^{-1} and $\Delta H_c = 43.9$ Jg^{-1}. With the ΔH_{ref} determined in Chapter 2, the crystallinity at the temperature of the intersection with the melt extrapolated base line was calculated via $\left(\frac{\Delta H}{\Delta Href}\right) * 100$ %, resulting in 46.9 % and 45.6 %. ΔH_{ref} is temperature dependent (Chapter 2). Here, values for ΔH_{ref} were selected at the temperatures of the above mentioned intersections, which for the heating and cooling run are slightly different but close to 130 °C ($\Delta H_{ref} \sim 96.4$ Jg^{-1}).

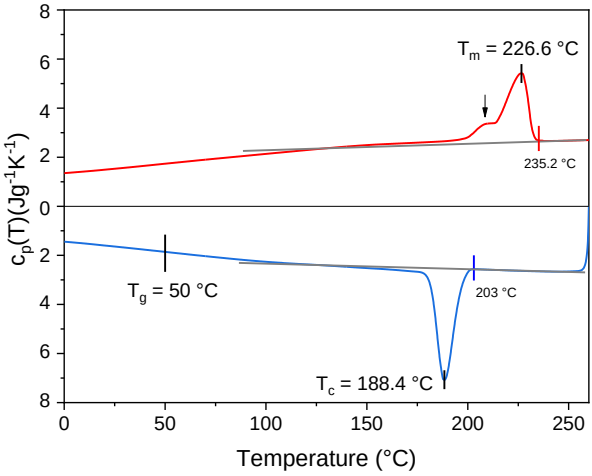


Figure 38. *$c_p(T)$ values of PCCD during cooling (blue) and subsequent heating (red) following protocol in* ***Figure 31a****. The T_m, T_g and T_c are indicated as well as the onset crystallization (upon cooling) and melting (upon heating).*

The arrow **Figure 38** indicates a shoulder to the melting peak, suggesting a Melting-Recrystallization-Remelting (MRR). The shoulder represents the melting of initially formed crystals, but they readily recrystallize to remelt again, which is seen by the large, overlapping high melting peak. The melting peaks observed in the $c_p(T)$ heating curves at different heating rates are shown in **Figure 39**. Recrystallization was restricted by increasing the heating rate, at the expense of the high-temperature

melting peak. This confirms that the multiple melting observed at 10 K/min is due to an MRR event, which is consistent with the behavior of PCCD-PTHF.

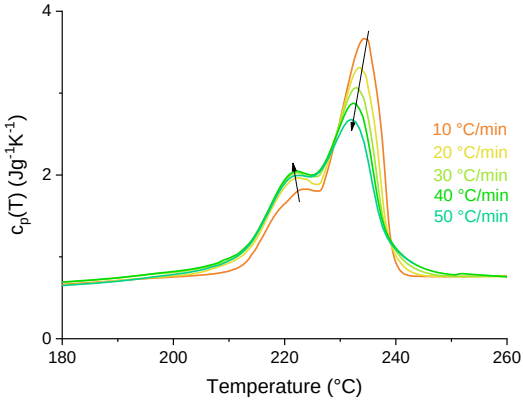


Figure 39. *Melting peaks of PCCD heating curves at the indicated scanning rates after cooling at 10 K/min. The arrows indicate the evolution of the melting peaks upon increasing the cooling rate and confirm the melting-recrystallization-remelting origin of the double melting peaks.*

Previous findings agree that irrespective of the stereochemistry, most PCCD materials can crystallize at standard DSC cooling rates (up to 20 °C/min),[4,21] including a PCCD sample with an M_n of 7000 g/mol and a 94% *trans* D content (similar to PCCD used in the current study).[44] However, one study reported unusually slow crystallization for a high-M_n (M_n = 47,860 g/mol, 91% *trans* D) sample, which did not crystallize when cooled more rapidly than 2 K/min.[69] They found a T_c of 141 °C at 2 K/min, and upon subsequent heating at 10 K/min, a significant cold crystallization peak at 116 °C along with a double melting peak, with the highest temperature estimated to be around 230 °C, although not discussed by the authors. The precise reason for these results are unclear as the other studies on PCCD[4,21] with a similar and higher M_w*'s* (and similar D *trans* percentage), reported crystallization at faster rates than 2 K/min and without the low temperature cold crystallization peak.

A cooling rate experiment was conducted on PCCD where the rates ranged from 2 to 50 K/min (see **Figure 40a**) and the subsequent heating rates were kept at 10 K/min (see **Figure 40b**). When cooled at 2 K/min, crystallization clearly takes place

showing a very sharp peak. The T_c decreases with increasing cooling rates. Upon heating, the low temperature shoulders, corresponding to the melting of the crystals formed during cooling, also shift to lower temperatures with increasing cooling rate. These are expected behaviors.

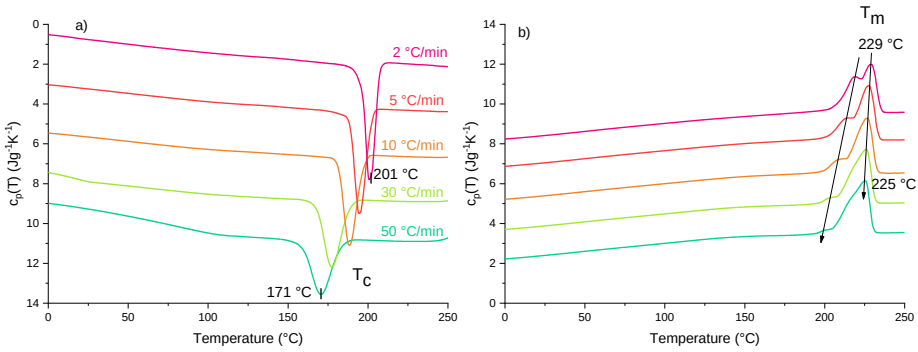


Figure 40. *Cooling rate experiment on PCCD where the rates ranged from 2 to 50 K/min. The cooling curves at the corresponding rates are shown in a) and the subsequent heating curves at 10 K/min in b). The T_c and T_m of the lowest and highest cooling rate are indicated as well as the evolution of the positions of the peaks with the arrows in b). The curves were shifted vertically for visibility.*

In Chapter 2, the T_g of the PCCD block in the studied copolymer was estimated at 58.8 °C (10 K/min) using the Fox equation. For the present semi-crystalline PCCD sample cooled at 10 K/min, T_g was estimated to be 50 °C (**Figure 38**). The T_g of the fully amorphous state was also determined by quenching molten PCCD in liquid N_2 and subsequently heating it in the DSC oven at 10 K/min. The corresponding heating curve, shown in **Figure 41**, reveals a distinct T_g step at around 40 °C. As expected, T_g increases with crystallinity, since rigid crystalline domains restrict chain mobility in the connected surrounding amorphous phase.[70] Upon heating, quenched PCCD undergoes crystallization, as indicated by a pronounced exothermic cold-crystallization peak, followed by melting at higher temperatures.

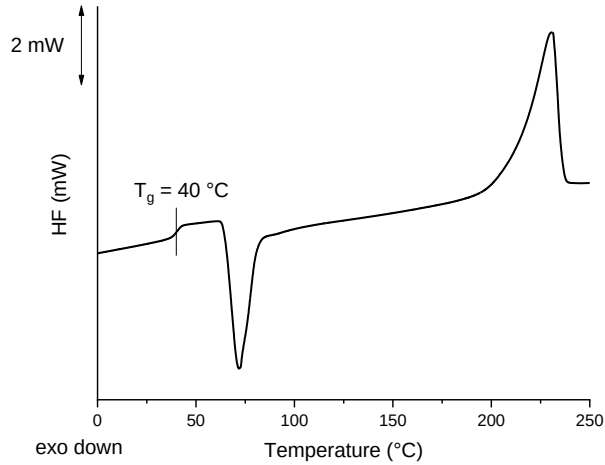


Figure 41. *PCCD heating curve at 10 K/min after quenching in liquid N_2, showing a clear T_g step at 40 °C, followed by a cold crystallization peak and the corresponding melting peak. This confirms the successful amorphization of the sample.*

3.3.4 POM

PCCD is semi-crystalline upon cooling at 10 K/min, similar to PCCD-PTHF. In Chapter 2, PCCD was found to crystallize into lamellae that further grow into space-filling spherulites. **Figure 42a-d** reveal no structures in the melt at 220 °C, followed by the formation and growth of birefringent spherulites at 200 °C (b) and 190 °C (c). Full impingement was reached at about 170 °C (d) after which little changes occurred upon further cooling to 30 °C (e), expect for an increase in definition within the spherulites. PCCD-PTHF thus crystallizes into space filling spherulites of which the earliest formed, largest ones reach a diameter of approximately 50 µm. This is half the size of the PCCD–PTHF spherulites.

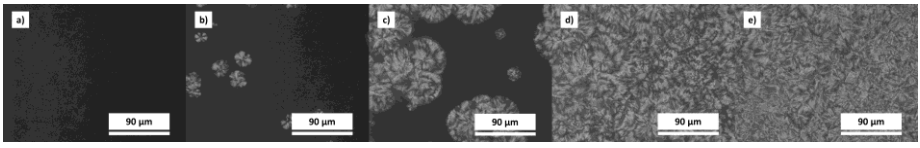


Figure 42. *POM micrographs of PCCD-PTHF during cooling at 10 K/min at a) 220 °C, b) 200 °C, c) 190 °C, d) 170 °C and e) 30 °C. The error on the temperature is ±1 °C. The micrographs show the growing of spherulites.*

This experiment suggests that pure PCCD also crystallizes into spherulitic superstructures from lamellar structures, thereby supporting the application of the lamellar model in the SAXS analysis presented in the following section.

3.3.5 Time-resolved SAXS/WAXS

As for PCCD-PTHF, a time-resolved SAXS/WAXS experiment was conducted during cooling and heating at 10 K/min. The SAXS range was again selected to overlap with the WAXS range. The combined, azimuthally averaged SAXS/WAXS pattern at room temperature after cooling at 10 K/min is shown in **Figure 43**. The powder pattern of PCCD matches that of PCCD-PTHF, confirming that both materials adopt the same crystalline lattice. Consequently, the unit cell parameters (*a*, *b*, *c*, α, β and γ) determined for PCCD-PTHF are also applicable to pure PCCD, and the crystallographic planes (hkl) are labeled using the same Miller indices as in **Figure 21**.

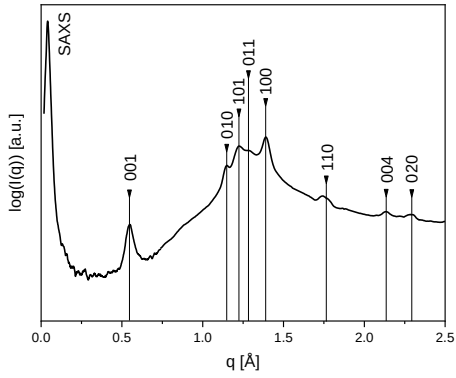


***Figure 43**. Room temperature azimuthally averaged powder pattern of PCCD cooled at 10 K/min. The pattern is a merged synchrotron SAXS and WAXS pattern. Strong reflections are labeled with the Miller indices found for PCCD-PTHF.*

The WAXS-based crystallinity could not be calculated in the same way as for PCCD–PTHF (right panels), because crystallization during cooling and melting

during heating overlapped. As a result, there is no temperature point where both a semi-crystalline (upon cooling) and an amorphous (upon heating) pattern are available for comparison. Only the frame recorded at room temperature after cooling was suitable to estimate the absolute crystallinity.

To determine the amorphous contribution, the WAXS pattern of PCCD quenched from the melt into liquid N_2 at 25 °C was used as a purely amorphous reference. The rapid quench prevented crystallization, freezing the polymer chains in a disordered state. **Figure 44** presents the normalized WAXS pattern of PCCD cooled at 10 K/min (black solid line). At $q > 1.1$ Å^{-1}, the scattering consists of overlapping crystalline and amorphous signals, while at lower q-values only the broad amorphous halo is observed. The slope of this halo depends on the amorphous fraction. By comparing the data with the quenched reference, the most probable amorphous contribution was identified and subtracted, yielding the crystalline scattering pattern (blue dotted line). The resulting crystallinity of 43% agrees well with DSC-based values, confirming the reliability of the reference enthalpy for PCCD established in Chapter 2.

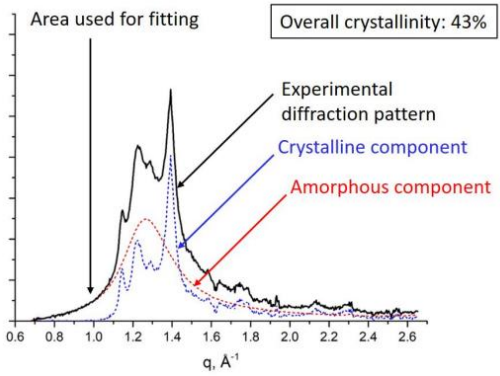


Figure 44. PCCD WAXS patterns at 25 °C in the semi-crystalline and amorphous state. The amorphous pattern was scaled (red) to overlap with the semi-crystalline pattern (black) at q-values below 1.1 Å^{-1}. The difference corresponds to the crystalline share in the semi-crystalline pattern (blue), the enclosed area of which corresponds to 43 % of the semi-crystalline pattern.

The time-resolved 001 WAXS reflection (which was collected on the SAXS detector) and the SAXS were used to further analyze the morphology of PCCD.

The integral breadth L_{001} of the time-resolved 001 WAXS reflection was calculated, generating the crystallite size D_{001} via the Scherrer equation (equation 23). Assuming that the inclination of the 001 planes with respect to the lamellar normal is the same as for PCCD-PTHF and that it is temperature independent, l_c was computed via $l_c = D_{001}\cos(27.2°)$. As the cooling and heating data were found to follow the same evolution, they were approached by a single second order polynomial to reduce the noise (Figure B.1 in Appendix B) due to the low intensity of the 001 reflection. The resulting l_c values upon heating and cooling are given in **Figure 45b**. The l_c seems to increase gradually upon cooling, and levels off when T_g is approached. At room temperature, PCCD forms lamellae of $l_c = 88$ Å. The number of PCCD repeating units of 13.28 Å per chain is $88/13.28$ or ~ 7 PCCD units across the lamellar thickness. The lamellar thickness and therefore the number of repeating units are very close to PCCD-PTHF even though the PCCD chains are longer, consisting of 6,142/280 or ~ 21 repeating units.

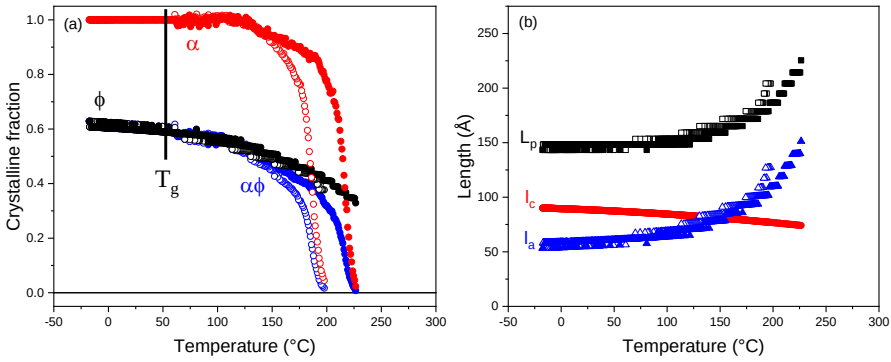


Figure 45. *PCCD parameters upon cooling (open symbols) and heating (closed symbols). a), the average local crystallinity within the semi-crystalline layers stacks, ϕ (black), the volume fraction of semi-crystalline stacks, α (red), and the overall SAXS based crystallinity, $\alpha\phi$ (blue). b) the crystalline lamellar thickness, l_c, the long period or periodicity, L_p, and the amorphous layer thickness,l_a.*

Finally, the time-resolved SAXS data were used to retrieve the remaining structural information. In addition to the corrections described in the experimental section, melt pattern and Lorentz corrections were applied on the data (q < 0.2). The

melt correction involved two steps. At first, a constant background intensity was subtracted, estimated by taking the average intensity around q = 0.3 $Å^{-1}$ (**Figure 43**). At this q-value, the actual SAXS pattern intensities declines to zero, except for the constant background. In a second step, the as corrected melt pattern at 250 °C of the cooling run was subtracted from all other SAXS pattern after scaling to match the experimental intensity of each pattern at the lowest collected q-value, i.e. at q = 0.18 $Å^{-1}$. Finally, the melt pattern corrected data were Lorentz corrected by multiplication with q^2. The resulting SAXS intensity curves for cooling at 10 K/min are shown in **Figure 46a**.

The q-values at the peak maximum were used to calculate the lamellar stack periodicity L_p via $L_p = 2\pi/q$ (see **Figure 45b**). From that was calculated the amorphous layer thickness $l_a = L_p - l_c$ and the average local crystallinity within the semi-crystalline stacks $\phi = l_c/L_p$ (**Figure 45a**). Then, the Lorentz corrected SAXS peaks were integrated to obtain the invariant, $Q = C\alpha\phi(1-\phi)(\rho_c - \rho_a)^2$, and these values were divided by $\phi(1-\phi)$ to obtain $C\alpha(\rho_c - \rho_a)^2$ (see **Figure 46b**). Remark that these intensities lose their temperature dependence below 51 °C as a result of a strongly reduced temperature dependence of the amorphous electron density, ρ_a, due to vitrification. Indeed, the stabilization of the intensity corresponds to the T_g found by DSC as indicated in the **Figure 38**. To define the volume fraction of semi-crystalline stacks, α, the data in the range of 65–127 °C were approached with a linear curve (blue line in **Figure 46**). In this temperature range, α, is assumed to be equal to 1 (in accordance with the POM observation of space-filling spherulites) and by consequence the linear curve represents $C(\rho_c - \rho_a)^2$. Dividing the $C\alpha(\rho_c - \rho_a)^2$ data by the extrapolated linear regression yields temperature dependent α values. These data are included in **Figure 45a** and were set equal to 1 below 61 °C as the trend of $C(\rho_c - \rho_a)^2$ is not applicable below T_g and as it is obvious that α remains equal to 1 also below T_g. Finally, the total SAXS crystallinity $\alpha\phi$ was calculated and added to **Figure 45a**.

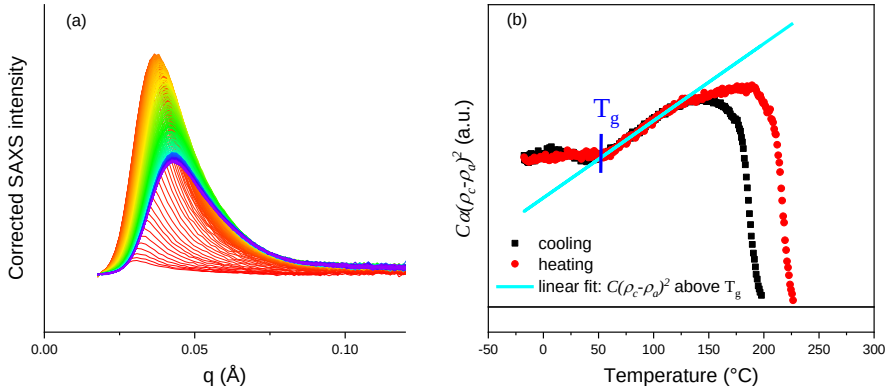


***Figure 46**. a) PCCD SAXS intensity after melt background and Lorentz correction and b) PCCD invariant divided by $\phi(1-\phi)$ upon cooling (black squares) and heating (red circles) with the linear fit between 65 and 127 °C used to approximate the product $C(\rho_c-\rho_a)^2$. These data are rather constant below T_g.*

The SAXS crystallinity at 25 °C is higher than the WAXS crystallinity, likely as a result of non-crystalline defects within the PCCD lamellae. The SAXS crystallinity shows the onset of crystallization upon cooling at around 200 °C, in good agreement with the DSC and POM results. The stacks are truly space filling below approximately 140 °C, which is earlier than for PCCD–PTHF for which stack filling continued down to room temperature. The further moderate increase up to when reaching T_g, is most likely due to a slight thickening of the already formed lamellae.

Figure 45a shows that ϕ remains within the range $0.4 < \phi < 0.6$. In this range, classical SAXS approaches, making use of correlation function or interface distributions are notoriously cumbersome. For that reason, and to remain consistent with the approach in Chapter 2, l_c was extracted from the 001 reflection and the Scherrer equation and L_p was obtained from the maximum in the Lorentz corrected SAXS patterns, thereby avoiding Fourier transformations.

The extracted l_c and l_a values intersect at ~150 °C, corresponding to a crystallinity of 50%. The rise of l_a (and the associated drop in ϕ with increasing temperature results from selective melting of the least stable crystallites, leaving thicker amorphous layers. Unlike PCCD–PTHF, no increase in l_c is observed toward the end of heating, where the latter showed thickening attributed to MRR. Although the DSC data of PCCD indicate MRR-like behavior, the effect is likely too small to

be discerned from the noise at the weak 001 reflection at high temperatures. Given the noise, it can also not be excluded that the moderate decrease of l_c at higher temperatures is an artifact. After all, upon heating the most stable, thickest lamellae are expected to remain and surface melting – as suggested by the decreasing l_c – is rather unlikely for rigid polymers.

3.3.6 Instability of PCCD and end-capping

PCCD was found to be unstable when maintained at elevated temperatures for extended periods of time. To investigate this, DSC experiments were carried out following the protocol shown in **Figure 32**, using both hermetically sealed and open aluminum pans. In the open pans, the sample could anneal under an inert, dry atmosphere due to the continuous N_2 flow, whereas the closed pans trapped residual gases and moisture. The corresponding cooling and heating curves are presented in **Figure 47**. For both sealed and open pan, the crystallization peaks upon cooling shift to lower temperatures and nearly disappeared after 24 h. Similarly, the melting peaks shift to lower temperatures and broaden, with this effect being most pronounced in the hermitically closed pans.

Interestingly, after annealing a few hours in an open pan, the crystallization peaks are only very weak upon cooling, however, the material is still able to crystallize during the subsequent heating via cold crystallization, similarly to what was seen for quenched and fully amorphous PCCD (**Figure 41**). Here too, the T_g step becomes more prominent. Clearly, different events are taking place during annealing in closed or open pans.

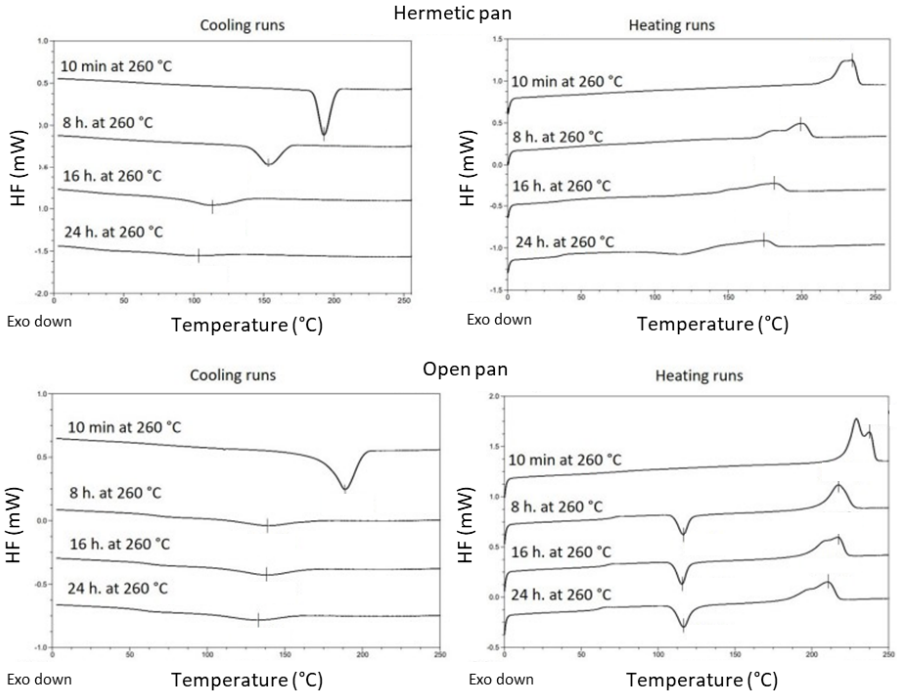


Figure 47. *PCCD cooling and subsequent heating HF curves after annealing at 260 °C for the indicated total times in hermetically closed (top) and open (bottom) pans. In both pans, the crystallization peak (crystallization) as well as the melting peak (heating) decrease in size and shift to lower temperatures. An extra cold crystallization peak upon heating appears for the open pan.*

The most likely processes occurring under either of these conditions are chain elongation or shortening, as well as *trans*-to-*cis* conversion of the cyclohexane moieties. The reduction and temperature shift of the crystallization peak indicate increasingly hindered crystallization, consistent with either longer chains or a higher fraction of *cis*-isomers—both of which reduce packing efficiency.

Chain scission (shortening) or extension (elongating) can be rationalized by hydrolysis or esterification reactions respectively (see **Figure 48**). In the presence of H_2O, as in the sealed pans, ester bonds in the PCCD chain can hydrolyze, producing two chain ends: –COOH (from D) and $–CH_2OH$ (from C). By contrast, in open pans exposed to N_2 flow, where water is absent, chain elongation can occur: a $–COOCH_3$ end group (from D) and a $–CH_2OH$ group (from C) can react via esterification, releasing methanol and forming a new ester bond. Accordingly, annealing in closed

pans most likely promotes chain shortening, whereas in open pans chain extension is favored.

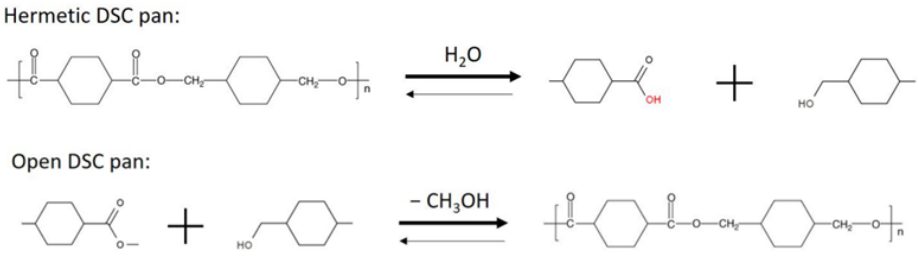


Figure 48. *Reactions of hydrolysis (top) in a hermetically closed pan and esterification (bottom) in an open pan.*

This alone, however, cannot account for the change in crystallization behavior observed in **Figure 47**. Annealing in a closed pan leads to a decrease in T_c and overall crystallizability, even though chain shortening would be expected to enhance chain mobility and thus, crystallization. This apparent contradiction can be resolved by considering isomerization: an increase in the *cis* fraction of the cyclohexane units would hinder efficient chain packing and thereby reduce the crystallization tendency. Therefore, an ^{1}H NMR spectroscopy experiment was performed before and after 24 h of annealing in a closed and open pan. The relevant parts of NMR spectra were isolated and are shown in **Figure 49**. The left NMR peaks are from the end groups -$COOCH_3$ or -CH_2OH to follow the chain length change. Upon annealing in a closed pan, the signals of the -CH_2OH groups became more pronounced, supporting the hydrolysis hypothesis. The signal of -$COOCH_3$ split in two less intense peaks due to the two different *cis* and *trans* positions where the *cis* signal increased significantly due to the higher amount of *cis* configuration of the D molecules. Indeed, the *trans* % of D reduced from 97 to 67 %. This probably counteracts the expected increase in crystallizability due to the shorter chains, explaining the decrease in crystallizability after prolonged annealing (**Figure 47**). Contrarily, annealing in an open pan indeed causes chain lengthening via eg. esterification since the end group signals decrease drastically. The *trans* content decreases to 86 %. In this system, both chain lengthening and isomerization contribute to a slower crystallization. The chains can

still participate in crystallization and will do so via cold crystallization during heating. The different contributions of the chemical processes in the two pan types, explain why after 8 h of annealing (**Figure 47**) the crystallization is more suppressed in an open pan (longer chains and higher *cis* content).

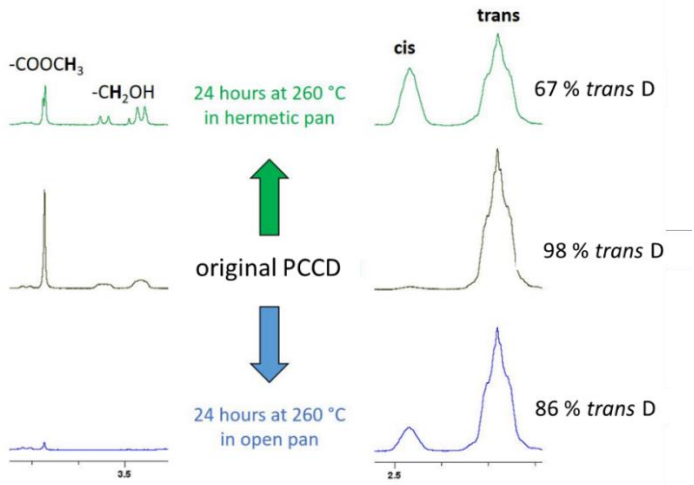


Figure 49. *Parts of NMR spectra of PCCD showing the influence of annealing in either open or hermetically closed pans. In a hermetic pan, the CH_2OH end group signal and the isomerization of D is higher than in an open pan. The spectra are scaled.*

A notable finding is that the extent of isomerization differed between the two environments. This variation may be linked to hydrolysis. In the hermetically sealed pan, hydrolysis generates –COOH end groups, which are known to catalyze the isomerization of 1,4-cyclohexylene rings. As hydrolysis progresses, the concentration of carboxylic end groups increases; once a critical threshold is reached, protons catalyze the isomerization of D units. In contrast, in the open pan no carboxylic groups are formed, leading to a comparatively slower isomerization rate. To verify this hypothesis, an additional experiment was conducted in which PCCD was pre-dried for 24 h at 60 °C under vacuum and then analyzed in a sealed pan under the same

conditions as in **Figure 48**. As shown in **Figure 50**, crystallization and subsequent melting were less suppressed, most likely due to reduced trans-to-cis conversion.

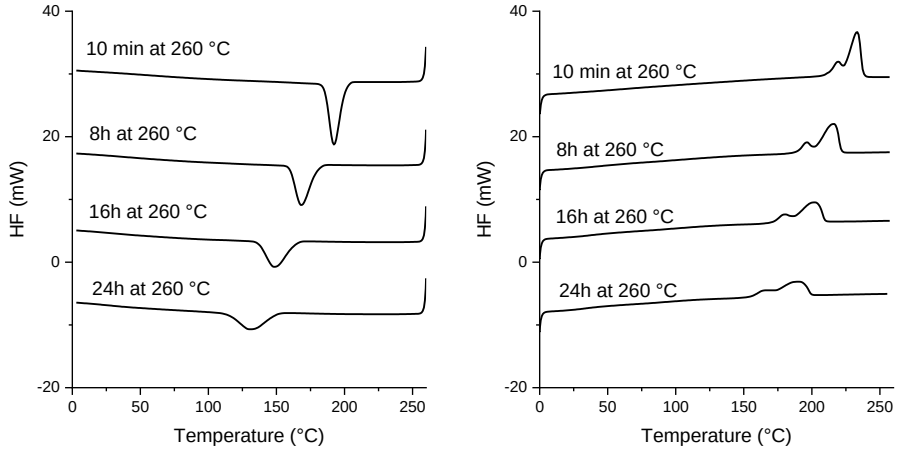


Figure 50. *Dried PCCD cooling (left) and subsequent heating (right) HF curves at 10 K/min after annealing at 260°C in a hermetically closed pan for the indicated total times. The crystallization peak (cooling) and melting peaks (heating) decrease in size and shift to lower temperatures with increasing annealing time.*

Clearly, regardless of the choice of pan type, PCCD is chemically unstable during prolonged heating. This poses a problem in methods and techniques where the same sample is reused multiple times and exposed to high temperatures, for example in calorimetric measurements such as DSC and Fast-Scanning Chip Calorimetry (FSC). In Chapter 3, PCCD is used for an isothermal crystallization study with FSC, where it is exposed to multiple heating/cooling cycles to 260 °C. Since the FSC chips are open systems flushed with N_2, chain lengthening was expected which could be avoided by deactivating the end-groups. Therefore, PCCD was end-capped.

End-capping

A chemical end-capping strategy was employed in which 200 mg of PCCD was dissolved in 50 mL of dichloromethane (DCM) and magnetically stirred for one hour. Then, 1 mL of acetyl chloride and 2 mL of triethylamine (Et_3N) were added dropwise in large excess, and the reaction mixture was stirred at room temperature for

24 h. The product was precipitated by adding an excess of acetone (a non-solvent for PCCD), filtered, washed four times with acetone and dried in air for 24 h.

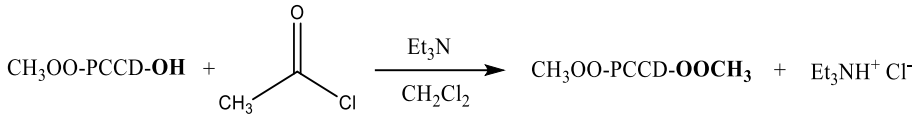


***Figure 51**. Reaction for end-capping PCCD.*

The success of the end-capping reaction was confirmed by ^{1}H NMR: after end-capping, the characteristic –CH_2OH signal disappeared from the spectrum in **Figure 52**. Isomerization of the cyclohexane moieties was not detected, which is consistent with the fact that no sufficiently high annealing temperatures were applied to activate such a process. The end-capped PCCD therefore has the same *cis*/*trans* contents as non-treated PCCD.

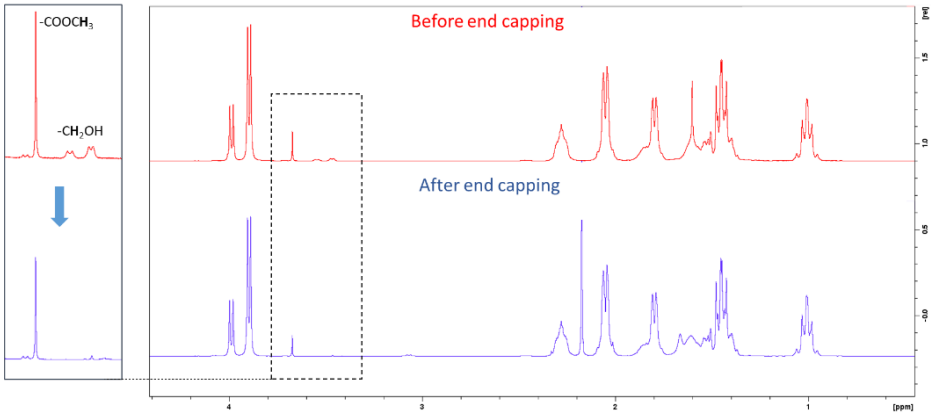


***Figure 52.** PCCD ^{1}H NMR spectrum before (top) and after (bottom) end-capping.*

Thermal stabilization of the end-capped polymer was verified by DSC using the protocol shown in **Figure 33**. Even after several thermal cycles, the T_c and the sharpness of the crystallization peak upon cooling remained unaltered, while non-treated PCCD shows a decrease of crystallization and T_c.

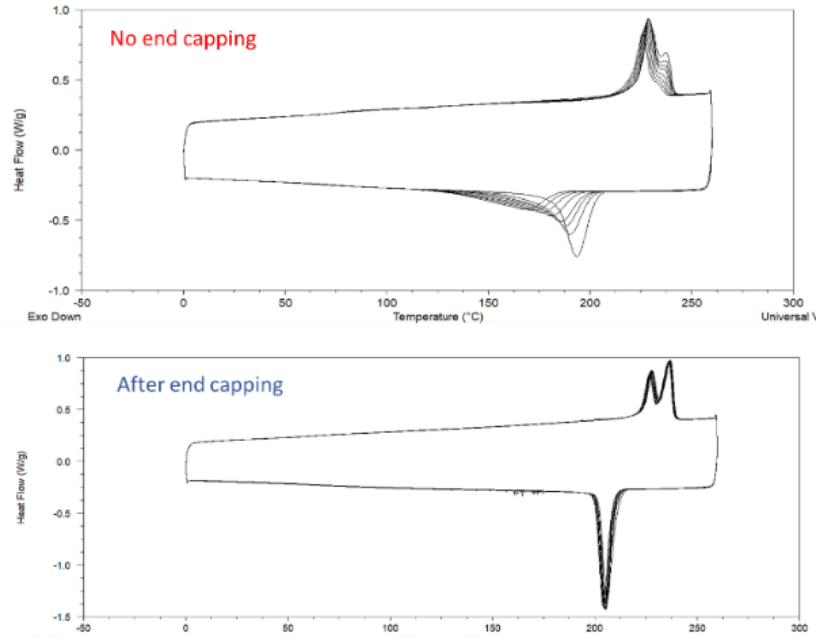


Figure 53. *The multiple heating cooling experiments of PCCD in open pans before and after end-capping. The end-capping procedure thermally stabilized the sample.*

These stabilization steps ensure that subsequent crystallization experiments reflect the material behavior, free from interference by ongoing chemical or structural transformations.

3.4 Conclusions

This study investigated the poly(1,4-cyclohexylidene cyclohexane-1,4-dicarboxylate) (PCCD) homopolymer, which is the crystallizable block of PCCD-PTHF. It was synthetized so that it would have the same *trans* contents of the monomeric moieties as the copolymer.

The thermal behavior during cooling and heating at different rates was analyzed using standard DSC. The PCCD crystallinity at 25 °C was determined with WAXS and nicely coincides with the DSC based crystallinity, implying that the earlier defined reference melting enthalpy for PCCD-PTHF is realistic, also for pure PCCD. Temperature-resolved POM revealed that the material crystallizes spherulitically

through the formation of lamellar PCCD crystallites. Processing of the time resolved SAXS data in combination with a crystal thickness retrieved from the WAXS 001 reflection, revealed a crystallinity evolution which aligns well with the DSC and POM observations. Semi-crystalline stacks are formed, which become space filling at about 130 °C, i.e. below which DSC no longer produces significant exothermic heat by crystallization. However, according to X-ray scattering, the stack internal crystallinity increases slightly even after the space filling state was reach, probably because of crystallite thickening although this observation could be a measuring artifact. The lamellar crystallite thickness was found to be 88 Å at RT.

PCCD was also found to be thermally unstable at elevated temperatures, with crystallization being reduced due to hydrolysis (chain shortening) or esterification (chain lengthening). This instability under inert atmospheric conditions was effectively mitigated by end-capping.

Chapter 4

The Isothermal Crystallization of the Segmented PCCD-PTHF Block Copolymer and pure PCCD from the Glass Transition Temperature to the Melting Point

Author contributions

Mouna Hamid: Conceptualization, Investigation, Methodology, Formal analysis, Writing – original draft. **Bart Goderis**: Supervision, Conceptualization, Methodology, Formal analysis, Writing – review and editing.

4.1. Introduction

In Chapter 2 and 3 the crystallization behavior and morphology of PCCD-PTHF and PCCD were investigated under typical DSC rates upon cooling and heating. These, however, are not typical conditions used in applications. Isothermal crystallization is more common, as in eg. SLS.

In the PCCD-PTHF system, most PTHF blocks are isolated macrodiols embedded between PCCD segments, with a most probable PCCD block length of seven repeating units.[71] The pure PCCD has a chain length of 6,142 g/mol, which corresponds to approximately 21 repeating units.

Upon cooling at 10 K/min from a homogeneous melt, PCCD-PTHF crystallizes into spherulites composed of lamellae, initially leaving large amorphous pools between primary crystalline stacks. During secondary crystallization, these pools gradually convert into randomly oriented lamellar stacks with similar lamellar thicknesses. PCCD also crystallizes into spherulites but the secondary crystallization probably consists of a slight perfectioning of the existing lamellae. For both poymers, the PCCD chains align perpendicular to the lamellar surfaces, and at RT the lamellae have a thickness of ~73 Å (PCCD-PTHF) and ~88 Å (PCCD). Upon heating, MRR is observed for both polymers.

Building on this structural insight, the current work investigates the isothermal crystallization kinetics of PCCD-PTHF and its homopolymer PCCD, and the resulting morphology of PCCD-PTHF.

Isothermal crystallization at a crystallization temperature, T_c, reached from either the melt (i.e. from a temperature, T, higher than the melting point or $T > T_m$) or the glassy state ($T < T_g$) is governed by a balance of thermodynamic driving force and molecular mobility, often resulting in a bell-shaped crystallization rate curve in

homopolymers (Chapter 1). However, some (homo)polymers exhibit a bimodal crystallization behavior, demonstrating two-overlapping bell-shaped curves, such as polypropylenes,[72–80] polyamides,[81–88] polyesters,[89–92] polyvinylidene fluoride (PVDF),[93] polyvinylidene chloride (PVC) and poly(L-lactic acid) (PLLA).[94] Some random copolymers from polyamides, propylenes/ethylenes and polyesters show bimodality as well.[83,95,96] The origin of bimodality is usually explained by different nucleation mechanisms at different supercooling. Usually, homogeneous nucleation is dominant at high supercooling (low temperatures) and heterogeneous nucleation at low supercooling (high temperatures). Also, it has been observed for some polymers that the overall crystallization rate of a homopolymer at low supercooling is increased when T_c is reached from the glassy state instead of from the melt. The augmented rate leads to an attenuation or disappearance of the bimodal crystallization behavior. The preceding stay in the dense glassy state likely generates (precursors to) nuclei, which become active when brought above T_g for isothermal crystallization at T_c.[42,72]

Furthermore, in various polymers, including polyamide 12 (PA12),[81] polyamide 11 (PA11)[97] and isotactic polypropylene (i-PP)[72,73] a link has been observed between the bimodality and crystal polymorphism. In these cases stable polymorphs form at higher T_c in the heterogeneous nucleation regime while mesomorphic phases grow at lower T_c where homogeneous nucleation dominates.

Studies on homopolymers report a minimal impact of the polymer molecular weight on the crystallization rate in the homogeneous nucleation regime but a reduction of the crystallization rate under heterogeneous nucleation conditions.[97,98] This reduction was related to the negative impact of larger chain lengths on the growth rate, which governs the crystallization rate at low supercooling. For extremely short chains, this trend of increasing crystallization rate with reduced molecular weight may reverse as the equilibrium melting point, T_m^0, of very short molecules is lower than that of high molar mass polymers.[96,99–101] Additionally, the bimodality in the crystallization rate has been shown to diminish for very low molar masses.[96,97]

For the homopolymer PCCD, isothermal crystallization from the melt has been partially documented. However, systematic isothermal studies across the full temperature range from T_g to T_m^0 are lacking. Sandhya (2003) conducted isothermal crystallization experiments on PCCD and found bimodality but its behavior at deep

supercooling, not accessible with standard DSC, remains unexplored.[69] Zhou et al. (2016) reported isothermal data on a material described as PCCD, though subsequent analysis of patent literature confirms it was in fact a PCCD–PTHF copolymer.[39,102] Their work covered only the high-temperature regime using DSC, and did not explore crystallization from the glassy state.

For more extended work, Fast Scanning Calorimetry (FSC) is needed as this allows for extremely high cooling and heating rates, which suppress crystallization during the cooling or heating ramps and enable access to deep levels of supercooling.

For segmented block copolymers, detailed crystallization studies across the full temperature range between T_g to T_m^0 are scarce. Only recently, Mongilyov et al. (2025) investigated a poly(butylene terephthalate)-poly(ethylene glycol) (PBT-PEG) block copolymer and compared its crystallization kinetics with that of a PBT homopolymer with similar total molecular weight.[96] Contrary to PCCD-PTHF, the soft PEG block in PBT-PEG can crystallize at very low T_c. At high crystallization temperatures, PEG remains amorphous. In this temperature regime, the PBT crystallization rate is enhanced at high supercooling because the PEG blocks act as plasticizer and increase the segmental mobility. At low supercooling, the PEG segments reduce the PBT crystallization rate as they impede the diffusion of PBT chains toward the crystallization front.[103,104] On top of this kinetic effect, there is also a thermodynamic origin to the reduced copolymer crystallization rate at low supercooling. The mixing with PEG in the melt results in a reduction of the PBT T_m^0, by which the supercooling at a given T_c is reduced compared to for the PBT homopolymer.

A comprehensive investigation of isothermal crystallization in both PCCD and PCCD-PTHF has not yet been conducted. This study fills that gap, with two main objectives: (1) to evaluate and compare the isothermal crystallization kinetics of PCCD and PCCD-PTHF using DSC and FSC across the full temperature range between T_g and T_m^0 from both the melt and glassy state, and (2) to correlate these kinetic profiles to the resulting morphology as analyzed by POM, WAXS and SAXS.

Prior to the experiments, thermal stabilization of the materials was required as they showed non-reproducible thermal behavior upon repeated heating and cooling. As described in Chapter 3, PCCD was end-capped after synthesis and PCCD-PTHF

was stabilized through a DSC-based conditioning protocol that is described in the current chapter.

The insights gained here deepen our understanding of isothermal crystallization in PCCD-based materials and offer valuable guidelines for their processing in advanced applications.

4.2 Experimental section

4.2.1 Materials

PCCD-PTHF

The PCCD-PTHF block copolymer examined in this study was supplied in pellet form by Eastman Chemical Technology BV (Ghent, Belgium)[39] and has number-average (M_n) and weight-average (M_w) molecular weights of 12.7 kg/mol and 75.3 kg/mol, respectively. The dispersity (M_w/M_n) is 5.95. A full characterization of the polymer can be found in Chapter 2. **Figure 11a** shows the PCCD-PTHF molecular structure in detail. The *trans* content of the 1,4-cyclohexanedicarboxylate (D) residues (green in **Figure 11a**) is 95% and that of the 1,4-cyclohexanedimethanol (C) residues (orange in **Figure 11a**) is 70 %.

PCCD

PCCD was synthesized and stabilized via end-capping as described in Chapter 3. The *trans* content of the D residues is 98% and that of the C residues is 70 %.

4.2.2 Methods

^{1}H NMR spectroscopy

^{1}H NMR was performed with a Bruker Avance III HD 400 MHz Spectrometer. Approximately 5 mg of the materials was dissolved in deuterated (99.9

%) chloroform and complemented with 0.1 (v/v)% tetramethylsilane (TMS) as reference. The data were analyzed using the Topsin 4.0 software.

Differential Scanning Calorimetry (DSC)

DSC experiments were performed with a Q2000 heat-flux DSC (TA instruments, New Castle, USA), calibrated for the temperature and heat flow (HF) with indium and sapphire standards. The samples were measured in open Tzero aluminum pans without lid under a constant nitrogen flow of 50 mL/min.

PCCD-PTHF was thermally stabilized through DSC by performing multiple heating and cooling cycles, minimizing shifts in thermal transitions upon repeated scans. The applied thermal protocol is shown in **Figure 54a**.

The isothermal crystallization experiments from the melt (protocol in **Figure 54b**) were then conducted using the stabilized samples. The exothermic signal in the isothermal segment was corrected for an empty pan and was integrated over time.

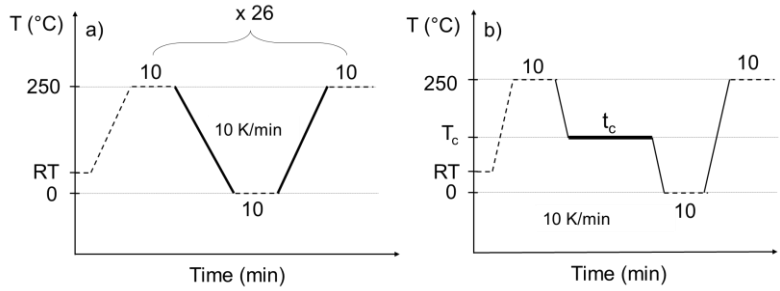


Figure 54. *DSC thermal profiles for a) the ageing of PCCD-PTHF and b) isothermal crystallization. For profile b) the T_c's range from 145 to 160 °C for PCCD-PTHF and 200 to 220 °C for PCCD. The t_c values range from 120 to 240 min. Only the segments indicated with continuous lines were used for analysis.*

The normalized isothermal crystallization data were first plotted as a function of log(t_c) and then fitted by the following equation, which combines a sigmoidal increase, visible at short log(t_c), with a further linear increase at higher log(t_c):

$$f(\log(t_a) = A \cdot \Phi\left(\frac{\log(t_c - \mu}{\sigma}\right) \cdot (B \cdot \log(t_c)) + D) \quad (39)$$

with A the area, Φ the cumulative Gaussian distribution function, μ the mean (average) of the distribution function, σ the standard deviation, B the slope of the linear part and D the intercept. All the parameters explained here were used as fitting parameters. The half-time $t_{1/2}$ was calculated as 10^{μ} and the crystallization rate as the reciprocal of $t_{1/2}$. An example is given in Figure C.1d in Appendix C. Although modified Avrami models can be used to account for secondary crystallization, their application typically requires several assumptions regarding nucleation mechanisms, growth dimensionality, and rate constants, which are not straightforward to verify for the present system. To avoid introducing such system-specific assumptions and maintain a purely empirical description, equation 39 was used. This approach provided an accurate fit to the experimental data while remaining physically interpretable and assumption-free.

Thermogravimetric Analysis (TGA)

The same apparatus was used as described in Chapter 2. The experiment was performed on a 6 mg PCCD-PTHF sample in an open aluminum pan by following the thermal protocol in **Figure 54a**.

Fast-Scanning Calorimetry (FSC)

FSC experiments were carried out using a Flash DSC 1 (Mettler Toledo, Columbus, USA) paired with a Huber TC100 intracooler (Huber, Offenburg, Germany) under a continuous nitrogen flow. Small fragments, weighing less than a microgram, were cut from the material under a microscope and carefully positioned on the chips. Prior to sample placement, the Multistar UFS1 chips underwent conditioning and temperature calibration.[42] Isothermal experiments were performed with FSC, however, it was not possible to retrieve isothermal crystallization Heat Flow (HF) signals from the isothermal segments as the signal was below the detection limit. Therefore, an indirect measuring method was used via the thermal protocols in **Figure 55a-b**. The heating (thick segment) after the isothermal event reflects what was formed during isothermal crystallization by the presence of melting peaks. Experiments were performed with different crystallization times t_c ranging from 0.1 to 1000 s for every T_c and the melting peaks were integrated for every measurement

using a linear baseline via melt extrapolation. These integration values were then plotted as a function of time, representing the evolution of the crystallization. A few examples can be found in Figure C.1(a-c) in Appendix C. The crystallization rate was retrieved following the same method as described for the DSC experiments. Note: for low T_c's, the heating runs showed a large exothermic signal due to cold crystallization. The associated area below the melt extrapolated baseline was counted as a negative contribution to the total area calculation and directs this integration to the exothermic heat developed isothermally.

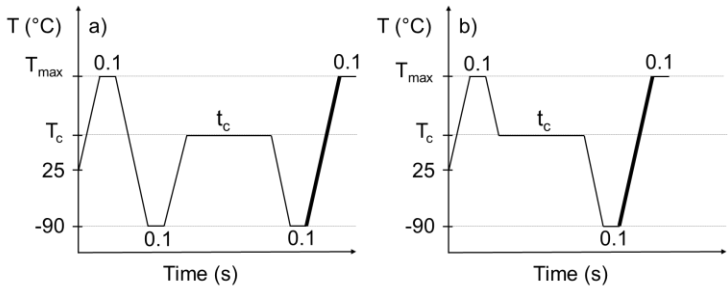


Figure 55. *Thermal protocol for isothermal crystallization from a) the glassy state and b) the melt state for FSC. The T_c values for PCCD-PTHF were a) 50 – 140 °C and b) 35 – 130 °C. For PCCD, the values were a) 90 – 195 °C and b) 70 – 190 °C. The t_c values range from 0.1 to 1000 s. The T_{max} and scanning rate were 250 °C and 1000 K/s for PCCD-PTHF and 260 °C and 2000 K/s for PCCD, respectively.*

Polarized Optical Microscopy (POM)

Room temperature POM experiments were conducted using a BHS polarized light microscope (Olympus, Tokyo, Japan), equipped with a TK-C1381 color camera (JVC, Kanagawa, Japan) and operated via the Leica Qwin imaging software (Leica Microsystems, Solms, Germany). Samples were prepared using a quenching setup described in the next paragraph (Setup 2), in which a film of polymer was sandwiched between two cover glasses and mounted onto a custom sample holder. The samples were first melted at 250 °C for 10 min to erase thermal history, followed by quenching to the desired isothermal crystallization temperature. Following a 10-min isothermal treatment, the samples were extracted from the apparatus and cooled to ambient conditions prior to microscopic examination.

Synchrotron Small-Angle (SAXS) and Wide-Angle X-ray Scattering (WAXS)

SAXS/WAXS experiments were performed at BM26, the Belgian beam line at the European Synchrotron Radiation Facility (ESRF) in Grenoble, France. Two setups were used, with an X-ray wavelength λ of 0.95 Å for setup 1 and 1.03 Å for setup 2.

In **setup 1**, a fast-scanning chip calorimeter was used. The setup, based on an earlier design,[105] was modified for sub-ambient conditions by cooling the FSC cell with liquid nitrogen to −80 to −100 °C. To prevent condensation, the entire unit was enclosed in a nitrogen-purged chamber with mica windows for beam access. Scattering patterns were collected by a Pilatus 1M detector at 0.20 m from the sample after an evacuated tube. Structural information was retrieved over the range $0.23 \leq q \leq 3.96\ \text{Å}^{-1}$. PCCD-PTHF chip samples were prepared as in the FSC experiments described in the previous paragraph and subjected to the thermal protocol in **Figure 56** for isothermal crystallization from either the melt (left) or the glassy (right) state. A few images were recorded at the end of the isothermal crystallization event at T_c. After crystallization, the sample was quenched to −20 °C, where five images were captured and averaged. The images taken at −20 °C were used for analysis.

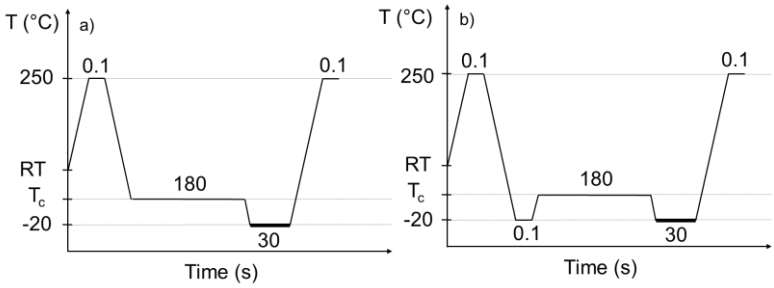


Figure 56. *Thermal protocol for isothermal crystallization of PCCD-PTHF when coming from the melt state (a) and the glassy state with a T_c range of 65 − 155 °C and 65 − 165 °C, respectively. The crystallization time was limited by the FSC instrument to 180 s. The scanning rate was 1000 K/s.*

Setup 2 involved a custom-built quenching device (**Figure 57**), positioned in front of the beamline, enabling time-resolved observation of crystallization from a glassy-derived state. A full description of the setup is available in reference [106]. First,

the sample was fully molten at 250 °C under nitrogen for 5 min. It was then quenched in liquid nitrogen and placed in the upper sample holder at room temperature. From there, the sample was propelled into a preheated Mettler oven, aligned with the beam and held at the target isothermal T_c. After 10 min of isothermal treatment, the sample was reheated to 250 °C at 10 K/min.

Simultaneous SAXS and WAXS data were collected using a Pilatus 1M detector (1.20 m from the sample after an evacuated flight tube) and a Pilatus 300k detector positioned near the sample, respectively during the isothermal and subsequent heating steps. Structural information was retrieved over the ranges $0.02 \leq q \leq 0.80$ Å^{-1} for SAXS and $0.60 \leq q \leq 3.60$ Å^{-1} for WAXS. Note: the state from which the sample was brought to T_c was not a true glassy state but rather a structure formed at room temperature following quenching from the glass. Upon transfer to T_c, this intermediate structure is expected to melt completely and recrystallize. Consequently, the structural evolution should closely resemble that of crystallization directly from the glassy state. However, the brief exposure to room temperature may have slightly affected the crystallization kinetics compared to a direct transition from the glass to T_c.

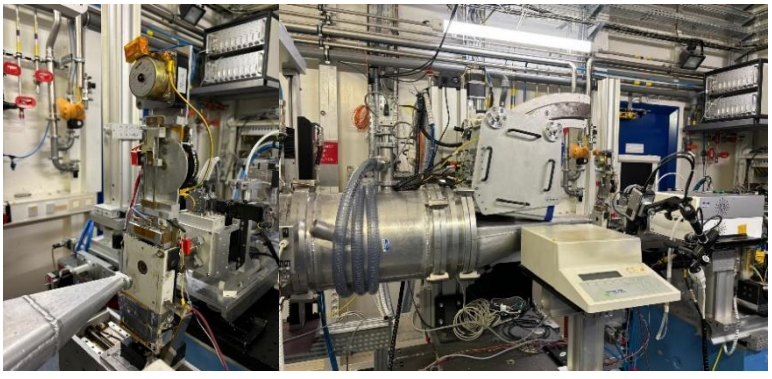


Figure 57. *Quench setup* [106] *at BM26 at the ESRF. Further details are given in the text.*

For both setups, the scattering angles were calibrated against α-alumina and silver behenate standards and the isotropic powder patterns were azimuthally averaged using ConeX software.[43] The one-dimensional data were corrected for the scattering of an empty sample holder, taking the sample transmission into account as derived from the

transmitted primary beam intensity measured by a photodiode downstream from the sample. Intensities were normalized to the intensity of the incoming beam, measured by an ionization chamber upstream from the sample.

4.3 Results and Discussion

4.3.1 Thermal stabilization or ageing of PCCD-PTHF

PCCD-PTHF and PCCD were found not to be stable at high temperatures, which makes it unsuitable for experiments or applications that require long annealing times or a high number of stays at high temperatures.

Before conducting isothermal crystallization experiments, both PCCD-PTHF and PCCD required stabilization to ensure reproducible thermal behavior during repeated heating, particularly those involved in FSC. Without this step, a gradual depression of T_c and T_m were observed upon repeated heating (see **Figure 53** for PCCD and **Figure 58a** for PCCD-PTHF). As explained in Chapter 3, PCCD was stabilized via end-capping.

For PCCD-PTHF, a method was found to stabilize the material consisting of 26 consecutive heating/cooling cycles in the DSC (**Figure 54a**) in an open DSC pan under a steady N_2 flow. The resulting heat flow curves are depicted in **Figure 58a**. After every cycle, both the crystallization and melting peaks gradually shifted to lower temperatures across successive scans (blue to green), with the shift in T_c being significantly more pronounced than that in T_m. This indicates that the process occurring slows down crystallization greatly until reaching an almost equilibrium point. PCCD-PTHF after the heat treatment is further referred to as "**aged PCCD-PTHF**".

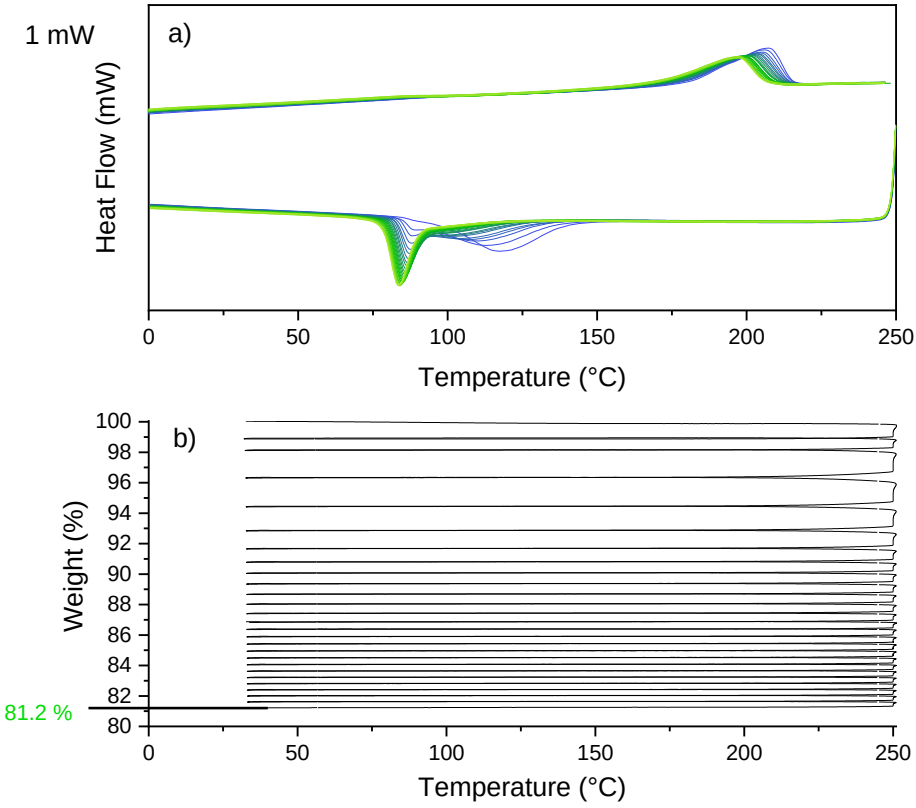


Figure 58. *PCCD-PTHF ageing: a) HF heating and cooling curves (exo down) at 10 K/min from blue to green and b) TGA weight loss curve, following the same thermal protocol. The gradual shift of the crystallization peak to lower temperatures in a) occurs together with a gradual decrease in sample mass in b).*

Integration of the crystallization peaks, yielding the enthalpy ΔH, revealed that the overall crystallinity decreased progressively with each thermal cycle. This trend is illustrated in **Figure 59** (red squares), which shows the percentage of remaining ΔH after each cycle normalized to the first one. A sharp reduction was observed after the initial cycles, followed by a more gradual decline toward the final cycles. A comparable trend was obtained from TGA measurements performed under identical thermal and experimental conditions (**Figure 58b**). In this case, the decrease in enthalpy can be directly related to the reduction in sample mass as it will be

demonstrated in **Figure 61** that the mass loss is related to the PCCD fraction only. From the 100% initial mass, ~19% is lost at the end of the protocol (**Figure 58b** and **Figure 59**, black squares). As there is 75wt% PCCD in the sample, it implies that only (75-19)/75 or 75% of the PCCD is left. This is equal to the % remaining crystallization enthalpy. In other words, the PCCD mass loss leads to a proportional loss in PCCD crystallinity

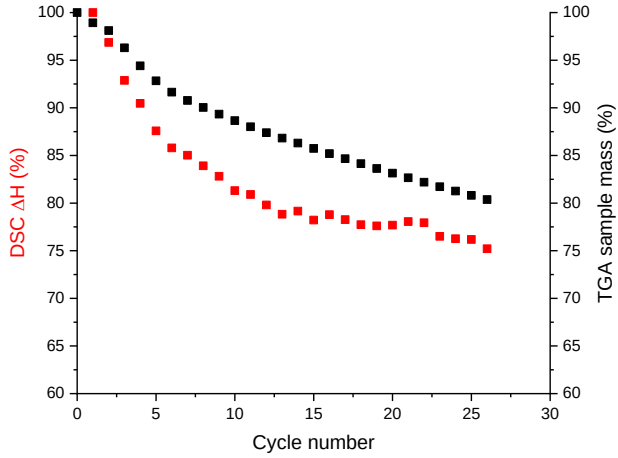


Figure 59. *Crystallinity loss from DSC and mass loss from TGA. The crystallinity percentage are the enthalpy values compared to the first value (after the first cooling) The mass loss of TGA is determined as the percentage at RT after a cooling.*

To investigate the behavior of PCCD-PTHF during heat treatment and to better understand its stabilization, a ^{1}H NMR experiment was performed at room temperature after the DSC experiment shown in **Figure 48a**. The corresponding spectrum is presented in **Figure 60**.

Overall, the spectrum and peak assignments were consistent with those of non-aged PCCD-PTHF, except for the additional presence of an H_2O signal. Quantitative analysis of the integrated signals, however, revealed subtle differences. In particular, a partial *trans*-to-*cis* isomerization was detected: the *trans* content of D (DMCD) decreased from 98% to 92%, while that of C (CHDM) decreased slightly from 70% to 69%. These values were derived from the relative intensities of the H_{1c}/H_{1t} (D) and H_{3c}/H_{3t} (C) proton signals, respectively. The observed shift is

consistent with known thermally induced isomerization, but the magnitude of the change is too small to account for the pronounced decrease in T_c. However, in that case a corresponding decrease in T_m would be expected, which was not observed. Also, isomerization cannot explain the mass loss observed.

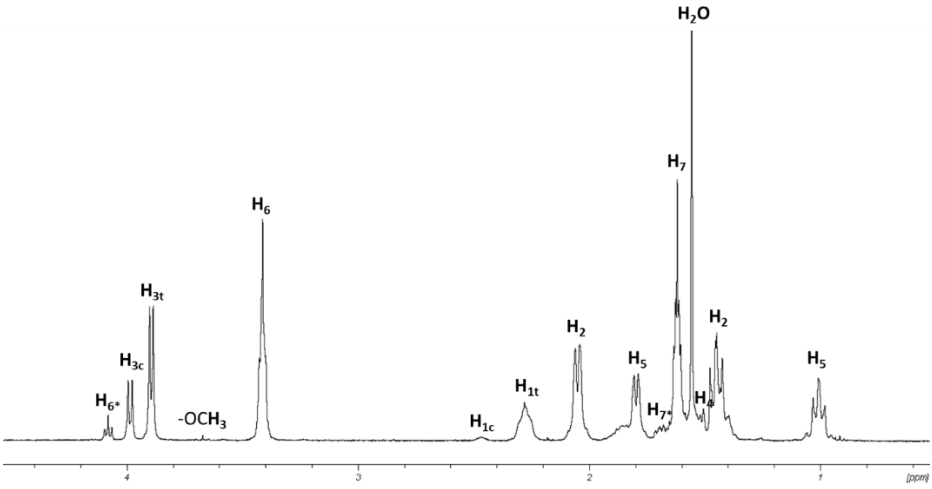


Figure 60. *[1]H NMR of aged PCCD-PTHF with the identified peaks (chemical shift, relative peak area) corresponding to H_{6*} (4.08 ppm, 9.9453), H_{3c} (25.7726 ppm, 0.30), H_{3t} (3.90 ppm, 56.6775), H_6 (3.41 ppm, 100.00), H_{1c} (2.47 ppm, 3.8809), H_{1t} (2.28 ppm, 43.1209), H_2 (2.05 ppm, 84.9972), H_5 (1.80 ppm, 53.6843), H_7 (1.62 ppm, 121.7568), H_2 (1.45 ppm, 108.3405), ppm, 0.99) and H_5 (1.01 ppm, 108.3405).*

The molar composition of the polymer was found to change upon aging. The molar fractions of the monomeric units φ_D, φ_C and φ_P shifted from 0.508, 0.446, and 0.046, respectively, in non-aged PCCD-PTHF (Chapter 2) to 0.504, 0.443, and 0.052 in aged PCCD-PTHF. These values were calculated from the integrals of the H_{1c}/H_{1t} peaks for D, H_{3c}/H_{3t} for C, and H_{6*} for P. Here, φ_D represents the total amount of D and D′. The molar fraction of D′ within φ_D was determined to be 0.009, a significant decrease from 0.017 in the non-aged sample. Since a lower D′ fraction implies fewer chain end-groups, this result indicates longer polymer chains. From this analysis, the M_n was estimated to be 19,978 g/mol, nearly twice that of the non-aged PCCD-PTHF.

This finding clearly demonstrates that a chemical process occurred during aging, leading to substantial chain extension. A plausible reaction mechanism is

proposed in **Figure 61a**, involving transesterification, specifically an intermolecular ester–ester interchange between the ester bond of a D′ chain end and the ester bond connecting C and D′ units. This reaction results in the coupling of two polymer chains, thereby increasing M_n, while simultaneously releasing a DMCD-molecule. Such a process – the associated increase of M_n in particular – provides a convincing explanation for the decrease in T_c. In addition, volatilization of the released DMCD contributes to the observed mass loss. The boiling point of DMCD at atmospheric pressure is approximately 259 °C in bulk, which is sufficiently low for volatilization under the applied thermal treatment especially in the presence of a nitrogen flow that prevents recondensation, and considering the small sample mass.[107]

Chain-lengthening transesterification of this type has been previously reported for various block copolymers.[108] Notably, after several heating–cooling cycles, the T_c no longer shifts. If chain extension is indeed the primary driver of the T_c depression, this plateau suggests that the process slows or ceases once the chains become sufficiently long. This behavior is consistent with known limitations in polyester systems: although transesterification is thermodynamically favorable, increasing chain length, diffusion constraints, and depletion of reactive end groups eventually hinder further reaction progress.

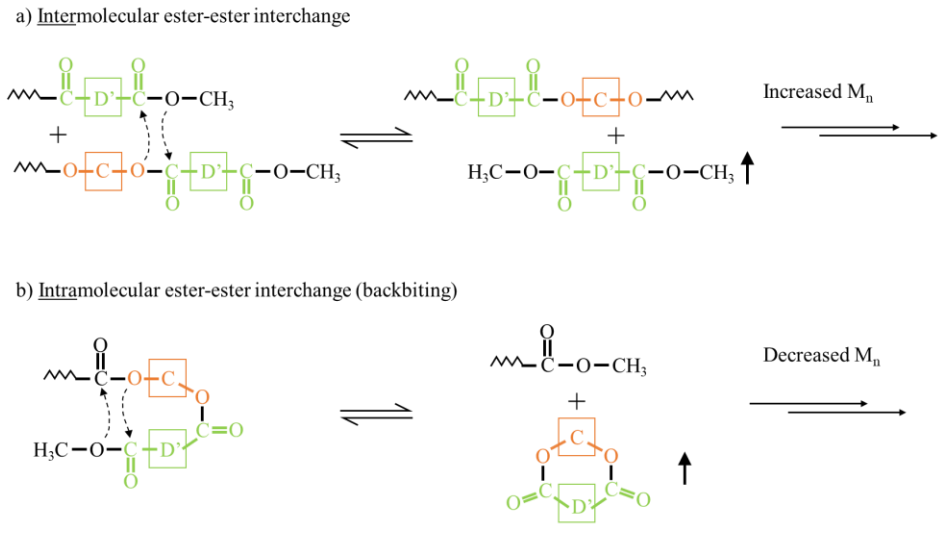


***Figure 61**. The a) intermolecular and b) intramolecular reaction mechanisms of ester-ester interchange of PCCD-PTHF. a) is based on [108] and the rectangles indicate*

the end-chain DMCD (D') and CHDM (C) moieties. The intermolecular reaction results in the release of one D monomer and increases greatly the M_n. The intramolecular reaction results in the release of one repeat unit (D-C) and decreases slightly the M_n.

This reaction pathway alone, however, cannot account for the observed decrease in the molar fraction of C. The compositional changes described earlier correspond to a 12.7% reduction in both D and C. To explain this, a second ester–ester interchange mechanism with the production of volatiles is proposed, illustrated in **Figure 61b**. In this case, the transesterification occurs intramolecularly through a so-called "backbiting" mechanism. Here, an ester group at the chain end reacts with an ester bond within the same chain, leading to the release of a D′–C unit in the form of a cyclic oligomer. As a result, the chain length and its M_n are slightly reduced. Depending on the location of the reactive ester bond, larger cyclic species such as D′–C–D–C or D′–P units could also be generated. However, among these, only the small D′–C oligomers are likely to volatilize under the applied DSC conditions, thereby contributing both to the reduction in molar fractions and to the measured mass loss. Although the boiling point of this small cyclic compound is unknown, it is expected to be sufficiently low for volatilization at high temperature in the DSC, particularly given the high volatility of esters (and diesters in particular) and the continuous flushing with nitrogen, which further promotes removal of volatile products. To verify this hypothesis, Thermogravimetry–Mass Spectrometry (TG-MS) could be employed in future work to directly identify the released species. The backbiting transesterification mechanism is well established and frequently reported in PET and PBT, although there it typically involves reactions between –OH and –COO groups, whereas in the case of PCCD-PTHF, the reaction likely occurs between two –COO groups.[108]

This analysis suggests that the first chain-extending transesterification reaction most likely reaches an equilibrium state just like the downward shift of the crystallization temperature does, while the backbiting reaction continues over time. The latter explains the ongoing mass loss beyond the melting point stabilization as shown in **Figure 59**, but as it only slightly decreases M_n, its influence on crystallization remains limited.

Thus, three key processes are suggested to occur during the thermal aging of PCCD-PTHF: (i) a *trans*-to-*cis* isomerization of the cyclohexane-based units, (ii) an intermolecular transesterification and (iii) a backbiting transesterification.

Finally, one might wonder why there is no mass increase and associated drop of the crystallization temperature in pure (endcapped) PCCD due to similar transesterification reactions when subjected to multiple thermal cycles. A plausible explanation lies in the synthesis route: PCCD–PTHF was most likely prepared using a Ti(IV) catalyst, as described in its synthesis patent.[39] Titanium catalysts are known to promote transesterification reactions,[108] and residual catalyst may still be present in the pellets, thereby facilitating the processes observed during thermal treatment. In contrast, PCCD underwent several purification steps during synthesis (Chapter 3), and the subsequent end-capping step was specifically intended to remove all traces of catalyst. As a result, transesterification is most probably strongly suppressed in PCCD.

It should also be noted that Lewis acids, such as the Ti(IV) catalyst used here, can facilitate the degradation of PTHF during annealing. This degradation involves cleavage of the C–O bonds and the subsequent release of tetrahydrofuran (THF) molecules, which have a boiling point of 66 °C. However, this catalytic effect is less pronounced for complexing cations with high charge densities, such as Ti(IV), and when annealing is performed under an inert nitrogen atmosphere. [109] Under inert conditions, pure PTHF typically begins to degrade significantly only above 350 °C, whereas in air degradation already occurs from around 200 °C. Therefore, under the conditions used in this work (inert atmosphere and temperatures up to 260 °C), substantial PTHF degradation is unlikely. This conclusion is further supported by the molecular weight data: if significant degradation had occurred, the associated decrease in molecular weight would have offset the observed increase caused by intermolecular transesterification (**Figure 61**a) or even resulted in a net molecular weight reduction.

Although the above coherently explains all observation, there remains one pending issue. Based on NMR, 12.7% of both D and C are lost in PCCD-PTHF, which would lead to an overall mass loss of approximately 9.6%. It is unclear why this

estimate is so much lower than the ~19% measured by TGA. One possibility is that the mass loss in DSC (which was used to prepare the sample for NMR) is truly lower than in TGA because of slightly different experimental conditions, such as e.g. the nitrogen gas flow around the sample. If this is the case, it would suggest that the crystallinity loss (as measured by DSC) is not simply proportional to the (PCCD) mass loss but actually more pronounced. This is plausible, considering that the increase in M_n hinders crystallization.

One might question whether this ageing process could have influenced the results and conclusions presented in Chapter 2. All experiments were conducted under identical thermal conditions, meaning that even if the material experienced some degree of ageing after one heating, particularly an increase in chain length, the overall results and interpretations remain valid. The only exception is the NMR spectroscopy experiment, which was performed on material that had not undergone the same thermal history. Nevertheless, this effect is expected to be minimal, as the simulated block length distributions based on the NMR data correspond closely with the outcomes of the other experiments.

4.3.2 Overall isothermal crystallization behavior of PCCD-PTHF and PCCD

The isothermal crystallization kinetics of PCCD-PTHF and PCCD were studied with FSC and DSC by following the protocols in **Figure 54c** and **Figure 55**. For both polymers, the crystallization evolution as a function of log(t) shows a sigmoidal evolution from the primary crystallization, followed by an increase due to secondary crystallization (see examples in Figure C.1 in Appendix C). As described in the experimental section, the crystallization rates were calculated by considering only the primary crystallization, which was done by taking the reciprocal of the half-time ($1/t_{1/2}$). An overview of the logarithm of $1/t_{1/2}$ as a function of the isothermal crystallization temperature is given in **Figure 62**, indicating whether the crystallization temperature was reached from the melt (red circles) or the glassy state (blue squares). The range of temperatures was selected between the T_g (6 °C[71] for

PCCD-PTHF and 41 °C for PCCD) and the onset of the melting peak T_m at 10 K/min with DSC (162°C for PCCD-PTHF[71] and 212 °C for PCCD).

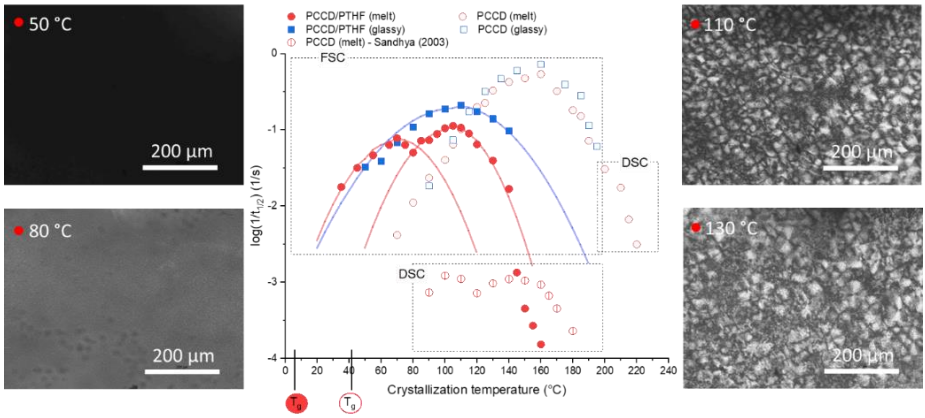


Figure 62. *Overall crystallization rates of PCCD-PTHF (filled symbols) and PCCD (open and open-crossed symbols) as a function of the (isothermal) crystallization temperature reached from the melt state (red circles) and the glassy state (blue squares), indicated if they are measured by FSC or DSC. The T_g of both polymers are given. In addition, the PCCD-PTHF POM images measured at room temperature after crystallizing from the melt at the indicated temperatures, are shown. The lines exclusively serve to guide the eyes. The PCCD data from Sandhya (2003) is also plotted.*[69]

Figure 62 shows a double bell-shaped curve for PCCD-PTHF when coming from the melt. As said in the *Introduction* section, this double melt curve represents a combination of two overlapping single bell-shaped curves. In this case, they indicate two distinct kinetic regimes each governed by a different nucleation mechanism: homogeneous nucleation at high supercooling (low T_c) and heterogeneous nucleation at low supercooling (high T_c). For PCCD-PTHF, the transition occurs at approximately 80 °C. POM images were taken of PCCD-PTHF at RT after 10 min of isothermal crystallization from the melt at low (50 °C), intermediate (80 and 110 °C) and high (130 °C) temperatures. These are included in **Figure 62**. They clearly show that the supercooling has a direct impact on the micrometer morphology. At 50 °C, no distinct structures are detected although crystallization took place with $t_{1/2}$ being 21.6 s. This means that the crystal aggregates are so small they were not perceived on the image and/or are not birefringent. The image at 80 °C shows birefringence but again

no structures could be distinguished. At 110 °C and 130 °C, spherulites are clearly present and space-filling. The large difference in morphology between the two lowest and two highest temperatures, suggests the occurrence of two different nucleation mechanisms: mainly homogeneous nucleation at low temperatures and mainly heterogeneous at high temperatures.

Androsch et al. (2015) found similar results for PBT.[90] To explain the bimodality in the crystallization rate of PBT (from the melt), they performed POM experiments after crystallization at high and low T_c's. The POM experiments showed that high temperatures allowed the formation of large spherulitic superstructures and at the T_c of the low-temperature maximum no superstructures could be distinguished. This was explained by the huge increase in primary nuclei density due to a higher contribution of homogeneous crystallization.

In **Figure 62**, the DSC data at the highest temperatures were expected to follow the extrapolated heterogeneous nucleation flank from the FSC data. The slight deviation is explained by the higher surface-to-volume ratio of the FSC sample which probably stimulates heterogeneous primary nucleation on the calorimetric chip. Schick (2016) reported that crystallization rates of PBT measured by DSC are approximately two orders of magnitude lower than those measured by FSC.[110] Crystallization from the glassy state exhibits a characteristic single bell-shaped curve, in contrast to the bimodal behavior observed during crystallization from the melt. It follows the low-temperature flank of the melt curve, where homogeneous nucleation dominates, indicating that the state prior to reaching T_c does not affect the crystallization when homogeneous nucleation prevails. At higher temperatures, crystallization rates from the glassy state continue to increase and exceed those observed throughout the heterogeneous nucleation regime when crystallizing from the melt. As discussed in the *Introduction*, this behavior can be attributed to the preceding quenching to below T_g, which increases the homogeneous nucleation rate and, consequently, the primary crystallization rate. It is expected that the melt and glassy data of PCCD-PTHF both extrapolate to a zero-crystallization rate at the highest temperatures (not measured) in the vicinity of equilibrium melting point, T_m^0. This seems to be not so in the present case, likely because of being too far away from T_m^0.

The crystallization kinetics of PCCD show very similar rates over the whole temperature range, regardless of whether T_c is reached from the melt or the glassy state. The crystallization curves of PCCD-PTHF are shifted by approximately 45 °C to lower temperatures compared to PCCD, reflecting its lower T_g and T_m^0. Additionally, PCCD-PTHF exhibits lower crystallization rates than PCCD at low temperatures, while the opposite is observed at higher temperatures, a trend also reported for PBT-PEG systems.[96] This behavior can be attributed to the plasticizing effect of the PTHF blocks, which increase segmental mobility and lower T_g. At higher temperatures, dilution by PTHF reduces T_m^0, thereby decreasing the degree of supercooling and hindering the diffusion of PCCD blocks to the crystallization front, ultimately limiting the growth rate (see *Introduction* section). It is important to note that the PCCD blocks in the copolymer (M_n = 1,960 g/mol [71]) are significantly shorter than the PCCD homopolymer (M_n = 6,142 g/mol), which could theoretically enhance segmental mobility at low temperatures and thus contribute to the higher crystallization rates observed for PCCD-PTHF. However, the PCCD blocks in PCCD-PTHF are coupled to the PTHF blocks, which precludes making such simplified considerations on potential molar mass effects. Secondly, previous results have shown that crystallization rates at low temperatures are largely independent of molar mass. Therefore, the increased rates for PCCD-PTHF are most likely attributable to the presence of the plasticizing PTHF block alone.

Another observation is that the PCCD material (M_n = 47,860 g/mol, t,t = 91 %) data from Sandhya (2003) are situated at much lower rates than the PCCD in this work.[69] They also reported that no crystallization was seen upon cooling at rates above 2 K/min. It seems that, the higher M_n lowered the rates and induced a bimodal behavior.[42,96] The *t,t* content (91%) is significantly higher than that of the PCCD used in this study (*t,t* = 68.6 %), and indicates a higher T_m^0 from the extrapolation of the data by Sandhya (2003).[69] This, however, is counter-intuitive as the higher crystallization rates are expected to be higher due to an increased supercooling. It thus seems that the higher M_n prevails and leads to a reduced crystallization rate.

The non-birefringent crystal aggregates in the POM images in **Figure 62** (left) indirectly suggest that the nanocrystals they are composed of at low temperatures

are small, disordered and thus less stable, making them more susceptible to recrystallization upon heating. This anticipated behavior is corroborated by the heating scans following isothermal crystallization in the FSC experiments for both PCCD-PTHF (**Figure 63**) and PCCD (not shown). The heat flow (HF) curves of PCCD-PTHF, after various isothermal durations at low, intermediate, and high T_c, display distinct melting–recrystallization–remelting (MRR). This MRR behavior indicates that the initial crystals formed during cooling are unstable and undergo partial melting and cold (re)crystallization into more stable crystalline structures upon heating. The effect is particularly pronounced following low-temperature crystallization, where homogeneous nucleation dominates. In contrast, at higher T_c, crystallization is primarily governed by heterogeneous nucleation, resulting in larger, more stable crystals and a less pronounced MRR response.

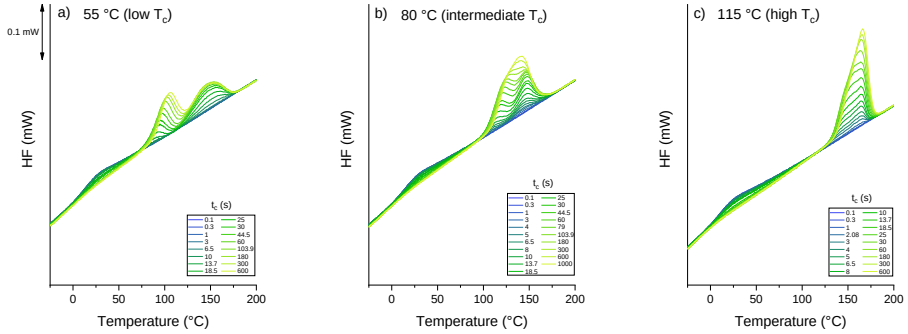


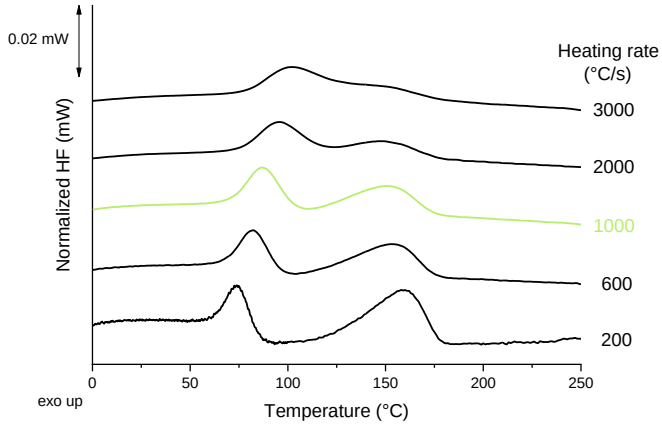
Figure 63. *PCCD-PTHF HF curves of the heating after isothermal crystallization from the melt at a) 55 °C, b) 80 °C and c) 115 °C for a) 0.1 to 600 s, b) 0.1 to 1000 s and c) 0.1 to 600 s. The colors of the curves evolve from blue to green with increasing time.*

At the three indicated T_c's, the low temperature melting peak corresponds to the melting of crystals formed directly at that specific T_c. As expected, this peak is highly dependent on the crystallization temperature, a behavior that has been previously observed in various polymer systems such as PA11[86], PA12[86] and s-PP[72]. In contrast, the high-temperature peak arises from the melting of recrystallized, more stable crystals formed during the subsequent heating at 1000 K/s.

Given that the primary crystallization rates (**Figure 62**) indicate short half-times, it is primarily the secondary crystallization that is influenced by prolonged isothermal times t_c. Beyond the initial sigmoidal increase (on a logt scale) of the

enthalpy due to primary crystallization, a further linear increase is observed beyond the sigmoidal enthalpy curves (Figure C.6 in Appendix C). This increase is also accompanied by a shift to higher temperatures of the first melting peak, suggesting that secondary crystallization, besides an increase of the crystallinity, also includes crystal stabilization and perfectioning.

To confirm the presence of the MRR, an additional heating rate experiment was performed where the heating rate was varied from 200 to 3,000 K/s after isothermal crystallization at 35 °C for 600 s. The curves are shown in **Figure 64** and



confirm a heating rate dependent MRR behavior.

Figure 64. *HF curves of PCCD-PTHF at the indicated heating rates after crystallization from the melt at 35 °C for 600 s. The evolution of the melting peaks with increasing cooling rate indicates the melting-recrystallization-remelting origin of the double melting behavior.*

The melting behavior displays dependence on the crystallization temperature (T_c), as shown in **Figure 63**, across the full temperature range from T_g to the melting point for both PCCD-PTHF and PCCD, regardless of whether crystallization occurred from the melt or the glassy state (**Figure 65**). The heat flow (HF) curves were processed by subtracting a linear baseline, after which the resulting horizontal baselines and associated data were vertically shifted to align with the corresponding T_c (y-axis). The melting points, determined from the maximum of each peak, are

represented by filled circles positioned on these baselines. Additionally, a $T_m = T_c$ reference line was included to facilitate interpretation of the plot as a Hoffman-Weeks (HW) plot. This approach is inspired by previous analyses of isothermal crystallization from the melt in PA11 and PA12 .[86] Similar to these polyamides, both PCCD-PTHF and PCCD exhibit the expected shift in melting peak position with T_c and demonstrate a clear dependence of melting-recrystallization-remelting (MRR) behavior on T_c. Specifically, the low temperature melting peaks shift to higher temperatures as T_c increases, reflecting the increasing stability of the crystals formed at higher T_c. At sufficiently high T_c, the high-temperature peaks associated with recrystallization/remelting begin to overlap with the low-temperature peaks, indicating that the initially formed crystals are stable enough to suppress MRR, even at a heating rate of 1000 K/s. To our knowledge, this is the first report of HW plots spanning the full range from T_g to the melting point for the segmented block copolymer PCCD-PTHF and its corresponding homopolymer PCCD.

Following the HW theory, the evolution of first melting peak position is expected to intersect the $T_m = T_c$ reference line when extrapolated to high T_c. This intersection then corresponds to T_m^0. Here, the experimental T_m evolution seems to run parallel to the reference line, suggesting that crystal stabilization is not reducing with higher temperatures and that T_m^0 is far away at much higher temperatures beyond the investigated crystallization temperatures.

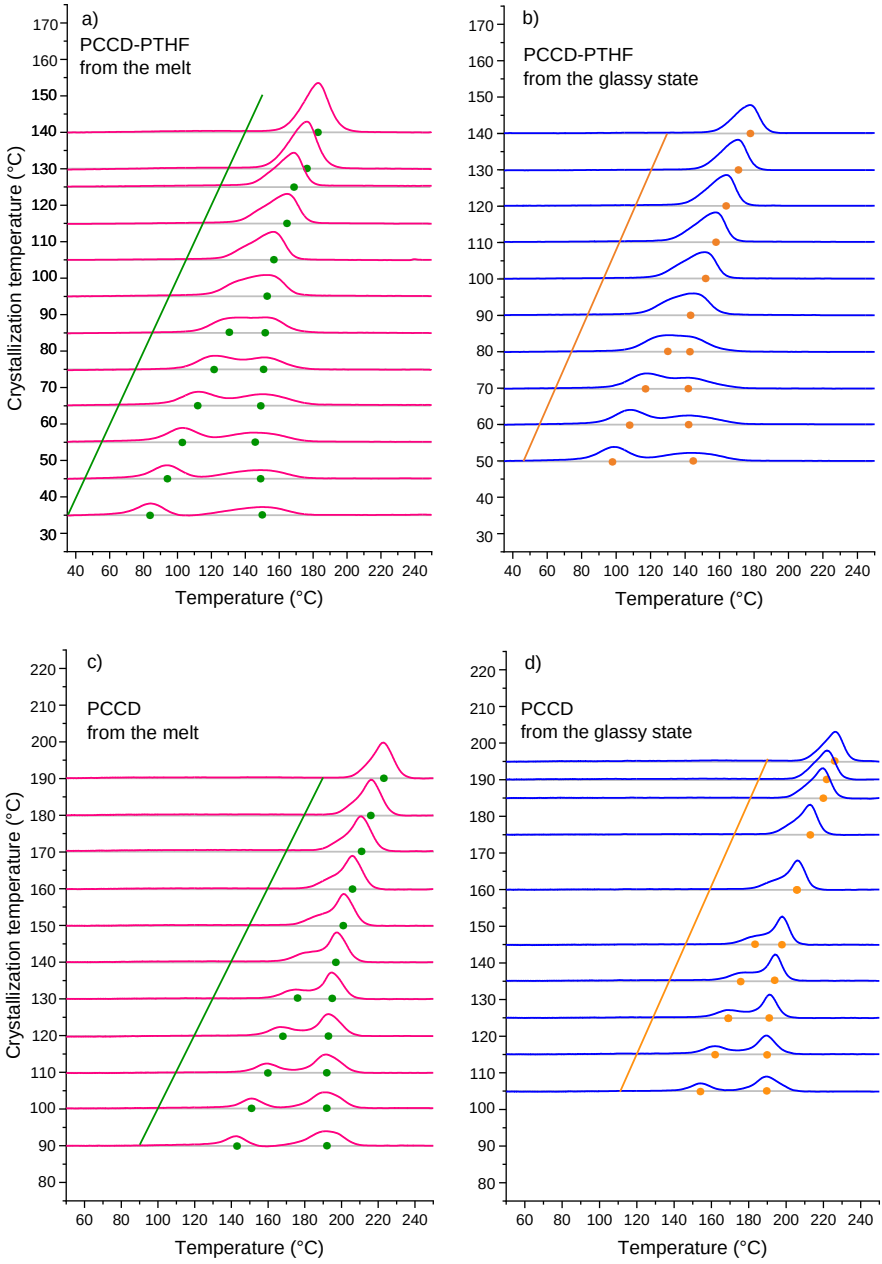


Figure 65. *Heat flow curves of the heatings at 1000 K/s after 300 s of isothermal crystallization of PCCD-PTHF (a,b) and PCCD (c,d) at the indicated temperatures when coming from a)& c) the melt and b)&d) the glassy state. A linear baseline was subtracted from the HF curves and the resulting horizontal baselines (gray) and*

associated data were vertically shifted to align with the corresponding T_c. the green (a,c) and orange (c,d) dots indicate the maximum temperature of the melting peaks. The green (a,c) and orange (b,d) lines are the T_m=T_c lines.

Since the linear increase in crystallinity observed during isothermal crystallization after the primary stage is attributed to secondary crystallization, one would expect the overall crystallinity after 300 s at various T_c values to increase with decreasing temperature as secondary crystallization is more pronounced at lower temperature during cooling at 10 K/min. To examine this, the enthalpy values were determined by integrating the PCCD-PTHF heat flow curves in **Figure 65** over the range from 50 to 240 °C (see **Figure 66**). From a T_c of approximately 100 °C upward, the crystallinity decreases with increasing T_c, consistent with enhanced secondary crystallization at lower temperatures. Below 80 °C, however, an opposite trend is observed—crystallinity decreases with decreasing T_c—which is likely due to reduced segmental mobility, hindering crystal development. This temperature-dependent crystallinity can be explained by the interplay between thermodynamic driving forces (i.e., degree of supercooling) and kinetic limitations (i.e., segmental mobility). This interpretation aligns well with the crystallization rates shown in **Figure 62**.

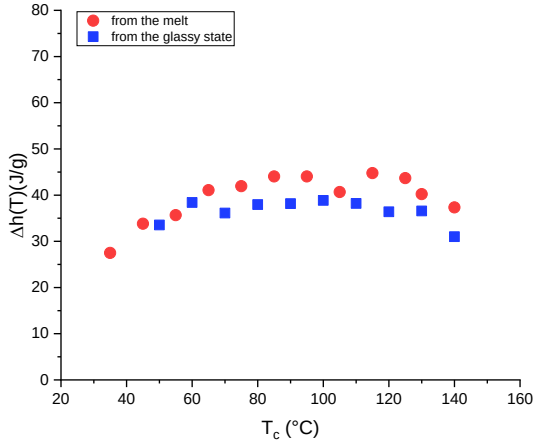


Figure 66. *Enthalpy values of PCCD-PTHF after 300 s of isothermal crystallization at T_c, retrieved from integrating the melting peaks upon subsequent heating at 1000 K/s from 50 to 240 °C using the baselines depicted in **Figure 65**. The data from reaching the T_c from the melt (red circles) and from the glassy state (blue squares) are shown.*

It is of interest to explore how the melting behavior—reflecting crystal stability—at different T_c values correlates with crystal size and crystallization mechanism. As discussed in the *Introduction* section, PCCD-PTHF showed increasing crystallinity during cooling at 10 K/min (and a corresponding decrease upon heating), attributed to both primary and secondary crystallization. Notably, the average crystalline lamellar thickness (l_c) remained constant, with the secondary lamellae formed at low temperatures having the same l_c as the primary lamellae, formed at high temperature.

However, as will be shown in the next section, the l_c of PCCD-PTHF was found to vary with T_c during isothermal crystallization. This indicates that the crystallization mechanism under isothermal conditions differs from that observed during non-isothermal crystallization.

4.3.3 Morphology of PCCD-PTHF

Simultaneous FSC and WAXS

An experiment combining FSC and WAXS, as described in the *Methods* section (Setup 1), was conducted to obtain structural information on PCCD-PTHF following isothermal crystallization under the same conditions as in **Figure 62** (see **Figure 56**). The only difference was that, after 180 s of isothermal crystallization the samples were quenched to -20 °C where 5 diffraction frames were recorded. The WAXS patterns captured at -20 °C were found to correspond to those observed at the end of the crystallization event at T_c (not shown), except for a slight effect on all reflections of of thermal contraction. Therefore, it can be concluded that the crystals structure of PCCD-PTHF at -20 °C accurately reflects the final structure formed during isothermal crystallization.

To rule out polymorphism as possible origin of the bimodal crystallization rates in PBT, Androsch *et* al (2015) performed WAXS experiments and found that the pattern characteristic of the crystals formed at high temperatures were also found at low temperatures.[90] They concluded that the origin of the bimodality was a difference in the primary nucleation mechanism and not the formation of different polymorphs

with different growth rates. For PCCD-PTHF, the same patterns were found as the patterns (not shown) upon cooling at 10 K/min at the corresponding temperatures (Chapter 2). The shift of the 100 reflection, which was attributed to thermal contraction, was also seen here. This indicates that polymorphism should not be considered.

The frames at -20 °C were averaged to reduce noise, and the l_c was determined from the averaged WAXS pattern using the Scherrer equation on the 001 reflection, following a similar methodology as described in Chapter 2. Specifically, the 001 reflection at q = 0.54 Å^{-1} was isolated and fitted using a Gaussian function, while the background was approximated by a linear baseline. An example is shown in Figure C.5 in Appendix C. The peak breadth, obtained as a fitting parameter, was used to calculate the crystallite size D_{001} via the Scherrer equation. This value corresponds to the crystallite size along the direction tilted 27.2° from the lamellar normal, which is also the orientation of the polymer chains. Accordingly, the lamellar thickness was calculated by correcting for the tilt angle via $l_c = D_{001}\cos(27.2°)$, assuming the tilt angle remains constant across the temperature range studied. The error bars were calculated based on the standard deviation on the fitting parameter FWHM (see C.6 in Appendix C).

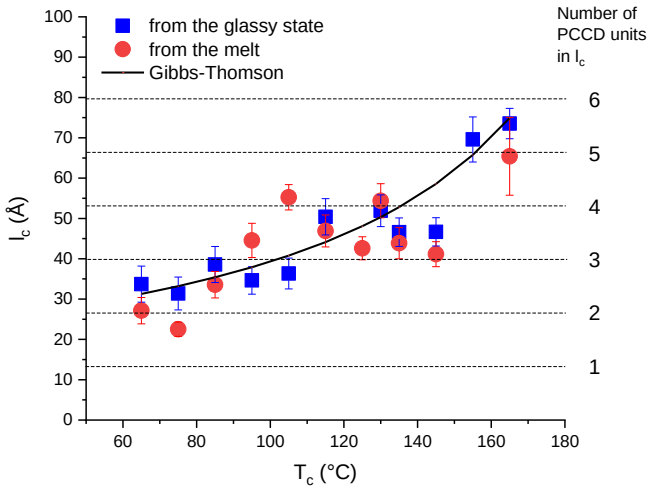


Figure 67. *Average lamellar thickness l_c of PCCD-PTHF at -20 °C after 180 s of crystallization at the given T_c coming from the melt (red circles) and the glassy state (blue squares). The error bars are calculated based on the standard deviation on the*

fitting parameter FWHM (C.6 in Appendix C). The horizontal black dashed lines represent the number of PCCD units in a certain l_c with 13.28 Å the size of one PCCD unit.[71] *The black curve is the approximation of the Gibbs-Thomson equation $l_c = B/(T_m^0 - T_c)$ where B and T_m^0 were used as fitting parameters, with $B = \frac{2\sigma_e T_m^0}{\Delta H_v}$ (see Chapter 1).*

The l_c values obtained for crystallization from the melt or the glassy state are comparable. As shown by the black curve in **Figure 67**, l_c increases with increasing crystallization temperature, in agreement with the Gibbs-Thomson theory and the evolution of the melting peaks in the HW plot in **Figure 65a,b**. Correspondingly, the number of PCCD repeating units per lamella also increases, ranging from approximately 2 units at the lowest temperatures to about 5.5 units at the highest.

Notably, following crystallization at a cooling rate of 10 K/min, the lamellae formed at 25 °C were also reported to consist of approximately 6 PCCD units (Chapter 2). At a cooling rate of 10 K/min, the l_c of the PCCD-PTHF copolymer remains approximately constant. This was attributed to the gradual crystallization of the PCCD blocks, which occurs within an increasingly PTHF-rich amorphous matrix as cooling progresses. This compositional evolution leads to a progressive dilution of the crystallizable PCCD segments, effectively lowering both the local equilibrium melting temperature T_m^0 and the T_c. As a result, the supercooling $\Delta T = T_m^0 - T_c$ remains nearly constant throughout the crystallization process, which explains the observed invariance in lamellar thickness.

In contrast, under FSC conditions, where the material is rapidly quenched to a fixed temperature, the supercooling varies directly with the set temperature as there is no PCCD dilution due to preceding crystallization, resulting in a corresponding variation in l_c.

Time-resolved SAXS/WAXS

The T_c's of 110 and 130 °C were selected for the time-resolved WAXS experiments on aged PCCD-PTHF. The samples were quenched from the glassy state to the respective T_c values, held isothermally for 600 s to allow crystallization, and subsequently heated from T_c to 250 °C at a rate of 10 K/min. Due to limitations of the quenching setup, crystallization from the melt could not be investigated under the

same conditions. However, as will be demonstrated, the structural evolution observed upon crystallization from the glassy state can be extrapolated to describe the behavior following crystallization from the melt.

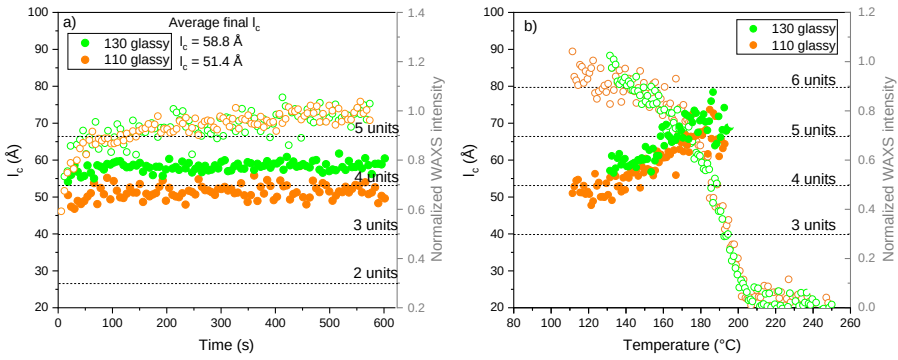


Figure 68. *PCCD-PTHF l_c values (full circles) and WAXS intensity (open circles) during a) isothermal crystallization at 110 and 130 °C when coming from the glassy state and b) subsequent heating at 10 K/min. The average l_c is calculated from the 10 last l_c data points. The horizontal black line in b) represents the l_c of PCCD-PTHF after crystallizing at 10 K/min.* [71]

In **Figure 68a** (filled circles) the l_c stays relatively constant during crystallization at both studied temperatures. The average l_c of 130 °C is higher than 110 °C, which agrees with the trend in **Figure 67** and the values from both experiments are comparable, within the error range. It is therefore assumed that that the surface-to-volume ratio difference between the small FSC sample (**Figure 67**) and the larger sample used in the quench setup (**Figure 68**) does not fundamentally change the final morphology.

At 110 °C, the lamellae consist of approximately 4 PCCD units, while at 130 °C they grow to about 4.5 units. This modest increase of half a unit can be attributed to the contribution of a distribution of PCCD block lengths to the average lamellar thickness l_c, the incorporation of one additional monomeric unit, or the inclusion of an extra diacid moiety connecting the PCCD and PTHF blocks. Upon subsequent heating (**Figure 68b**, filled circles), the l_c at both temperatures increases linearly, ultimately reaching ~73 Å (corresponding to 5.5 PCCD units), which matches the value observed after non-isothermal crystallization upon cooling at

10 K/min (Chapter 2). This continuous growth is attributed to MRR, involving the reorganization of existing crystals into thicker lamellae. To support this interpretation, the WAXS intensity—calculated by integrating the area under the 001 reflection at $q = 0.54$ Å^{-1}—was used as a measure of relative crystallinity. During isothermal crystallization, the WAXS intensity (**Figure 68a,** open circles) exhibits an initial sharp increase corresponding to primary crystallization, followed by a prolonged linear increase associated with secondary crystallization without change in crystal thickness. Upon heating (**Figure 68b**, open circles), the intensity decreases until the sample is fully molten at around 200 °C, reflecting the progressive melting of thinner crystals formed at lower T_c values and their recrystallization into thicker ones (MRR). Importantly, MRR already starts 20 °C above T_c, which is different from heating after crystallizing at 10 K/min (Chapter 2), where a large part of the initial melting is related to the melting of secondary crystallites, despite having comparable l_c, indicating that MRR depends on the crystallization pathway (isothermal vs. non-isothermal).

Finally, the SAXS crystallinity $\alpha\phi$, was calculated to compare with the WAXS 001 reflection intensity in **Figure 69**. The average local crystallinity within the semi-crystalline layer stacks ϕ was calculated as $l_c/L_{p,}$ with L_p the periodicity as the minimum of the IDF (not shown) and l_c retrieved from the Scherrer equation. α, which represents the volume fraction of semi-crystalline stacks, was calculated via $\alpha = Q_{id}/(\phi(1-\phi)(\rho_c - \rho_a)^2)$ with $(\rho_c - \rho_a)$ taken from the contrast function in Chapter 2 and Qid the invariant retrieved from the integral of the Lorentz corrected SAXS curve. α was then scaled to $0.75/\alpha_{max}$ where 0.75 is the value at 120 °C during heating after cooling at 10 K/min (**Figure 24b**), and α_{max} the average α value found at the end of the isothermal event at the T_c. Note that α cannot be determined on an absolute scale and requires scaling to a certain 'realistic' value. In many cases it is scaled to 1 where it is believed that the stacks are space filling. As such condition is likely not met after crystallization at 110 and 130 °C, an alternative scaling was used.

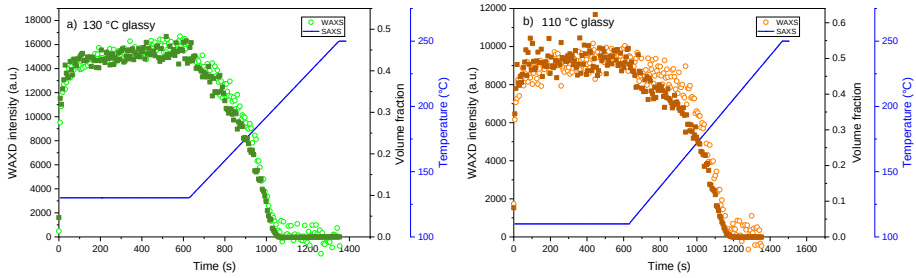


***Figure 69**. SAXS and WAXS intensities of PCCD-PTHF during crystallization from the glassy state at 130 °C and 110 °C, and subsequent heating at 10 K/min. The blue curve shows the temperature profile.*

The SAXS and WAXS evolutions show very low intensities at the start of isothermal crystallization, confirming that the crystallization at T_c was reached from a virtually amorphous state at room temperature after quenching in liquid nitrogen and the successful temperature jump by the setup from room temperature. The SAXS and WAXS crystallinity indices follow the same evolution over the isothermal event and the subsequent heating, which shows consistency. These findings strongly support the proposed interpretation of the isothermal crystallization and melting behavior described in the preceding paragraph.

According to **Figure 67**, the l_c does not dependent on whether the T_c is reached from the melt or the glassy state, strongly suggesting that the nucleation mechanism does not systematically determine l_c. Consequently, both SAXS and WAXS intensity evolutions are expected to resemble those observed during crystallization from the melt at the same T_c. Moreover, given that the nucleation mechanism has a limited effect, experiments performed at lower crystallization temperatures (where homogeneous nucleation dominates) are also expected to follow the same similar trends. This includes comparable scattering features during both primary and secondary crystallization, as well as analogous MRR behavior upon heating.

4.4 Conclusions

This work presents a comprehensive study of the isothermal crystallization behavior of PCCD and its block copolymer PCCD-PTHF across the full temperature range from T_g to the melting point, using FSC, POM, DSC and SAXS/WAXS. It also rationalizes the mechanism of high-temperature ageing of PCCD-PTHF based on *trans*-to-*cis* isomerization and transesterification.

By systematically varying the crystallization temperature and comparing crystallization from both the melt and the glassy state, new insights into crystallization of PCCD-based materials were gained. The crystallization kinetics study revealed bimodal behavior for PCCD-PTHF when crystallizing from the melt, attributed to a transition from heterogeneous to homogeneous nucleation with decreasing temperature. In contrast, crystallization from the glassy state exhibited a single bell-shaped rate curve with higher rates at lower supercooling, indicating a dominant contribution of homogeneous nucleation. PCCD showed a similar single bell-shaped curve regardless of whether crystallization proceeded from the melt or the glassy state.

Secondary crystallization was consistently observed, which partly also leads to reorganization of less stable crystals into more stable structures. Structurally, the l_c of PCCD-PTHF increased with crystallization temperature for both melt- and glass-derived crystallization, in agreement with the Gibbs-Thomson theory and largely independent of the nucleation mechanism. This supports the conclusion that T_c, rather than the pathway to T_c, governs the final lamellar structure of PCCD-PTHF. Overall, these findings deepen the understand of isothermal crystallization at high supercooling, which is typical for various processing methods.

Chapter 5

Non-Isothermal Crystallization of PCCD-PTHF and Amphora SP1621

Author contributions

Mouna Hamid: Conceptualization, Investigation, Methodology, Formal analysis, Writing – original draft. **Sara Salhane**: Investigation, Methodology, Formal analysis. **Bart Goderis**: Supervision, Conceptualization, Methodology, Formal analysis, Writing – review and editing.

5.1 Introduction

Up to this point, this thesis has primarily focused on PCCD-PTHF to develop a fundamental understanding of its crystallization behavior. As previously discussed, there is limited published information on the crystallization mechanisms and kinetics of both PCCD-PTHF and the commercial formulation Amphora SP1621. One aspect not yet addressed, either in this thesis or in the literature, is the non-isothermal crystallization behavior and its effect on crystal structure for the specific PCCD-PTHF grade used here, as well as for Amphora SP1621. While earlier chapters relied on insights from PCCD-PTHF to deduce aspects of Amphora SP1621, no direct measurements on the commercial formulation have been presented until now.

To fill these gaps, a non-isothermal crystallization study was conducted on both materials. To our knowledge, only one previous non-isothermal crystallization study on PCCD-PTHF exists.[102] However, as mentioned in Chapter 1, that work likely examined a different grade, as the reported T_c at 10 K/min was ~153 °C, whereas the material studied here exhibits a T_c of ~118 °C under the same conditions (Chapter 2). That study used cooling rates between 2 and 100 K/min. Their results showed a sigmoidal evolution of relative crystallinity during cooling, which plateaued without significant secondary crystallization. In contrast, the PCCD-PTHF studied here exhibits pronounced secondary crystallization continuing down to room temperature (Chapter 2). Although the authors acknowledged some secondary crystallization due to spherulitic impingement, the behavior observed in this thesis suggests a more extended process.

As discussed in Chapter 2, secondary crystallization in PCCD-PTHF occurred following the formation of spherulites at 10 K/min and involved the development of

additional lamellar stacks with similar thickness to the primary lamellae. This process led to a continued increase in SAXS and WAXS crystallinity up to room temperature. Upon reheating, these changes were fully reversible, and the material displayed complex MRR behavior.

The isothermal crystallization study in Chapter 4 revealed a bimodal crystallization mechanism: when cooling from the melt to the crystallization temperature, T_c, crystallization could occur in either a heterogeneous nucleation dominated regime at higher T_c or a homogeneous nucleation dominated regime at lower T_c, with a transition around 80 °C. This resulted in the formation of large superstructures (spherulites) in the heterogeneous regime and smaller crystalline domains in the homogeneous regime. It is important to note that these isothermal experiments were performed on heavily aged PCCD-PTHF.

As a reminder, ageing of PCCD-PTHF consisted of subjecting the sample to a heat treatment of 26 heating/cooling cycles under a constant nitrogen flow following protocol in **Figure 54a**. During the heat treatment, *trans*-to-*cis* isomerization of the cyclohexane moieties was suggested to occur, as well as transesterification reactions that increased the M_n drastically.

To further explore the crystallization behavior and kinetics of PCCD-PTHF, and to investigate how these are influenced by the cooling rate, a series of non-isothermal experiments were conducted. DSC was used for moderate cooling rates, and FSC extended the study to much higher rates. Unlike previous work, this study directly links cooling rate to resulting morphology using structural characterization techniques. The same approach was applied to Amphora SP1621 to enable a direct comparison. Therefore, non-aged PCCD-PTHF was used.

Accordingly, the two main objectives of this chapter are i) to investigate the non-isothermal crystallization behavior of PCCD-PTHF, including the influence of cooling rate on morphology and ii) to characterize Amphora SP1621 directly, using PCCD-PTHF as a benchmark for comparison and to better understand its crystallization behavior.

To achieve these objectives, a combination of DSC and FSC was used to assess the crystallization kinetics and melting behavior over a wide range of cooling

rates. Complementary techniques including SAXS/WAXS and POM were employed to analyze the resulting crystal structures and morphologies of both materials.

Although Amphora SP1621 remains less characterized in the literature, this comparative study offers valuable insights into the key differences in crystallization kinetics and morphology between both materials. These differences are likely influenced by variations in formulation and the presence of additives. A better understanding of these factors can help optimize the printing process of Amphora SP1621.

5.2 Experimental section

5.2.1 Materials

Non-aged PCCD-PTHF (M_n = 12,654 g/mol, M_w = 75,304 g/mol, Đ = 5.95) pellets and commercial Amphora SP1621[1] (M_n = 5,968 g/mol, M_w = 31,129 g/mol, Đ = 5.22 [2]) powder were kindly provided by Eastman Chemical Technology BV (Ghent, Belgium). The company communicated that anti-oxidants and flow agents were added to the Amphora SP1621 powder. **Importantly, throughout this chapter, "PCCD-PTHF" refers to non-aged material unless explicitly stated otherwise.**

5.2.2 Methods

Differential Scanning Calorimetry (DSC)

The same DSC apparatus and pans as described in Chapter 2 were used for the experiments in this chapter. The sample masses were about 8 mg. The thermal protocols for the cooling rate experiments on PCCD-PTHF and Amphora SP1621 are shown in **Figure 70**, with cooling rates, β, ranging from 5 to 50 K/min. A fresh sample was used for each measurement and the measurements were done under a constant nitrogen flow. From the HF signals of the cooling and subsequent heating segments, the heat flow data were converted into specific heat capacity $c_p(T)$ ($Jg^{-1}K^{-1}$) values by

subtracting an empty pan measurement and subsequent normalization to the scanning rate and sample mass.

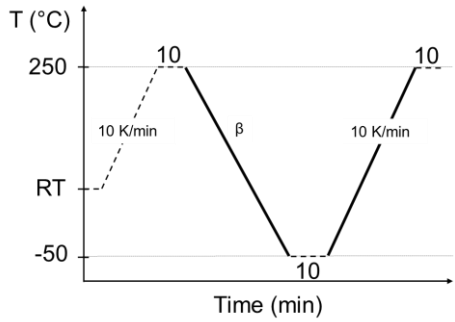


Figure 70. *Thermal protocol for the cooling rate experiments where the cooling rate β was chosen as 5, 10, 20 and 50 K/min.*

Fast-Scanning Calorimetry (FSC)

The apparatus used is described in detail in Chapter 2, as well as all details about the sample preparation. The specific thermal protocol applied in this chapter is shown in **Figure 71**. The HF curves were used as recorded, without additional post-processing. For these experiments, all the experiments were performed on the same sample and the measurements were performed under a constant nitrogen flow.

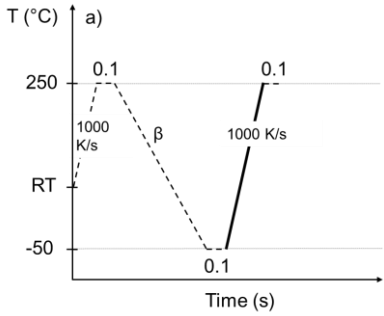


Figure 71. *Thermal protocols for PCCD-PTHF (β = 0.17-500 K/s) and Amphora SP1621 (β = 10-500 K/s).*

Static Small and Wide-Angle X-ray Scattering (SAXS/WAXS)

The experimental setup, the data correction procedures and the angle calibration were identical to those described in Chapter 2 for the static SAXS/WAXS measurements using the XeuSS X-ray camera (Xenocs, Sassenage, France). Samples of non-aged PCCD-PTHF and Amphora SP1621 were prepared in the DSC in Tzero aluminum pans according to the thermal protocol shown in **Figure 70** up until reaching –50 °C. After reaching this temperature, the samples were removed and allowed to return to room temperature. Cooling rates ranged from 5 to 50 K/min, and all static SAXS/WAXS measurements were subsequently performed at RT.

Polarized Optical Microscopy (POM)

The same setup was used as described in Chapter 2. Amphora SP1621 was heated to 250 °C at 10 K/min, held for 10 min at 250 °C and was cooled down to RT at the same rate. The image at RT was used for analysis. PCCD-PTHF was heated to 240 °C at 10 K/min, cooled after 10 min at that temperature to RT at 5 or 50 K/min. The PCCD-PTHF experiments were time-resolved and the images were taken every 1 °C (12 s) for 5 K/min and 0.83 °C (1 s) for 50 K/min.

5.3 Results and discussion

5.3.1 Cooling rate dependent crystallization in PCCD-PTHF and Amphora SP1621

To comprehensively evaluate the effect of cooling rate on the non-isothermal crystallization kinetics and the underlying crystallization mechanism, cooling rates both above and below 10 K/min were investigated. The data and results obtained in Chapter 2 for PCCD-PTHF crystallized at a cooling rate of 10 K/min were employed as a reference point. The commercial sintering material Amphora SP1621 was included as a comparative benchmark to assess differences in crystallization behavior relative to PCCD-PTHF.

For PCCD-PTHF and Amphora SP1621, increasing the cooling rate results in a decrease in the main crystallization peak temperature as progressively less time

is given for (slow) crystallization at a higher temperature (**Figure 72a,c**). Crystallization only really takes off at lower temperatures when the supercooling and associated crystallization rate are high enough to match the permitted time. Overall, the crystallization peaks of Amphora SP1621 occur at higher temperatures and are much sharper than of PCCD-PTHF, indicating facilitated crystallization and thus higher non-isothermal crystallization kinetics. As the base polymer of Amphora SP1621 is PCCD-PTHF, it can be speculated that some of the additional components present in Amphora SP1621, such as anti-oxidants and flow agents, facilitate the primary nucleation. Flow agents are usually small inorganic particles of less than 1 µm that adsorb on the surface of the powder particles to increase the powder flow.[111] The exact nature of the particles for the current system is not known.

The lower M_n of Amphora SP1621 could also contribute to the observed behavior.

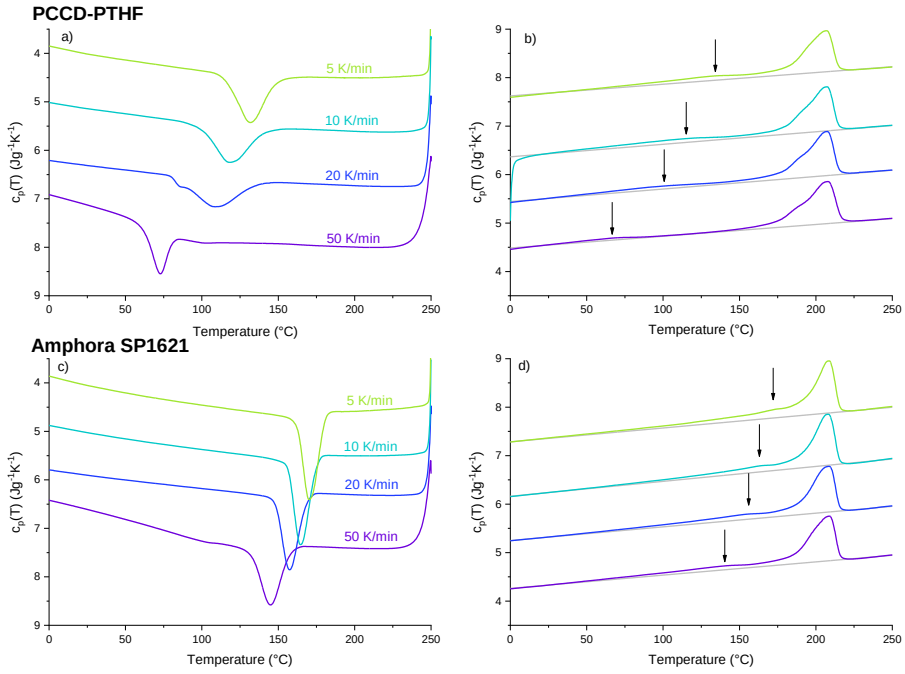


Figure 72. *DSC $c_p(T)$cooling curves recorded at the indicated cooling rates for (a) PCCD-PTHF and (c) Amphora SP1621. Subsequent DSC heating curves were obtained at a constant rate of 10 K/min for (b) non-aged PCCD-PTHF and (d) Amphora SP1621. Baselines employed for integration are shown as well.*

Enhanced primary nucleation for Amphora SP1621 was confirmed by POM. In Chapter 2, POM experiments revealed that the lamellae in PCCD-PTHF during cooling at 10 K/min organize into space-filling spherulitic superstructures (**Figure 17**).The same POM experiment performed on Amphora SP1621 reveals the presence of numerous much smaller birefringent structures (**Figure 73**) at RT after cooling at 10 K/min. Clearly, the number of superstructures is significantly higher compared to PCCD-PTHF. Given that the crystallization peak temperature of Amphora SP1621 is higher than that of PCCD-PTHF, this elevated nucleation density is most likely a result of enhanced heterogeneous (primary) nucleation.

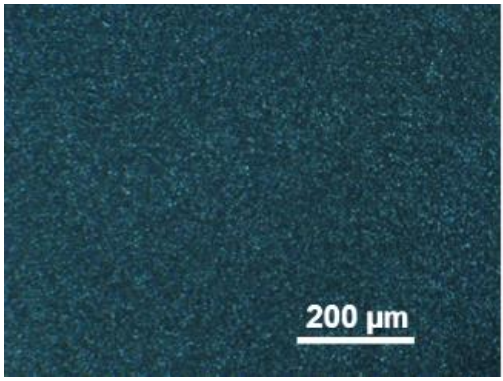


***Figure 73**. POM-image of Amphora SP1621 at RT after cooling at 10 K/min, showing small birefringent entities.*

In Chapter 2, the evolution of the mass fraction crystallinity of PCCD-PTHF during cooling at 10 K/min, based on both DSC enthalpy values and WAXS intensity, showed a pronounced initial increase followed by a slower, steady rise (**Figure 13b**). This behavior was attributed to primary and secondary crystallization, respectively. In the present chapter, however, the cooling runs are affected by baseline curvature—even after subtraction of the empty pan signal—making it difficult to compute crystallinity values directly (**Figure 72a,c**). Nevertheless, qualitative analysis indicates that cooling at 5 K/min produces a similar trend, with a sharp high-temperature crystallization peak followed by a broader signal at lower temperatures.

Interestingly, when cooling at 20 K/min, the main crystallization peak shifts to lower temperatures and becomes bimodal. It is suggested that this splitting is not due to the sequential occurrence of primary and secondary crystallization, but rather to a change in the mechanism of primary crystallization. At an even higher cooling rate of 50 K/min, the low-temperature peak dominates in area over the high-temperature signal and appears as a distinct, sharp peak.

This is interpreted as evidence for the presence of two competing primary nucleation mechanisms, with the low temperature mechanism being favored below approximately 80 °C. A similar change in mechanism was previously observed during isothermal crystallization of aged PCCD-PTHF, as discussed in Chapter 4. In that case, homogeneous nucleation dominated over heterogeneous nucleation at temperatures below 80°C and this change in primary nucleation mechanism was reflected in a bimodal evolution of the crystallization rate as function of the isothermal crystallization temperature (**Figure 62**). At a cooling rate of 50 K/min, crystallization thus appears to proceed primarily via homogeneous nucleation below 80 °C.

It is important to note that as a result of progressive high temperature ageing, through which the molecular weight of PCCD-PTHF increases, the primary crystallization peak also shifts to lower temperatures even though the cooling rate was maintained at 10 K/min (**Figure 58a**). Furthermore, this primary crystallization passes a double peak regime and finally also only exhibits a sharp low temperature crystallization peak. At this final stage, the thermal behavior stabilizes as it is governed by homogeneous nucleation, which is a local process, depending little on the polymer molecular weight and the associated chain mobility compared to when nucleation is heterogeneous and spherulite growth follows. It is here observed that cooling a non-aged sample more rapidly leads to a similar shift toward the homogeneous crystallization regime (**Figure 72a**). In both scenarios, rapid cooling and ageing, a residual high-temperature crystallization tail remains, suggesting a remaining fraction of material that nucleates heterogeneously and grows spherulitically.

POM images were collected on PCCD-PTHF during cooling at 5 and 50 K/min. The initial frames, depicted on the left side in **Figure 74**, were taken at the

crystallization onset, which correspond well to the DSC based onset temperature (**Figure 72a**), taking into account the high temperature tail at 50 K/min. The images in the center were taking during the crystallization and the final image at the right side is at RT. Spherulitic structures were observed at both cooling rates, with two notable differences: the degree of space-filling and the size of the spherulites. Slow cooling results in large, space-filling spherulites, while rapid cooling leads to the formation of smaller, more widely spaced, not space-filling spherulites. The absence of space filling is likely due to their growth being stopped by massive homogeneous nucleation in the remaining matrix when 80 °C is surpassed. The differences with the image of aged PCCD-PTHF after isothermal crystallization at 80 °C (**Figure 62**) can be explained by the fact that for crystallization at 80 °C, the sample is quenched directly into the homogeneous nucleation regime, bypassing crystallization in the heterogeneous nucleation regime. If aged PCCD-PTHF would have been crystallized during cooling at 10 K/min, a similar morphology as in **Figure 74f** would likely show up. This experiment was not performed.

These cooling rate dependent experiments were not repeated on Amphora SP1621 due to time limitations, however, it is expected that experiments at 5 and 50 K/min would show similar images as **Figure 73** due to the low cooling rate dependency of crystallization and the supposed high nuclei density which limits the growth of the spherulites.

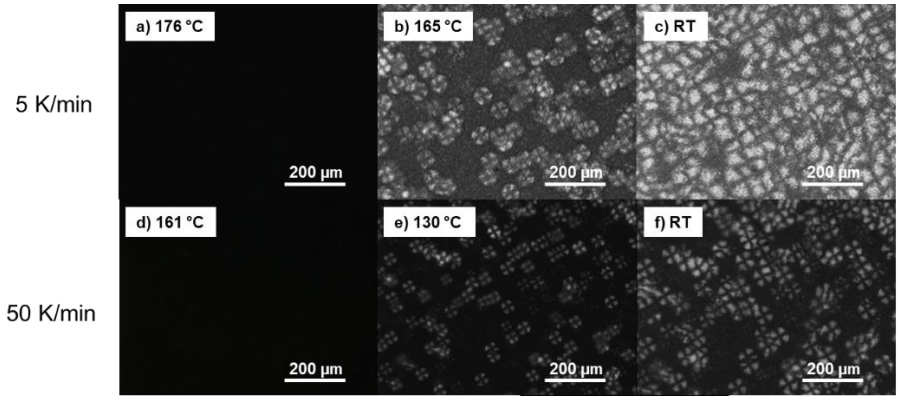


Figure 74. *Images of time-resolved POM of non-aged PCCD-PTHF during cooling at 5 (a,b,c) and 50 K/min (d,e,f), showing space-filling spherulites and sparsely*

distributed spherulites, respectively. The corresponding temperatures are indicated on the images.

As explained in Chapter 2 for crystallization during cooling at 10 K/min, the subsequent heating at the same rate in DSC is quite complex. A broad, low intensity endotherm at low temperatures indicates the gradual melting of the secondary crystals. At the highest temperatures a more outspoken, sharp endotherm is present, corresponding to the melting of the spherulite forming primary crystallites. The latter partially melt, recrystallize and remelt (MRR) as revealed by the bimodal character of the high temperature melting peak. This phenomenology is also observed during heating at 10 K/min after cooling at 5 or 20 K/min as illustrated in **Figure 72b**, although the main signal associated with the melting of secondary crystals shifts to lower temperatures with increasing preceding cooling rate (arrows in **Figure 72b**), likely indicating smaller or less perfect crystallites. Furthermore, MRR becomes more pronounced for higher preceding cooling rates, as the low temperature peak of the bimodal signal shifts to lower temperatures, away from the main melting signal at the highest temperature. The latter is primarily governed by the heating rate and remains relatively unchanged irrespective of the preceding cooling conditions. This trend is continued for heating after cooling at 50 K/min but in this case the melting peak associated with the melting of secondary crystallites is much reduced. In fact, for cooling at this rate, the separation between primary and secondary crystallization likely is not applicable for matter that crystallized under the homogeneous nucleation regime. Such crystallites are triggered over the entire remaining volume without much growth or segregation of PTHF rich segments. Therefore, these crystallites are likely very defective and small and prone to early melting and recrystallization upon heating. Consequently, their melting signal is significantly annihilated by exothermic recrystallization heat, which could explain why their low temperature melting is not reflected in a clear low temperature endotherm. Recrystallized material may contribute to the high temperature peak due to the melting of primary crystallites from the spherulitic fraction.

The changeover to the homogeneous nucleation regime and the creation of more defective crystallites in PCCD-PTHF for cooling at 50 K/min is also reflected in a lower material crystallinity. The quality of the heating runs of **Figure 72b**

permitted calculating the temperature dependent crystallinity according to procedures outlined in Chapter 2 and is depicted in **Figure 75a**. To attain these crystallinity values, the endothermic DSC signals from **Figure 72b** were integrated using the plotted baselines, determined via extrapolation from the melt. From the integrated enthalpies, the mass fraction crystallinities $w_C(T)_{PCCD}$ were calculated using the reference enthalpy $\Delta h_{ref}(T)_{PCCD}$ derived in Chapter 2 (see equation 20). The crystallinity at room temperature in this graph is the crystallinity reached after cooling and is very comparable after cooling at 5, 10, and 20 K/min. Only cooling at 50 K/min yields a noticeably lower $w_C(T)$, very likely due to the changeover to the homogeneous nucleation regime as explained above.

The crystallization behavior of Amphora SP1621**Figure 72c** depends less on the cooling rate compared to PCCD-PTHF, and so does the ensuing melting behavior (**Figure 72d**) and crystallinity (**Figure 75b**). No signs of homogeneous nucleation can be detected because of a highly efficient heterogeneous nucleation, which ensures that crystallization remains above the temperature at which the nucleation mechanism switches. Irrespective of the cooling rate, the main characteristics of the thermal behavior of Amphora SP1621 can be understood in terms primary and secondary crystallization and a reversed process upon heating with some MRR at the highest temperatures. As the ultimate melting point of Amphora SP1621 is similar to that of PCCD-PTHF, it appears that the crystals with the highest stability in both cases have a similar size and perfection.

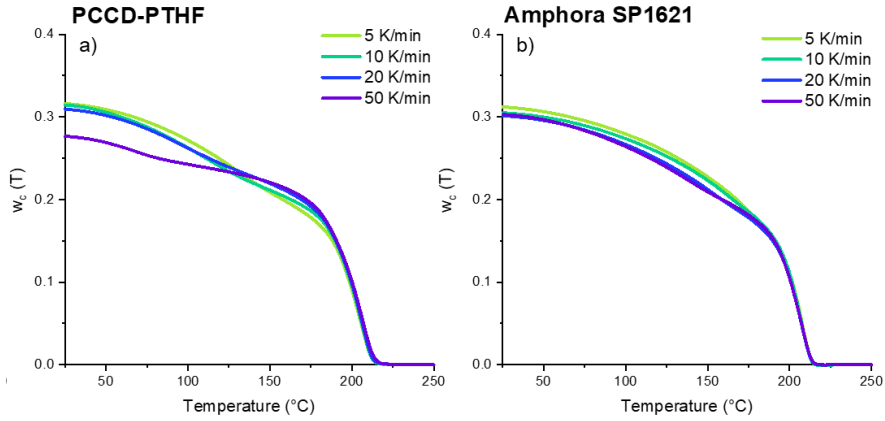


Figure 75. *w_c (T) as a function of temperature during heating at 10 K/min after cooling at the indicated rates for a) non-aged PCCD-PTHF and b) Amphora SP1621.*

To investigate potential differences in semi-crystalline morphology, room temperature SAXS/WAXS measurements were conducted on both PCCD-PTHF and Amphora SP1621 after cooling at the different rates (**Figure 76**). The main features of the WAXS patterns (right panel) of Amphora SP1621 resemble those of PCCD-PTHF, having reflections due to PCCD crystallites for which Miller indices were proposed in Chapter 2. However, the WAXS reflections are narrower and more well-defined for Amphora SP1621, indicating more ordered crystals, likely because of being formed at higher temperature. For both materials, it holds that the WAXS reflections become broader as the cooling rate increases, indicating less crystalline order.

On top of that, the position of the 100 reflection shifts to lower q-values as the cooling rate increases. This effect is less pronounced for Amphora SP1621. In Chapter 2 it was found through temperature dependent WAXS measurements that higher temperatures also induced such a downward shift. This shift was associated with a thermal expansion effect. However, as this shift is also seen at room temperature for more rapidly cooled samples, it seems that the expansion (and specifically that of the crystal a-dimension) is not determined solely by the temperature. The lack of unit cell contraction upon rapid cooling suggests that the initially formed, more open crystals do not fully succeed to rearrange and densify

upon cooling and that their initial structure is preserved down to room temperature. This trapping may result from the lack of disentangling and hard segment segregation when the cooling rate is high and crystallization is conducted at higher supercooling. The mentioned downward 100 peak shift is most pronounced for PCCD-PTHF cooled at 50 K/min for which crystallization predominantly is realized via homogeneous nucleation. Amphora SP1621 shows a reduced cooling rate dependency of the densification compared to PCCD-PTHF because heterogeneous crystal nucleation is induced at higher temperatures where chain reshuffling at crystallization is more efficient.

The suggested lack of chain reshuffling and crystallization-induced segment segregation is supported by the SAXS peak position (**Figure 76**, left panel), which shift to higher q-values for PCCD-PTHF when higher cooling rates were used. This indicates segregation on a smaller length scale and potentially also smaller crystallites. Unfortunately, it was not possible to verify this presumed crystal size reduction because accurately calculating the crystal thickness, l_c, from the 001 WAXS reflection via the Scherrer equation (as in Chapter 2) was not possible due to the low signal-to-noise ratio of the WAXS data.

The maxima of the SAXS peaks of Amphora SP1621 occur at high q-values outside the experimental window, except for the sample cooled at 50 K/min. Assuming a similar lamellar morphology as for PCCD-PTHF, this may indicate segment segregation at larger length scale and potentially thicker lamellae, which again could not be verified via the 001 WAXS reflection. Although the SAXS peaks fall outside the observation window, **Figure 76** still suggests that the SAXS peak position of Amphora SP1621 also shifts to higher q-values when higher cooling rates are used. In fact, the SAXS peak after cooling at 50 K/min is detected and approaches the position of the SAXS peak for PCCD-PTHF after cooling at 5 K/min. This similarity suggests that the segment segregation is governed by the crystallization temperature because **Figure 72** reveals that cooling Amphora SP1621 at 50 K/min leads to a crystallization maximum at approximately the same temperature as for PCCD-PTHF cooled at 5 K/min.

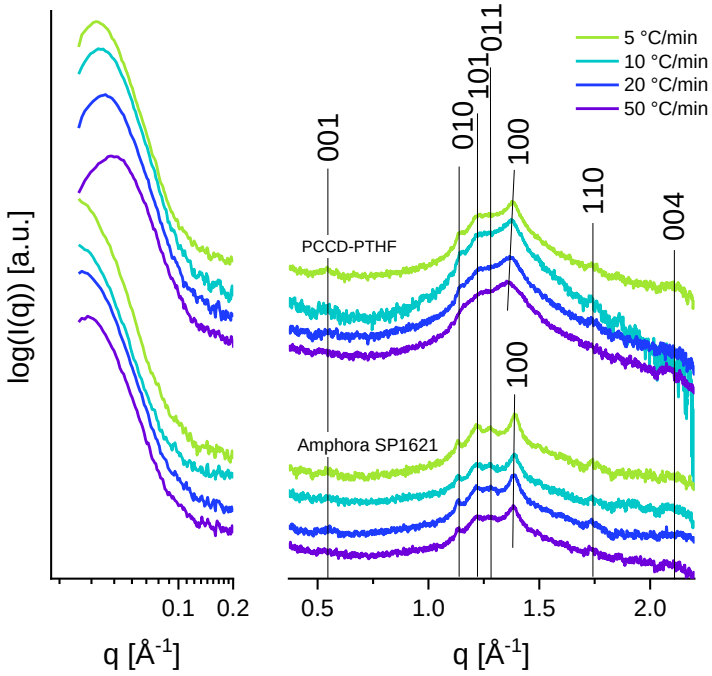


Figure 76. *SAXS/WAXS of non-aged PCCD-PTHF and Amphora SP1621 at RT after cooling at 5, 10, 20 and 50 K/min. The reflections determined in Chapter 2 are indicated.*

To validate the above hypotheses, additional quantitative structural data are required. This can be obtained through temperature-resolved synchrotron SAXS/WAXS experiments. SAXS data enable the calculation of interface distribution and correlation functions, allowing the extraction of parameters such as layer thicknesses and SAXS-based crystallinity. Furthermore, by analyzing WAXS patterns using an appropriate amorphous reference, the absolute mass fraction crystallinity can be determined. A well-resolved 001 reflection may also allow for estimation of the crystal thickness using the Scherrer equation.

5.3.2 FSC: extending the cooling rate range up to amorphization

To further investigate the effect of rapid solidification, cooling rate experiments beyond the limits of conventional DSC were conducted. This section presents the results obtained at higher cooling rates, enabling a deeper understanding of crystallization behavior under more extreme processing conditions. The remark should be made that the FSC experiments were performed on a single chip for each material, and therefore on the same sample.

PCCD-PTHF and Amphora SP1621 were cooled up until 500 K/s. The subsequent melting curves were used exclusively, as cooling signals lacked sufficient resolution. This limitation is consistent with the known issue that, at low FSC cooling rates (<10–100 K/s), the signal-to-noise ratio is too low to reliably capture crystallization behavior during cooling.[42] The heating curves of PCCD-PTHF and Amphora SP1621, following cooling at the specified rates, are shown in **Figure 77**. Similar to the DSC-based analysis, it is assumed that the mass fraction crystallinity after cooling is proportional to the latent heat measured in the subsequent heating curve. The melting peaks of PCCD-PTHF at the lowest rates, equivalent to the 10, 20 and 50 K/min DSC cooling rates in **Figure 72a,b**, are very broad since they show less MRR compared to the DSC curve due to the higher scanning rate. The MRR is not completely suppressed at 1000 K/S, similarly to what was seen for aged PCCD-PTHF in Chapter 4 after isothermal crystallization (**Figure 65a**).

The T_m's of the FSC melting peaks are considered realistic, when taking into account that higher heating rates can result in higher T_m.

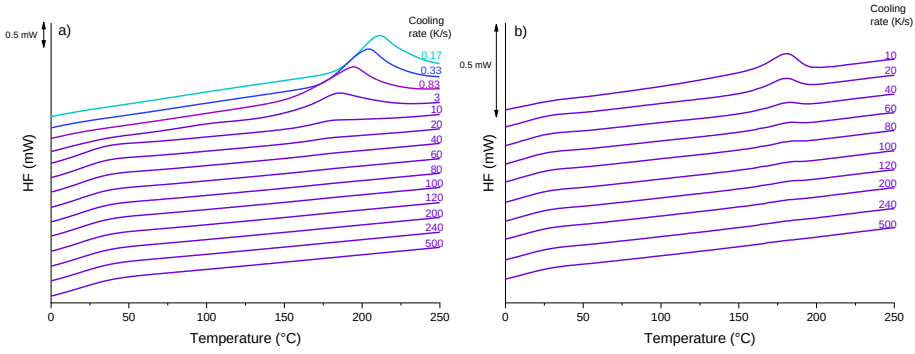


Figure 77. *The HF heating 1000 K/s curves (exo down) at 1000 K/s of a)* ***non-aged PCCD-PTHF*** *and b)* ***Amphora SP1621*** *after crystallization upon cooling at the*

indicated rates. For both materials, the melting peak decreases in size and shifts to lower temperatures with increasing cooling rate.

Extending the cooling rates to higher rates, shows a logic continuation to the DSC rates for PCCD-PTHF (**Figure 77a**) and Amphora SP1621 (**Figure 77b**). In both materials, the cooling rate influences the melting peak size, position and shape. Low cooling rates yield sharper, high-temperature melting peaks, indicating a high crystallinity and well-formed crystals. Intermediate rates result in broader, lower-temperature peaks, reflecting a broader crystal size distribution and/or MRR, and reduced crystal stability. High rates show no melting peaks, implying full amorphization. Amorphization thresholds are 40 K/s for PCCD-PTHF and 500 K/s for Amphora SP1621—consistent with the idea that Amphora SP1621 has much faster crystallization kinetics than PCCD-PTHF. The melting peaks of Amphora SP1621, appear at the same temperatures and only decrease in intensity.

In addition, the T_g steps of PCCD-PTHF and Amphora SP1621 shift to higher temperatures with increasing cooling rates, a change attributed to the larger fraction of non-crystallized PCCD in the amorphous phase, as shown in Chapter 2. Chapter 2 confirms that the PCCD and PTHF blocks form a homogeneous melt, evidenced again here by the presence of a single T_g step. After cooling at the lowest rates, it manifests as a very broad (almost not visible) step, likely because of a spread in chemical composition of the amorphous fraction after partial crystallization. The T_g of amorphous PCCD-PTHF and Amphora SP1621 are similar, suggesting a similar composition of PCCD and PTHF blocks.

5.4 Conclusions

This chapter addressed two key objectives: (i) to investigate the non-isothermal crystallization behavior of PCCD-PTHF with a focus on the effect of cooling rate on crystallization kinetics and morphology, and (ii) to characterize the crystallization behavior of Amphora SP1621 and compare it directly to PCCD-PTHF, providing a first insight into its structure–processing relationships.

Amphora SP1621 was found to crystallize more readily than PCCD-PTHF due to highly efficient heterogeneous primary nucleation. In contrast, PCCD-PTHF crystallizes through homogeneous nucleation below ~80 °C and heterogeneous nucleation above this temperature. Rapid cooling or ageing shifts its crystallization predominantly into the homogeneous regime, resulting in smaller, fewer, and non-space-filling spherulites. The MRR was more pronounced at higher cooling rates, reflecting the formation of smaller, less stable crystals, and translating into a reduced crystalline mass fraction. Amphora SP1621 showed little sensitivity to cooling rate because of its effective heterogeneous nucleation, though it also exhibited MRR. Ultimately, both polymers formed stable crystals of similar size and perfection.

The results also suggest that the a-dimension expansion depends not only on temperature but also on cooling rate. At high cooling rates, PCCD-PTHF tends to form open crystals via homogeneous nucleation that cannot densify efficiently, making it highly cooling-rate dependent. In contrast, Amphora SP1621 crystallizes predominantly via heterogeneous nucleation, reducing its sensitivity to cooling rate. PCCD-PTHF, is dependent on segmental segregation between PCCD and PTHF blocks, which in turn depends on T_c.

Together, these findings provide a deeper understanding of the crystallization kinetics and morphology of both PCCD-PTHF and Amphora SP1621 under non-isothermal conditions. By identifying the influence of cooling rate on nucleation mechanisms and structural order, this study establishes a solid foundation for further optimizing the processing conditions of Amphora SP1621 in selective laser sintering. In particular, the insights into its fast crystallization behavior and thermal response will be instrumental in tailoring print parameters for improved part quality and reliability.

Chapter 6

Physical Ageing of Glassy Amorphous PCCD and PS over a Wide Temperature Range far below T_g

Author contributions

Mouna Hamid: Conceptualization, Investigation, Methodology, Formal analysis, Writing – original draft. **Bart Goderis**: Supervision, Conceptualization, Methodology, Writing – review and editing.

6.1 Introduction

Just like printing crystalline materials, printing amorphous materials presents their own set of challenges. The bed temperature is typically chosen just below the glass transition temperature (T_g) for optimal sintering. However, this temperature range is also where physical ageing is most pronounced.[23] As explained in Chapter 1, physical ageing is a segmental relaxation process that leads to increased brittleness of the material. Prolonged exposure to these temperatures can therefore negatively impact the final product's quality.

This chapter discusses an ageing study conducted on glassy, amorphous poly(1,4-cyclohexanedimethyl-1,4-cyclohexanedicarboxylate) (PCCD), low-M_n polystyrene (PS), high-M_n PS and intermediate-M_n PS with a higher dispersity Đ than the low- and high- M_n PS. Although these samples were not intended for printing, the observed behaviors, particularly in PCCD, offer valuable insights into the relaxation process, a phenomenon that remains extensively studied but still not fully understood. For an introduction to relaxation mechanisms, readers are referred to Section 1.3. The concepts of physical ageing and T_g have been studied for decades, yet many questions remain unresolved. An extensive review on the matter was done by McKenna and Simon (2017) on the matter.[34] Disagreements still exist regarding 1) the underlying molecular dynamics of relaxation below T_g and structural recovery during heating, 2) the relationship to T_g and 3) the so-called "deviations" observed in the relaxation intrinsic isotherms (Chapter 1).

The first two issues are only briefly addressed in this chapter, as an in-depth exploration is beyond the scope of this thesis. The third point, however, is critical for interpreting relaxation intrinsic isotherms and is therefore discussed in more detail through a literature overview in Section 6.2, with particular focus on polystyrene (PS).

Important to note is that the term “relaxation” and “ageing” are used interchangeably throughout this chapter.

To the best of our knowledge, no relaxation study has previously been performed on amorphous PCCD. A related study on the polyether poly(1-4 cyclohexane di-methanol) (PCDM), which also contains 1,4-cyclohexane units, explored ageing at a wide temperature range below T_g (10 to 50 °C below T_g).[53] That study found maximum ageing rates at about 20 °C below T_g, which is typical for many polymers. Interestingly, a second, faster mechanism than the main α-relaxation was detected at low temperatures. The authors deduced this from the much shorter relaxation times than expected from α-relaxation alone—claiming this to be the first observation of such intermediate plateaus in a bulk sample.

The **PCCD** sample used here has a low M_n (3,053 g/mol), and a **PS** sample with a similar M_n (2,850 g/mol) was included for comparison. To our knowledge, no prior relaxation studies have examined PS of such a low M_n over a broad range of temperatures. A prior study used PS of M_n = 6,796 g/mol with DSC[112] but this method could not access temperatures far below T_g. Even so, that work also proposed the involvement of an additional relaxation mechanism beyond α-relaxation.

In the current study, a **high-M_n PS** sample (117,600 g/mol) was also included to study the influence of molecular weight on relaxation intrinsic isotherms, by comparing it to the low-M_n PS. As higher-M_n polymers generally have less free volume due to a lower number of end groups, relaxation tends to be reduced, according to the Free Volume theory (Chapter 1). However, the number of entanglements also plays a significant role. Rosa et al. (2016) investigated two PS samples (212,000 and 2,000,000 g/mol) with M_w*’s* far above the entanglement molecular weight (M_e) (14,000 - 18,000 g/mol[113]) and found similar intrinsic isotherms, suggesting that further M_w increases had little additional effect.[114] This is in agreement with the work of Andreozzi et al. (2005) on a series of poly(methyl methacrylates) (PMMA) samples with molar weights under and above M_e, where they suggested that the influence of M_w levels off above M_e.[115] The same observation was done by Boucher et al. (2011) on two PS samples with M_n of 6,796 g/mol and 83,333 g/mol.[112] Interestingly, both studies suggest that low M_n samples show a weaker temperature-dependence of the relaxation times when deviating from the VFT

behavior (Chapter 1), which means that ageing is a somewhat slower than their high molecular weight counterparts.

In the current study, low-M_n PS and high-M_n PS represent two extremes: low-M_n PS ($M_n << M_e$), which is unlikely to form entanglements and high-M_n PS ($M_n >> M_e$), far above M_e, represents an entangled system. The effect of entanglements is not eluded yet but is probably having a direct or indirect influence even if relaxation occurs at the segmental, much smaller scale.

Finally, a **PS grade Dynoseeds T20** with an intermediate M_n of 44,229 g/mol and a Đ higher than the other PS sample was analyzed. The material was in the form of microbeads with a size of 20 µm, but they were considered as bulk material (the relaxation mechanism occurs at much smaller scale) and therefore most probably are not showing confinement effects. Because of the difference in M_n between the Dynoseeds and the other two PS samples, the study did not aim to investigate the influence of Đ in depth, but rather to assess whether it could play a role. Although this powder grade was not sold as a sintering powder, it has been printed by Strobbe et al. (2017) and different printing parameters were tested and assessed through mechanical property experiments.[116] Investing and mapping out the physical ageing under different conditions, could help understand and estimate the properties of the final product when the same conditions are used for printing. To our knowledge, this sample has not previously been studied in the context of ageing.

Thus, a systematic relaxation study was conducted on these four samples across a wide temperature range—extending to about 50 °C below T_g using Fast Scanning Calorimetry (FSC), which enabled access to these temperatures without inducing ageing during cooling. Since ageing can also occur upon cooling, additional non-isothermal ageing experiments were carried out on PCCD, PS3, and PS118 across a broad range of rates from 0.1 to 30,000 K/s.

6.2 Background

In Chapter 1, the concept of physical ageing was introduced and discussed. In this section, additional information is provided that is crucial for the discussion of

the results. **Figure 78** illustrates the evolution of the system upon (a) isothermal and (b) non-isothermal ageing in terms of enthalpy of the system. It shows the enthalpy evolution during heating via devitrification from the glassy to the melt state, after isothermal ageing was allowed (red) or not (purple). After an ageing experiment, the devitrification occurs with enthalpy recovery (overshoot peak) to destroy the segmental rearrangement achieved during ageing. The corresponding devitrification temperature is the fictive temperature T_f and was defined as the intersection point of two quadratic fits: one describing the high-temperature (melt) regime and the other the low-temperature (glassy) regime of the enthalpy curve. T_g is defined here as the T_f when no ageing occurred.

A sample is said to be 'fully aged' when it has reached equilibrium, i.e. when $H_a = H_{eq}$ or $T_f = T_a$. In terms of enthalpy, the maximum extent of ageing is therefore $H_{a0} - H_{eq}$. Also,

the **degree of ageing (Jg^{-1})** after a certain ageing time t_a is

$$\frac{(H_a - H_{eq})}{(H_{a0} - H_{eq})} * 100\ \% \tag{40}$$

the **ageing rate ($Jg^{-1}s^{-1}$)** is

$$\frac{1}{\tau} \tag{41}$$

with **τ (s) the relaxation time**. In this thesis the term "relaxation time" should be understood as a *characteristic timescale* of a broad distribution of relaxation processes rather than a finite time or τ_{KWW} (Chapter 1). τ depends on the induction time, relaxation kinetics and the maximum extent of relaxation $H_{a0} - H_{eq}$.

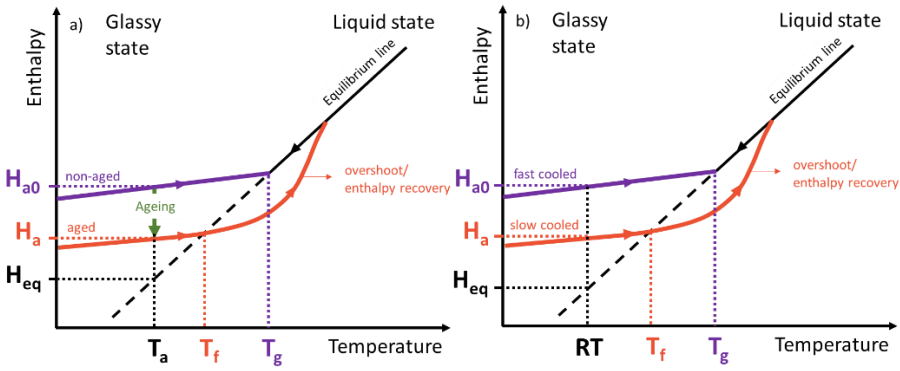


Figure 78. *Illustration of the evolution of enthalpy upon devitrification after a) isothermal and b) non-isothermal ageing. With increasing ageing, the enthalpy decreases as well as the devitrification temperature represented by the fictive temperature T_f. Further details can be found in the text and in Chapter 1.*

Polystyrene (PS) is the most extensively studied amorphous material in physical ageing research. For example, isothermal relaxation intrinsic isotherms have been reported for high-M_n PS (≥ 400,000 g/mol, Đ ~ 1) using FSC.[54,117–123]
Two types of "deviations" in the ageing intrinsic isotherms mentioned in the *Introduction* persist as:

1) The inability to reach H_{eq} after full relaxation, and
2) The occurrence of a two-step recovery process, suggesting a multi-step ageing process.

Cowie and co-workers were among the first to suggest that equilibrium is not always reached after apparent full relaxation.[124–126] However, they were criticized for not accounting for the non-linearity of structural recovery which may have led to an overestimation of the degree of ageing and neglecting of the breadth of the glass transition.[127,128] Other studies also revealed non-equilibrium behavior in PS (M_n = 83,333 g/mol, Đ = 1.02 and M_n = 6,796 g/mol, Đ = 1.03),[112] GeSe glasses[129] and poly poly(methylmethacrylate).[130] In the latter, Cangialosi and co-workers (2011) originally supported the idea that equilibrium was not achieved, but later revised that

this was an intermediate plateau and proposed a **two-step recovery** for PS and polycarbonate with different molecular weights.[131]

It is now widely discussed that physical ageing and/or structural recovery proceed through a more complex mechanism—or a combination of mechanisms, rather than a single, continuous α-relaxation, particularly at temperatures well below T_g. The concept of a multi-step relaxation process challenges traditional theories, including Kovacs' monotonic recovery based on dilatometric studies which typically assume a single mechanism.[132]

Simon and co-workers, however, rejected the idea of an intermediate plateau based on their 2013 study, which showed that PS (M_n = 92,800 g/mol, Đ = 2.38) could reach equilibrium when relaxed at T_g – 15°C.[133]

At the time, experimental limitations hindered the investigation of relaxation at temperatures well below T_g, as slow kinetics made measurements difficult. Also, insufficient cooling rates made it hard to isolate initial relaxation effects. To overcome this, researchers started to use **nanoconfined samples** (e.g., films or nanospheres) to accelerate relaxation, combined with FSC for fast cooling. Cangialosi and co-workers demonstrated that relaxation could be accelerated this way.[134,135] They observed intermediate plateaus, which they attributed to multiple relaxation mechanisms.[54,136] Meanwhile, Simon's group also studied PS (ultra)thin films with FSC7.[119–122] They found no visible plateau in the range between T_g and T_g - 50 °C, though this was challenged due to the shorter timeframes compared to Cangialosi's work.

Ngai and co-workers [137] supported the two-step recovery hypothesis using the Coupling Model (CM), which proposes that structural recovery consists of an α-relaxation followed by sub-Rouse processes. Cangialosi *et al* (2011)[131] highlighted the similar temperature dependence of the relaxation time τ for both low- and high-M_n PS. More recently, Jin and McKenna (2022)[138] re-examined Cangialosi's intermediate plateau findings by comparing the data with VFT model predictions (Chapter 1), applying a temperature correction, and showed that the data align, suggesting that only primary α-relaxation occurs. They argued that the observed "deviations" could stem from experimental limitations, including frosting and water condensation during DSC experiments exceeding 24 hours, or temperature inhomogeneity in vacuum ovens during longer tests. Moreover, they stated that it is

unlikely that a secondary relaxation could occur near T_g – 17 °C for high-M_n PS or T_g – 10 °C for low M_n PS, as claimed by Cangialosi's group, citing that the first secondary relaxation (β-relaxation) for PS begins only around T_g – 45 °C (M_n = 211,000 g/mol, Đ = 1.98) based on dilatometry.[139] However, they did not address the two-step relaxation identified by Cangialosi's group using confined PS and FSC.[54]

Clearly, many questions remain open regarding relaxation in polystyrene and amorphous materials more broadly. This overview is intended to contextualize the discussion of the results and to demonstrate the complexity of the issue.

The aim of the current study is to report, understand and explain the differences and similarities in ageing behavior between the various materials, rather than investigate the relaxation processes and mechanisms in-depth. In that context, the main focus of this study is to map the ageing kinetics of poorly studied materials to broaden the knowledge on physical ageing. The influence of molecular structure (PCCD vs low-M_n PS), the M_n (low-M_n vs high-M_n PS) and Đ (high-M_n PS vs PS Dynoseeds) was studied.

6.3 Experimental section

6.3.1 Materials

The polymeric materials investigated were low-M_n PS (PS3) and high-M_n PS (PS118) from Agilent Technologies (Santa Clara, USA), PS Dynoseeds with a particle size of 20 µm (DTS20) from Microbeads AS (Norway), and amorphous PCCD (PCCD3) synthesized for this study. The synthesis procedure for PCCD3 followed the same protocol as for the semi-crystalline PCCD described in Chapter 3, except that the monomers had a different initial *trans* content: 22% for DMCD and 70% for CHDM. The resulting PCCD was amorphous, transparent, and brittle. The PS samples were supplied as white powders. **Table 2** summarizes the characteristics of all samples. M_n and Đ were provided for PS3 and PS118, while the remaining properties were determined as described in the next section.

Table 2. *M_n, Đ, glass transition temperature (T_g), glass transition temperature upon heating (T_{gh}) and glass transition temperature upon heating (T_{gc}) values of the different samples.*

	M_n (g/mol)	Đ	T_g (°C)	T_{gh} (°C)	T_{gc} (°C)
PS3	2,850	1.04	73.7	71.4	69.2
PS118	117,600	1.06	123.3	101.4	98.2
DTS20	44,229	2.57	116.5	98.8	95.3
PCCD3	3,053	/	37.4	23.0	18.5

6.3.2 Methods

^{1}H Nuclear Magnetic Resonance (NMR) Spectroscopy

A RT experiment on PCCD3 was performed with a Bruker Avance III HD 400 MHz Spectrometer. The sample of approximately 5 mg was dissolved in deuterated (99.9 %) chloroform and complemented with 0.1 (v/v)% tetramethylsilane (TMS) as reference. The data were analyzed using the Topsin 4.0 software. The spectrum is shown in **Figure 79**. The cyclohexane moieties can have a *cis* (c) or *trans* (t) configuration. The corresponding proton signals are labeled H_{1c} and H_{1t} for D, and H_{3c} and H_{3t} for C. The D and C *trans* contents are 25% and 71% respectively. The M_n was estimated to be 3,053 g/mol. This value was derived from the integration of the methyl ester end-group signal, using the equation: $M_n = M_{unit} * \frac{3}{2} * \frac{[H_{1c}]+[H_{1t}]}{[-OCH_3]} = 3{,}053\ g/mol$.

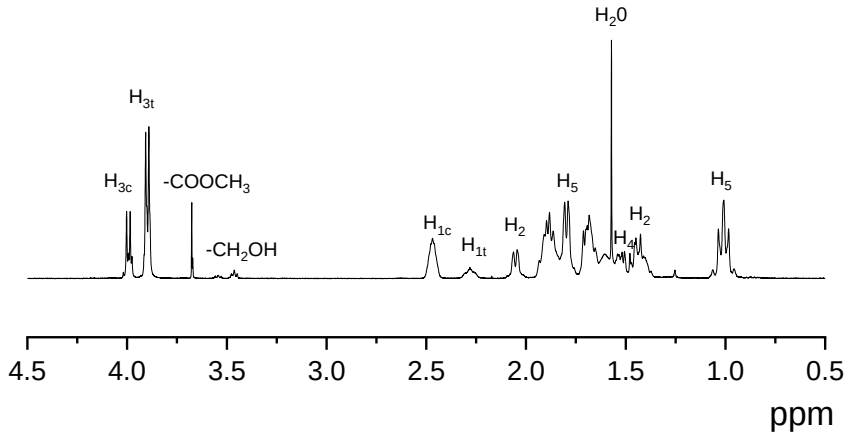


Figure 79. *^{1}H NMR of PCCD3 with the identified peaks (chemical shift, relative peak area) corresponding to H_{3c} (3.99 ppm, 3.96), H_{3t} (3.90 ppm, 9.45), -$COOCH_3$ (3.67 ppm, 1.00), H_{1c} (2.47 ppm, 5.44), H_{1t} (2.28 ppm, 1.83), H_2 (2.05 ppm, 3.64) and H_5 (10.45 ppm, 0.60).*

Gel Permeation Chromatography (GPC)

A measurement on DTS20 was performed using a Shimadzu LC20 system (Shimadzu, Japan) equipped with PLgel 5 μm MIXED-C column, an LC-20AT pump, a CBM-20A controller, and both SPD-20A and RID-20A detectors. Tetrahydrofuran (THF) was used as the mobile phase. The system was calibrated with polystyrene standards dissolved in THF. Before analysis, the sample was completely dissolved in THF at a concentration of approximately 1 mg/mL and filtered through a 0.2 μm pore size filter. The resulting M_n and Đ are given in Table 2.

Differential Scanning Calorimetry (DSC)

The same apparatus was used as described in Chapter 2. For this study, a typical heating-cooling-heating DSC experiment (**Figure 80**) was performed on all samples to determine the glass transition temperature upon cooling (T_{gc}) and heating (T_{gh}) at 10 K/min (Table 2). The maximum temperature of 190 °C is under the degradation temperatures of the samples (see TGA experiment in Chapter 4 for PCCD3). The samples were measured in open Tzero aluminum pans without lid under a constant nitrogen flow of 50 mL/min.

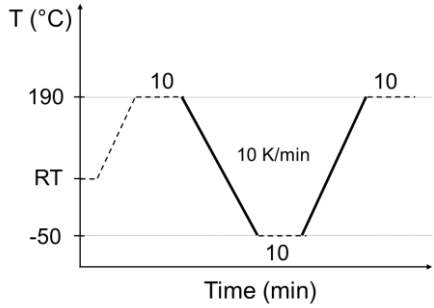


Figure 80. *DSC profile for the determination of T_{gc} and T_{gh} of PS3, PS118, DTS20 and PCCD3.*

Fast-Scanning Calorimetry (FSC)

The same apparatus was used as described in Chapter 2. Prior to sample deposition, the Multistar UFS1 chips were conditioned and temperature-corrected.[42] **Figure 81** shows the thermal protocols used for the isothermal (a and b) and non-isothermal (c) ageing experiments. The isothermal experiments were up-jump, where the ageing temperature T_a was reached from the glassy, quenched state (**Figure 81a**) or down-jump, where the T_a was reached from the melt state (**Figure 81b**).

The maximum temperature T_{max}, the ageing temperatures T_a, the ageing times t_a and the cooling rates β for each sample and each protocol in **Figure 81** are given in Table 3-4.

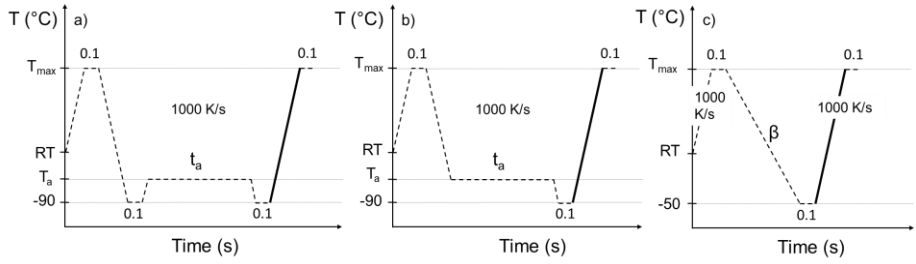


Figure 81. *Thermal protocols of a) the isothermal up-jump b) the isothermal down-jump and c) the non-isothermal experiments. The T_a and t_a are the ageing temperature and time, respectively, and β is the cooling rate. Except when marked with 'β', all the*

scanning rates were 1000 K/s. The bold segments were the heating curves used for analysis.

Table 3. *Parameter values from the experiment in* ***Figure 81****a.*

	T_{max} (°C)	T_a (°C) range	T_g - T_a (°C) range	t_a (s) range
PS3	190	23.4 – 73.5	50.3 – 0.2	0.001-10,000
PS118	190	72.5 – 117.5	50.8 – 5.8	0.001-10,000
DTS20	190	66.5 – 116.5	50 - 0	0.001-10,000
PCCD3	150	-20.6 – 29.4	58 - 8	0.001-10,000

Table 4. Parameter values from the experiment in ***Figure 81b****.*

	T_{max} (°C)	T_a (°C)	T_g - T_a (°C)	t_a (s)
PS3	190	68.5	5.2	0.001-10,000
PCCD3	150	4.4	33	0.001-10,000

Table 5. Parameter values from the experiment in ***Figure 81****c.*

	T_{max} (°C)	β (K/s)
PS3	195	0.1 – 30,000
PS118	195	0.1 – 30,000
PCCD3	195	1 – 30,000

After completing the experiments, the $c_p(T)$ curves were obtained from the heat flow (HF) heating scans by correcting for the heating rate and the sample mass. The $c_p(T)$ data were then fitted to the reference values by correcting them with a third-order polynomial function. For the non-aged $c_p(T)$ curve, the sample mass was also

included as a fitting parameter, but once determined, this mass was kept constant across all subsequent measurements performed on the same chip.

For PS, the reference values were taken from the ATHAS database.[68] In contrast, no reference $c_p(T)$ data were available for PCCD3, so a different approach was required. DSC measurements (protocol shown in **Figure 80**) were carried out on both PCCD3 and a reference PS sample. After correcting the HF signals for the empty pan, heating rate, and sample mass, the $c_p(T)$ of the PS sample was fitted to the ATHAS curve using a linear function, giving the calibration equation $-0.29 + 1.12 \cdot T$. This calibration was then applied to the PCCD3 DSC $c_p(T)$ data to obtain reference values for PCCD3. These corrected data were subsequently used to fit the PCCD3 FSC data, analogous to the procedure for PS, thereby yielding its absolute $c_p(T)$ values.

Finally, the **enthalpy values** were calculated by integrating the difference between:

- the ATHAS reference and the experimental data (for PS), or
- the PCCD3 reference curve and its experimental data,

and the H_{a0}, H_a and H_{eq} were determined as well as T_g and T_f.

6.4 Results and Discussion

6.4.1 Isothermal ageing of amorphous PCCD and PS

From the FSC heating scans after ageing (**Figure 81a**), the enthalpy recovery from the $c_p(T)$ curves of PCCD3, PS3, PS118 and DTS20 were calculated for all ageing temperatures and times listed in Table 3 and shown in **Figure 82-83**. The results are grouped per T_a, arranged from the lowest T_a (furthest from the T_g) to the highest T_a (closest to T_g). The reference curves used for fitting the FSC data are shown as black solid curves.

At all temperatures, longer ageing times lead to increased enthalpy recovery, reflected in larger overshoot peaks, since the samples had more time to evolve toward equilibrium and thereby increase the degree of ageing. For a given t_a, the ageing temperature determines how much ageing occurs within that time frame, and thus the size of the recovery peak. The enthalpy recovery at fixed t_a depends on both the ageing kinetics and the maximum enthalpy change H_{a0}-H_{eq}, both of which are strongly temperature dependent. At intermediate temperatures, ageing kinetics are fastest but the (H_{a0}-H_{eq}) remains relatively high, which explains why the recovery peak continues to increase even at the longest t_a. Near T_g, (H_{a0}-H_{eq}) is very small, so equilibrium is reached within the studied time periods, as indicated by the saturation of the recovery. At temperatures far below T_g, ageing is extremely slow, but (H_{a0}-H_{eq}) is large, meaning that equilibrium cannot be reached within the experimental window.

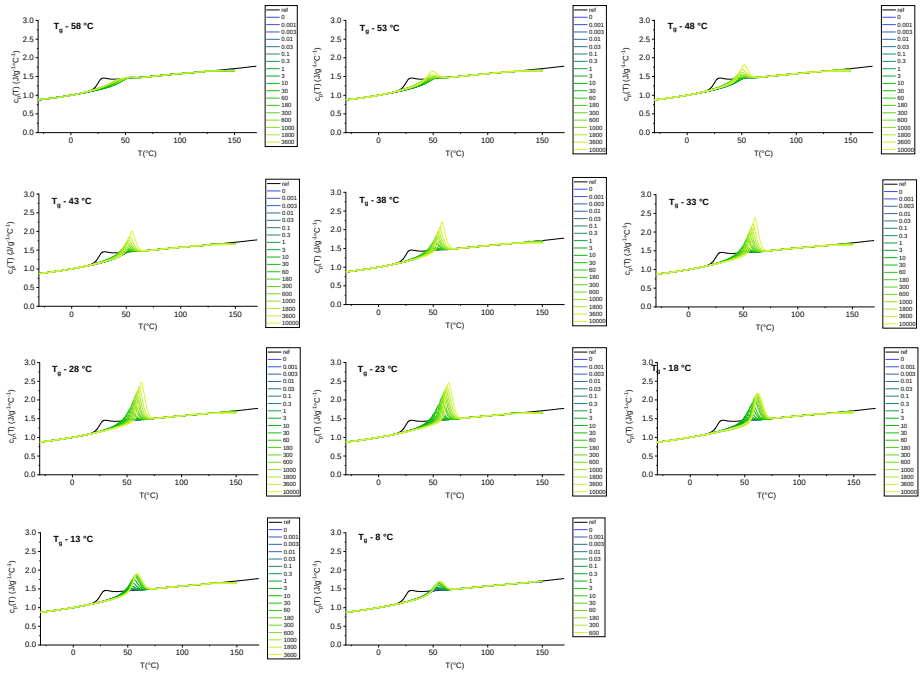


Figure 82. *c_p(T) heating curves of PCCD3 after ageing at indicated temperatures and for indicated time periods. The black lines are the reference c_p(T) values. The color scale progresses from dark to light with increasing time.*

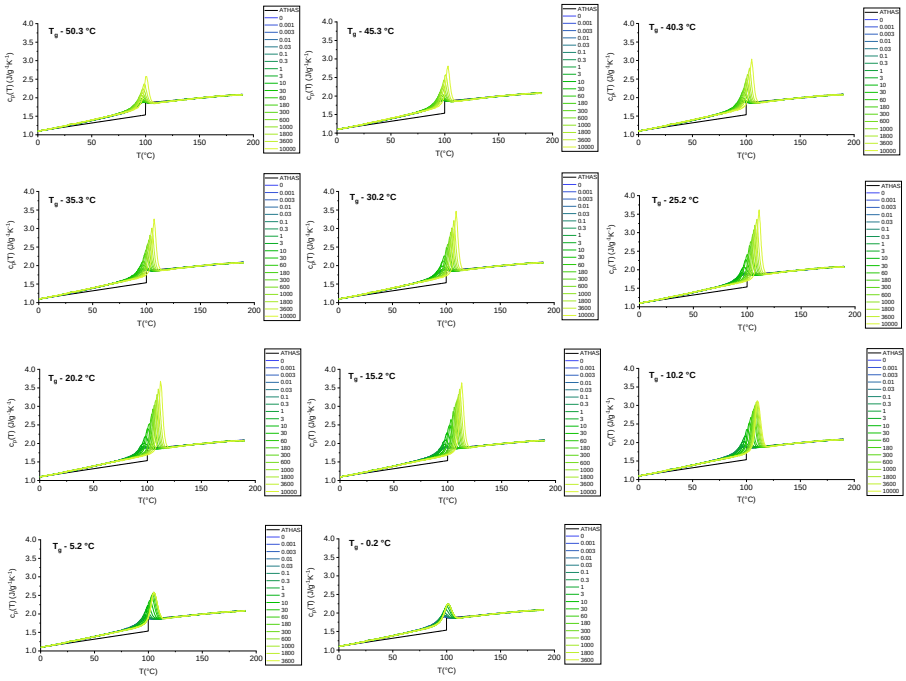


Figure 83. *c_p(T) heating curves of PS3 after ageing at indicated temperatures and for indicated time periods. The black curves are the ATHAS reference c_p(T) data. The color scale progresses from dark to light with increasing time.*

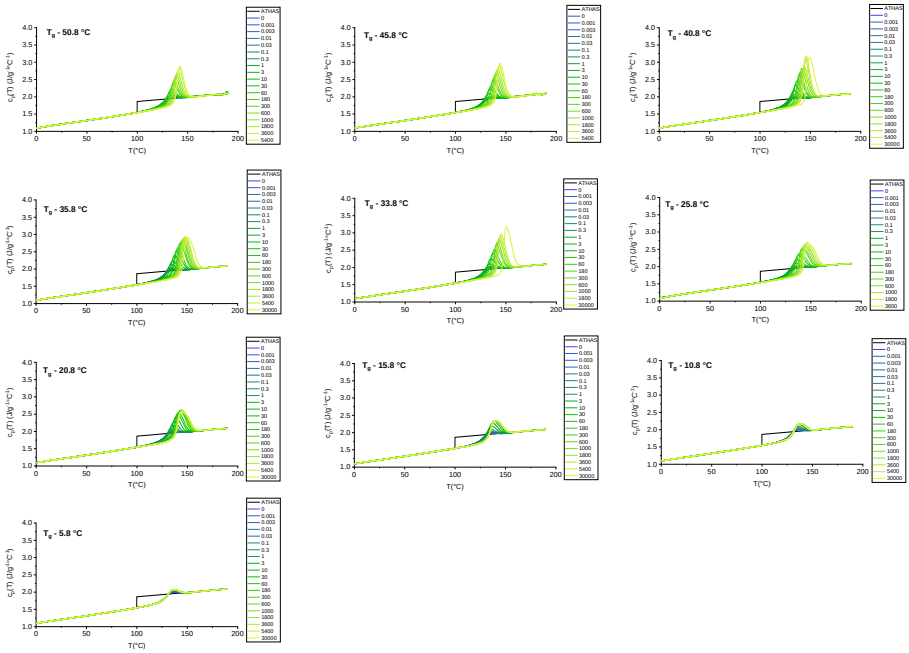


Figure 84. *$c_p(T)$ heating curves of PS118 after ageing at indicated temperatures and for indicated time periods. The black curves are the ATHAS reference $c_p(T)$ data. The color scale progresses from dark to light with increasing time.*

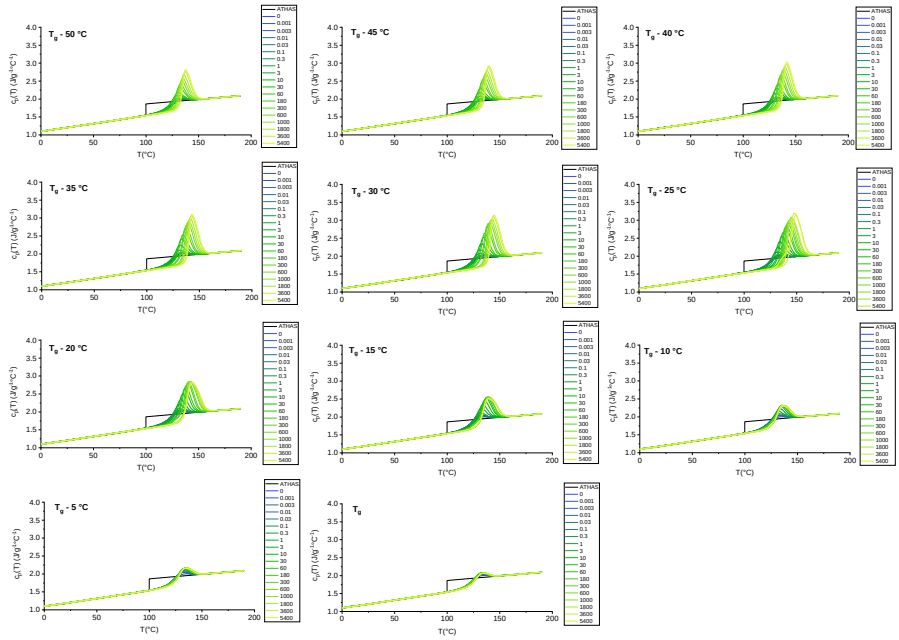


Figure 85. *$c_p(T)$ heating curves of DTS20 after ageing at indicated temperatures and for indicated time periods. The black curves are the ATHAS reference $c_p(T)$ data. The color scale progresses from dark to light with increasing time.*

To construct the so-called relaxation **intrinsic isotherms**, the $c_p(T)$ curves were integrated to obtain the enthalpy recovery after ageing (H_a) while the equilibrium enthalpy (H_{eq}) was estimated by extrapolating the equilibrium line (**Figure 78**). $H_a - H_{eq}$ was then plotted as a function of $\log(1/t_a)$ to generate the intrinsic isotherms (**Figure 86**). Although it is also possible to follow $T_f - T_a$ instead of $H_a - H_{eq}$, describing ageing relaxation in terms of enthalpy is advantageous for potential future work that aims to link thermal relaxation to mechanical properties, as enthalpy and mechanical parameters share more directly comparable units.[140]

Figure 86 presents the calculated relaxation intrinsic isotherms for PCCD3 and the PS samples, where ageing time increases from right to left on the log(1/t)-axis. During ageing, the value of $H_a - H_{eq}$ decreases toward zero, as the system approaches equilibrium. Thus, the maximum degree of ageing at a given T_a is achieved at $H_a - H_{eq} = 0\ Jg^{-1}$. All intrinsic isotherms begin with an initial plateau (right-hand side) during which no measurable relaxation occurs, corresponding to the

induction time. This induction time becomes noticeably longer at lower temperatures, reflecting the higher activation energies involved, as first described by Struik (1976)[24] and later confirmed for systems such as PS.[119] Following this induction period, ageing proceeds and $H_a - H_{eq}$ gradually decreases as the system relaxes toward equilibrium.

As anticipated from the $c_p(T)$ curves (**Figure 82-83**), complete ageing was only reached within the experimental timeframe at the highest temperatures, close to T_g. This is reflected in the appearance of a final plateau (**Figure 86**, left-hand side), where no further enthalpy recovery occurs.

At lower temperatures, however, the initial $H_a - H_{eq}$ values ($= H_{a0}$) were much higher, meaning the system is further from equilibrium. Consequently, a greater degree of ageing was theoretically possible, although equilibrium was not reached within the measurement window. Therefore, the relaxation time τ is said to be governed not only by the induction time and relaxation kinetics, but also by the magnitude of H_{a0}.

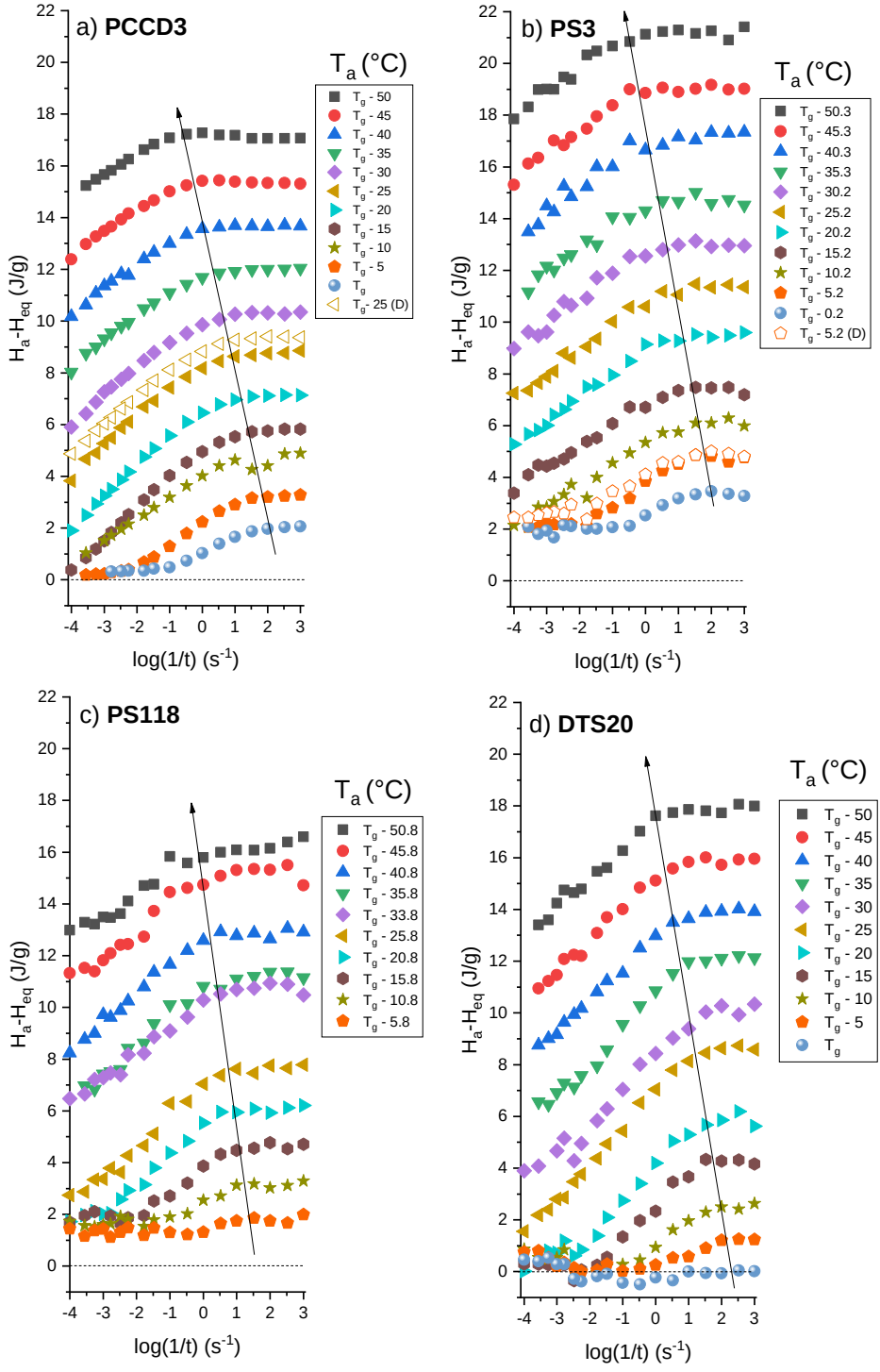

a) PCCD3
T_a (°C)
T_g - 50
T_g - 45
T_g - 40
T_g - 35
T_g - 30
T_g - 25
T_g - 20
T_g - 15
T_g - 10
T_g - 5
T_g
T_g - 25 (D)
H_a-H_{eq} (J/g)
log(1/t) (s^{-1})
b) PS3
T_a (°C)
T_g - 50.3
T_g - 45.3
T_g - 40.3
T_g - 35.3
T_g - 30.2
T_g - 25.2
T_g - 20.2
T_g - 15.2
T_g - 10.2
T_g - 5.2
T_g - 0.2
T_g - 5.2 (D)
H_a-H_{eq} (J/g)
log(1/t) (s^{-1})
c) PS118
T_a (°C)
T_g - 50.8
T_g - 45.8
T_g - 40.8
T_g - 35.8
T_g - 33.8
T_g - 25.8
T_g - 20.8
T_g - 15.8
T_g - 10.8
T_g - 5.8
H_a-H_{eq} (J/g)
log(1/t) (s^{-1})
d) DTS20
T_a (°C)
T_g - 50
T_g - 45
T_g - 40
T_g - 35
T_g - 30
T_g - 25
T_g - 20
T_g - 15
T_g - 10
T_g - 5
T_g
H_a-H_{eq} (J/g)
log(1/t) (s^{-1})

Figure 86. *Intrinsic isotherms of enthalpy recovery for PS3, PS118, PCCD3, and DTS20 at the indicated ageing temperatures (T_a). The data show the evolution from right to left upon ageing, with an initial plateau where no ageing occurs, followed by a decrease in enthalpy. The arrow indicates the evolution of the induction times, which become longer at lower temperatures. The dotted horizontal line represents the equilibrium value. Data marked with (D) correspond to down-jump experiments.*

Even though full relaxation was expected at temperatures close to T_g, neither PS3 nor PS118 reach the equilibrium enthalpy H_{eq} in that range. Instead, the enthalpy recovery curves level off at a value approximately 2 J/g above H_{eq}. In contrast, PCCD3 did not show this premature plateau, nor did PCDM.[53] This incomplete relaxation behavior has been reported in several previous studies, as discussed in Section 6.2. The central question is whether this plateau represents a true thermodynamic limit, or whether it results solely from kinetic constraints. Boucher *et al* (2011) observed a similar deviation in both high-M_n PS (M_n = 83,333 g/mol, Đ = 1.02) and low-M_n PS (M_n = 6,796 g/mol, Đ = 1.03).[112] In their work, the final enthalpy states after both up-jump and down-jump temperature profiles were identical, suggesting that the relaxation thermodynamic endpoint is path-independent. Based on this, they concluded that the observed plateau corresponded to a local thermodynamic minimum and they later proposed that such enthalpy plateaus might be related to distinct underlying relaxation mechanisms.[54] To examine this within the current study, a similar down-jump experiment was conducted on PS3 at T_g – 5.2 °C, following the thermal protocol illustrated in **Figure 81b**. The corresponding intrinsic isotherm is presented alongside the up-jump data in **Figure 86b**. While minor differences in the relaxation path were observed, both conditions converge to the same final enthalpy value H_a, thereby supporting the path-independence of the relaxation endpoint. The leveling-off observed during aging may be linked to limitations in chain mobility, which prevent the material from ever reaching a genuine equilibrium state. Several factors could play a role: subtle differences in the supercooled liquid structure or the emergence of locally aggregated domains. In the case of DTS20, the presence of shorter chains could enhance the mobility of longer ones by which a zero $H_a - H_{eq\text{-}value}$ is ultimately reached. In addition, variations such as heterogeneities or trace impurities in the commercial DTS20 sample cannot be ruled out. Pinpointing the exact cause of these sample-to-sample differences, as well as understanding why full equilibrium is never achieved in two of the three PS samples, remains a complex challenge. Over

the years, many theoretical models have been developed to address these issues, often revising or challenging the earliest views of physical aging and the glass transition. A detailed theoretical treatment lies beyond the scope of this thesis; however, the reader is referred to the review by McKenna and Simon (2017) for further information.[34]

Even though not all intrinsic isotherms reach equilibrium, they can still be used for further analysis. This is done by constructing master curves, which is a model-independent method. Master curves provide a robust and broadly applicable approach across a wider temperature range. To construct these, the intrinsic isotherms from **Figure 86** were shifted via time–temperature superposition (TTS). In this procedure, the curve at the highest temperature (closest to T_g) was kept fixed, while the other curves were shifted horizontally along the logarithmic time axis to achieve optimal overlap of the relaxation regions (excluding the initial induction and final plateau zones). The resulting master curves are shown in **Figure 87**.

An important remark must be made here. By applying TTS, all ageing curves are forced to share the same slope across temperatures. This implies that the relaxation kinetics follow Vogel–Fulcher–Tammann (VFT) behavior (kinetics neat T_g) and are therefore assumed to be temperature independent. However, this is not entirely valid. The intrinsic isotherms in **Figure 86** may in fact consist of two different slopes, though the experimental noise prevents a clear identification. Only the most prominent VFT regime could be isolated.

The slope of the master curves of PS (which is only meaningful for T_a close to T_g), appear very similar and independent of molecular weight. Indeed, ageing kinetics, governed by segmental mobility, are generally regarded as chain-length independent.[141] This was confirmed, for example, in linear PS with M_n ranging from 5,000 to 152,000 g/mol, where volume recovery experiments conducted at temperatures between $T_g - 5$ and $T_g - 50$ °C showed no significant molecular weight dependence. Again, this holds only for T_a values close to T_g.

In contrast, the master curves reveal differences in the maximum extent of ageing. For instance, at the lowest temperature, PS3 is much further from equilibrium (larger $H_a - H_{eq}$) than PS118. This likely originates from the higher free volume in PS3 due to its greater number of chain ends, resulting in a larger volume reduction required during ageing to reach equilibrium.

For PCCD3, however, a single master curve could not be constructed because two distinct slopes were clearly distinguished (**Figure 87a**). Close to T_g, only one regime (slope 1) was observed, corresponding to the slower α-relaxation that follows VFT behavior. Ageing curves transitioned from slope 1 to a steeper slope 2, indicating that the temperature dependency of ageing kinetics changes. The transition became increasingly distinct at lower temperatures, whereas at intermediate temperatures it was more gradual. This suggests the emergence of an additional, faster relaxation mechanism at low T_a. For PCDM, it was previously proposed that below T_g – 22 °C, the dominant α-relaxation was followed by a faster process, shifting from super-Arrhenius to more Arrhenius-like kinetics.[53] A similar scenario is likely for PCCD3. Because these underlying mechanisms do not scale uniformly with temperature, strict TTS could not be applied to the PCCD3 intrinsic isotherms.

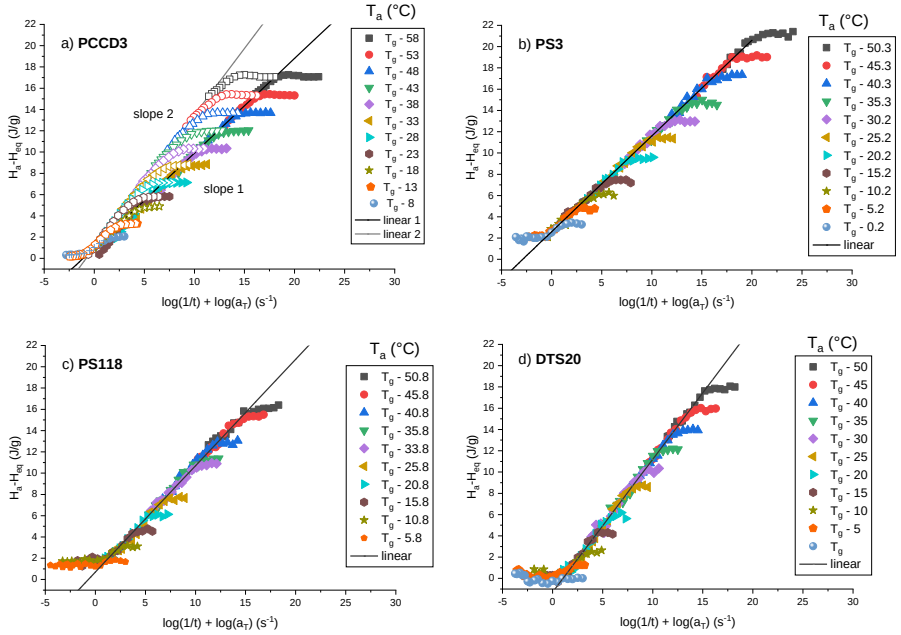


***Figure 87**. Master curves of PS3, PS118, PCCD3 and DTS20 resulted from the time-temperature shift of the intrinsic isotherms in **Figure 86**. Straight lines are drawn through the master curves as guidance for the eyes.*

As mentioned, the master curves of PS seem to suggest the α-relaxation mechanism as single mechanism and at all temperatures. To study this, the shift

factors resulting from the TTS were extracted and plotted as a function of $1000/T_a$ for PS3, PS118 and DTS20 (**Figure 88b-d**). Since these shift factors are primarily determined by the height and duration of the initial plateau—that is, by the initial enthalpy and the induction time, it can be interpreted as a relative measure of the relaxation time τ. Thus, the data in **Figure 88b-d** represent the temperature dependence of τ. The data is compared to an estimation of the VFT behavior, which was calculated from an adaptation of equation 2:[30–32]

$$log a_T \sim \frac{1}{(T_a - T_0)} \tag{42}$$

with T_0 as the Vogel temperature and a_T the shift factor. For the three PS samples, the two data points at T_a closest to T_g (left-hand side) were used for the fitting. The T_0 values for PS3, PS118 and DTS were 302.2, 333.3 and 340.6 K respectively. These are realistic as similar values for PS were found in literature.[112,142]

The VFT curves describe an exponential behavior with respect to $1/T_a$, which corresponds to super-Arrhenius kinetics. The data, however, deviate dramatically from this behavior, especially for temperatures well below T_g (right-hand side). The samples show a more linear behavior, approaching Arrhenius-like behavior. This clearly shows that an extra, faster relaxation mechanism accelerates the total ageing kinetics at low temperatures. The relaxation time of low-M_n PS initially increases more sharply than that of high-M_n PS, then levels off. This was also found by Cangialosi et al. (2013).[131] The PS118 and DTS20 show comparable behaviors. This suggests that the ageing kinetics upon reaching the equilibrium are similar, which corresponds to the idea that above M_e the ageing kinetics are less M_n dependent as mentioned in the introduction.

For PCCD3, another method was used to retrieve relaxation times. A common approach is to extract the relaxation times from the intrinsic isotherms in **Figure 86a** and to plot log(τ) vs $1000/T_a$ to form a crossover curve. The relaxation time was chosen as $\tau_{0.08}$, the time needed to reach a degree of ageing of 8 %. This percentage was chosen since that is the maximum that was reached at the lowest T_a (farthest from equilibrium). Also, T_g-T_a instead of T_a was used for easier plotting. The resulting crossover curve is given in **Figure 88a**. The curve clearly exhibits two distinct regimes separated by a smooth transition (indicated by the arrow). At

temperatures close to T_g (left), the data follow a VFT-like slope, assuming super-Arrhenius behavior. Upon further cooling (right), the slope changes, and the intrinsic isotherms adopt a more Arrhenius-like dependence. The transition between the two regimes is continuous but distinct, producing a kink-like change in slope rather than a single master curve as expected from conventional TTS. This crossover behavior indicates that PCCD3 ageing is also governed by different dominant mechanisms depending on the temperature regime. Such crossover behavior has been widely reported in glass-forming polymers and small-molecule glasses.[34,143] Also, Nozaki and Mashimo's dielectric relaxation studies reveal a transition from VFT-like (super-Arrhenius) to Arrhenius temperature dependence in the aging regime below T_g, particularly at long intrinsic isotherms.[144]

All these results suggest the presence of multiple relaxation mechanisms and/or different kinetics for PCCD3, PS3, PS118 and DTS20. The nature of these kinetic regimes remains speculative. Further experimental work (e.g., from dynamic light scattering or dielectric spectroscopy) on the specific samples are needed to clarify the exact origin of these relaxation mechanisms.

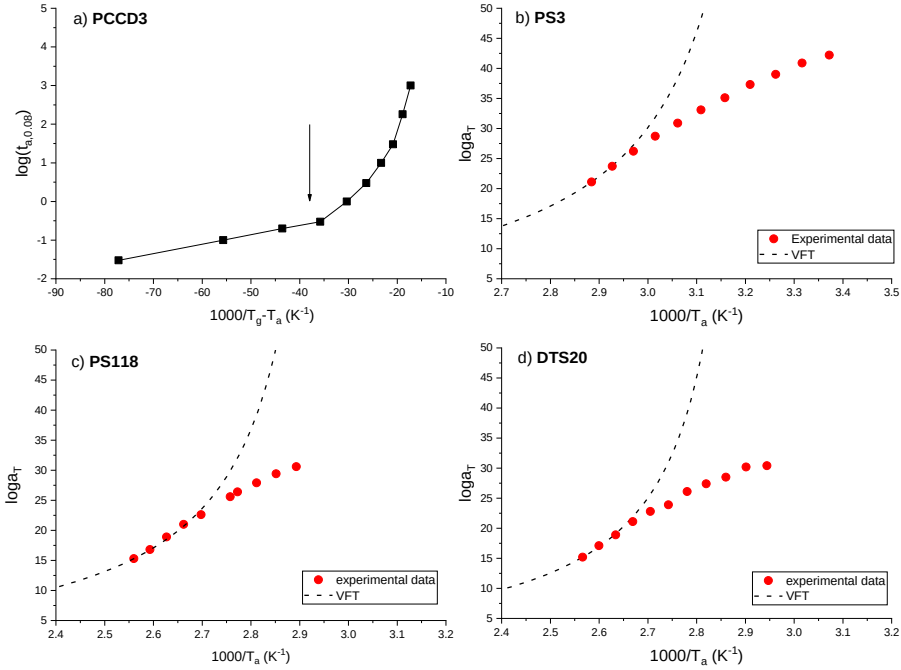


Figure 88. *a) a crossover curve of PCCD3 with the logarithm of relaxation time at 8 % ageing as a function of the inverse of (T_g-T_a) with an arrow indicating the crossover. The logarithm of the shift factors as a function of the inverse of the ageing temperature for b) PS3, c) PS118 and d) DTS20 are given as well as the estimation of the evolution of the VFT equation. For b-d) the data deviates from the VFT at low ageing temperatures.*

Lastly, the optimum ageing temperatures were determined via the devitrification kinetics. A T_g–T_f vs T_a–T_g plot was constructed for all ageing times and is shown in **Figure 89** for the four samples. The unimodal shape of the curves of all the samples reflects the expected competition between thermodynamic driving force and segmental mobility during relaxation,[36,53,54,145] similar to what governs crystallization kinetics (see Chapter 4). The thermodynamic driving force for relaxation increases with decreasing T_a (for $T_a < T_g$), while mobility increases with increasing T_a. The combination of these effects yielded curves with a distinct optimum relaxation temperature (rectangles in **Figure 89**) regardless of the ageing time, at least

within the studied range. This implies that for a fixed t_a, the ageing can be maximized (or minimized) by choosing the correct T_a, which is interesting for applications. For PCCD3 and DTS20, the optimum relaxation temperature appears near T_g−23 °C. For PS118, it is situated between T_g−26 °C and T_g−30 °C, and for PS3 between T_g−10 °C and T_g−12 °C. These are typical values for glassy polymers.

An extra observation was done on the distribution of the data around these maxima. The right-hand side of the curves show a sharp drop, while the left-hand side drops more gradually. Monnier *et al* (2021) explained this for PCDM by the presence of a second relaxation process as this resulted from ageing even further below the T_g than what would be expected if α-relaxation was the only mechanism.[53] Agreeing with the deviation from the VFT behavior in **Figure 88**, this again strongly suggests that a faster mechanism comes into play at low temperatures for PS and PCCD3.

Compared to PS3, PCCD3 shows a more sudden drop at the low temperature side, which means that the T_f and therefore the segmental mobility was more temperature-dependent and that PS3 had relatively high T_f even at very low temperatures. Determining a clear molecular rationale was not straightforward. One could imagine that the rigidity of the PCCD chain had an influence. Generally, the presence of ester linkages and bulky cyclic units restricts the freedom of movement, increasing chain rigidity. In contrast, atactic PS contains phenyl groups randomly distributed along a flexible linear backbone. The idea that more rigid chains increase the ageing rate has been shown for e.g. PS with different tacticity[123] and linear vs start-shaped PS[141] where the strongest influence was seen at temperatures far below T_g.

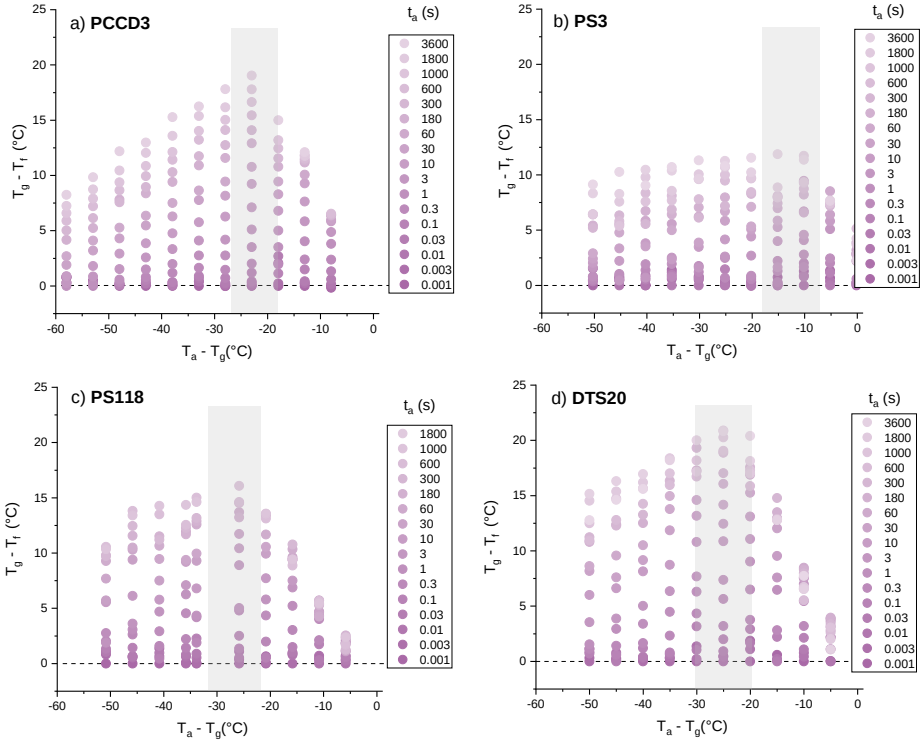


Figure 89. *T_g - T_f vs T_a-T_g for a) PCCD3, b) PS3, c) PS118 and d) DTS20 after ageing for different time periods (from dark to light colors). The grey boxes indicate the estimation of the position of the optimum ageing temperature (peak).*

6.4.2. Non-isothermal ageing of PCCD3 and PS

Ageing can also occur non-isothermally when the material is cooled slowly enough to permit segmental motions (**Figure 78**). The PS3, PS118, and PCCD3 samples were investigated in this respect through devitrification kinetics, i.e. T_f as a function of cooling rate. In general, slower cooling leads to a depression of T_f (see **Figure 78**). which was indeed observed for both PS and PCCD3 (**Figure 90a**).

For all three samples, the cooling-rate dependence of T_f deviates from the expected VFT behavior at low temperatures, especially PCCD3. Such deviations from the high-temperature, high-cooling-rate VFT trend toward weaker temperature

dependence clearly indicate the participation of mechanisms with non-α relaxation kinetics, which are known to delay vitrification and have been reported in bulk polymers.[146]

The existence of two distinct vitrification pathways—one driven by α relaxation and the other by a faster mechanism—leads to the appearance of "kinks" in first-order thermodynamic properties, particularly in the enthalpy. This effect was evident in all three samples, but most pronounced in PS118 (**Figure 90b**). The onset of ageing appeared below cooling rates of ~1,000 K/s, yielding two regimes: a high-rate regime (1,000–30,000 K/s) where no ageing occurs (plateau) and a low-rate regime (β < 1,000 K/s) where ageing sets in. On this basis, the choice of 1,000 K/s as a threshold to suppress ageing during cooling in isothermal ageing experiments (**Figure 81**) was justified.

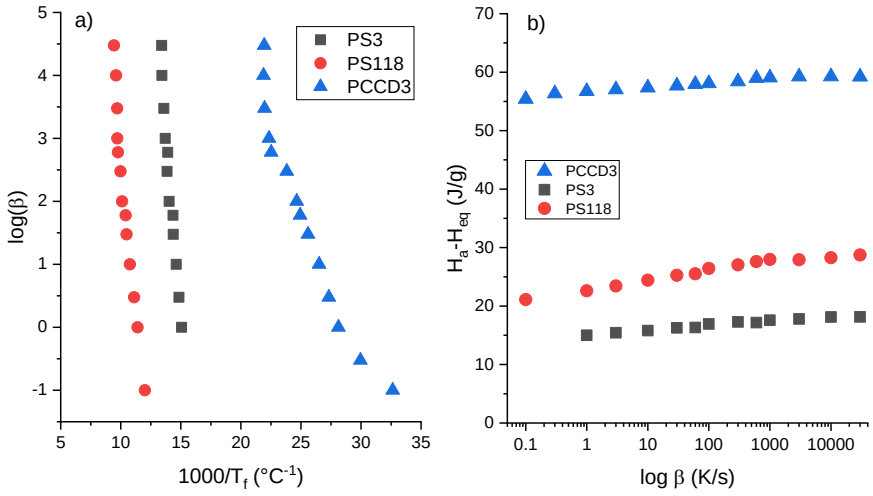


***Figure 90**. The influence of cooling rate β on a) T_f and b) H_a-H_{eq} at 25 °C for PCCD3, PS3 and PS118.*

Interestingly, the enthalpy plateau at high β was located at much higher values for PCCD3 than for PS, meaning that PCCD3 vitrifies further away from equilibrium and therefore exhibits a greater maximum ageing capacity. Among the PS samples, PS118 appeared to be about 10 J/g further from equilibrium than PS3. This

implies that PS3 more effectively follows the cooling path at high rates, postponing vitrification compared to PS118, which is consistent with its higher chain mobility.

It should be emphasized that the relationship between T_g and molecular mobility is not fully established. Vitrification kinetics and molecular mobility are increasingly regarded as distinct aspects of glassy dynamics: the former probed by cooling-rate experiments (nonlinear perturbations), and the latter by isothermal experiments (linear perturbations). Decoupling between both phenomena was suggested, for example, in nanoconfined polystyrene, where a depression of T_g relative to bulk PS was observed while molecular mobility remained unchanged.[136] This implies that changes in T_g cannot be explained solely in terms of molecular mobility, but must also involve other factors.

6.5 Conclusions

When amorphous polymers are held in the glassy state close to or below their T_g, they undergo physical ageing. This process reflects the slow segmental relaxation of chains, leading to increased stiffness and brittleness—an undesirable outcome for applications such as additive manufacturing, where mechanical resilience is essential. In this work, amorphous PCCD was examined together with three PS samples of different molecular characteristics, spanning a broad range of isothermal and non-isothermal conditions. Ageing was monitored isothermally between T_g and T_g−50°C, and during cooling at rates ranging from 0.1 to 30,000 K/s.

To the best of our knowledge, PCCD has not previously been investigated in this context. The results showed that it ages significantly even well below T_g, with relaxation times revealing two distinct regimes. At higher temperatures ageing was strongly temperature-dependent, while at deeper supercooling the dependence became weaker, suggesting a crossover in the controlling mechanism.

For polystyrene, the ageing times could be shifted to form master curves, in contrast to PCCD. The shift factors deviated from the classical VFT prediction at lower temperatures. Similarly to PCCD, this deviation indicates that relaxation at deep supercooling is faster than VFT would suggest. The fictive temperature analysis

further confirmed a reduced temperature dependence at lower temperatures for all samples.

The low-M_n PS showed deviations from VFT at higher temperatures than the high-M_n sample. Interestingly, only the commercial Dynoseeds sample appeared to reach a true equilibrium state after extended ageing, which may be linked to its broader polydispersity or sample heterogeneity that promotes relaxation. This, however, was not confirmed.

Finally, experiments performed during cooling supported the isothermal findings and hinted at the presence of a secondary relaxation mechanism.

Chapter 7

Conclusions and Outlook

7.1 General conclusions

This doctoral dissertation investigated the crystallization and glassy, physical ageing of poly(1,4-cyclohexylidene cyclohexane-1,4-dicarboxylate) (PCCD)-based materials and related systems, with the overarching goal of developing a structure–property understanding relevant to the processing and performance of Amphora™ SP1621, a recyclable powder for additive manufacturing. Through a systematic combination of calorimetric, scattering, and microscopic methods, complemented by modeling and simulations, the work provides a comprehensive view of how molecular structure, thermal history, and experimental conditions govern morphology, crystallization kinetics, and ageing phenomena.

Chapter 1 provided a foundational introduction, outlining the basic concepts of crystallization and physical ageing in polymers and situating PCCD-based systems within this context. This set the stage for the subsequent experimental investigations and highlighted the importance of linking molecular architecture to macroscopic behavior.

Chapter 2 focused on the identification and full characterization of PCCD-PTHF in Amphora™ SP1621, providing a detailed understanding from molecular structure to crystallization mechanism. The material was established as a semi-crystalline, segmented block copolymer, and stochastic simulations were employed to determine the PCCD block length distribution. The simulation approach, which accounts for the finite molecular weight of the chains, can be readily applied to other segmented block copolymers, provided molecular weight averages are available. Thermal and structural analyses, including DSC, WAXS, SAXS, POM, and AFM, revealed the semi-crystalline morphology and the crystallization mechanism. Primary crystallization led to the formation of space-filling spherulites composed of lamellar PCCD crystallites, leaving significant amorphous pools between the primary stacks. Secondary crystallization occurred within these amorphous pools, forming randomly oriented lamellar stacks. A new SAXS data interpretation scheme was introduced to quantitatively estimate the fraction of amorphous pools that convert into semi-crystalline stacks during secondary crystallization. In addition, reference melting

enthalpy values for pure PCCD were calculated. This chapter thus established the foundational molecular and morphological framework that underpins the subsequent investigations of crystallization kinetics and ageing.

Chapter 3 focused on the PCCD homopolymer, synthesized once it was established that Amphora™ SP1621 is PCCD-based. The homopolymer was designed to match the *trans* content of the PCCD-PTHF moieties. Using DSC, SAXS, WAXS, and POM under the same conditions as the copolymer, it was shown that PCCD also crystallizes into space-filling spherulites upon cooling. Primary crystallization ended at 130 °C and continued increase in stack crystallinity suggested slight lamellar thickening. Long high-temperature annealing revealed that PCCD is not fully thermally stable: hydrolysis (chain shortening) and esterification (chain lengthening) reduced its crystallization efficiency. By isolating and characterizing PCCD as a reference system, this work provides a model for understanding the crystallization and degradation behavior of PCCD-based copolymers and other rigid aliphatic polyesters. Such knowledge is also valuable for the design of thermally stable, recyclable polyester materials for high-temperature processing environments.

Chapter 4 investigated the isothermal crystallization kinetics of PCCD and PCCD-PTHF across the full temperature range from T_g to T_m. Prior to the isothermal studies, PCCD-PTHF was found to be thermally unstable under repeated heating and cooling, undergoing three key processes: (i) *trans*-to-*cis* isomerization of the cyclohexane-based units, (ii) intermolecular transesterification, and (iii) backbiting transesterification. These processes eventually stabilized and were used to prepare PCCD-PTHF for the isothermal experiments. The insights gained into the ageing process and stabilization approach can be applied to other polyesters exhibiting similar thermal behavior. In particular, variations in chain length may have significant consequences for applications in which viscosity plays a critical role. In the context of SLS, viscosity governs the coalescence of powder particles and thus directly influences the structure and properties of the printed parts. Isothermal crystallization experiments revealed mechanistic distinctions between the homopolymer and the copolymer. PCCD exhibited a single bell-shaped crystallization rate curve, whereas PCCD-PTHF displayed a bimodal response when crystallizing from the melt, reflecting a transition between different nucleation pathways at lower temperatures.

Crystallization from the glassy state produced a single rate curve. Secondary crystallization thickened and stabilized lamellae, and lamellar thickness was primarily governed by crystallization temperature rather than nucleation pathway. The crystallization rates and times obtained in this work can be directly applied to optimize processing parameters in various applications, ensuring that the desired degree of crystallinity is achieved. Furthermore, for PCCD-PTHF, the processing temperature provides an effective means of controlling the resulting morphology: operating within the heterogeneous nucleation regime promotes the formation of larger spherulites, whereas processing within the homogeneous regime favors the development of finer, less ordered structures.

Chapter 5 shifted the focus to non-isothermal crystallization, directly addressing processing-relevant conditions. Here, PCCD-PTHF was compared to Amphora SP1621, with a particular emphasis on cooling rate effects. The results showed that Amphora crystallizes more readily due to highly efficient heterogeneous nucleation, leading to robust crystallization largely independent of cooling rate. In contrast, PCCD-PTHF displayed strong rate sensitivity: fast cooling promoted homogeneous nucleation, yielding smaller and less stable crystals and a reduced crystalline fraction. Controlling the cooling rate and nucleation efficiency during printing is therefore crucial for regulating the final morphology. For instance, during the crystallization stage at the end of the printing process, it is essential that the entire build crystallizes uniformly to prevent warpage or curling. Despite the differences observed between PCCD-PTHF and Amphora SP1621, both materials ultimately formed crystals of comparable size and perfection after sufficient annealing. This observation is particularly significant, as the resulting morphology directly governs the mechanical and thermal properties of the printed part and must therefore be carefully controlled.

Chapter 6 focused on the physical relaxation behavior of amorphous PCCD, motivated by the fact that SLS of amorphous polymers is performed at temperatures close to T_g, where relaxation and ageing effects are most pronounced. To enable this study, a new PCCD homopolymer was synthesized with M_n ~ 3,000 g/mol and a very low *trans* content of the cyclohexane moieties, which rendered it fully amorphous. Its physical relaxation was investigated in terms of enthalpy recovery and devitrification

using FSC. PCCD was found to undergo pronounced structural relaxation far below T_g, with two distinct kinetic regimes suggesting changes in the temperature dependence of its relaxation processes. This marks the first detailed investigation of physical ageing in PCCD, establishing a baseline understanding of how its molecular architecture governs configurational stability. Comparisons with PS provided context, revealing notable differences in time–temperature superposition and deviations from classical Vogel–Fulcher–Tammann behavior, but the primary emphasis remained on PCCD. These results demonstrate that PCCD, even in its amorphous state, is highly susceptible to thermal history, with its relaxation potentially affecting mechanical properties. Importantly, this particular amorphous PCCD polymer was synthesized solely for fundamental investigation and is not intended for printing applications.

Taken together, the results of Chapters 2–6 provide a unified perspective on how crystallization and ageing in PCCD-based systems are governed by the type of polymer and the processing conditions, supported by new analytical approaches. In the context of SLS, these results can be correlated with the behavior of the printed material, provided that the exact temperature profile experienced during processing is known. The dissertation therefore offers both fundamental insights into morphology, crystallization mechanisms, and ageing kinetics, which are relevant aspects for additive manufacturing. Nevertheless, additional processing factors may also influence the final morphology and properties of printed parts. For instance, variations in the local temperature profile can affect crystallization behavior, the development of increased porosity, and consequently the extent of warpage or curling. Furthermore, the potential impact of partially melted or unmolten powder particles should be taken into account in future investigations.

7.2 Outlook

Even though this thesis provides extensive insights into the crystallization and relaxation behavior of PCCD and its derivatives, research on this material family is still in its early steps. As this dissertation was mostly fundamental, the outlook will primarily focus on this aspect.

For the crystallization mechanism of PCCD-PTHF, it would be particularly valuable to perform **time-resolved AFM during cooling and heating**. While only room-temperature experiments have been performed so far, extending these to dynamic conditions would allow direct observation of secondary crystallization and confirm the formation of new stacks with the same lamellar thickness. Such measurements could also provide direct validation of the proposed melting process.

For **semi-crystalline PCCD**, repeating the time-resolved SAXS/WAXS experiments is necessary to ensure reproducibility of the results. Complementary determination of WAXD-based crystallinity, in comparison with DSC values, would further strengthen the conclusions. Additionally, preparing and analyzing oriented PCCD samples—similar to what was done for PCCD-PTHF—could confirm the correctness of the crystallographic unit cell and ultimately lead to a true crystal structure. Beyond this, synthesizing and studying PCCD with various M_n values and *trans* contents would provide crucial insight into their influence on crystallization behavior, thereby contributing to the broader understanding of polyesters derived from two cyclohexane monomers.

For both **PCCD-PTHF and PCCD**, the proposed molecular reactions as a result of high temperature treatments should be further verified by advanced techniques such as infrared spectroscopy and TGA-MS. Moreover, in-situ X-ray scattering during annealing could directly reveal how molecular transformations affect crystallization behavior.

In the context of the **isothermal crystallization study**, complementary microscopy during isothermal periods, as well as extending X-ray experiments to a broader temperature range and crystallization from both melt and glassy states, would be highly beneficial. Similar strategies could also be applied to non-isothermal crystallization. Altogether, mapping the multi-scale morphology as a function of temperature and time would not only deepen the understanding of crystallization mechanisms in these polymers but also provide valuable information for processing-related applications. These studies, however, should be performed on thermally stabilized materials and therefore cannot be directly linked to Amphora™ SP1621.

With **Amphora SP1621** in mind, a promising avenue would be to study its amorphous state or that of PCCD-PTHF, where the block architecture may lead to a complex interplay between physical ageing and crystallization. Furthermore, performing mechanical property tests after thermal treatments as realized by FSC would establish a direct link between thermal response, structural evolution, and macroscopic performance.

Appendices

Appendix A to Chapter 2

A.1 TGA measurement of PCCD-PTHF to determine its degradation temperature

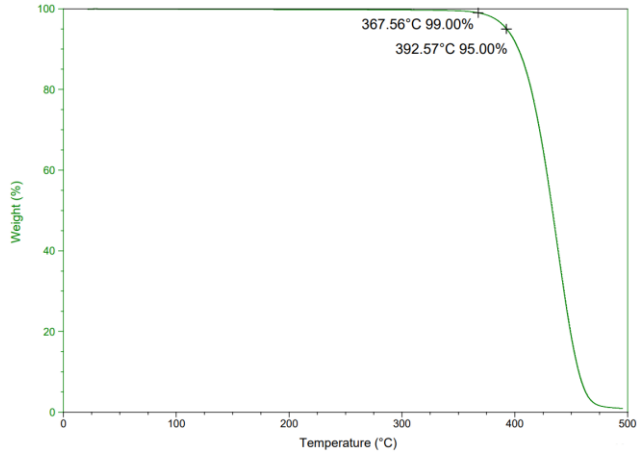


Figure A.1. *TGA weight loss profile at 10 K/min from room temperature to 500 °C with the temperatures at 1% and 5% weight loss indicated.*

A.2 2D COSY NMR spectrum of PCCD-PTHF

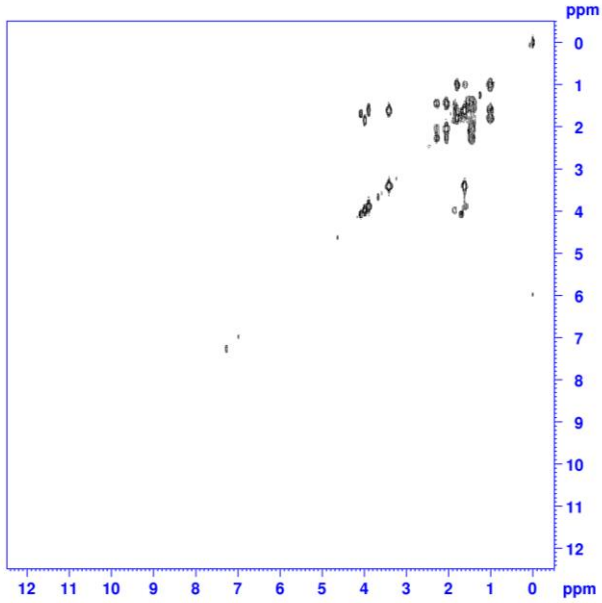


Figure A.2. *2D COSY NMR spectrum.*

A.3 2D NOESY NMR spectrum of PCCD-PTHF

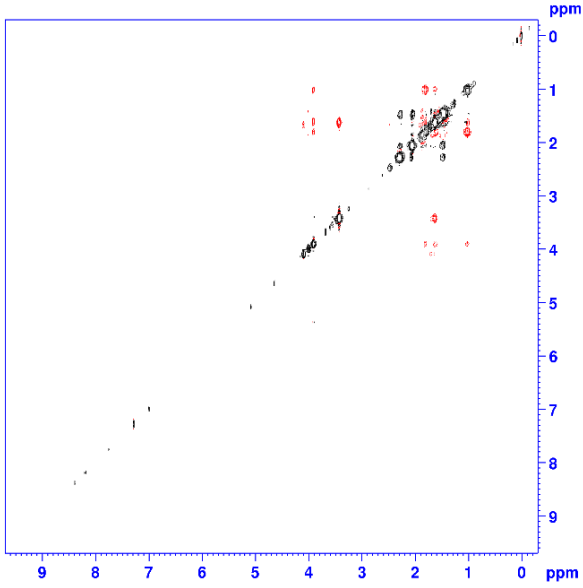


Figure A.3. *2D NOESY NMR spectrum.*

A.4 2D HMBC NMR spectrum of PCCD-PTHF

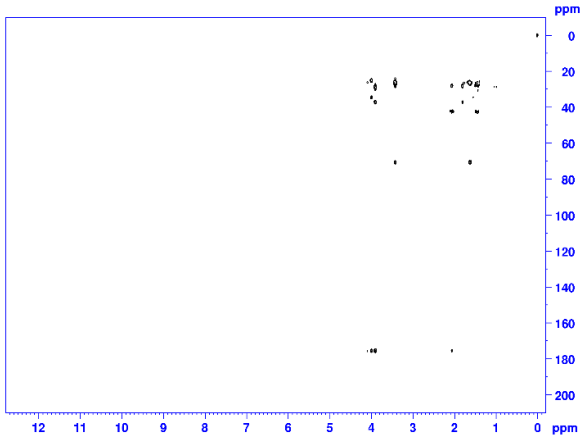


Figure A.4. 2D HMBC NMR spectrum.

A.5 Supporting information to section 2.3.2

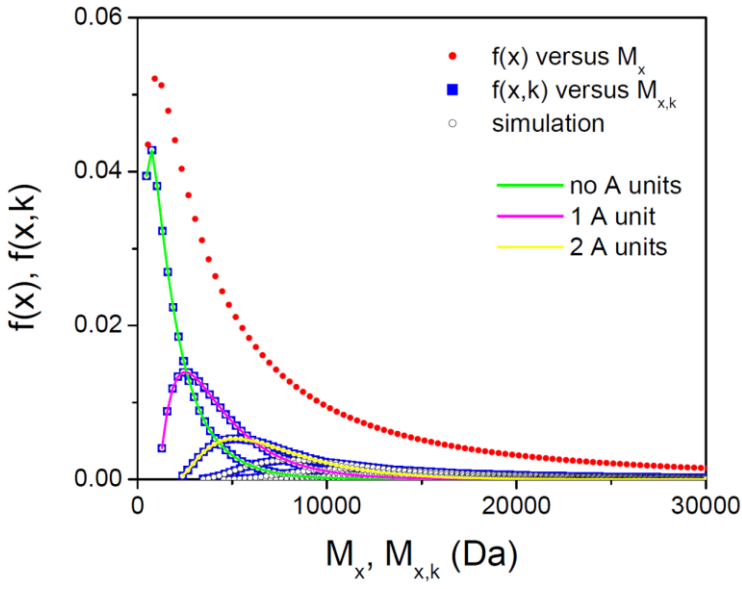


Figure A.5. *$f(x)$ based on equation 9 as a function of M_x from equation 12 (red) and $f(x,k)$ based on equation 14 as a function of $M_{x,k}$ from equation 15 (blue) compared*

with $f(x,k)$ from a stochastic simulation (black). The green, magenta and yellow curves highlight the molar masses of chains without (green), 1 (magenta) or 2 A units in the chain. This Figure is identical to **Figure 12** *of the manuscript where logarithmic coordinate axes are used.*

A.6 Supporting information to section 2.3.2

Table A.1 gives the comparison between the experimental and predicted q_{hkl}-positions (calculated from $q_{hkl} = \frac{2\pi}{d_{hkl}}$) of reflections from a triclinic unit cell with the following parameters: : a = 5.13 Å, b = 5.50 Å, c = 13.28 Å, α = 87.6 °, β = 62.8 ° and γ = 86.6 °. The unit cell volume, V, is 333 Å^3, based on $V = abc\sqrt{1 - cos^2\alpha - cos^2\beta - cos^2\gamma + 2\cos\alpha\, cos\beta\, cos\gamma}$. Predicted d_{hkl} values are calculated from:

$$\frac{1}{{d_{hkl}}^2} = \left[\frac{h^2 sin^2\alpha}{a^2} + \frac{k^2 sin^2\beta}{b^2} + \frac{h^2 sin^2\gamma}{c^2} + \frac{2hk}{ab}(cos\alpha\, cos\beta - cos\gamma) + \frac{2kl}{bc}(cos\beta\, cos\gamma - cos\alpha) + \frac{2lh}{ca}(cos\gamma\, cos\alpha - cos\beta)\right] / (1 - cos^2\alpha - cos^2\beta - cos^2\gamma + 2\cos\alpha\, cos\beta\, cos\gamma) \quad \text{(A-1)}$$

The fitting procedure involved varying the unit cell parameters up to a close match between the experimental and observed q_{hkl} values, i.e. by minimizing the sum of squared errors.

Table A.6*. Comparison between the experimental and predicted q_{hkl}-positions of reflections from the triclinic unit cell parameters*

hkl Miller index	Experimental q_{hkl} (Å^{-1})	Theoretical q_{hkl} (Å^{-1})	Theoretical d_{hkl} (Å)
001	0.5499	0.5319	11.8117
010	1.1490	1.1441	5.4917
101	1.2313	1.2313	5.1029
011	Not determined	1.2535	5.0126

100	1.3792	1.3792	4.5557
110	1.7521	1.7521	3.5861
004	2.1233	2.1278	2.9529
020	2.2858	2.2882	2.7458

A.7 Time-resolved synchrotron WAXS for thermal expansion

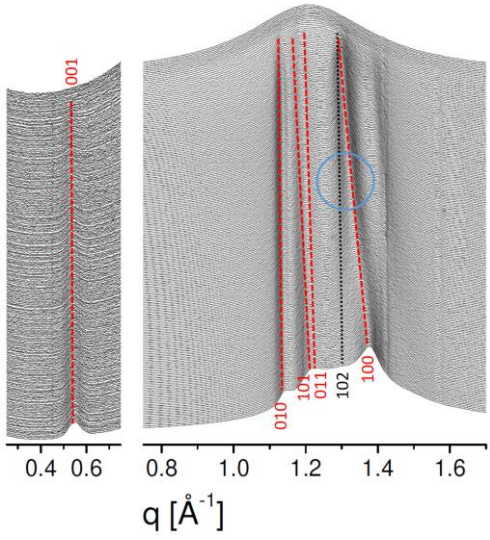


Figure A.7*. The time-resolved synchrotron* 001 *reflection (left) and WAXS (right) q-ranges during heating (b) at 10 K/min. From the top to the bottom, patterns are depicted from 220 °C to 22 °C. This Figure is a copy of the two right side panels of* ***Figure 22*** *to which the temperature tracks of selected reflections are indicated in red. The 100 reflection displays the strongest shift to lower q-values with increasing temperature, suggesting a strongest thermal expansion along the unit cell a axis. At about 110 °C, the* 100 *reflection seems to display a kink in its track (this region is highlighted with the blue circle). Whether this is due to a splitting of the 102 and 100 reflections toward lower temperatures (as suggested in the graph) or to a polymorphic transition, remains to be explored with a dedicated, highly crystalline pure PCCD sample. The continuous linear evolution of the SAXS contrast function (****Figure 29*** *of Chapter 2) over the temperature range of the mentioned kink seems to favor the first option since polymorphic changes are expected to lead to a discontinuity in the thermal expansion of the crystalline density, hence also in the contrast function.*

A.8 Supporting information to section 2.3.6

The equation used to fit the SAXS data to a lamellar model of alternating A and B layers, with average thickness d_A and d_B and Gaussian thickness distributions with standard deviations σ_A and σ_B is based on the paracrystalline layer stack model by Hosemann and Bagchi:[59]

$$I(q) = \frac{C(\rho_A-\rho_B)^2}{2\pi q^4} \cdot \frac{1}{(d_A+d_B)} \cdot \frac{1-A^2B^2-A(1-B^2)cos(qd_A)-B(1-A^2)cos(qd_B)}{1+A^2B^2-2ABcos(q(d_A+d_B))} \cdot e^{-\sigma^2q^2} + B_G \qquad \text{(A-2)}$$

Where $A = e^{-\frac{q^2\sigma_A^2}{2}}$ and $B = e^{-\frac{q^2\sigma_B^2}{2}}$. ρ_A and ρ_B are the electron densities of the A and B layers, σ is a parameter characterizing the thickness of the interfacial gradient [147] between the A and B layers, C is a factor accounting for not having conducted measurements on an absolute scale and B_G is a background given by:

$$B_G = B + fI(q)_{melt} \qquad \text{(A-3)}$$

Where B is a constant, f a factor between 0 and 1 and $I(q)_{melt}$ a melt SAXS pattern. Fitting was performed using a least squares procedure in which the following parameters were adjusted: B, f, d_A, d_B, σ_A, σ_B, σ and E, with $E = C(\rho_A - \rho_B)^2$. The fits systematically returned $\sigma = 0$, implying a two-phase system with sharp interfaces. Fittings over the range $0.019 \leq q \leq 0.37$ Å^{-1} were performed with the data and fitting equation set as $logI(q)$ rather than $I(q)$ to give a higher weight to the low intense data in the SAXS pattern tail regions.

Appendix B to chapter 3

B.1 PCCD crystallite size approached by polynomial fit

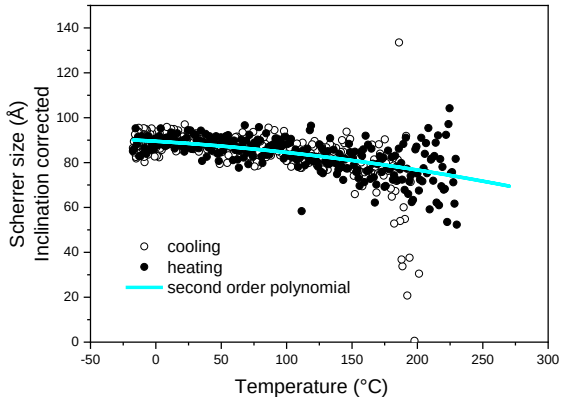


Figure B.1. *PCCD Scherrer size D upon cooling and heating at 10 K/min. A second order polynomial was used to describe the data.*

Appendix C to Chapter 4

C.1 Examples of PCCD-PTHF evolution of isothermal crystallization and fitting functions with FSC and DSC

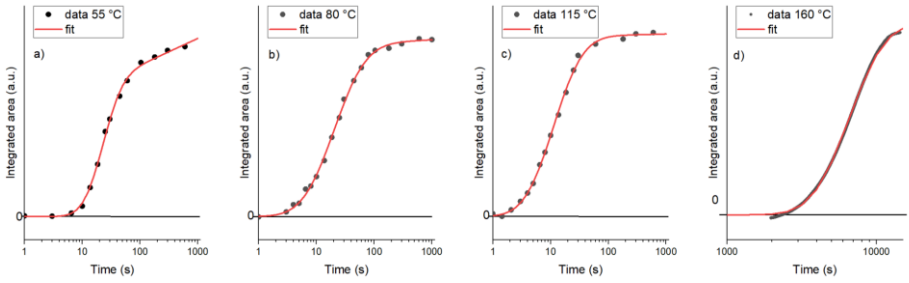


Figure C.1. *Evolution of isothermal crystallization from the melt in the form of integrated areas of PCCD-PTHF with a), b), c), FSC and d) DSC.*

C.2 PCCD HF curves after various time periods of isothermal crystallization low, intermediate and high temperature

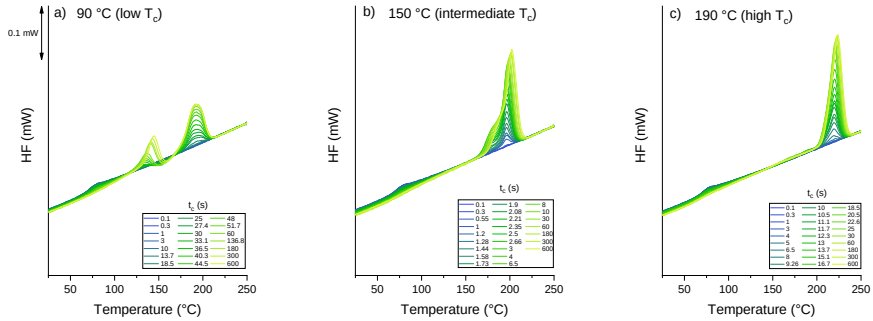


Figure C.2. *PCCD HF heating curves after isothermal crystallization from the melt at a) 90 °C, b) 150 °C and c) 190 °C.*

C.3 PCCD HF curves after 300 s isothermal crystallization at various temperatures

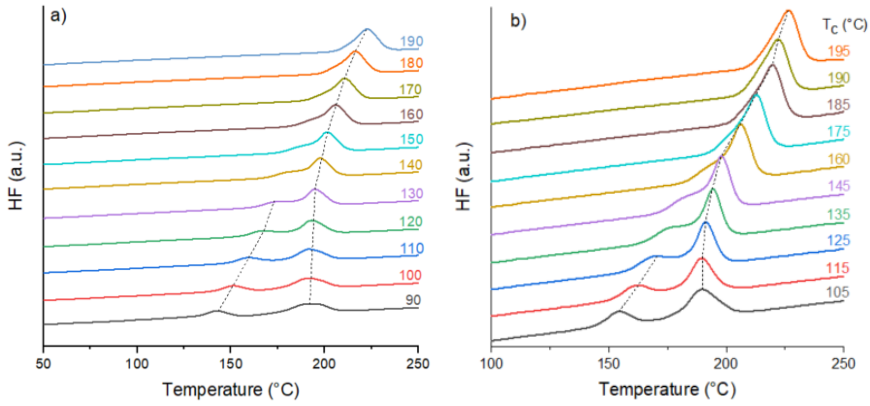


Figure C.3. *Heat flow curves for PCCD of the heating after 300 s of crystallization at the coming from the a) melt and b) glassy state.*

C.4 PCCD-PTHF WAXS patterns after isothermal crystallization coming from the glassy state

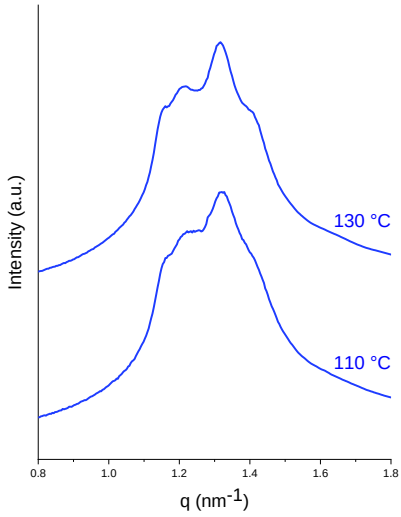


Figure C.4. *PCCD-PTHF WAXS patterns after 600 s at 110 and 130 °C from the glassy state, measured at the corresponding temperatures.*

The WAXS patterns are similar to the ones collected upon cooling and heating at 10 K/min and confirm the formation of crystals with the same unit cell as reported in reference [71]. The diffraction peaks at 130 °C are more pronounced than 110 °C, signifying a higher crystallinity of the sample. This is expected for higher temperatures.

C.5 Example of fitting of WAXS 001 reflection peak (isothermal crystallization experiment)

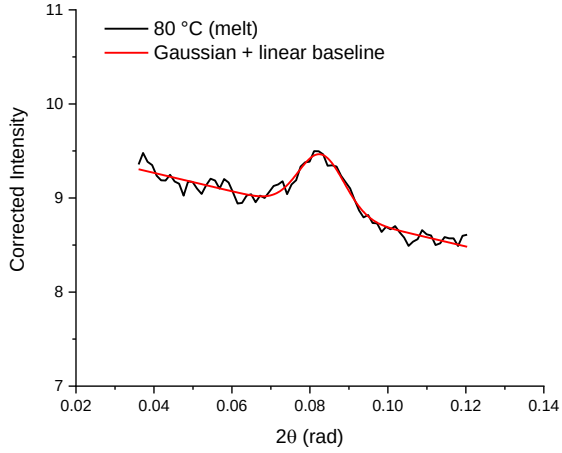


Figure C.5. *Example of 001 reflection peak at around q = 0.54 (2θ = 0.08 rad) for PCCD-PTHF after isothermal crystallization at 80 °C reached from the melt. The peak is fitted with a Gaussian function and a linear baseline. The full width at half maximum (FWHM) as one of the Gaussian parameters was used to calculate the crystallite size with the integral breadth and Scherrer equation.*

C.6 Error bars on l_c

The standard deviations on the full width at half maximum (FWHM) σ_{FWHM} of the peaks are retrieved from the fitting of the Gaussian function on the data. The standard deviation on l_c (σ_{l_c}) is calculated based on the method in reference [148] via

$$\sigma_D^2 = \sqrt{\left(-\frac{K.\lambda}{cos\theta}.\frac{1}{FWHM^2}\right)^2}.\ \sigma_{FWHM}^2 \qquad \text{(C-1)}$$

and

$$\sigma_{l_c} = \sigma_D \cdot \cos\,(27.2°) \qquad \text{(C-2)}$$

with σ_D the standard deviation on D.

List of publications

Hamid, M., Mongilyov, I., Ianiro, A., Van Puyvelde, P., & Goderis, B. (2025). The molecular structure and phase behavior of a segmented PCCD-PTHF block copolymer. *POLYMER*, *334*, 14 pages. doi:10.1016/j.polymer.2025.128705

Liu, Z., Vanderspikken, J., Mantegazza, P., Moro, S., **Hamid, M**., Mertens, S., . . . Goderis, B. (2024). Removing Homocoupling Defects in Alkoxy/Alkyl-PBTTT Enhances Polymer:Fullerene Co-Crystal Formation and Stability. *ADVANCED FUNCTIONAL MATERIALS*, 16 pages. doi:10.1002/adfm.202413647

Vanderspikken, J., Liu, Z., Wu, X., Beckers, O., Moro, S., Quill, T. J., . . . Maes, W. (2023). On the Importance of Chemical Precision in Organic Electronics: Fullerene Intercalation in Perfectly Alternating Conjugated Polymers. *ADVANCED FUNCTIONAL MATERIALS*, *33*(52), 11 pages. doi:10.1002/adfm.202309403

Vanheusden, C., Samyn, P., Goderis, B., Hamid, M., Reddy, N., Ethirajan, A., . . . Buntinx, M. (2021). Extrusion and Injection Molding of Poly(3-Hydroxybutyrate-co-3-Hydroxyhexanoate) (PHBHHx): Influence of Processing Conditions on Mechanical Properties and Microstructure. *POLYMERS*, *13*(22), 23 pages. doi:10.3390/polym13224012

Bibliography

1. Company, E. C. *Technical Data Sheet Amphora 3D Polymer SP1621 Natural*. vol. 123 (2019).
2. ALM. *TPE 360 Material Data Sheet*. www.alm-llc.com.
3. Verbelen, L. *et al.* Analysis of the material properties involved in laser sintering of thermoplastic polyurethane. *Addit. Manuf.* **15**, 12–19 (2017).
4. Brunelle, D. J. & Jang, T. Optimization of Poly(1,4-cyclohexylidene cyclohexane-1,4-dicarboxylate) (PCCD) Preparation for Increased Crystallinity. **47**, 4094–4104 (2006).
5. Brighenti, R., Cosma, M. P., Marsavina, L., Spagnoli, A. & Terzano, M. Laser-based additively manufactured polymers: a review on processes and mechanical models. *J. Mater. Sci.* **56**, 961–998 (2021).
6. Drummer, D., Greiner, S., Zhao, M. & Wudy, K. A novel approach for understanding laser sintering of polymers. *Addit. Manuf.* **27**, 379–388 (2019).
7. CustomPartNet. Selective Laser Sintering (SLS). https://www.custompartnet.com/wu/selective-laser-sintering (2008).
8. George, A. A. & Dadmun, M. D. Impact of polymer molecular weight and dispersity on the coalescence of polypropylene powders suitable for laser powder bed fusion. *Polymer (Guildf).* **312**, 127663 (2024).
9. Ryse, R. Vande *et al.* Setting the Optimal Laser Power for Sustainable Powder Bed Fusion Processing of Elastomeric Polyesters : A Combined Experimental and Theoretical Study. *Materials (Basel).* **15**, 1–18 (2022).
10. Corporation, A. M. C. *Material Data Sheet: PA 2200 Balance*. vol. 49 (2001).
11. Tan, L. J., Zhu, W. & Zhou, K. Recent Progress on Polymer Materials for Additive Manufacturing. **2003062**, 1–54 (2020).
12. Meijer, H. E. H. & Govaert, L. E. Mechanical performance of polymer systems: The relation between structure and properties. *Prog. Polym. Sci.* **30**, 915–938 (2005).
13. Mathot, V. B. F. & Pijpers, M. F. J. Heat capacity, enthalpy and crystallinity of polymers from DSC measurements and determination of the DSC peak

base line. *Thermochim. Acta* **151**, 241–259 (1989).

14. Hoffman, J. D., Davis, G. T. & Lauritzen, J. I. The Rate of Crystallization of Linear Polymers with Chain Folding. in *Treatise on Solid State Chemistry* 497–614 (New York: Plenum, 1976). doi:10.1007/978-1-4684-2664-9_7.
15. Strobl, G. *The physics of polymers: Concepts for understanding their structures and behavior*. *The Physics of Polymers: Concepts for Understanding Their Structures and Behavior* (2007). doi:10.1007/978-3-540-68411-4.
16. North, M. J. & Jenkins, M. J. The mechanisms of the secondary crystallisation process in polymers: A narrative review. *Polymer (Guildf).* **321**, 128122 (2025).
17. Hoffman, J. D. & Miller, R. L. Kinetics of crystallization from the melt and chain folding in polyethylene fractions revisited: theory and experiment. *Polymer (Guildf).* **38**, 3151–3212 (1997).
18. Lorenzo, A. T. & Müller, A. J. Estimation of the Nucleation and Crystal Growth Contributions to the Overall Crystallization Energy Barrier. *J. Polym. Sci. Part B Polym. Phys.* **46**, 1478–1487 (2008).
19. Marand, H., Xu, J. & Srinivas, S. Determination of the equilibrium melting temperature of polymer crystals: Linear and nonlinear Hoffman-Weeks extrapolations. *Macromolecules* **31**, 8219–8229 (1998).
20. Matsumoto, O. & Hotta, A. Structural, thermal and rheological studies on newly developed polyesters randomly copolymerized with poly (tetramethylene glycol) (PTMG). *Mater. Res. Soc. Symp. Proc.* **1151**, 2–7 (2009).
21. Berti, C. *et al.* Poly(1,4-cyclohexylenedimethylene 1,4-cyclohexanedicarboxylate): Influence of Stereochemistry of 1,4-Cyclohexylene Units on the Thermal Properties. *J. Polym. Sci. Part B Polym. Phys.* **46**, 619–630 (2008).
22. Schmalz, H. & Abetz, V. Block Copolymers with Crystallizable Blocks: Synthesis, Self-Assembly and Applications. *Polymers (Basel).* **14**, 1–5 (2022).
23. Struik, L. C. E. *Physical Aging in Amorphous Polymers and Other Materials.*

(Elsevier, 1978).

24. Struik, L. C. E. Physical Aging in Amorphous Glassy Polymers. *Ann. N. Y. Acad. Sci.* **279**, 78–85 (1976).
25. Hutchinson, J. M. Physical Aging of Polymers. **20**, 703–760 (1995).
26. Sobieski, J. W., Simon, S. L. & Plazek, D. J. Dilatometric studies of physical aging of polyetherimide. *J. Therm. Anal.* **49**, 455–460 (1997).
27. Simon, S. L., Sobieski, J. W. & Plazek, D. J. Volume and enthalpy recovery of polystyrene. *Polymer (Guildf).* **42**, 2555–2567 (2001).
28. Bernazzani, P. & Simon, S. L. Volume recovery of polystyrene: Evolution of the characteristic relaxation time. *J. Non. Cryst. Solids* **307**–**310**, 470–480 (2002).
29. Kohlrausch, R. Theorie des elektrischen Rückstandes in der Leidener Flasche. *Ann. Phys.* **167**, 56–82 (1854).
30. Vogel, H. Temperaturabhängigkeitsgesetz der Viskosität von Flüssigkeiten. *Phys. Zeitschrift* **22**, 645–646 (1921).
31. Fulcher, G. Analysis of recent measurements of the viscosity of glasses. *J. Am. Ceram. Soc.* **8**, 339–355 (1925).
32. Tammann, G. & Hesse, W. Die Abhängigkeit der Viskosität von der Temperatur von unterkühlten Flüssigkeiten. *Zeitschrift fü Anorg. und Allg. Chemie* **156**, (1926).
33. Williams, M. L., Landel, R. F. & Ferry, J. D. The Temperature Dependence of Relaxation Mechanisms in Amorphous Polymers and Other Glass-forming Liquids. *J. Am. Chem. Soc.* **77**, 3701–3707 (1955).
34. Mckenna, G. B. & Simon, S. L. 50th Anniversary Perspective : Challenges in the Dynamics and Kinetics of Glass-Forming Polymers. (2017) doi:10.1021/acs.macromol.7b01014.
35. Caporaletti, F. *et al.* A microscopic look at the Johari-Goldstein relaxation in a hydrogen-bonded glass-former. *Sci. Rep.* **9**, 1–10 (2019).
36. Boucher, V. M., Cangialosi, D., Alegría, A. & Colmenero, J. Complex nonequilibrium dynamics of stacked polystyrene films deep in the glassy state. *J. Chem. Phys.* **146**, (2017).
37. Verbelen, L. *et al.* Characterization of polyamide powders for determination

of laser sintering processability. *Eur. Polym. J.* **75**, 163–174 (2016).

38. Wudy, K. & Drummer, D. Aging effects of polyamide 12 in selective laser sintering: Molecular weight distribution and thermal properties. *Addit. Manuf.* **25**, 1–9 (2019).
39. Davis, B., Gray, T. F. & Musser, H. R. COPOLYESTERETHERS. (1982).
40. Caldwell, J. R. & Gilkey, R. Fiber-Forming Polyesters from trans-1,4-cyclohexanedicarboxylic Compounds and 1,1-cyclohexane dimethanol. 1–6 (1959).
41. Kiber, C. J., Bell, A. & Smith, J. G. Linear Polyesters and Polyester-Amides from 1,4-Cyclohexanedimethanol. (1959).
42. Schick, C. & Mathot, V. *Fast Scanning Calorimetry*. (Springer International Publishing, 2016).
43. Gommes, C. J. & Goderis, B. CONEX, a program for angular calibration and averaging of two-dimensional powder scattering patterns. *J. Appl. Crystallogr.* **43**, 352–355 (2010).
44. Colonna, M., Celli, A., Marchese, P., Sisti, L. & Gioia, C. Solid-state polymerization process for the preparation of poly(cyclohexane-1,4-dimethylene cyclohexane-1,4-dicarboxylate) polymers with high melting temperature and crystallinity. *Polym. Eng. Sci.* **58**, 1981–1986 (2018).
45. Datta, J. & Kasprzyk, P. Thermoplastic polyurethanes derived from petrochemical or renewable resources: A comprehensive review. *Polym. Eng. Sci.* **58**, E14–E35 (2018).
46. De Almeida, A., Nébouy, M. & Baeza, G. P. Bimodal Crystallization Kinetics of PBT/PTHF Segmented Block Copolymers: Impact of the Chain Rigidity. *Macromolecules* **52**, 1227–1240 (2019).
47. Flory, P. J. Theory of crystallization in copolymers. *Trans. Faraday Soc.* **51**, 848–857 (1955).
48. Righetti, M. C., Gazzano, M., Di Lorenzo, M. L. & Androsch, R. Enthalpy of melting of α′- and α-crystals of poly(L-lactic acid). *Eur. Polym. J.* **70**, 215–220 (2015).
49. Poly(ethylene terephthalate) (PET) Heat Capacity, Enthalpy, Entropy, Gibbs Energy: Datasheet from ‘The Advanced THermal Analysis System (ATHAS)

Databank – Polymer Thermodynamics' Release 2014 in SpringerMaterials. https://materials.springer.com/polymerthermodynamics/docs/athas_0110.

50. Polyoxytetramethylene (PO4M) Heat Capacity, Enthalpy, Entropy, Gibbs Energy: Datasheet from 'The Advanced THermal Analysis System (ATHAS) Databank – Polymer Thermodynamics' Release 2014 in SpringerMaterials. https://materials.springer.com/polymerthermodynamics/docs/athas_0065.
51. Fox, T. G. & Loshaek, S. Influence of molecular weight and degree of crosslinking on the specific volume and glass temperature of polymers. *J. Polym. Sci.* **15**, 371–390 (1955).
52. Hodge, I. M. Enthalpy relaxation and recovery in amorphous materials. *J. Non. Cryst. Solids* **169**, 211–266 (1994).
53. Monnier, X. *et al.* Physical aging behavior of a glassy polyether. *Polymers (Basel).* **13**, 1–12 (2021).
54. Perez-De-Eulate, N. G. & Cangialosi, D. Double Mechanism for Structural Recovery of Polystyrene Nanospheres. *Macromolecules* **51**, 3299–3307 (2018).
55. Balko, J. *et al.* Clarifying the Origin of Multiple Melting of Segmented Thermoplastic Polyurethanes by Fast Scanning Calorimetry. *Macromolecules* **50**, 7672–7680 (2017).
56. Koberstein, J., Russell, T. P. & Stein, R. S. Total Integrated Light-Scattering Intensity From Polymeric Solids. *J. Polym. Sci. Polym. Phys. Ed.* **17**, 1719–1730 (1979).
57. Crist, B. & Schultz, J. M. Polymer spherulites: A critical review. *Prog. Polym. Sci.* **56**, 1–63 (2016).
58. Bamford, C. H. & Jenkins, A. D. Density of Amorphous Polyethylene Terephtalate. *Nature* **176**, 78–79 (1955).
59. Hosemann, R. & Bagchi, S. N. *Direct Analysis of Diffraction by Matter.* (North Holland Publishing, 1962).
60. Goderis, B., Reynaers, H., Koch, M. H. J. & Mathot, V. B. F. Use of SAXS and Linear Correlation Functions for the Determination of the Crystallinity and Morphology of Semi-Crystalline Polymers. Application to Linear Polyethylene. *J Polym Sci B Polym Phys* **37**, 1715–1738 (1999).

61. Ruland, W. The evaluation of the small-angle scattering of lamellar two-phase systems by means of interface distribution functions. *Colloid Polym. Sci.* **255**, 417–427 (1977).

62. Crist, B. Analysis of Small-Angle X-Ray Scattering Patterns. *J. Macromol. Sci. Part B Phys.* **39**, 493–518 (2000).

63. Turner, S. R., Seymour, S. W. & Dombroski, J. R. Amorphous and Crystalline Polyesters based on 1,4-Cyclohexanedimethanol. *Copolyesters, Mod. Polyesters Chem. Technol. Polyesters Copolyesters* 267–292 (2004).

64. Patel, B. R. & Smith, G. Crystalline Polyester Resins and Process for their Preparation. vol. 1 (2002).

65. Kricheldorf, H. R. & Schwarz, G. New polymer syntheses, 17. Cis/trans isomerism of 1,4-cyclohexanedicarboxylic acid in crystalline, liquid-crystalline and amorphous polyesters. *Die Makromol. Chemie* **188**, 1281–1294 (1987).

66. Brunelle, D. J. & Jang, T. Optimization of poly(1,4-cyclohexylidene cyclohexane-1,4-dicarboxylate) (PCCD) preparation for increased crystallinity. **47**, 4094–4104 (2006).

67. Totaro, G. *et al.* Ageing of PCCD aliphatic polyesters : Effect of stereochemistry and ionic chain terminals. *"Journal Photochem. Photobiol. A Chem.* **292**, 42–48 (2014).

68. Gaur, U., Lau, S. F., Wunderlich, B. B. & Wunderlich, B. Heat Capacity and Other Thermodynamic Properties of Linear Macromolecules. VIII. Polyesters and Polyamides. *J. Phys. Chem. Ref. Data* **12**, 1001–1049 (1981).

69. Sandhya, T. E. Synthesis and Characterization of Aliphatic-Aromatic Polyesters. (2003).

70. Askadskii, A., Popova, M., Matseevich, T. & Kurskaya, E. The influence of the degree of crystallinity on the glass transition temperature of polymers. *Adv. Mater. Res.* **864**–**867**, 751–754 (2014).

71. Hamid, M., Mongilyov, I., Ianiro, A., Van Puyvelde, P. & Goderis, B. The Molecular Structure and Phase Behavior of a Segmented PCCD-PTHF Block Copolymer. *Polymer (Guildf).* **334**, (2025).

72. Supaphol, P. & Spruiell, J. E. Isothermal melt- and cold-crystallization

kinetics and subsequent melting behavior in syndiotactic polypropylene: A differential scanning calorimetry study. *Polymer (Guildf).* **42**, 699–712 (2001).

73. De Santis, F., Adamovsky, S., Titomanlio, G. & Schick, C. Isothermal nanocalorimetry of isotactic polypropylene. *Macromolecules* **40**, 9026–9031 (2007).
74. Silvestre, C., Cimmino, S., Duraccio, D. & Schick, C. Isothermal crystallization of isotactic poly(propylene) studied by superfast calorimetry. *Macromol. Rapid Commun.* **28**, 875–881 (2007).
75. Cocca, M., Androsch, R., Righetti, M. C., Malinconico, M. & Di Lorenzo, M. L. Conformationally disordered crystals and their influence on material properties: The cases of isotactic polypropylene, isotactic poly(1-butene), and poly(l-lactic acid). *J. Mol. Struct.* **1078**, 114–132 (2014).
76. Mileva, D., Androsch, R., Zhuravlev, E., Schick, C. & Wunderlich, B. Formation and reorganization of the mesophase of isotactic polypropylene. *Mol. Cryst. Liq. Cryst.* **556**, 74–83 (2012).
77. Luijsterburg, B. J., De Kort, G. W., Van Drongelen, M., Govaert, L. E. & Goossens, J. G. P. Fast cooling of (non)-nucleated virgin and recycled poly(propylenes): Effect of processing conditions on structural and mechanical properties. *Thermochim. Acta* **603**, 94–102 (2015).
78. Schawe, J. E. K., Vermeulen, P. A. & Van Drongelen, M. Two processes of α-phase formation in polypropylene at high supercooling. *Thermochim. Acta* **616**, 87–91 (2015).
79. Androsch, R., Monami, A. & Kucera, J. Effect of an alpha-phase nucleating agent on the crystallization kinetics of a propylene/ethylene random copolymer at largely different supercooling. *J. Cryst. Growth* **408**, 91–96 (2014).
80. Mileva, D. & Androsch, R. Effect of co-unit type in random propylene copolymers on the kinetics of mesophase formation and crystallization. *Colloid Polym. Sci.* **290**, 465–471 (2012).
81. Paolucci, F., Baeten, D., Roozemond, P. C., Goderis, B. & Peters, G. W. M. Quantification of isothermal crystallization of polyamide 12: Modelling of

crystallization kinetics and phase composition. *Polymer (Guildf).* **155**, 187–198 (2018).

82. Van Drongelen, M. *et al.* Microfocus wide-angle X-ray scattering of polymers crystallized in a fast scanning chip calorimeter. *Thermochim. Acta* **563**, 33–37 (2013).
83. Schick, C. & Mathot, V. *Fast scanning calorimetry*. *Fast Scanning Calorimetry* (Springer International Publishing, 2016). doi:10.1007/978-3-319-31329-0.
84. Mollova, A., Androsch, R., Mileva, D., Schick, C. & Benhamida, A. Effect of supercooling on crystallization of polyamide 11. *Macromolecules* **46**, 828–835 (2013).
85. Rhoades, A. M., Wonderling, N., Schick, C. & Androsch, R. Supercooling-controlled heterogeneous and homogenous crystal nucleation of polyamide 11 and its effect onto the crystal/mesophase polymorphism. *Polymer (Guildf).* **106**, 29–34 (2016).
86. Verkinderen, O., Baeten, D., Van Puyvelde, P. & Goderis, B. The crystallization of PA11, PA12, and their random copolymers at increasing supercooling: From eutectic segregation to mesomorphic solid solutions. *Polym. Cryst.* **4**, 1–51 (2021).
87. Rhoades, A. M., Williams, J. L. & Androsch, R. Crystallization kinetics of polyamide 66 at processing-relevant cooling conditions and high supercooling. *Thermochim. Acta* **603**, 103–109 (2015).
88. Faraj, J. *et al.* Crystallization kinetics of new low viscosity polyamides 66 for thermoplastic composites processing. *Thermochim. Acta* **624**, 27–34 (2016).
89. Pyda, M. *et al.* Melting and Crystallization of Poly(butylene terephthalate) by Temperature-Modulated and Superfast Calorimetry. *J. Polym. Sci. Part B Polym. Phys.* 1364–1377 (2006) doi:10.1002/polb.
90. Androsch, R., Rhoades, A. M., Stolte, I. & Schick, C. Density of heterogeneous and homogeneous crystal nuclei in poly (butylene terephthalate). *Eur. Polym. J.* **66**, 180–189 (2015).
91. Wurm, A. *et al.* Temperature dependency of nucleation efficiency of carbon nanotubes in pet and PBT. *Macromol. Mater. Eng.* **300**, 637–649 (2015).

92. Zhuravlev, E., Schmelzer, J. W. P., Wunderlich, B. & Schick, C. Kinetics of nucleation and crystallization in poly(ε-caprolactone) (PCL). *Polymer (Guildf).* **52**, 1983–1997 (2011).

93. Gradys, A., Sajkiewicz, P., Zhuravlev, E. & Schick, C. Kinetics of isothermal and non-isothermal crystallization of poly(vinylidene fluoride) by fast scanning calorimetry. *Polymer (Guildf).* **82**, 40–48 (2016).

94. Androsch, R. & Schick, C. Crystal nucleation of polymers at high supercooling of the melt. *Adv. Polym. Sci.* **276**, 257–288 (2017).

95. Cavallo, D. *et al.* Continuous cooling curves diagrams of propene/ethylene random copolymers. The role of ethylene counits in mesophase development. *Macromolecules* **43**, 2890–2896 (2010).

96. Mongilyov, I., Rosenthal, M., Van Puyvelde, P. & Goderis, B. Crystallization Competition in a Double Crystallizable Poly(butylene Terephthalate)/Poly(ethylene Glycol) Block Copolymer at High Supercooling. *Macromolecules* (2025) doi:10.1021/acs.macromol.5c00510.

97. Vanden Poel, G., Istrate, D. & Mathot, V. Full-Temperature- Range Crystallization Rates of Polyamides by Fast Scanning Calorimetry as Key to Processing. in *Fast Scanning Calorimetry* 611−632 (Springer International Publishing, 2016).

98. Paolucci, F., van Mook, M. J. H., Govaert, L. E. & Peters, G. W. M. Influence of post-condensation on the crystallization kinetics of PA12: From virgin to reused powder. *Polymer (Guildf).* **175**, 161–170 (2019).

99. Maclaine, J. Q. G. & Booth, C. Effect of molecular weight on spherulite growth rates of high molecular weight poly(ethylene oxide) fractions. *Polymer (Guildf).* **16**, 191–195 (1975).

100. Fernández-Tena, A. *et al.* Effect of Molecular Weight on the Crystallization and Melt Memory of Poly(ϵ-caprolactone) (PCL). *Macromolecules* **56**, 4602–4620 (2023).

101. Point, J. J. & Dosière, M. Crystal growth rate as a function of molecular weight in polyethylene crystallized from the melt: an evaluation of the kinetic theory of polymer crystallization. *Polymer (Guildf).* **30**, 2292–2296 (1989).

102. Zhou, Y. G., Wu, W. Bin, Lu, G. Y. & Zou, J. Isothermal and non-isothermal

crystallization kinetics and predictive modeling in the solidification of poly(cyclohexylene dimethylene cyclohexanedicarboxylate) melt. *J. Elastomers Plast.* **49**, 132–156 (2016).

103. Greco, A. & Ferrari, F. Thermal behavior of PLA plasticized by commercial and cardanol-derived plasticizers and the effect on the mechanical properties. *J. Therm. Anal. Calorim.* **146**, 131–141 (2021).
104. Wadkin-Snaith, D., Mulheran, P. A. & Johnston, K. The impact of plasticisers on crystal nucleation, growth and melting in linear polymers. *Polymer (Guildf).* **304**, 127095 (2024).
105. Baeten, D. *et al.* Simultaneous Synchrotron WAXD and Fast Scanning (Chip) Calorimetry : On the (Isothermal) Crystallization of HDPE and PA11 at High Supercoolings and Cooling Rates up to 200 ° C s − 1. *Macromol. Rapid Commun.* 1184–1191 (2015).
106. Basiura, M. *et al.* Rapidly Cooled Polyethylenes : On the Thermal Stability of the Semicrystalline Morphology. 8399–8411 (2006).
107. *Technical Data Sheet Eastman DMCD*. (2025).
108. Puglisi, C. & Samperi, F. Exchange Reaction Mechanisms in the Reactive Extrusion of Condensation Polymers. in *Reactive Extrusion: Principles and Applications* (eds. Beyer, G. & Hopmann, C.) (Wiley-VCH Verlag GmbH & Co. KGaA, 2018).
109. Costa, L., Luda, M. P., Cameron, G. G. & Qureshi, M. Y. Thermal and thermo-oxidative degradation of poly(tetrahydrofuran) and its complexes with LiBr and LiI. *Polym. Degrad. Stab.* **67**, 527–533 (2000).
110. Schick, C. *Calorimetry*. *Reference Module in Materials Science and Materials Engineering* (Elsevier Ltd., 2016). doi:10.1016/B978-0-12-803581-8.01340-0.
111. Lexow, M. M. & Drummer, D. New Materials for SLS: The Use of Antistatic and Flow Agents. *J. Powder Technol.* **2016**, 1–9 (2016).
112. Boucher, V. M., Cangialosi, D., Alegría, A. & Colmenero, J. Enthalpy recovery of glassy polymers: Dramatic deviations from the extrapolated liquidlike behavior. *Macromolecules* **44**, 8333–8342 (2011).
113. Huang, C. L., Chen, Y. C., Hsiao, T. J., Tsai, J. C. & Wang, C. Effect of

tacticity on viscoelastic properties of polystyrene. *Macromolecules* **44**, 6155–6161 (2011).

114. Rosa, M., Grassia, L., D'Amore, A. & D'Escamard, G. Enthalpy Relaxation of Polystyrene at Different Molecular Weight Using Fast Calorimetry. *Procedia Eng.* **167**, 265–269 (2016).
115. Andreozzi, L., Faetti, M., Giordano, M. & Zulli, F. Molecular-Weight Dependence of Enthalpy Relaxation of PMMA. *Macromolecules* **38**, 6056–6067 (2005).
116. Strobbe, D. Tuning process parameters and polymer powder formulation for Laser Sintering. (2020).
117. Koh, Y. P. & Simon, S. L. Structural Relaxation of Stacked Ultrathin Polystyrene Films. *J. Polym. Sci. Part B Polym. Phys.* **46**, 2741–2753 (2008).
118. Koh, Y. P., Grassia, L. & Simon, S. L. Structural recovery of a single polystyrene thin film using nanocalorimetry to extend the aging time and temperature range. *Thermochim. Acta* **603**, 135–141 (2015).
119. Koh, Y. P., Gao, S. & Simon, S. L. Structural recovery of a single polystyrene thin film using Flash DSC at low aging temperatures. *Polymer (Guildf).* **96**, 182–187 (2016).
120. Koh, Y. P. & Simon, S. L. The glass transition and enthalpy recovery of a single polystyrene ultrathin film using Flash DSC. *J. Chem. Phys.* **146**, (2017).
121. Grassia, L., Koh, Y. P., Rosa, M. & Simon, S. L. Complete Set of Enthalpy Recovery Data Using Flash DSC: Experiment and Modeling. *Macromolecules* **51**, 1549–1558 (2018).
122. Koh, Y. P. & Simon, S. L. Enthalpy recovery of ultrathin polystyrene film using Flash DSC. *Polymer (Guildf).* **143**, 40–45 (2018).
123. Grigoriadi, K. *et al.* Physical ageing of polystyrene: Does tacticity play a role? *Macromolecules* **52**, 5948–5954 (2019).
124. Cowie, J. M. G. & Ferguson, R. Physical ageing of poly(methyl methacrylate) from enthalpy relaxation measurements. *Polymer (Guildf).* **34**, 2135–2141 (1993).
125. Cowie, J. M. G., Harris, S. & Mcewen, I. J. Physical ageing in poly(vinyl

acetate) 1. Enthalpy relaxation. *J. Polym. Sci. Part B Polym. Phys.* **35**, 1107–1116 (1997).

126. Cameron, N. R., Cowie, J. M. G., Ferguson, R. & McEwan, I. Enthalpy relaxation of styrene-maleic anhydride (SMA) copolymers. Part 1. Single component systems. *Polymer (Guildf).* **41**, 7255–7262 (2000).
127. Li, Q. & Simon, S. L. Enthalpy recovery of polymeric glasses: Is the theoretical limiting liquid line reached? *Polymer (Guildf).* **47**, 4781–4788 (2006).
128. Hutchinson, J. M. & Kumar, P. Enthalpy relaxation in polyvinyl acetate. *Thermochim. Acta* **391**, 197–217 (2002).
129. Zhao, H. Y., Koh, Y. P., Pyda, M., Sen, S. & Simon, S. L. The kinetics of the glass transition and physical aging in germanium selenide glasses. *J. Non. Cryst. Solids* **368**, 63–70 (2013).
130. Andreozzi, L., Faetti, M., Giordano, M., Palazzuoli, D. & Zulli, F. Enthalpy relaxation in polymers: A comparison among different multiparameter approaches extending the TNM/AGV model. *Macromolecules* **36**, 7379–7387 (2003).
131. Cangialosi, D., Boucher, V. M., Alegría, A. & Colmenero, J. Direct evidence of two equilibration mechanisms in glassy polymers. *Phys. Rev. Lett.* **111**, 1–5 (2013).
132. Kovacs, A. J. La contraction isotherme du volume des polymères amorphes. *J. Polym. Sci.* **30**, 131–147 (1958).
133. Koh, Y. P. & Simon, S. L. Enthalpy recovery of polystyrene: Does a long-term aging plateau exist? *Macromolecules* **46**, 5815–5821 (2013).
134. Boucher, V. M., Cangialosi, D. & Colmenero, J. Enthalpy Recovery in Nanometer to Micrometer Thick Polystyrene Films. (2012).
135. Cangialosi, D., Alegría, A. & Colmenero, J. Effect of nanostructure on the thermal glass transition and physical aging in polymer materials. *Prog. Polym. Sci.* **54**–**55**, 128–147 (2016).
136. Perez-de-Eulate, N. G., Di Lisio, V. & Cangialos, D. Glass transition and molecular dynamics in polystyrene nanospheres by fast scanning calorimetry. *ACS Macro Lett.* **6**, 859–863 (2017).

137. Ngai, K. L., Capaccioli, S. & Wang, L. Segmental α - Relaxation for the First Step and Sub-Rouse Modes for the Second Step in Enthalpy Recovery in the Glassy State of Polystyrene. (2019) doi:10.1021/acs.macromol.8b02125.

138. Jin, S. & McKenna, G. B. Anomalous structural recovery in the near glass transition range in a polymer glass: Data revisited in light of temperature variability in vacuum oven-based experiments*. *Polym. Eng. Sci.* **62**, 1124–1136 (2022).

139. Greiner, R. & Schwarzl, F. R. Thermal contraction and volume relaxation of amorphous polymers. *Rheol. Acta* **23**, 378–395 (1984).

140. Engels, T. A. P., Govaert, L. E. & Meijer, H. E. H. *Mechanical Characterization of Glassy Polymers: Quantitative Prediction of Their Short- and Long-Term Responses*. *Polymer Science: A Comprehensive Reference, 10 Volume Set* vol. 2 (Elsevier B.V., 2012).

141. Frieberg, B. R., Glynos, E., Sakellariou, G., Tyagi, M. & Green, P. F. Effect of Molecular Stiffness on the Physical Aging of Polymers. *Macromolecules* **53**, 7684–7690 (2020).

142. Hintermeyer, J., Herrmann, A., Kahlau, R., Goiceanu, C. & Rössler E, E. A. Molecular weight dependence of glassy dynamics in linear polymers revisited. *Macromolecules* **41**, 9335–9344 (2008).

143. Cangialosi, D., Boucher, V. M., Alegría, A. & Colmenero, J. Physical aging in polymers and polymer nanocomposites: Recent results and open questions. *Soft Matter* **9**, 8619–8630 (2013).

144. Nozaki, R. & Mashimo, S. Dielectric relaxation measurements of poly(vinyl acetate) in glassy state in the frequency range 10− 6–106 Hz. *J. Chem. Physi* **87**, 2271–2277 (1987).

145. Righetti, M. C., Gazzano, M., Delpouve, N. & Saiter, A. Contribution of the rigid amorphous fraction to physical ageing of semi-crystalline PLLA. *Polymer (Guildf).* **125**, 241–253 (2017).

146. Cangialosi, D. Physical aging and vitrification in polymers and other glasses: Complex behavior and size effects. *J. Polym. Sci.* **62**, 1952–1974 (2024).

147. Koberstein, J. T., Morra, B. & Stein, R. S. The Determination of Diffuse-Boundary Thicknesses of Polymers by Small-Angle X-ray Scattering. *J. Appl.*

Crystallogr. **13**, 34–45 (1980).

148. Mongkolsuttirat, K. & Buajarern, J. Uncertainty evaluation of crystallite size measurements of nanoparticle using X-Ray diffraction analysis (XRD). *J. Phys. Conf. Ser.* **1719**, (2021).

Statement on the use of generative AI

I did not use generative AI assistance tools during the research/writing process of my thesis, except for mere language assistance. The use of GenAI tools for language assistance does not need to be further specified.

Generative AI was used for:

- ~~*Generative AI* was used as a search engine to learn about a particular topic.~~
- ~~*Generative AI* was used for carrying out a literature review.~~
- ~~*Generative AI* was used for short-form input assistance.~~
- ~~*Generative AI* was used for generating programming code.~~
- ~~*Generative AI* was used to generate new research ideas.~~
- ~~*Generative AI* was used to generate visuals.~~
- ***Other:*** ChatGPT was used to support improvements in grammar, spelling, punctuation and sentence flow throughout the text. All generated suggestions were based on content originally written by the author.

The text/code/ images in this thesis are my own (unless otherwise specified) and generative AI has only been used in accordance with the KU Leuven guidelines and appropriate references have been added. I have reviewed and edited the content as needed and I take full responsibility for the content of the thesis.

FACULTY OF SCIENCE
DEPARTMENT OF CHEMISTRY
POLYMER CHEMISTRY AND MATERIALS
Celestijnenlaan 200J box 2404
BE-3001 LEUVEN, Belgium
mouna.hamid@kuleuven.be



Cover design by Lilly Jenisch
“Crys-tile-ization”
lmjenisch@gmail.com